FINAL REPORT

to

Air Force Office of Scientific Research (AFOSR)

Project Title

Influence of Surface Roughness on the Second Order Transport of Turbulence in Non-Equilibrium Boundary Layers

AFOSR Contract No. F49620-02-1-0365

submitted by

M.A.R. Sharif, Ph.D., Principal Investigator

Aerospace Engineering and Mechanics Department

The University of Alabama, Tuscaloosa, AL 35487-0280

Subcontractor

R.D.W. Bowersox, Ph.D.

Aerospace Engineering Department

Texas A&M University, College Station, TX 77845

REPORT DOCUMENTATION PAGE

Form Approved
OMB No. 0704-0188

1. REPORT DATE *(DD-MM-YYYY)*	2. REPORT TYPE	3. DATES COVERED *(From - To)*
08-10-2006	Final Technical	07-01-2002 - 12-31-2005

4. TITLE AND SUBTITLE
Influence of Surface Roughness on the Second Order Transport of Turbulence in Non-Equilibrium Boundary Layers

5a. CONTRACT NUMBER

5b. GRANT NUMBER
F49620-02-1-0365

5c. PROGRAM ELEMENT NUMBER

6. AUTHOR(S)
M.A.R. Sharif
R.D.W. Bowersox

5d. PROJECT NUMBER

5e. TASK NUMBER

5f. WORK UNIT NUMBER

7. PERFORMING ORGANIZATION NAME(S) AND ADDRESS(ES)
The University of Alabama
Box 870104
Tuscaloosa, AL 35487-0104

8. PERFORMING ORGANIZATION REPORT NUMBER

9. SPONSORING/MONITORING AGENCY NAME(S) AND ADDRESS(ES)
USAF/AFRL
AFOSR
875 North Randolph Street
Arlington VA 22203
Rhett Jeffries

10. SPONSOR/MONITOR'S ACRONYM(S)
AFOSR

11. SPONSORING/MONITORING

AFRL-SR-AR-TR-06-0445

12. DISTRIBUTION AVAILABILITY STATEMENT
Approved for public release;
distribution unlimited

13. SUPPLEMENTARY NOTES

14. ABSTRACT

The principal objective of this project was to gain improved understanding for the mean and turbulent flow physics associated with non-equilibrium, strained, supersonic, compressible boundary layer flow over rough curved surfaces and elevated freestream turbulence levels. Measurements of mean flow and turbulence statistics within such boundary layers has been conducted using Particle Imaging Velocimetry (PIV) technique and the data are reported. Numerical simulation of the flow was also conducted using the eddy-viscosity turbulence models and comparison of the predictions with measurements was performed and reported.

This report consists of two parts. The experimental work in this project was subcontracted to R.D.W. Bowersox, Aerospace Engineering Department, Texas A&M University, TX. In Part I, the experimental work done by Bowersox and his group is reported. The pertinent experimental data is given at the end of Part I of this report. The numerical simulation is reported in Part II of this report.

15. SUBJECT TERMS

16. SECURITY CLASSIFICATION OF:			17. LIMITATION OF ABSTRACT	18. NUMBER OF PAGES	19a. NAME OF RESPONSIBLE PERSON
a. REPORT	b. ABSTRACT	c. THIS PAGE			19b. TELEPONE NUMBER *(Include area code)*
U	U	U	UU	157	

Work done at TEES

Experimental measurements of the mean flow and turbulent stresses within the boundary layer over a curved surface in a supersonic turbulent flow have been performed. Three different test section geometries to produce the supersonic flow with zero, medium, and strong favorable pressure gradients were studied. In each case two different surface roughness configurations were used. Supersonic flow was generated by expanding air at a total (stagnation) pressure of 689 kPa and total temperature of 320 K through a converging diverging nozzle to produce a Mach number of 2.86 at the nozzle exit. Measurements were taken at three axial locations along the test section in a surface normal direction into the flow.

Objectives

The principal objective of this project was to gain improved understanding for the mean and turbulent flow physics associated with non-equilibrium, strained, supersonic, compressible boundary layer flow over rough curved surfaces and elevated freestream turbulence levels. Measurements of mean flow and turbulence statistics within such boundary layers has been conducted using Particle Imaging Velocimetry (PIV) technique and the data are reported. Numerical simulation of the flow was also conducted using the eddy-viscosity turbulence models and comparison of the predictions with measurements was performed and reported.

This report consists of two parts. The experimental work in this project was subcontracted to R.D.W. Bowersox, Aerospace Engineering Department, Texas A&M University, TX. In Part I, the experimental work done by Bowersox and his group is reported. The pertinent experimental data is given at the end of Part I of this report. The numerical simulation is reported in Part II of this report.

Status of Effort

Experimental measurements of the mean flow and turbulent stresses within the boundary layer over a curved surface in a supersonic turbulent flow have been completed by Rodney Bowersox and his group at Texas A&M University. Three different test section geometries to produce the supersonic flow with zero, medium, and strong favorable pressure gradients were studied. In each case two different surface roughness configurations (smooth and rough) were used. Curved surfaces with a prescribed geometry were used for the nonzero pressure gradient cases whereas plane surface was

used for the zero pressure gradient case. Supersonic flow was generated by expanding air at a total (stagnation) pressure of 689 kPa and total temperature of 320 K through a converging diverging nozzle to produce a Mach number of 2.86 at the nozzle exit. Measurements were taken at three axial locations along the test section in a surface normal direction into the flow. The details of the experimental work are reported in Part I of this report.

Numerical simulation of the flow for the strong favorable pressure gradient case with smooth and rough surface configurations was also performed using the $k-\omega$ turbulence model. The predictions are compared with the experimental data in Part II of this report.

Accomplishments/New Findings

Experimental data for boundary layer profiles in a supersonic boundary layer over smooth and rough plane and curved surfaces have been obtained using the PIV technique. The major utility of this data would be the development and validation of the turbulence models for calculating similar flows. This type flow is representative of numerous real situations of practical interest to the Air Force. Examination of a realistic non-equilibrium flow is of basic fundamental importance.

Personnel Supported

Three graduate students at the University of Alabama (UA) and one graduate student at the Texas A&M University (TAMU) was provided financial support from this project. They are (1) Johnson Mendonca (UA), (2) Kiran Mothe (UA), (3) Guanghong

Guo (UA), and (4) Issac Ekoto (TAMU). The PI M. Sharif and subcontractor R. Bowersox also received summer salaries and faculty release funds from this project.

Publications

No peer-reviewed journal articles have been published yet. Two journal manuscripts have been submitted and are under review. These are;

1. Sharif, M.A.R. and Guo, G., "Computational Analysis of Supersonic Turbulent Boundary Layer Flow over Plane Rough Surfaces," *Applied Mathematical Modelling*, submitted.
2. Mendonca, J. and Sharif, M.A.R., "Computation of Turbulent Transonic Flow over Circular Arc Bumps with Surface Roughness in a Channel," *International Journal of Computational Fluid Dynamics*, submitted.

Interactions/Transitions

While the experimental setup was being designed, fabricated, and tested at TAMU during the initial phases of this project, the PI and his group at UA was involved in numerical simulation of supersonic and subsonic flows over plane and curved (circular bump) surfaces. This resulted in three articles which were presented in AIAA and ASME Conferences. These are listed below and are included in the appendix of this report.

1. Mendonca, J. and Sharif M.A.R., "Performance of Turbulence Models in the Computation of Transonic Flow over a Circular Arc Bump," *35th AIAA Fluid Dynamics Conference and Exhibit*, AIAA 2005-4637, Toronto, Ontario Canada, June 6-9, 2005.

2. Mothe, K.K. and Sharif M.A.R., "Assessment of Omega Based Models in the Prediction of Turbulent Flows over Rough Surfaces," AIAA-2006-0718, 44th AIAA Aerospace Sciences Meeting and Exhibit, January 9-12, 2006, Reno, Nevada.
3. Guo, G., and M.A.R. Sharif, "Analysis of Supersonic Turbulent Boundary Layers over Rough Surfaces Using the k-omega and Stress-omega Models," FEDSM2005-77443, *Proceedings of FEDSM2005, ASME Fluids Engineering Summer Conference*, Houston, Texas, June 19-23, 2005.

New Discoveries

None

Honors/Awards

None

PART I

(Experimental Investigation)

FINAL REPORT TO

The University of Alabama

Dr. M Sharif (AEM)

TEES Contract Number: C02-00573

Report Number

TAMUNAL – 2006-001

March 30, 2006

Title

Influence of Surface Roughness on the Second Order Transport of Turbulence in Non-Equilibrium Boundary Layers:

Experimental Investigation at Texas A&M University

By

Dr. Rodney D. W. Bowersox and Mr. Isaac W. Ekoto

Aerospace Engineering, Texas A&M University, College Station, TX 77845

1. Introduction

Experimental characterization of turbulent supersonic boundary layers has been performed on a Mach 2.86 Supersonic Wind Tunnel using digital particle image Velocimetry (DPIV). The following report details the design, construction, and performance characteristics of the test facilities along with a description of the experimental techniques that have been used and the associated error of all measurements.

1.1. Background

Low speed, smooth wall, zero pressure gradient (ZPG) turbulent boundary layer flow is understood to the point that flow fields are considered canonical and the semi-empirical correlations (law of the wall, defect law, and energy spectra scaling) and turbulent kinetic energy transport data are routinely used to validate turbulence modeling concepts. Numerous complete reviews of this subject are available [e.g., Schlichting (2003), Schetz (1993), White (2006), Sherman (1990). and Wilcox (1993)].

The fundamental thermodynamic characteristics for compressible flow fields are inherently different than their incompressible counterparts. Defining the shear stress and Reynolds shear stress tensors as:

$$\tau_{ij} = \mu\left(\frac{\partial u_i}{\partial x_j} + \frac{\partial u_j}{\partial x_i}\right) - \frac{2}{3}\mu\frac{\partial u_k}{\partial x_k}$$

$$\tau_{ij}^{T} = -\overline{\rho u_i' u_j'}$$

Then the complete compressible form of the Reynolds Stress Transport Theorem is given below in equation (1.1) as

$$\underbrace{\frac{\partial \tau_{ij}^T}{\partial t}+\frac{\partial \tilde{u}_k \tau_{ij}^T}{\partial x_k}}_{C_{ij}}=\underbrace{-\left(\tau_{jk}^T\frac{\partial \tilde{u}_i}{\partial x_k}+\tau_{ik}^T\frac{\partial \tilde{u}_j}{\partial x_k}\right)}_{P_{ij}}\underbrace{-\left(\overline{u_i''}\frac{\partial \overline{\tau}_{jk}}{\partial x_k}+\overline{u_j''}\frac{\partial \overline{\tau}_{ik}}{\partial x_k}\right)}_{VW_{ij}}+$$

$$\underbrace{\left(\overline{u_i''}\frac{\partial \overline{p}}{\partial x_j}+\overline{u_j''}\frac{\partial \overline{p}}{\partial x_i}\right)}_{PW_{ij}}\underbrace{-\overline{p'\left(\frac{\partial u_i''}{\partial x_j}+\frac{\partial u_j''}{\partial x_i}\right)}}_{R_{ij}}\underbrace{-\frac{\partial}{\partial x_k}\left(\overline{u_i''\tau_{jk}'}+\overline{u_j''\tau_{ik}'}\right)}_{D_{ij}^V}+ \qquad (1.1)$$

$$\underbrace{\frac{\partial}{\partial x_k}\left(\overline{p'u_i''}\delta_{jk}+\overline{p'u_j''}\delta_{ik}-\overline{\rho u_i''u_j''u_k''}\right)}_{D_{ij}^T}+\underbrace{\left(\overline{\tau_{jk}'\frac{\partial u_i''}{\partial x_k}}+\overline{\tau_{ik}'\frac{\partial u_j''}{\partial x_k}}\right)}_{\varepsilon_{ij}}$$

The term on the left hand side represents the convection of the turbulent stresses. The first term on the right hand side is the turbulent stress production while the second and third terms are the viscous and pressure work terms respectively. The fourth term is the pressure strain correlation term, the fifth and sixth terms are the viscous and turbulent diffusion respectively, and the final term is the viscous dissipation.

Morkovin (1961) first observed that many of the differences in the turbulent statistical properties across supersonic and subsonic smooth plate boundary layers can be explained, or at least correlated, by the thermodynamic property variations across the layer. Morkovin's hypothesis is based on smooth wall zero pressure gradient data and the flat plate form of the turbulent kinetic energy transport equation (i.e. a contraction of equation (1.1) neglecting the pressure work terms), and has provided the rationale for using incompressible turbulence models for flows up to Mach 5. While scaling for compressibility has been found to correlate the mean velocity with the low-speed database across smooth boundary layers [Van Driest (1951)] more recent experiments suggest that for turbulent quantities the current database is insufficient [Fernholz *et al.* (1981), Smits *et al.* (1989), Spina *et al.* (1994), Dussauge *et al.* (1996) and Smits and

Dussauge (1996)] even for smooth flat plate boundary layers and that Morkovin's hypothesis may be more restrictive than originally believed.

Numerous experiments on zero pressure gradient surface roughness flows have been performed on both low speed [Nikuradse (1933), Corrsin and Kistler (1955), Perry *et al.* (1969), Simpson (1973), Antonia and Wood (1975), and Schlichting (2003)], and high speed flows [Goddard (1959) and Berg (1979), Fan and Bowersox (1999), Latin and Bowersox (2000), and Pritchett and Bowersox (2001)]. In summary for fully rough boundary layer flows the basic trends show an increase of the turbulence intensities by as much as 30 – 40% and an increase skin friction by as much as a factor of 2, clearly representing an increase in the turbulent production mechanisms and an alteration of the turbulent dissipation. There is a downward shift of the logarithmic region of the law of the wall as a function of the equivalent sand grain roughness height Reynolds number k_s^+. For supersonic flows it has been shown that the increase in the turbulent properties and the downward shift of the law of the wall velocity profile follows the incompressible case when the Van Driest II compressibility transformation is used. The transverse-velocity-density correlation increased rapidly with roughness height. It has been shown that the influence of smaller roughness elements increased the skin frictional losses more than the boundary layer turbulence levels. However, as the roughness height was increased, the turbulence production relative to the frictional losses increased. In supersonic flow fields spectra data indicates that roughness has the effect of populating the boundary layer with higher energy eddies that are distributed over a narrower range of scales as compared to the smooth plate. Differences in roughness topology lead to

significant variances (up to 25%) in turbulent quantities, most likely due to shock boundary layer interactions.

The effects of pressure gradient on low-speed boundary layers have also been the subject of numerous investigations; e.g., reviews are presented in [Bradshaw (1973), Sherman (1990), White (2006) and Schetz (1993)]. In summary, the inner region boundary layer scaling (i.e., law of the wall) has been shown to hold in the presence favorable and adverse pressure gradients. The logarithmic region termination height has been shown to depend on the strength of the pressure gradient; for favorable pressure gradients, the height increases and for adverse pressure gradients it decreases. Near separation, the inner scaling breaks down. The outer region of the boundary layer is very sensitive to pressure gradient, and in general the defect law does not hold. However, Clauser (1956) defined a pressure gradient strength parameter (β) as the product of the axial pressure gradient (dp/dx) and the ratio of the boundary layer displacement thickness (δ^*) and wall shear stress (τ_{wall}) [i.e., $\beta = -(\delta^*/\tau_{wall})(dp/dx)$], and when β is constant, the boundary layers are in equilibrium; i.e., the defect scaling laws hold and the corresponding profiles are independent of axial location). Coles (1956) used this idea to generalize the law of the wake for equilibrium pressure gradient flows. For very strong adverse pressure gradients, the velocity profile is such that maximum shear stress moves away from the wall, and usual defect law scaling breaks down. Perry and Schofield (1969) introduced a new outer scaling law for strong adverse equilibrium and quasi-equilibrium (flows where the pressure gradients are mild enough that β depends only on local flow conditions) flows. Power law axial velocity distributions produce equilibrium (or quasi-equilibrium flows).

As observed for diffusers and nozzles, flows that have favorable pressure gradients without wall curvature (i.e., accelerating flows) has a reduction in turbulence levels; the opposite is true for adverse pressure gradients. Concave and convex curvature, with and without [Thomann (1968)] an associate pressure gradient, have been shown to have de-stabilizing and stabilizing effects, respectively, on the turbulent flow properties of across low-speed boundary layers [Bradshaw (1969, 1973)]. For convex curvature, the turbulence levels, turbulent shear stresses and wall friction all decrease relative to canonical flat surface values; the opposite is observed for concave curvature. These trends are explained by simple angular momentum arguments. The angular momentum terms in the Navier-Stokes equations for planar flow over curved surfaces are on the order of the ratio of the boundary layer thickness and radius of curvature of the wall turning; hence, the effects are first order. For laminar flow, the effects have been shown to be first order. However for turbulent flows, the effects of wall curvature are significantly larger (approximately a factor of 10) than expected, where heuristic empirical corrections are required to account for this effect in predictions [Bradshaw (1969, 1974)]. The effects of wall curvature are most pronounced in the outer region of the boundary layer, where for strong wall curvatures (e.g., ratio of the boundary thickness and wall radius of curvature of order 0.1), negative Reynolds shear stresses have been observed [Shivaprasad and Ramaprian (1978)]. Kim and Simon (1988) report that the turbulent heat flux is affected by curvature more than the turbulent shear stress.

Many of the observed differences between distorted supersonic and subsonic boundary layers can be explained in terms of the fluid property changes across the boundary layer [Spina *et al.* (1994), Smith and Smits (1994) and Bradshaw (1974)].

However, supersonic flows possess phenomena that do not have incompressible counterparts. For example, wave (expansion or compression) boundary layer interactions, where the longitudinal pressure gradients can lead to compression or dilatation, which in turn affects the velocity, pressure and density fluctuations, are not present in subsonic flow.

When a favorable pressure gradient in the axial direction is imposed on a supersonic boundary layer, the flow is distorted by both the effects of pressure gradient and by bulk dilatation. The ratio of the extra strain rates to the primary $\partial\overline{u}/\partial y$ velocity gradient, called the distortion parameter, has been used as a convenient means to classify a pressure gradient [Bradshaw (1973)]. A distortion is generally considered mild if $d_{max} \approx$ 0.01 and strong for $d_{max} \approx 0.1$ [Spina *et al.* (1994)]. If the distortion is applied for a time that is comparable to an eddy lifetime, then the impulse parameter (I), the time-integrated strain rate, may be a better choice [Smith and Smits (1994)]. For an impulsive perturbation resulting from a region of bulk compression, $I_p = ln(p2/p1)/\gamma$ [Smith and Smits (1994) and Hayakawa *et al.* (1984)]. For an impulse as a result of curvature, $I_\phi = \Delta\phi$ [Smits *et al.* (1979)].Even though the interactions between the strain rates are most likely nonlinear, the linear addition of the perturbation strengths is usually accepted for crude comparisons among different flows. Luker *et al.* (1998) present a generalization of the pressure gradient strength definition

Collectively, the available turbulence data [Donovan (1993), Smith and Smits (1991), Jarayam *et al.* (1987), Dussauge and Gaviglio (1987) and Thomann (1968)] indicate that the axial turbulence intensities decrease by 70-90% for I_p and I_ϕ values $\in$ (-0.4,-1.0) and (-0.1,-0.3), respectively. Because of the reduction in the fluctuating

properties, as well as reductions in the skin friction and heat transfer, favorable pressure gradients are often characterized as having a stabilizing effect. Relaminarization of part of the boundary layer is believed possible if the pressure gradient is strong enough [Spina *et al.* (1994) and Jarayam *et al.* (1987)]. Smith and Smits (1991) and Dussauge and Gaviglio (1987) estimated, using a rapid distortion analysis, that the majority of the turbulence reduction was the result of mean bulk dilatation.

Arnette *et al.* (1996) showed that the overall magnitude of the kinematic Reynolds shear stress was dramatically decreased across the entire boundary layer for 7.0 and 14.0 deg. centered and gradual expansions. They further defined an "apparent reverse transition," where the normal energy transfer from the mean flow had been reversed, to describe a sign changing of the Reynolds shear stress. Although the Arnette *et al.* (1996) study provided detailed turbulence information throughout the expansion, the axial spacing was not refined enough to resolve the axial strain rates.

Luker *et al.* (2000), Bowersox *et al.* (2000), Luker *et al.* (1998), and Bowersox and Buter (1996) performed detailed investigations of the influence of the wall curvature driven pressure gradients on the turbulent flow field including the turbulent shear stress transport. Focusing only on the favorable pressure gradient flow, the turbulence data indicated that the present favorable pressure gradient had a stabilizing effect on the turbulent quantities. The magnitude of the Reynolds shear stress was also reduced by the favorable pressure gradient; in the near-wall region it was approximately 25% of the zero pressure gradient value, and in the outer region ($y/\delta > 0.5$), the kinematic Reynolds shear stresses *were negative and the principle strain rates were positive.* The three-dimensional strain rate measurements and the associated extra production indicated that the overall

turbulence production was also negative in the outer half of the favorable pressure gradient boundary layer. In addition, the use of a body-intrinsic coordinate system contributed to the reduced shear stress levels. Also the data collectively indicated that the favorable pressure gradient was disintegrating the large-scale eddies into smaller ones. This redistribution of energy increased the amount of turbulent energy available for dissipation by the flow, which in turn had the observed stabilizing effect on the boundary layer. Numerical simulations using two-equation turbulence modeling demonstrated that the eddy viscosity approach was inadequate for these very mild pressure gradient flows.

All of the findings listed above are relevant to this work, however the negative shear stresses and the coordinate system dependency have received previous attention from a modeling perspective. Johnson *et al.* (1994) discuss the simulation of favorable pressure gradient boundary layers with negative turbulent shear stresses. They indicated that the experimental turbulent shear stresses could be made positive with a suitable coordinate transformation. They introduced on an *ad hoc* basis the "shear layer coordinated system," defined as parallel and perpendicular to streamline such that $\overline{u}/\overline{u}_{\infty} = 0.5$ for this purpose. Also noteworthy was the fact that when applied to the numerical results, the coordinate transformation had a much smaller effect on the turbulent shear stress levels than that for the experimental data. This smaller effect was the result of the numerical models' poor predictions of the axial shear stresses, which are important elements in the transformation.

1.2. Motivation

A large amount of research has been performed to quantify the effects of Mach number, roughness, and wall curvature on turbulent boundary layers. However, studies of

complex geometry flow that include measurements of second-order turbulence statistical moments are lacking; this finding is consistent with the article by Hefner (1999). As noted by Latin and Bowersox (2002) there is a redistribution of the turbulent energy towards larger eddies and a decrease range of the scales via an increase in the production mechanisms. The results by Luker and Bowersox (2000) however show that favorable pressure gradients have a stabilizing effect on the boundary layers and had a disintegrating effect on the larger eddies via a manipulation of the dissipation mechanisms. The current study will combine the large scale surface roughness present in the Latin (2000, 2002) study with the curvature driven favorable pressure gradients from the Luker (1998, 2000) study to examine their combined effects. It is believed that if the pressure gradients are strong enough, it may be possible to create a sort of relaminarization of the boundary layer as the large scale and small range of eddies caused by surface roughness is redistributed towards the smaller scales of turbulence by the favorable pressure gradients and potentially redistributed. The uniform roughness will also create shock boundary layer interactions that weren't present in the smooth plate Luker (1998, 2000) study.

1.3. Objective

A supersonic wind tunnel will be designed and built at the Oran W. Nicks Low Speed Wind Tunnel facility at Texas A&M University. The tunnel will be designed to produce low freestream turbulence intensities and will incorporate a circulation heater to ensure that adiabatic wall temperatures are maintained at the model surface. Models with three different curvature driven favorable pressure gradients and two different surface roughness patterns will be designed and fabricated. Experimental measurements of

instantaneous velocity flow fields will be obtained on using Particle Image Velocimetry. The flow fields will then be averaged together to produce mean and fluctuating velocity quantities so that the Reynolds Shear Stresses may be estimated.

2. Wind Tunnel Facilities

Data were collected in a supersonic wind tunnel located at Texas A&M University. The tunnel is a blow down facility. A finite-radius, half-nozzle was used to produce a freestream Mach number at the nozzle exit of 2.86. The contoured side of the nozzle was located along the tunnel ceiling. The stagnation pressure and temperature were 68.9 KPa ($\pm$ 5.0%) and 320K ($\pm$ 3.5%) respectively. A schematic of the facility is illustrated in Figure 1.

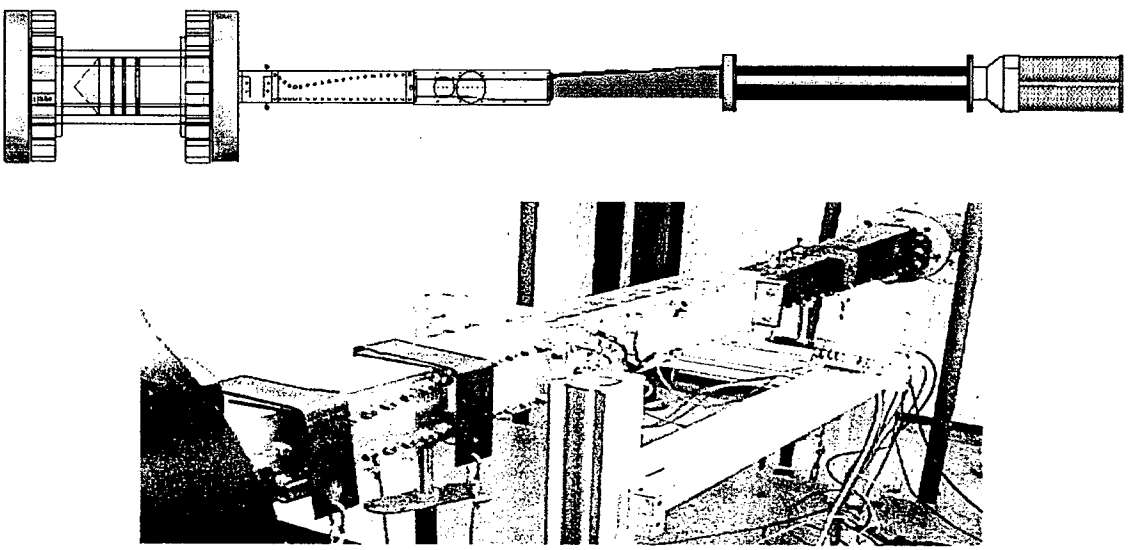

Figure 1: Mach 2.86 Supersonic Blow-Down Wind Tunnel

2.1. Compressed Air Facilities

Compressed Air is supplied by 2 four-stage Chicago Pneumatic TCB-4 compressors illustrated in Figure 2 that were formerly installed in a NASA rocket vehicle test facility. Each unit is powered by a 112 kilowatt motor and is rated to provide a mass

flow rate of 0.13 kg/s at 24.0 MPa. The maximum discharge pressure for each compressor is limited to 15.5 MPa. Moisture, oil, and other particulates produced by the compressors are removed by passing the air through a Domnick Hunter HDL-500 High Pressure Heatless Regenerative Air Dryer. The dryer is a high pressure dual tower heatless regenerative desiccant air dryer. Compressed air is dried by the desiccant in one tank while the other tank is regenerated. The tanks are alternated from a drying cycle to a regeneration cycle and every 5 minutes. The rated mass flow rate of the dryer is 0.28 kg/s at 13.8 MPa.

a) **b)**

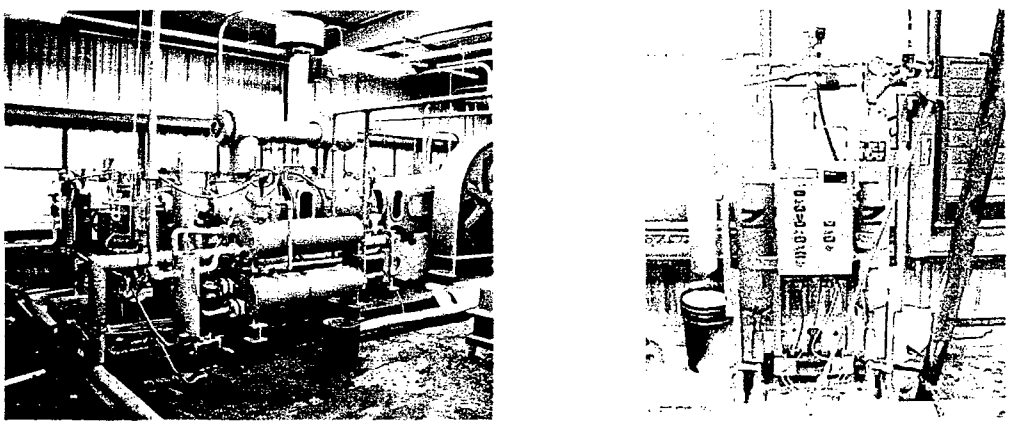

Figure 2: a) Chicago Pneumatic TCB-4 compressor. b) Domnick Hunter HDL-500 high pressure heatless regenerative air dryer

Compressed air is stored in an A. D. Smith high pressure storage tank, which has an internal volume of 23.3 cubic meters and a maximum operating pressure of 19.3 MPa. Between the wind tunnel and the storage tank, there is approximately 65 m of pipe. The pipe is made of schedule XX A105 carbon steel. It has an outer diameter of 11.4 cm, an inner diameter of 8.0 cm, and a maximum rated pressure of 27.9 MPa.

a) b)

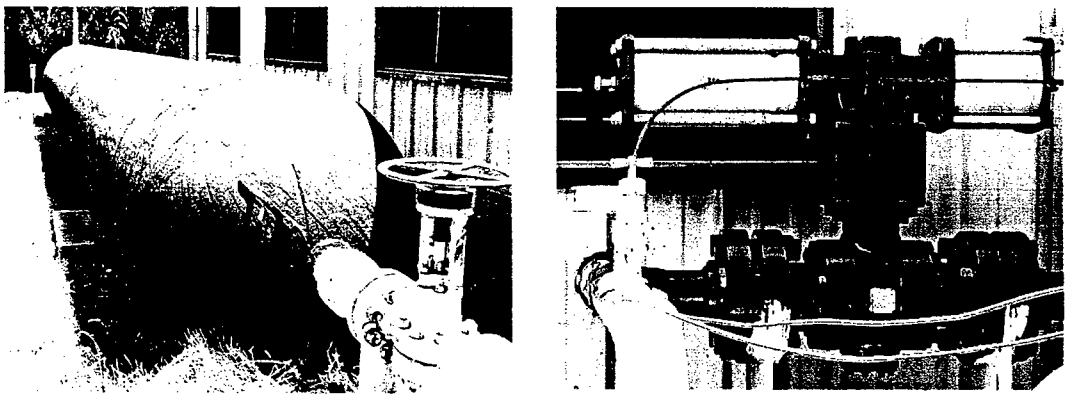

c)

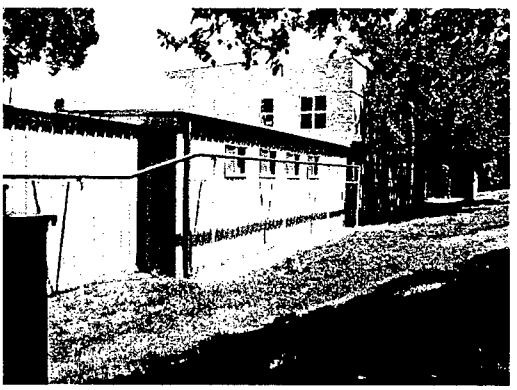

Figure 3: **a) A. D. Smith high pressure storage tank. b) Morin B series actuator controlling Virgo Engineers Trunion Mounted Ball Valve. c) Sch XX A105 carbon steel pipe main line.**

A 4-1500 full bore Virgo Engineers Trunion Mounted Ball Valve controlled by a B-270U-S100 Morin Series B pneumatic actuator has been placed between the storage tank and the wind tunnel. The actuator is a spring return quarter-turn model which requires a supply pressure of 0.69 MPa which is controlled by an ASCO 3-way normally closed solenoid valve that uses shop air.

Pressure from the main line is regulated down to the tunnel operating pressure using a Straval model PRH-0022-20T dome loaded pressure regulator. The regulator has a maximum inlet pressure of 20.7 MPa, and an adjustable outlet pressure of 0.45 – 1.31 MPa with a maximum flow rate of 3.36 kg/s.

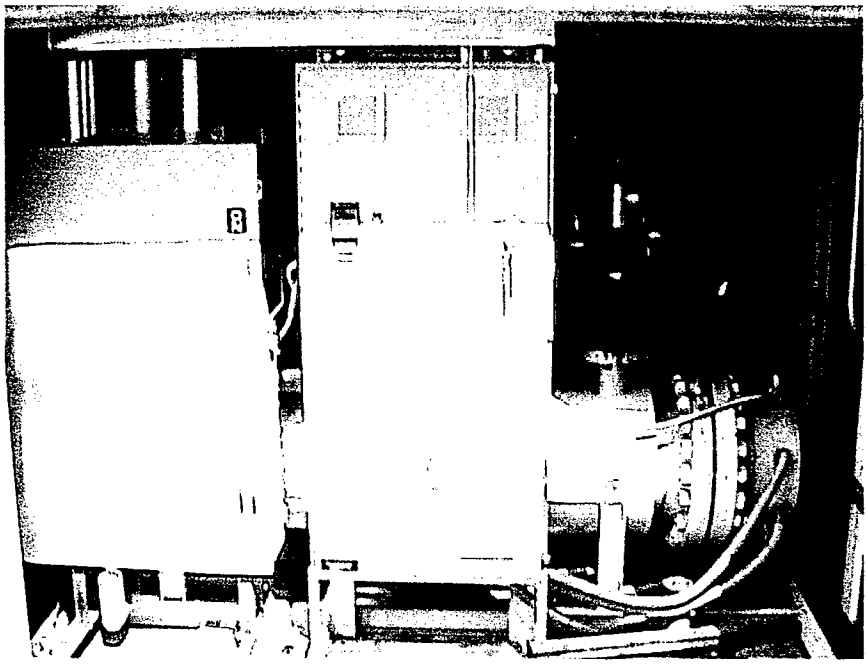

Figure 4: Chromalox 535 kW circulation heater

In order to eliminate heat transfer from model surfaces to the boundary layer, the incoming air is heated using a Chromalox 535 kW circulation heater so that the boundary layer adiabatic wall temperature closely matches the actual wall temperature. The adiabatic wall temperature is found by the following relation between adiabatic wall, boundary layer edge, and stagnation temperatures:

$$r = \frac{T_{aw} - T_e}{T_0 - T_e} \tag{2.1}$$

Where r is the *adiabatic recovery factor* which is approximated as $r \approx \sqrt[3]{\Pr}$ and Pr is the turbulent Prandtl number. For air with a Mach number of 2.9, $\Pr \approx 0.71$ and $r \approx 0.892$. The boundary layer edge temperature can be calculated in terms of the stagnation temperature using the isentropic temperature relation.

$$\frac{T_0}{T_e} = 1 + \frac{\gamma - 1}{2} M^2 \tag{2.2}$$

Combining equations (2.1) and (2.2) gives the following relation for the adiabatic wall temperature in terms of the total temperature, the adiabatic recovery factor, and the freestream Mach number.

$$\frac{T_{aw}}{T_0} = \frac{1 + r\frac{(\gamma - 1)}{2} M^2}{1 + \frac{(\gamma - 1)}{2} M^2} \tag{2.3}$$

Because of the small duration of the tunnel run times (> 90 seconds) and the low thermal conductivity of Plexiglas ($1.2 \times 10^{-4}\ cal/cm - s - ^{o} C$) it has been assumed that the tunnel surface temperatures remained constant at the lab temperature which was maintained at 296 K.

2.2. Settling Chamber

Smooth uniform flow with measured freestream turbulence intensities of less than 1%, are produced by passing the compressed air a through a settling chamber. The external structure of the settling chamber is constructed of 14" schedule 160 pipe carbon steel pipe 0.91m long, 0.36m in diameter, and with a wall thickness of 4.0cm. It is designed for a maximum working pressure of 1.55MPa. The settling chamber exterior is capped at each end by class 1500 blind and slip on flanges. The inlet blind flange has a 3" NPT hole placed where it connects with the main line, and the exit blind flange has a 7.62cm by 7.62cm square hole for the transition to the nozzle. A schematic of the settling chamber interior is given below in Figure 5. Initially air is passed through a 12.7cm diameter cylinder that is 12.7 cm long to quickly redistribute the mass of the air away

from the chamber centerline. It has 56 evenly spaced holes that are 12.7mm in diameter. The flow is straightened by passing it through a reverse cone that has 225 evenly spaced 4.8 mm diameter holes. Finally the turbulence intensities are minimized by passing the flow through 3 wire mesh screens evenly spaced 3.81cm apart. The mesh made of woven stainless steel wire with a diameter of 88.9μm with 28 x 28 strands per cubic centimeter. The open area of the mesh is 55% and the wire Reynolds number is $Re_w = 263$. The exit is constructed of 4 pieces of pipe that have been halved along their centerline, cut at 45 degree angles, and joined together to form a square. The outer diameter of the pipe is 6.03cm, the dimension of the inner square is 7.62cm x 7.62cm, and the dimension of the outer square is 16.2cm x 16.2cm. It was designed so that the inviscid core of the pipe flow is allowed to pass through, so that boundary layer growth doesn't begin until the inlet of the nozzle.

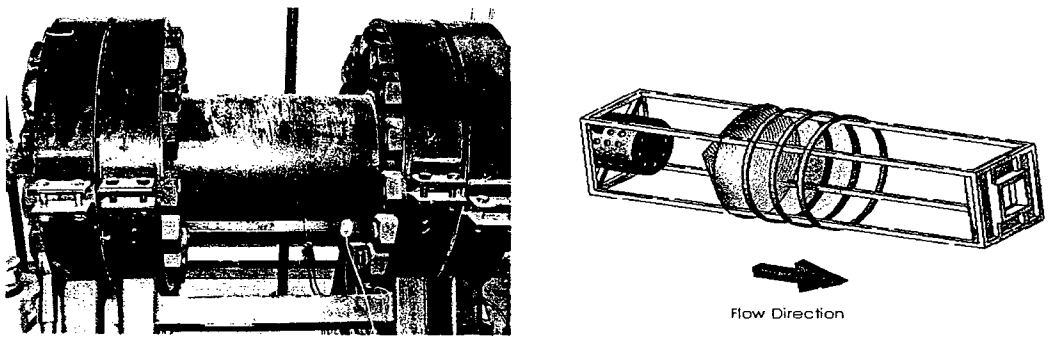

Figure 5: Settling Chamber and schematic of settling chamber flow straightener.

2.3. Nozzle

The nozzle is Mach 2.9 half-nozzle with 3 characteristic Mach wave reflections. The nozzle was constructed using aluminum 6061 and a schematic is listed in Figure 6. The nozzle inlet and exit height are 7.62cm, and the throat height is 1.68cm. The side walls of the nozzle are 2.54cm thick and the entire nozzle assembly is held together with 42 grade 8 bolts with a diameter of 1.27cm. Grooves for 3.81mm diameter o-rings have been created 4.45mm above the nozzle surface. A groove for an o-ring has also been milled around the nozzle exit.

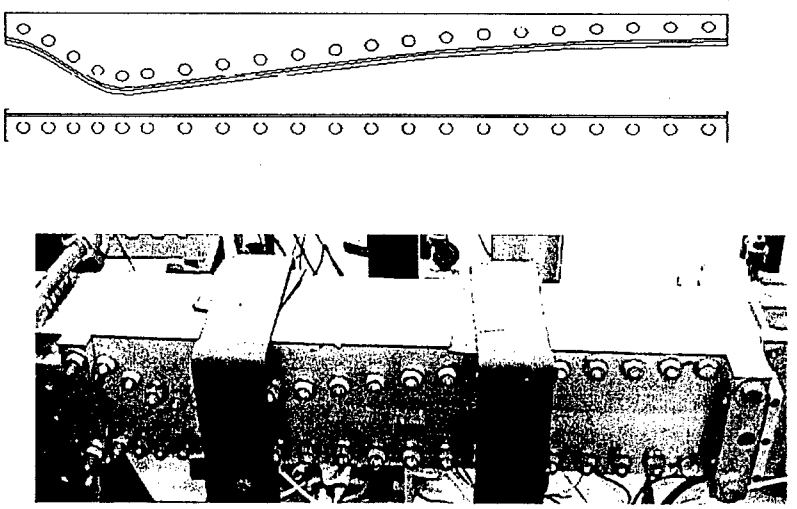

Figure 6: Mach 2.9 half-nozzle

2.4. Diffuser

A variable throat diffuser is used to reduce the required stagnation pressure required for running the wind tunnel. The inlet height of the diffuser is 7.62cm and the exit height increases to 14.0cm. An exhaust muffler has been placed at the end of the

diffuser to reduce noise. The muffler has four chambers, and has a maximum mass flow rate of 20.2 kg/s at 0.62 MPa. Noise from the diffuser is reduced by 17 to 22 decibels.

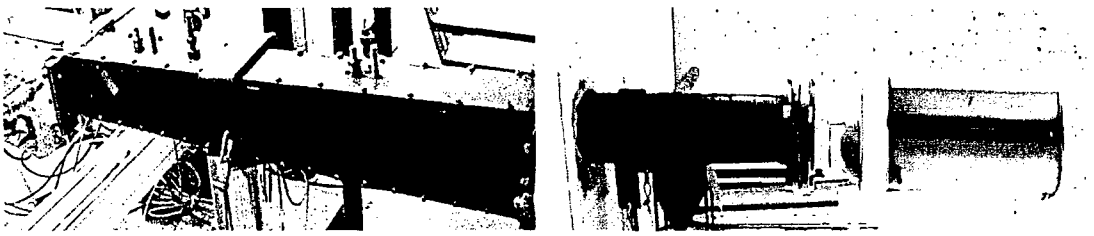

2.5. Test Section

The test section was designed so that DPIV measurements could be accurately and efficiently obtained. The sidewall is constructed of aluminum and is 71.1 cm long, 17.8 cm wide, and 1.27 cm thick. Symmetric mounting brackets are used to connect the sidewall to the nozzle exit and diffuser inlet. There are three different measurement locations located 15.9 cm, 29.8 cm, and 41.3 cm downstream of the nozzle exit respectively.

The DPIV sidewall has two fused silica windows placed along the test section's axial centerline. The first window is 10.2 cm in diameter and has been placed 15.9 cm downstream from the nozzle exit while the second window is 15.2 cm in diameter and is 29.8 cm downstream from the nozzle exit. Within each window hole there are two o-ring grooves for 2.38 mm thick o-rings. Because the sidewall mounts are symmetric, the location of the windows can be adjusted by rotating the sidewall about its lateral axis creating the third measurement location. The second sidewall is used to obtain static pressure measurements along the test section's axial centerline. On the outer side of the sidewall 1/8" NPT threaded holes have been distributed at 23 locations beginning 7.62

cm down from the nozzle exit, spaced 2.54 cm apart, and are 9.53 mm deep. On the tunnel side of the sidewall each NPT hole is joined by a 1.59 mm static pressure port hole. The Omega pressure transducers can be screwed into the sidewalls via a 1/4" - 1/8" F/M NPT adapter while the unused ports are plugged.

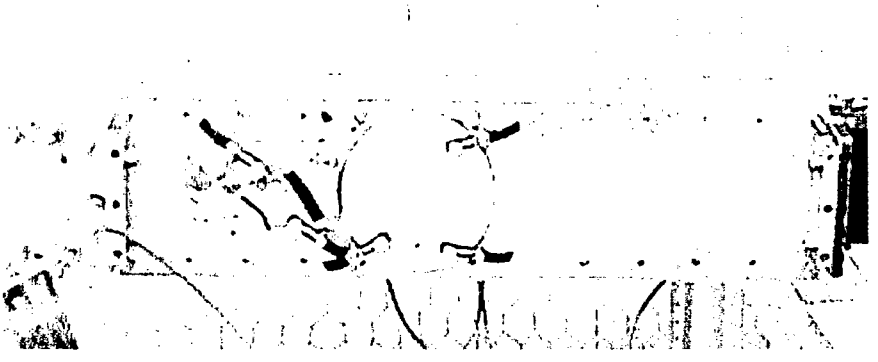

Figure 7: Mach 2.9 test section sidewall.

The ceiling and floors are constructed of Plexiglas most of the laser light is allowed to pass through them (~92%), minimizing wall reflection during PIV. The models vary between 2.54 and 4.45 cm in thickness depending on the model and the location of the curvature. The models contain seven 7.94 mm holes that are 1.27 cm up from the base of each model that are used to join the test section sidewalls and the floor and ceiling together.

2.6. Tunnel Control and Monitoring System

Total pressure is measured in the settling chamber via a pitot probe using an Omega PX303 voltage output pressure transducer. The transducer is capable of measuring 0 – 0.69 MPa and outputs this value a DC voltage between 0.5 – 5.5 volts DC. The total temperature is measured using an Omega JQSS model thermocouple and the

signal is amplified by an OMNI AMP-IV thermocouple amplifier. The tunnel static pressure is measured by 5 Omega PX303 voltage output pressure transducers with a range of 0 – 0.10 MPa. The accuracy of the transducers is 0.25% full scale. The first transducer is located at the nozzle exit, and the other 4 are distributed along the centerline of the test section sidewall. Data from the pressure transducers and thermocouples is collected in a personal computer and processed by a KPCI-3110 data acquisition board with a sampling rate of 1.25 MS/s. The board has 12 bit resolution and can support up to 32 single ended or 16 differential channels. The software used to process the data is TestPoint version 4.

3. Tunnel Models

The tunnel models were designed to incorporate the combined effects of surface roughness and favorable pressure gradient consistent with the goals presented in the introduction.

3.1. Roughness

An aerodynamically smooth plate and fully rough regularly spaced surface roughness pattern with k_s^+ values similar to those used in Latin and Bowersox (2000). The roughness elements used 3-D uniformly distributed squares that are 3.18 mm wide and were cut with a 1.59 mm ball end mill to a depth of 0.794 mm. Because production mechanisms that more closely resembled sand-grain roughness were desired, the 3-D elements were used. The uniform roughness was selected because it is simple to manufacture and to grid for CFD applications that use DES or LES rather than rough wall boundary conditions.

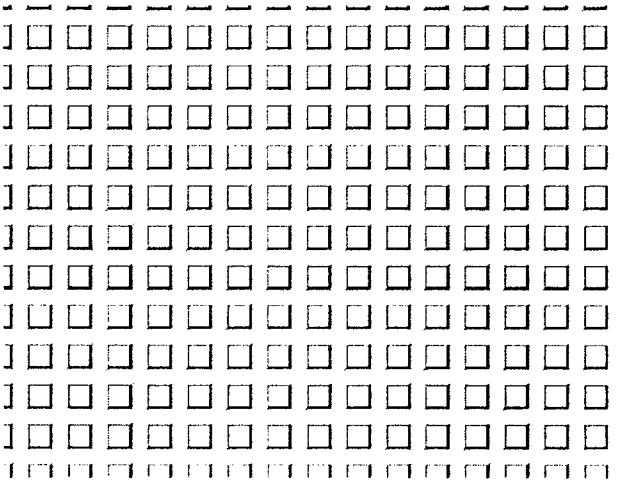

Figure 8: Roughness topology. Roughness elements are 3.18 mm square elements separated by 1.59 mm semi-circle channels.

3.2. Pressure Gradient Selection

The primary mechanisms of concern in the Reynolds Stress Transport Model are the production and pressure work terms from equation (1.1). The mean flow velocity and velocity gradients are negligible in the lateral direction. The resulting 2D component of the production and pressure work terms becomes respectively

$$P_{xy} \approx -\bar{\rho}\overline{v'^2}\frac{\partial \bar{u}}{\partial y} \tag{3.1}$$

$$PW_{xy} = -\overline{v''}\frac{\partial \bar{p}}{\partial x} \tag{3.2}$$

The relationship between the fluctuating velocities has been approximated by the $v' = Cu'$ where $C \approx -0.7$ based on experimental data. Production can thus be approximated as

$$P_{xy} = -C\bar{\rho}\overline{u'v'}\frac{\partial \bar{u}}{\partial y} \tag{3.3}$$

The equation of state for an ideal gas for fluctuating thermodynamic properties and the isentropic relations for fluctuating temperature are give as follows:

$$\frac{p'}{\bar{p}} = \frac{\rho'}{\bar{\rho}} + \frac{T'}{\bar{T}} \tag{3.4}$$

$$C_p\left(\bar{T}_t + T_t'\right) = C_p\left(\bar{T} + T'\right) + \frac{\bar{u}^2 + 2\bar{u}u' + u'^2}{2} \tag{3.5}$$

From the strong Reynolds analogy it can be assumed that and $p' = 0$. From boundary conditions and equation (3.4)

$$\frac{\rho'}{\bar{\rho}} = -\frac{T'}{\bar{T}} \tag{3.6}$$

An additional assumption that can be made using the SRA is that $T_t' = 0$. Using this assumption and equation (3.5) the following is obtained.

$$\frac{T'}{\bar{T}} = -\frac{\bar{u}u'}{C_p\bar{T}} \tag{3.7}$$

Which can be rewritten as:

$$\frac{T'}{\bar{T}} = -(\gamma - 1)\bar{M}^2\frac{u'}{\bar{u}} \tag{3.8}$$

Combining equations (3.6) and (3.8) multiplying both sides by v' and averaging produces

$$\frac{\overline{\rho'v'}}{\bar{\rho}} = \frac{(\gamma - 1)}{2}\bar{M}^2\frac{\overline{u'v'}}{\bar{u}} \tag{3.9}$$

Which can be rewritten as

$$\bar{\rho}\overline{u'v'} = \frac{2\bar{u}}{(\gamma - 1)\bar{M}^2}\overline{\rho'v'} \tag{3.10}$$

The production can now be written in terms of (3.3) and (3.10) to produce:

$$P_{xy} \approx -C \frac{2\bar{u}}{(\gamma-1)\bar{M}^2} \overline{\rho' v'} \frac{\partial \bar{u}}{\partial y} \tag{3.11}$$

The velocity gradient can be approximated by

$$\frac{\partial \bar{u}}{\partial y} \approx \frac{\bar{u}}{\delta}$$

Boundary layer growth rates need to be estimated for the different pressure gradients, but assuming there is no separation, to a first order approximation flat plate turbulent boundary layer assumptions are valid. The production now has the approximate solution:

$$P_{xy} \approx -C \frac{1}{\delta} \frac{2\bar{u}^2}{(\gamma-1)\bar{M}^2} \overline{\rho' v'} \tag{3.12}$$

For any Favre-averaged quantity, the following relation can be used.

$$\overline{f''} = -\frac{\overline{f'\rho'}}{\bar{\rho}}$$

Combining the above relation along with equation (3.2) gives the following expressing for the pressure work

$$PW_{xy} \approx \frac{\overline{v'\rho'}}{\bar{\rho}} \frac{\partial \bar{p}}{\partial x} \tag{3.13}$$

The pressure gradient is approximated by

$$\frac{\partial \bar{p}}{\partial x} \approx \frac{p_2 - p_1}{L}$$

where L is the distance between the beginning and end the axial curvature. A first order approximation of the pressure work using the estimate for the pressure gradient and equation (3.13) is

$$PW_{xy} \approx \frac{\overline{v'\rho'}}{\bar{\rho}} \frac{p_2 - p_1}{L} \tag{3.14}$$

Taking the ratio between the 2D pressure work (3.14) and production terms (3.12) produces a pressure work influence parameter ζ which is defined as the ratio between the pressure work and the turbulent production.

$$\zeta \equiv \frac{PW_{xy}}{P_{xy}} \approx -\frac{1}{C}(\gamma - 1)\bar{M}^2 \frac{p_2 - p_1}{2\bar{\rho}\bar{u}^2} \frac{\delta}{L} \tag{3.15}$$

The average Mach number can be estimated by assuming the pressure gradient in the transverse direction is negligible which implies that

$$\frac{T_w}{\bar{T}} \approx \frac{\bar{\rho}}{\rho_w} \tag{3.16}$$

Using equation (3.16) the average Mach number is given as

$$\bar{M}^2 = \frac{\bar{u}^2}{\gamma R T_w} \frac{\bar{\rho}}{\rho_w} \tag{3.17}$$

The final approximate form of the equation is given as

$$\zeta \approx -\frac{1}{C}(\gamma - 1)\frac{p_2 - p_1}{2\rho_w a_w^2} \frac{\delta}{L} \tag{3.18}$$

Because the wall temperature is adiabatic, equations (2.2) and (2.3) can be used with equation (3.16) and the equation of state to find all thermodynamic properties at the wall. The boundary layer height is estimated using simple flat plate turbulent boundary layer growth rates with corrections for the favorable pressure gradient based on experimental data and using an inviscid technique such as method of characteristics to estimate the thermodynamic properties at the boundary layer edge.

Table 1 lists the start and end location for the wall curvature along with the estimated value of ζ. A flat plate zero pressure gradient (ZPG) model, weak pressure gradient (WPG) model, and strong pressure gradient (SPG) model were created based on the parameter ζ. The curvature for the WPG model and the SPG model was created using a third order polynomial with the boundary conditions that the slope and the start and end points are zero, while the curvature began at 0 and ended and -1.91 cm in the y-direction. The parameter L was varied in equation (3.18) until the desired value of ζ was obtained.

	x_1	x_2	ζ
ZPG	N/A	N/A	0
WPG	24.54 cm	63.40 cm	0.015
SPG	24.54 cm	39.82 cm	0.15

Table 1: Wall curvature location and estimated value of the pressure work influence parameter ζ.

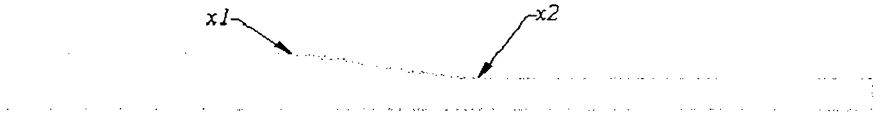

Figure 9: Schematic of test section models.

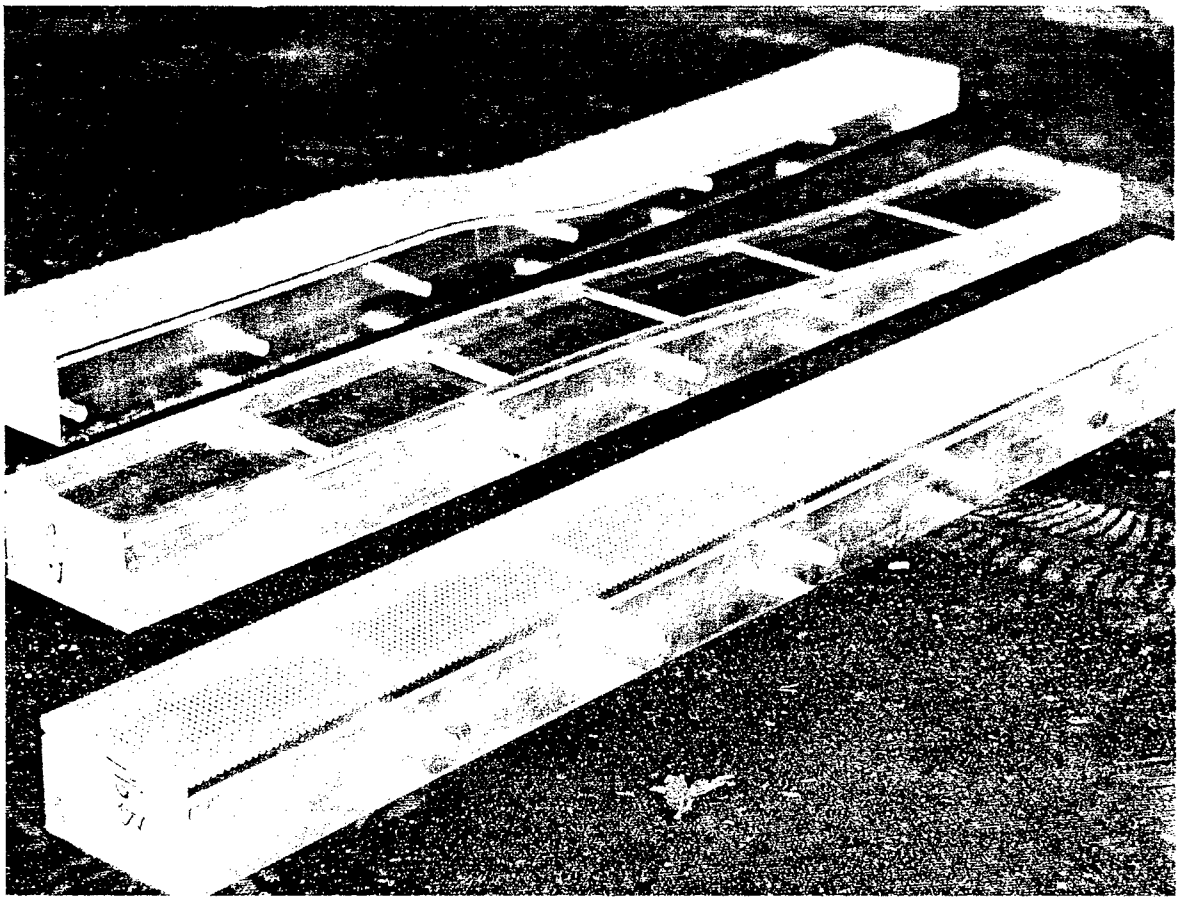

Figure 10: Illustration of three different pressure gradient models, with and without surface roughness.

The freestream Mach number has been calculated using static pressure ports that are distributed along the tunnel centerline. The Mach number is computed from the isentropic pressure relation:

$$M = \sqrt{\left[\left(\frac{p_0}{p}\right)^{\frac{\gamma}{\gamma-1}} - 1\right]\frac{2}{\gamma-1}} \tag{3.19}$$

The locations of the pressure taps from the nozzle exit are presented below in. Note that the first pressure tap is placed just before the nozzle exit, while the remaining four taps are located within the test section.

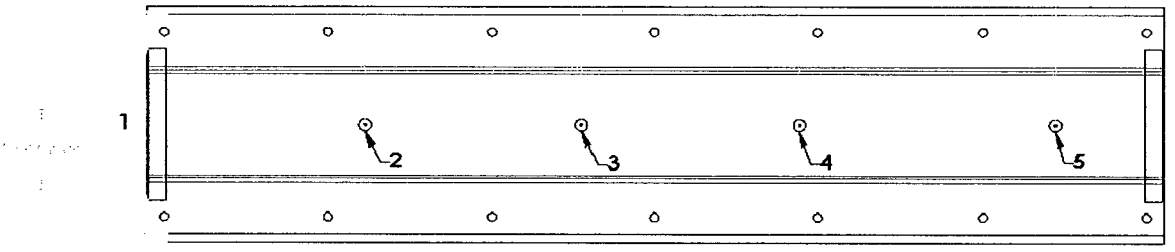

	1	2	3	4	5
Location	-1.27 cm	15.24 cm	30.48 cm	45.72 cm	63.50 cm

Figure 11: Static pressure port location.

The local freestream Mach number computed using equation (3.19) is given below at each static pressure port location.

Pressure Gradient	Roughness	M1	M2	M3	M4	M5
Zero	Smooth	2.86	2.85	2.87	2.77	2.76
Zero	Rough	2.86	2.82	2.83	2.71	2.72
Weak Favorable	Smooth	2.86	2.85	2.86	3.18	3.07
Weak Favorable	Rough	2.86	2.84	2.84	2.84	2.96
Strong Favorable	Smooth	2.86	2.82	2.89	3.05	2.33
Strong Favorable	Rough	2.86	2.84	2.87	3.05	2.44

Table 2: Computed freestream Mach number at each static pressure port location.

4. Particle Image Velocimetry

Digital Particle Image Velocimetry (DPIV) is a non-intrusive diagnostic technique that uses tracer particles illuminated by a light source (usually a laser) and up to four cameras to create a highly resolved velocity field in a variety of different applications. Short pulse lasers (3 – 5 nanoseconds) and high speed interline-transfer

cameras permit PIV measurements to be made in high speed flows. Near planar surfaces it becomes increasingly difficult to make accurate measurements. Smaller seed particles (0.5 – 1.0 μm) have very low Mie scattering signatures and are usually not detectable. Since the seed particles are usually injected into the freestream portion of the flow and entrained into the viscous region, in the near-wall region the seed density will thus be much lower and can become insufficient for accurate particle ensembles. Often it is not practical to increase the particle density from the flow seeder because seed accumulation on the windows can obscure the view of the test area. A possible solution is to be able to detect the previously invisible smaller particles. An additional complication is laser reflection from the surfaces. The reflection intensity can be so great that image blooming, a situation where neighboring pixels are saturated with excess charges producing a white band in the image, can occur making all particles in this region undetectable. Correcting for the first problem by increasing laser power has the undesirable effect that it also increases the wall reflection and hence image blooming. Conversely a reduction in laser power can reduce laser reflection, but also leads to a reduction in the visibility of the tracer particles.

4.1. Experimental Setup

A current method in use to eliminate surface reflection is to coat the surfaces with fluorescent paint capable of absorbing up to 99% of the incoming light and scatters the remaining light at a different

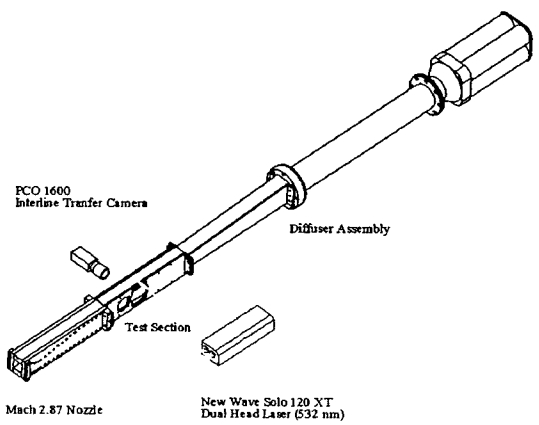

Figure 12: Schematics of PIV setup in Texas A&M Mach 2.9 blowdown wind tunnel.

wavelength. Using appropriate color filters it is possible to eliminate virtually all wall reflection.

For the current experiment it was not practical to paint the model surfaces because it was not known if the large shear stresses would remove the paint from the roughness elements. Instead various hardware setups and experimental techniques aimed at eliminating wall reflections while enhancing the visibility of the smaller tracer particles was used. A schematic of the PIV setup for both arrangements during a supersonic boundary layer experiment is shown in Figure 12. The tunnel is seeded by a TSI Six-jet Atomizer Model 9306 using Bertolli extra light olive oil producing particles with diameters on the order of 1.0 μm. All six jets are opened with the input pressure set at 1.14 MPa which produces an approximate aerosol output of 4.51×10^{14} particles per second.

Tracer particles are illuminated in the tunnel using a dual port/dual head New-Wave Solo 120XT PIV laser designed to provide a highly stable green light source (532 nm) for PIV applications. Each laser head has a maximum energy output of 120 mJ at 532 nm. The pulse width is 4 ns with a $\pm$ 1 ns jitter and a maximum frequency of 15 Hz. Perpendicular polarization of the beam coming out of port 2 is achieved by using a half wave plate. The plate is a crystal quartz optic designed to differentially retard the phase of a polarized beam. In front of the first laser port there is a high-energy polarizing cube beamsplitter that provides efficient narrowband polarization. The polarizer consists of a pair of precision right-angle prisms optically contacted together and has a damage threshold up to 10 J/cm^2. A high energy mirror is used to reflect Laser 1 into the high-energy polarizing cube beamsplitter. After the beams have been aligned there will be two

coincident beams; one with parallel polarization (Laser 1) and the other with perpendicular polarization (Laser 2).

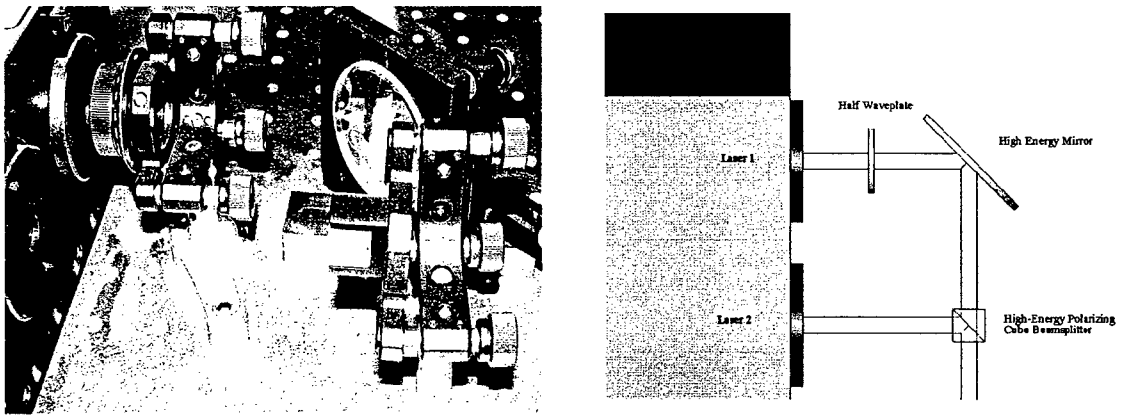

Figure 13: Laser polarization setup

The laser beams are guided to the test section using 90° bending prisms constructed of BK7 glass with AR coatings. A BK7 focus lens with a focal length of 500 mm is used to focus the beam so that the waist is located just above the test section floor. A laser sheet that is approximately 1.5 cm wide and 1 mm thick is formed on the test section floor using a BK7 Plano-concave cylindrical lens.

The camera used was a Cooke Corp. PCO 1600 high dynamic 14bit cooled interline-transfer CCD camera system with 1600 x 1200 pixel resolution, and the ability to perform image windowing. The image memory is integrated into the camera enabling image recording at 160MB/s. It features thermo-electrical cooling at -50°C below the ambient which is capable of a maximum dynamic range of 70dB. Image data are transferred to the computer via an IEEE 1394 (firewire) camera link. The cameras had an intrinsic delay time of the camera is 5.3 μs and a trigger delay time of 200 ns +- 13 ns. The camera trigger, laser Q-switch and laser flashlamp are all controlled by a Quantum

Composers Model 9618 pulse generator. The camera frame grabbing software was Camware version 2.13. A Nikon 60 mm lens was used to focus the camera onto the illuminated particles. Sample PIV images are presented below in Figure 12.

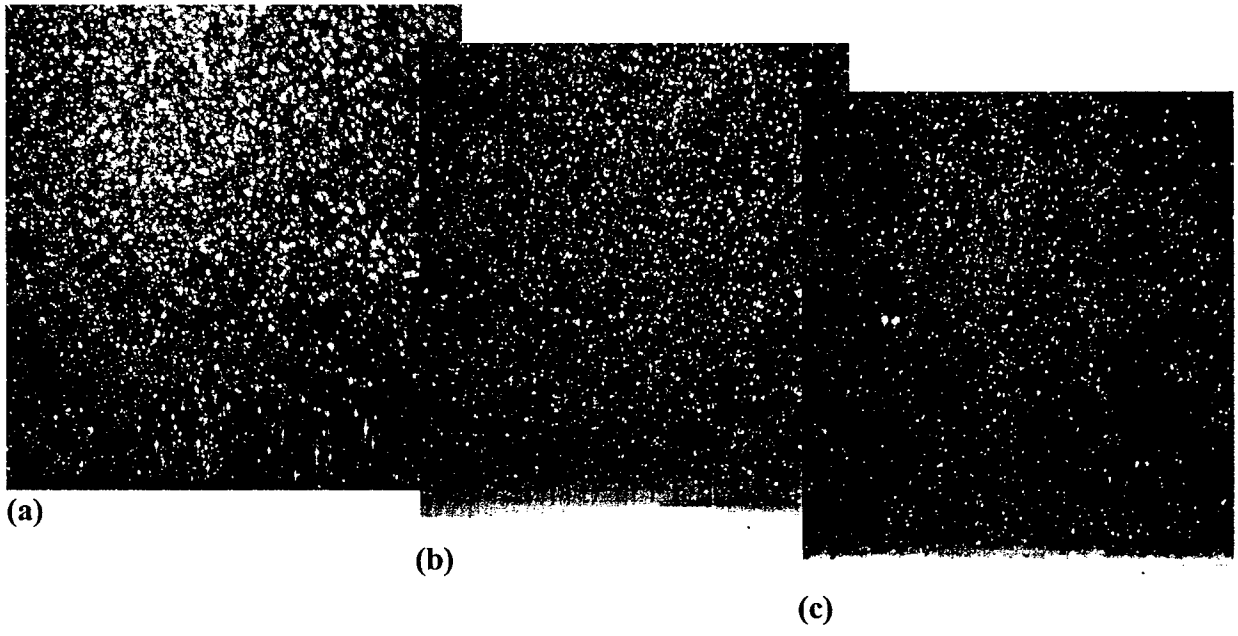

Figure 14 Sample PIV images

4.2. Post Processing

Velocity fields are created by calculating the displacements of particle ensembles from consecutive images using Innovative Scientific Solutions' dPIV 32-bit Analysis Code. A three-step adaptive correlation calculation using successive interrogation spot sizes of 128×64, 64×32, and 32×16 pixels, respectively, with 50% overlap was used to determine velocity vectors. In order to enhance the intensity of correlation peaks relative to random noise, a correlation multiplication process filter with all four correlation maps was turned on. A consistency post processing filter and a nearest neighbor dependency filter were turned on to improve the adaptive correlation calculation during the first and second steps and eliminate incorrect vectors during the third step.

First and second order turbulent statistics are created using an in house computer code that ensemble averages the averages the velocity vector fields. In order to minimize the effects of fluctuations in total temperature and pressure while the tunnel is running, the program bins the average velocity data and computes the fluctuating velocities relative to the average velocity from in the corresponding bin. The equation for the bin mean velocity is given below, where n is the number of samples per bin, and J_{max} is the total number of bins.

$$\overline{u}_{bin,j} = \frac{1}{n}\sum_{i=(j-1)n+1}^{j\cdot n} u_i, \quad j = 1 \ldots J_{\max} \tag{4.1}$$

The computed mean velocity is simply the ensemble average of the *bin* velocity:

$$\overline{u} = \frac{1}{J_{\max}}\sum_{j=1}^{J_{\max}} \overline{u}_{bin,j} \tag{4.2}$$

And the fluctuating velocity is give as:

$$\overline{u'u'} = \frac{1}{N}\sum_{i}^{N}\left(u_i - \overline{u}_{bin,j}\right)^2, \quad 1 \le i \le n \Rightarrow j = 1,\ldots,(J_{\max}-1)n+1 \le i \le J_{\max}n \Rightarrow j = J_{\max} \tag{4.3}$$

$$\overline{u'v'} = \frac{1}{N}\sum_{i}^{N}\left(u_i - \overline{u}_{bin,j}\right)\left(v_i - \overline{v}_{bin,j}\right), \quad 1 \le i \le n \Rightarrow j = 1,\ldots,(J_{\max}-1)n+1 \le i \le J_{\max}n \Rightarrow j = J_{\max} \tag{4.4}$$

4.3. Uncertainty

The dPIV code is capable of measuring particle ensemble displacements down to 1/10 pixel accuracy. The pixel displacement of the particles throughout the flow field is on the order of 10 pixels, leaving a 1% error in the instantaneous velocity measurements. To determine the confidence interval of the sample mean it was assumed that the samples are distributed normally. For a 95% confidence interval from the computed mean, the

computed mean velocity becomes $\overline{\phi} \pm 1.96\sqrt{\mathrm{var}(\phi)}$, and is tabulated below based on the roughly 3000 – 5000 valid samples per model.

Statistic	Variance	Maximum Interval
$\overline{u}$	$\overline{u'u'}$	±0.2%
$\overline{u'u'}$	$2\left(\overline{u'u'}\right)^2$	±5%
$\overline{v'v'}$	$2\left(\overline{v'v'}\right)^2$	±5%
$\overline{u'v'}$	$\left(\overline{u'u'}\right)\left(\overline{v'v'}\right)+\left(\overline{u'v'}\right)^2$	±4%

Table 3: Estimator variances multiplied by N and maximum interval

5. Results

For the results presented below, all field plots are presented in the tunnel coordinate system with the floor of the nozzle exit being the origin. All line plots were generated at the centerline of the measurement location. The line plots were taken normal to the surface, however, the velocities remains in the tunnel coordinate system. Spreadsheets of the data were submitted to The University of Alabama prior to this report.

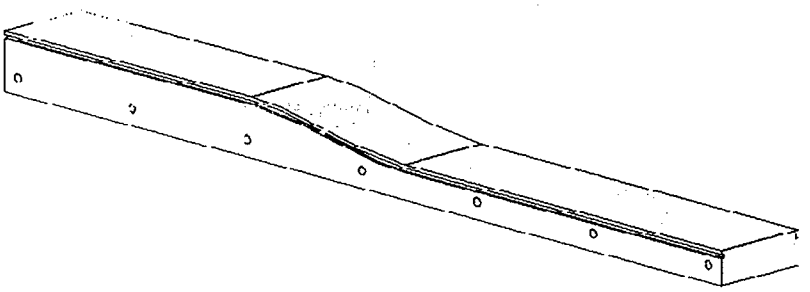

Figure 15: Schematic of test section model with wall normal coordinate system.

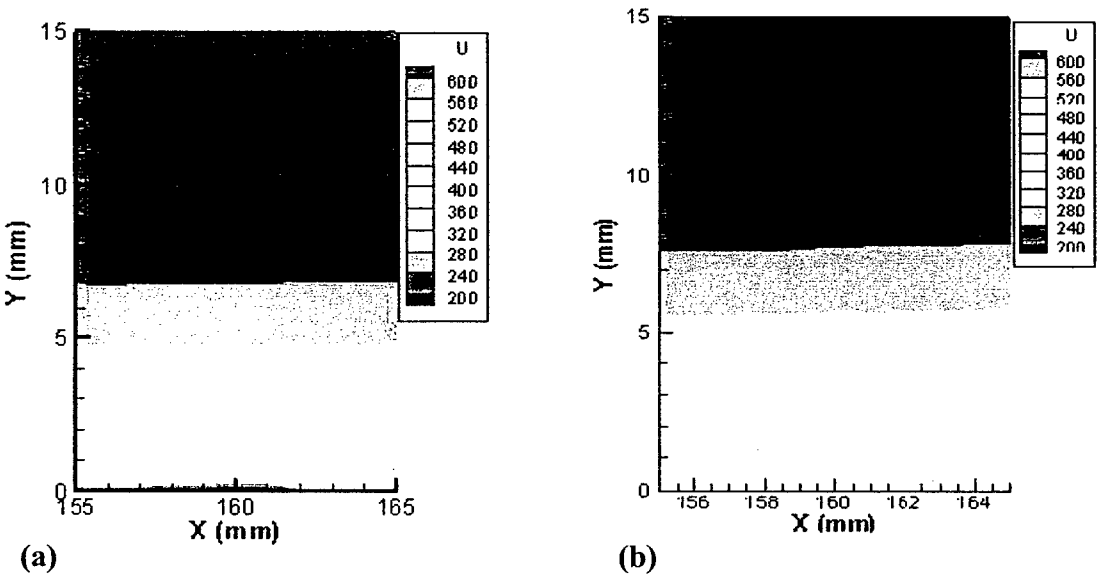

Figure 16: First measurement location $\overline{u}$ velocity field (a) smooth plate, (b) rough plate.

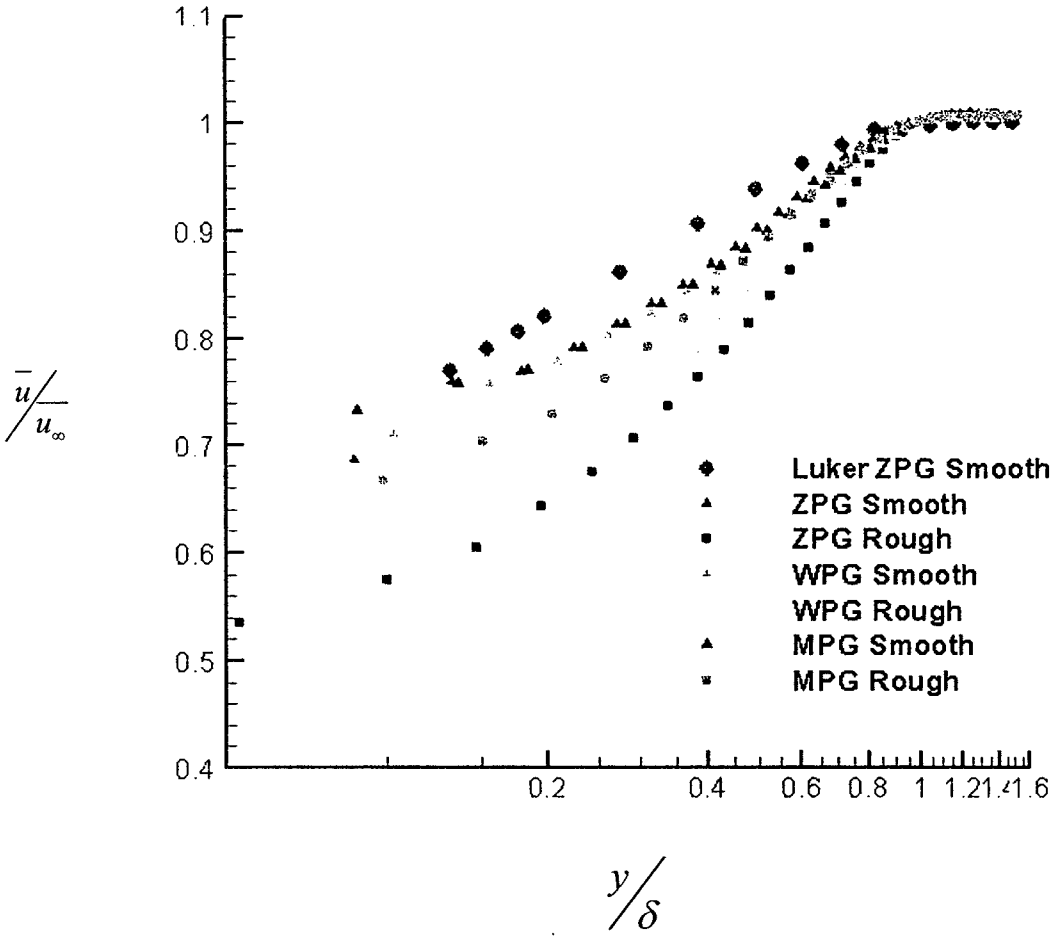

Figure 17: First measurement location velocity profile .

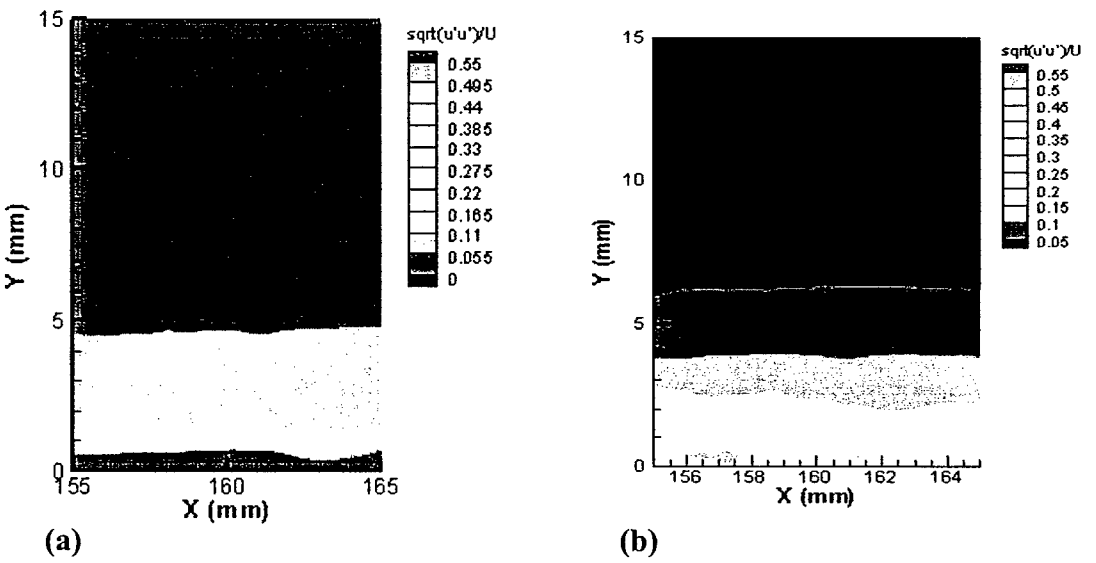

Figure 18: First measurement location axial turbulence intensity fields: (a) smooth plate, (b) rough plate.

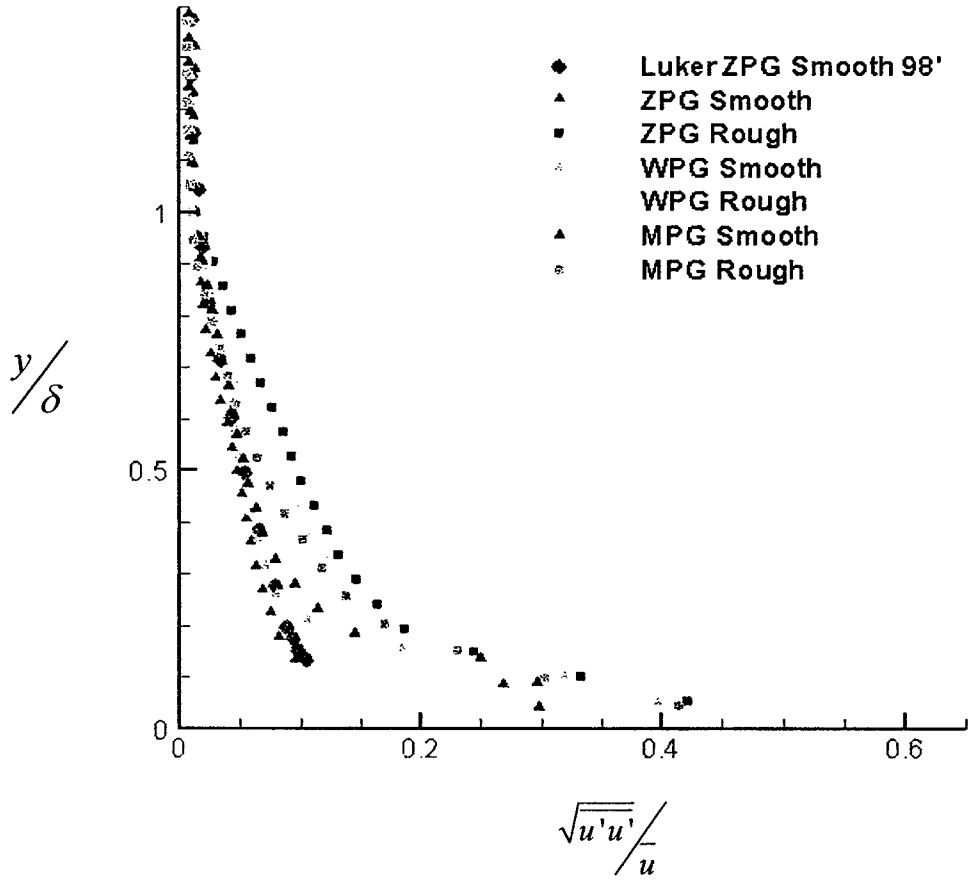

Figure 19: First measurement location axial turbulence intensities.

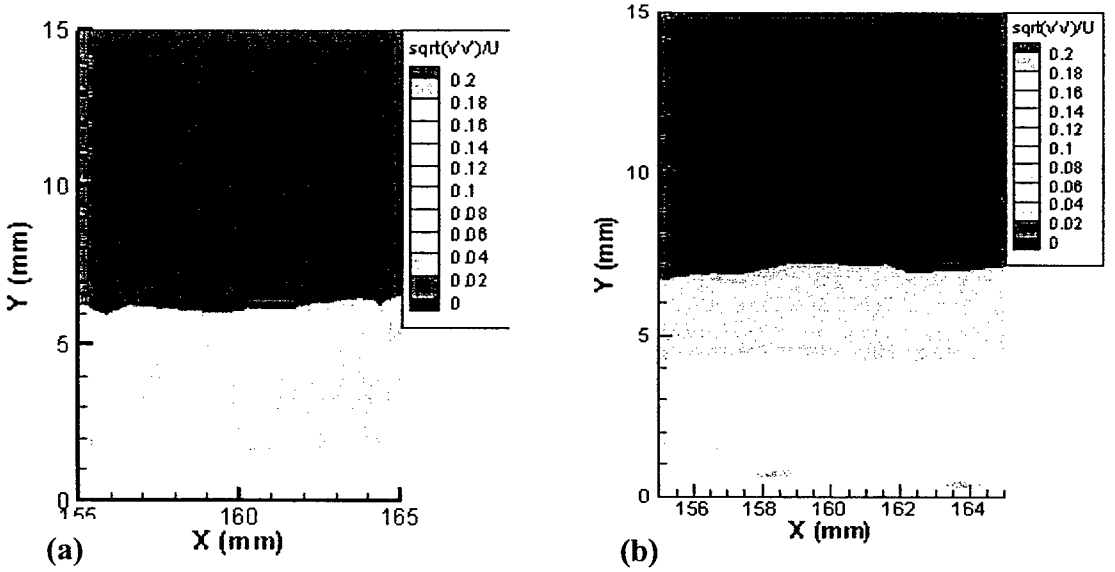

Figure 20: **First measurement location transverse turbulence intensity fields: (a) smooth plate, (b) rough plate.**

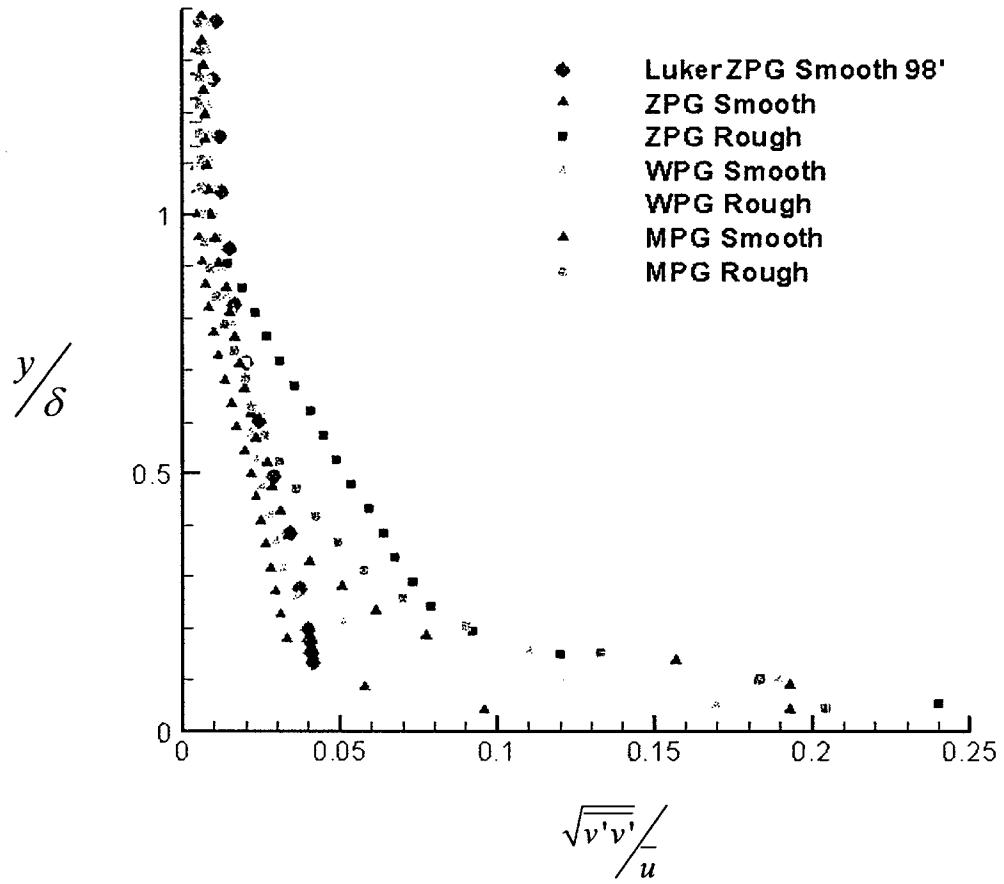

Figure 21: **First measurement location transverse turbulence intensities: (a) smooth plate, (b) rough plate.**

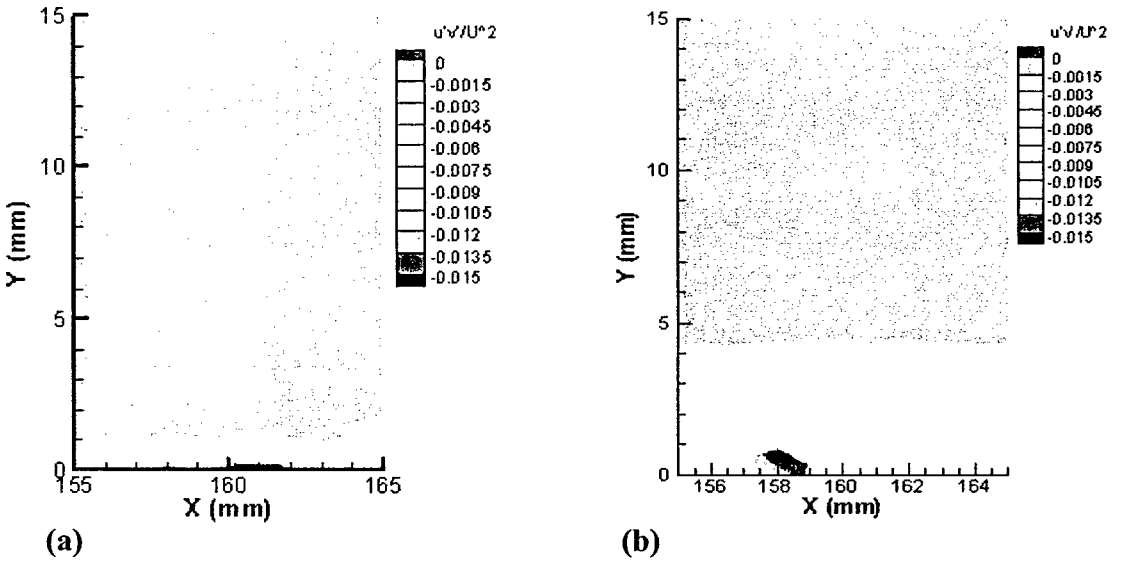

Figure 22: First measurement location normalized turbulent shear stress fields.

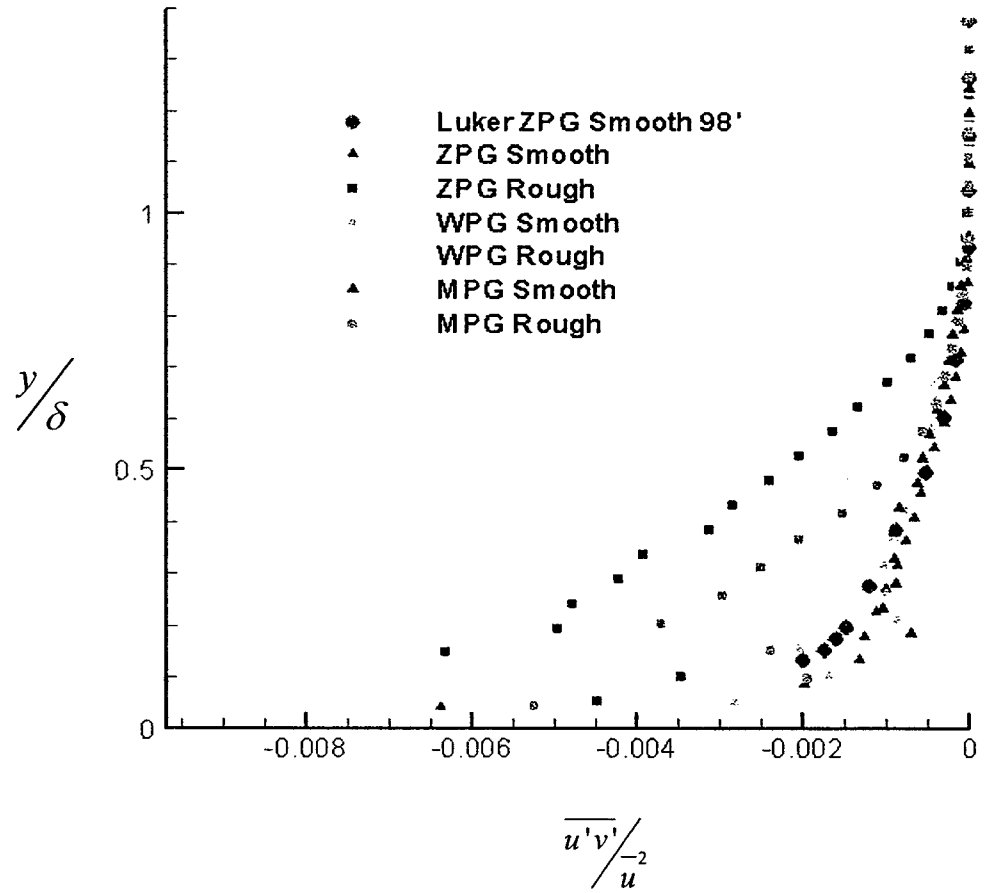

Figure 23: First measurement location normalized turbulent shear stress profiles.

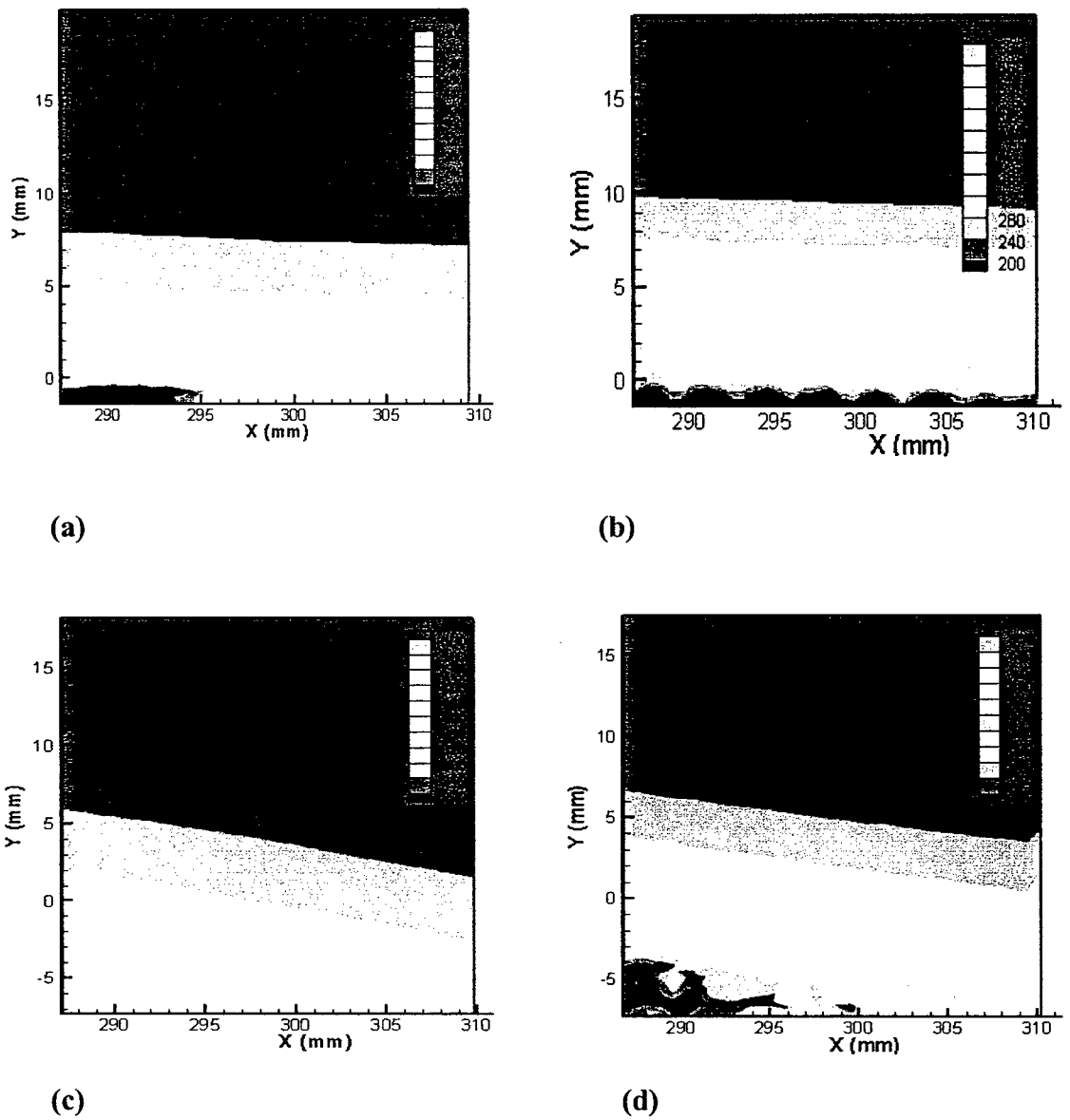

Figure 24: Second measurement location $\overline{u}$ velocity fields: (a) WPG smooth plate, (b) WPG rough plate, (c) MPG smooth, and (d) MPG rough.

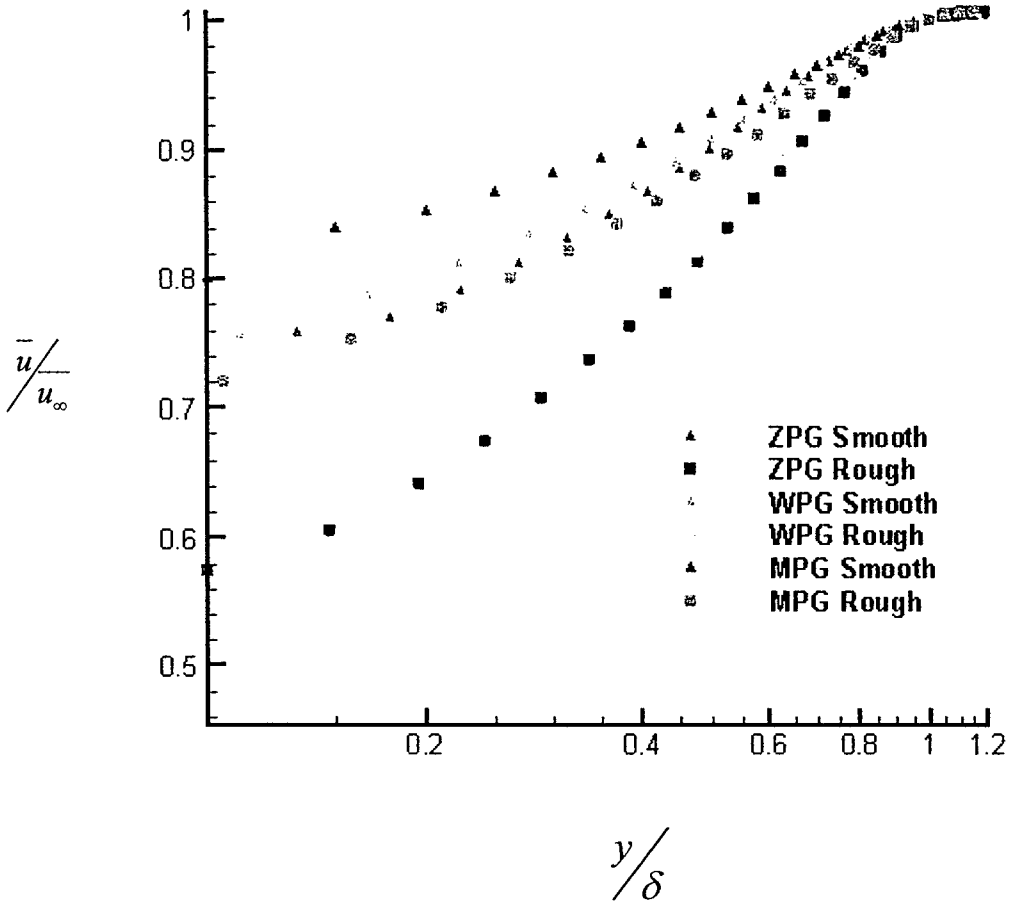

Figure 25: Second measurement location velocity profiles.

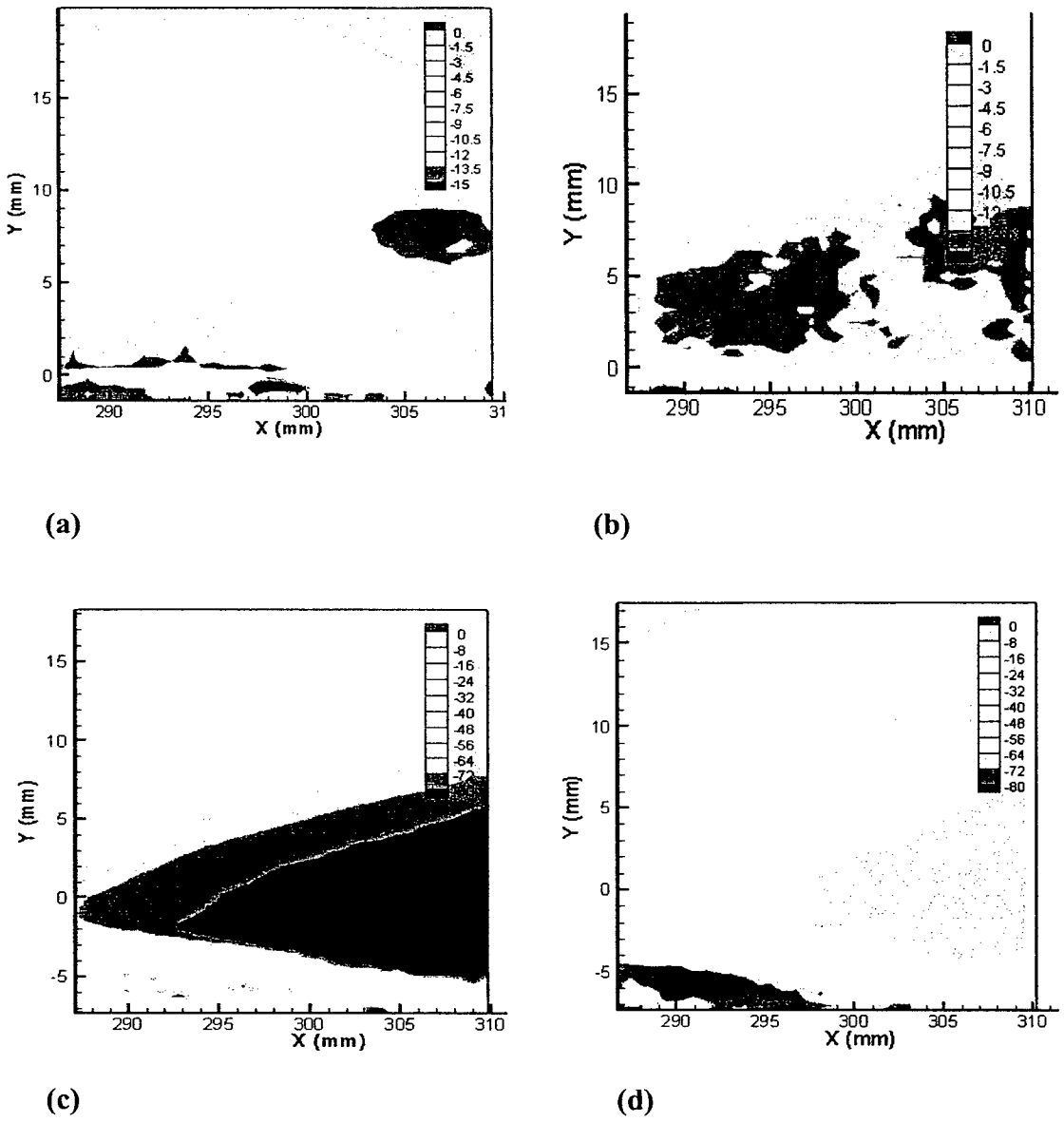

Figure 26: **Second measurement location $\overline{v}$ velocity fields: (a) WPG smooth plate, (b) WPG rough plate, (c) MPG smooth, and (d) MPG rough.**

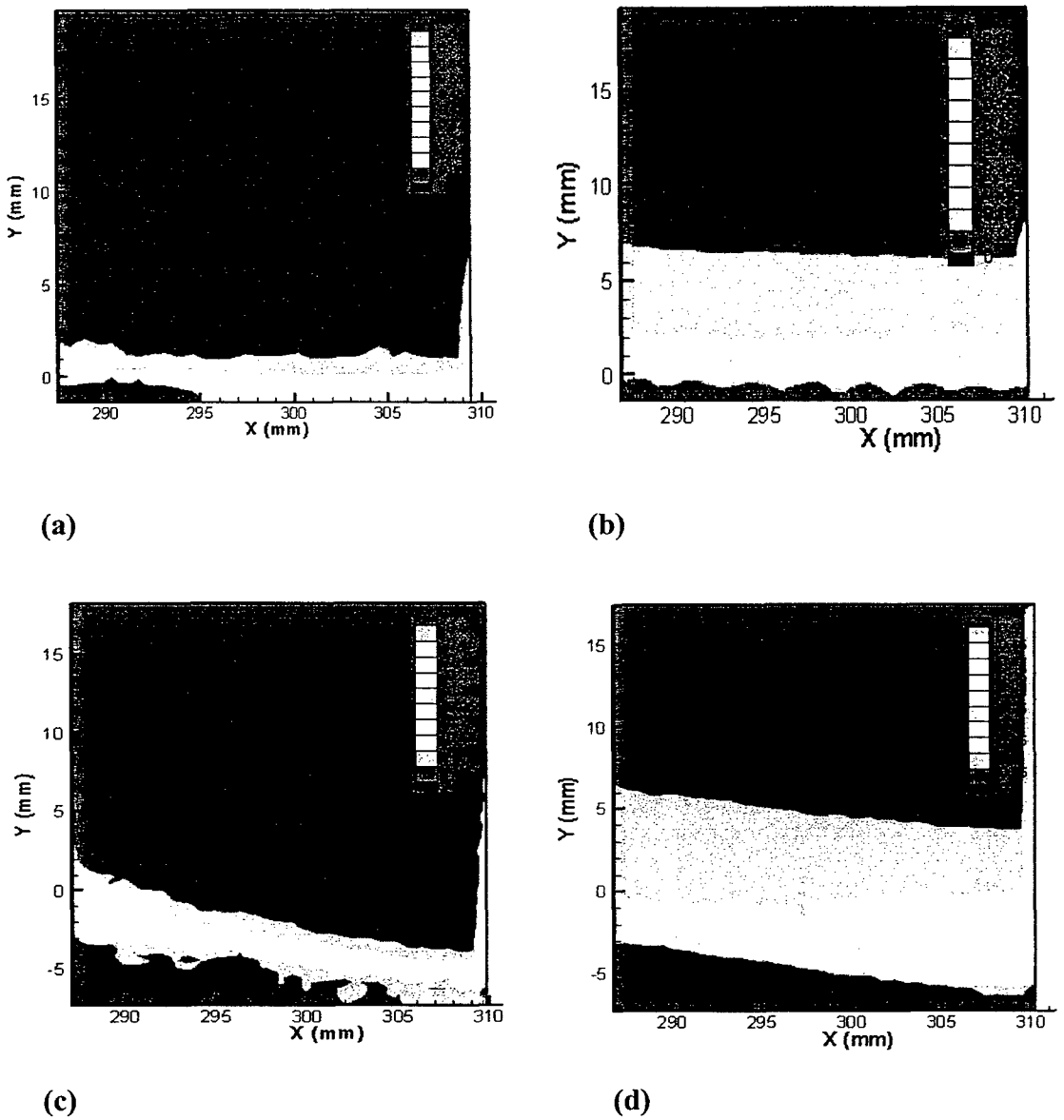

Figure 27: **Second measurement location axial turbulence intensity fields: (a) WPG smooth plate, (b) WPG rough plate, (c) MPG smooth, and (d) MPG rough.**

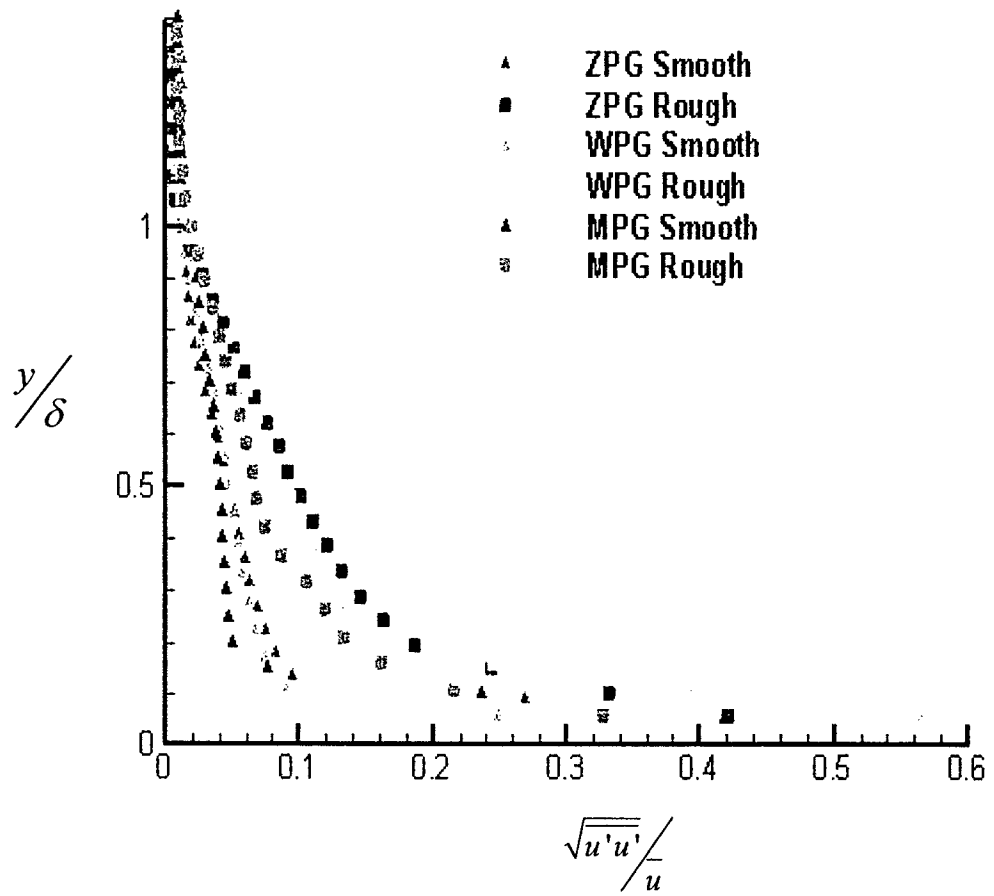

Figure 28: Second measurement location axial turbulence intensities.

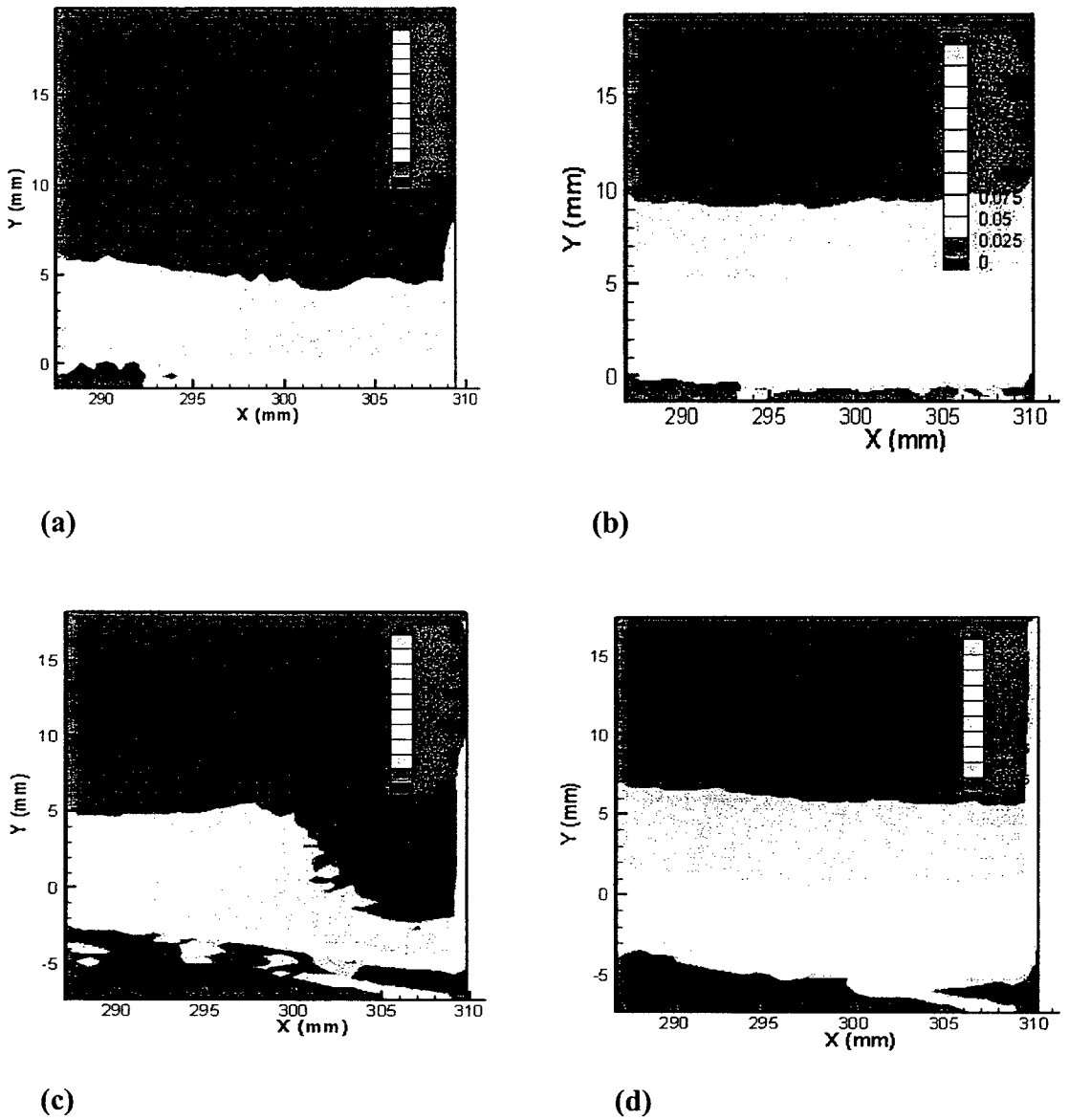

Figure 29: **Second measurement location transverse turbulence intensity fields: (a) WPG smooth plate, (b) WPG rough plate, (c) MPG smooth, and (d) MPG rough.**

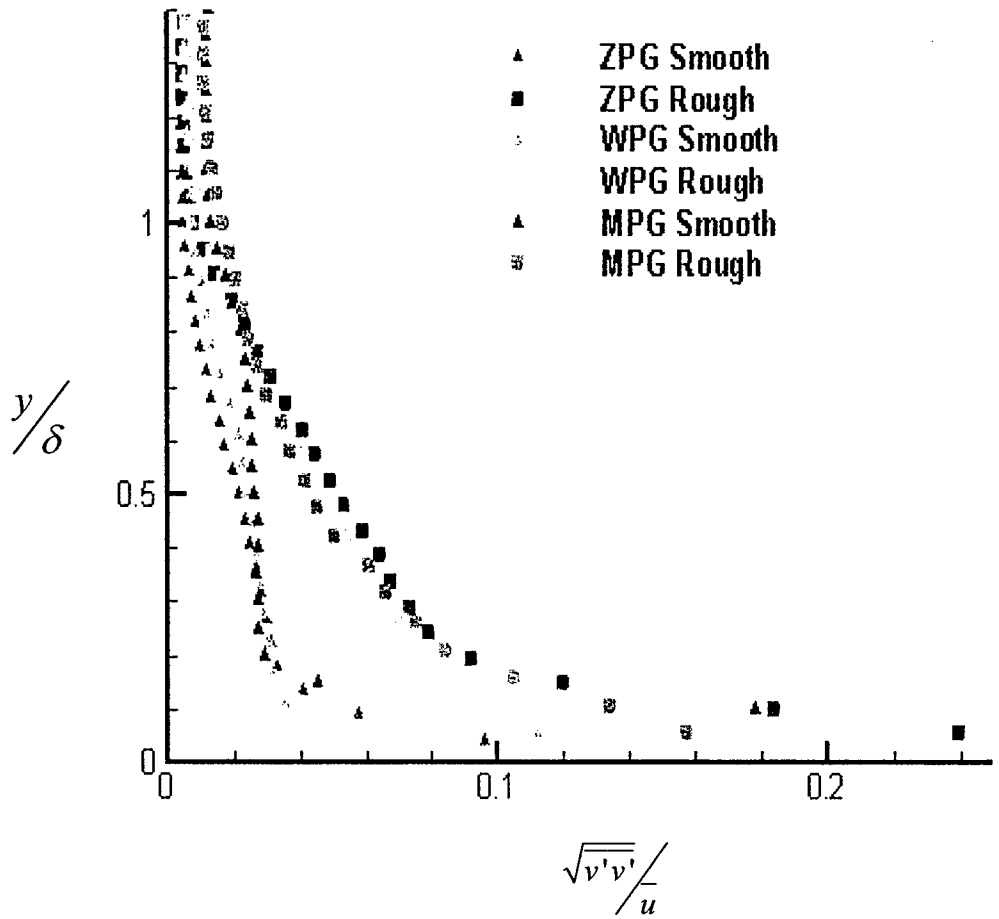

Figure 30: Second measurement location transverse turbulence intensities.

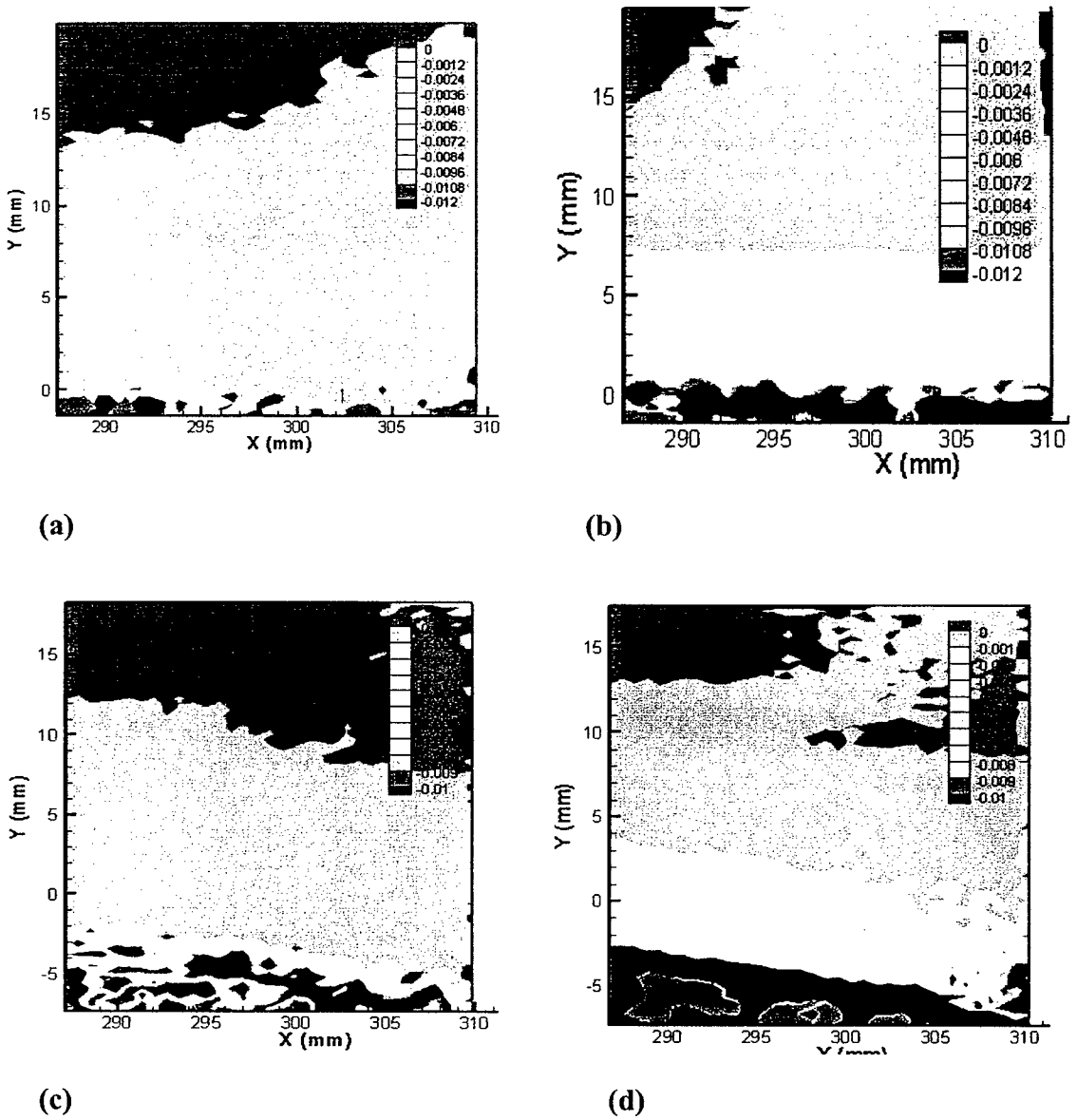

Figure 31: **Second measurement location normalized turbulent shear stress fields: (a) WPG smooth plate, (b) WPG rough plate, (c) MPG smooth, and (d) MPG rough.**

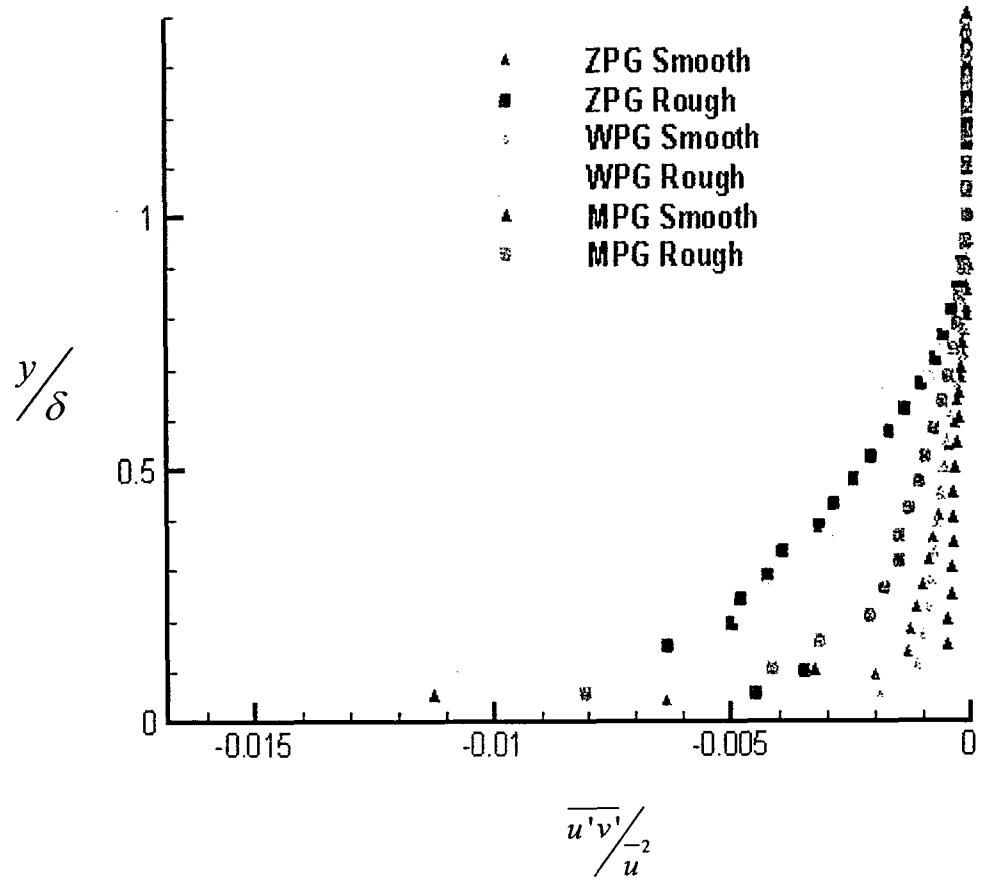

Figure 32: Second measurement location normalized turbulent shear stress profiles.

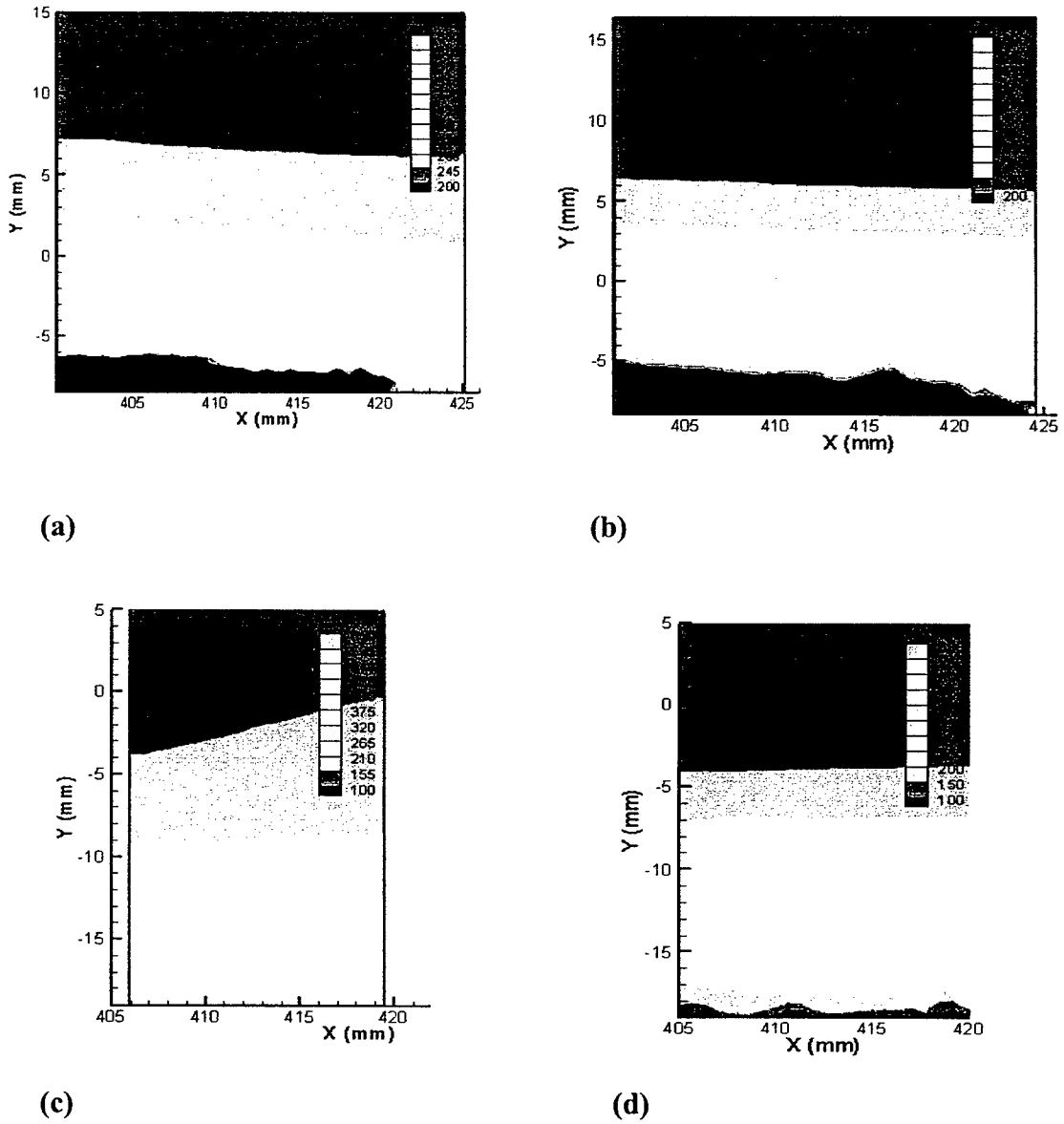

Figure 33: **Third measurement location $\overline{u}$ velocity fields: (a) WPG smooth plate, (b) WPG rough plate, (c) MPG smooth, and (d) MPG rough.**

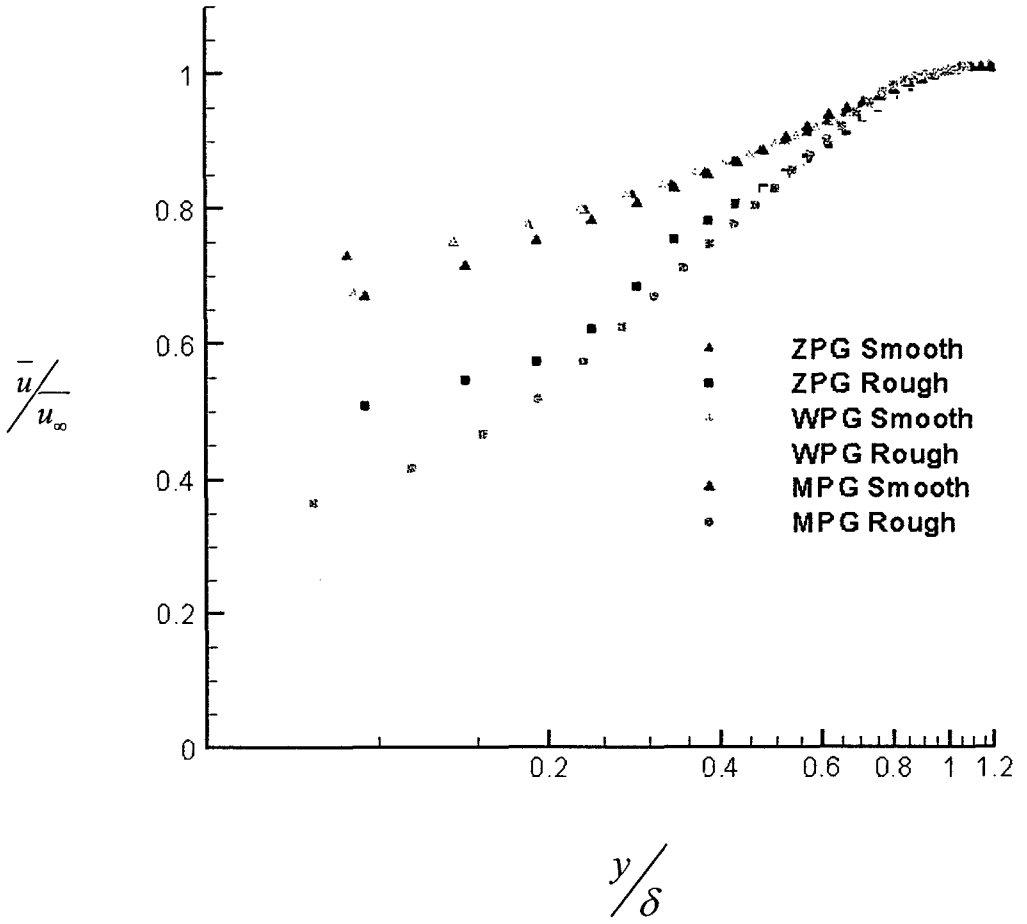

Figure 34: Third measurement location velocity profiles.

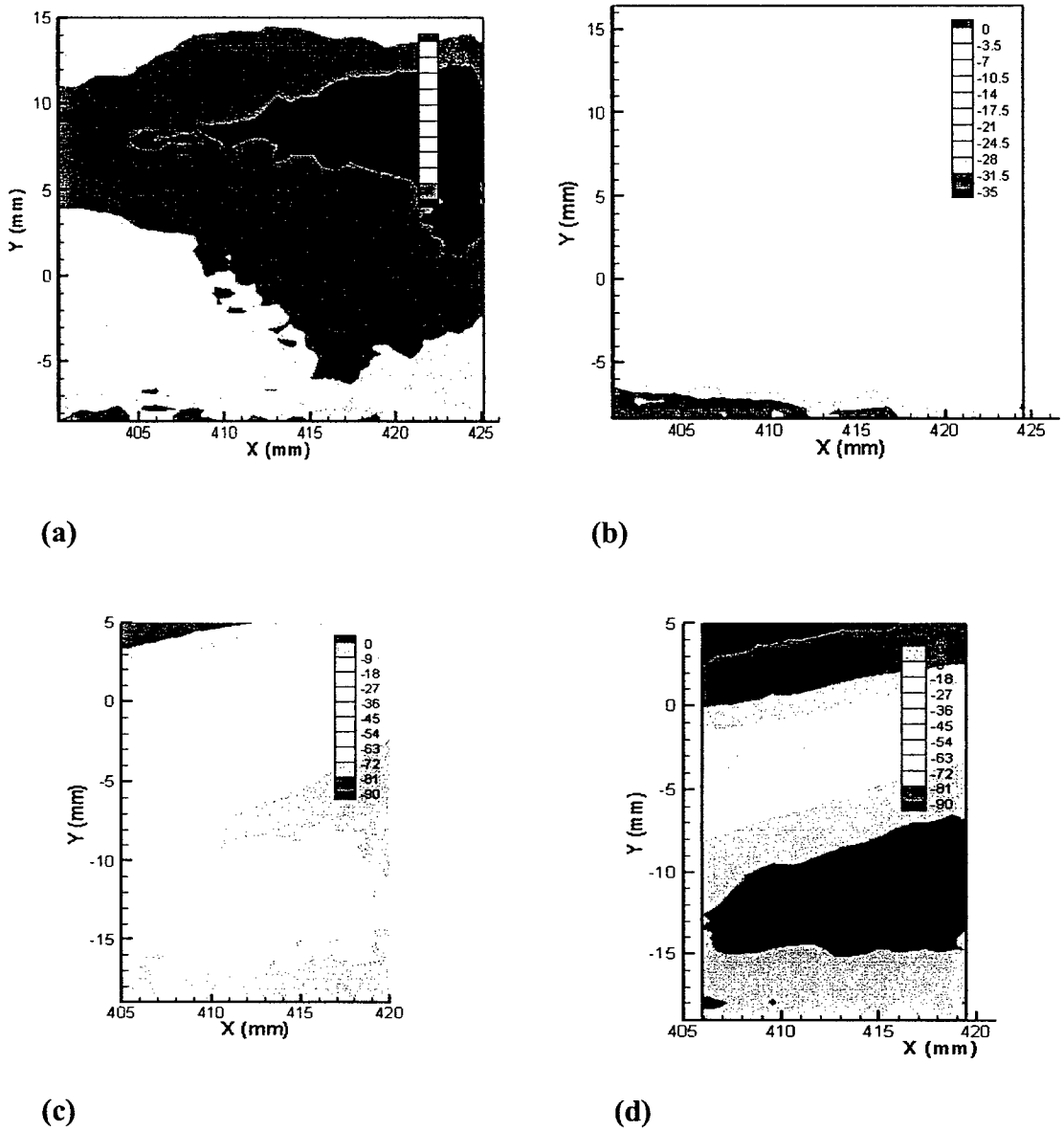

Figure 35: **Third measurement location $\overline{v}$ velocity fields: (a) WPG smooth plate, (b) WPG rough plate, (c) MPG smooth, and (d) MPG rough.**

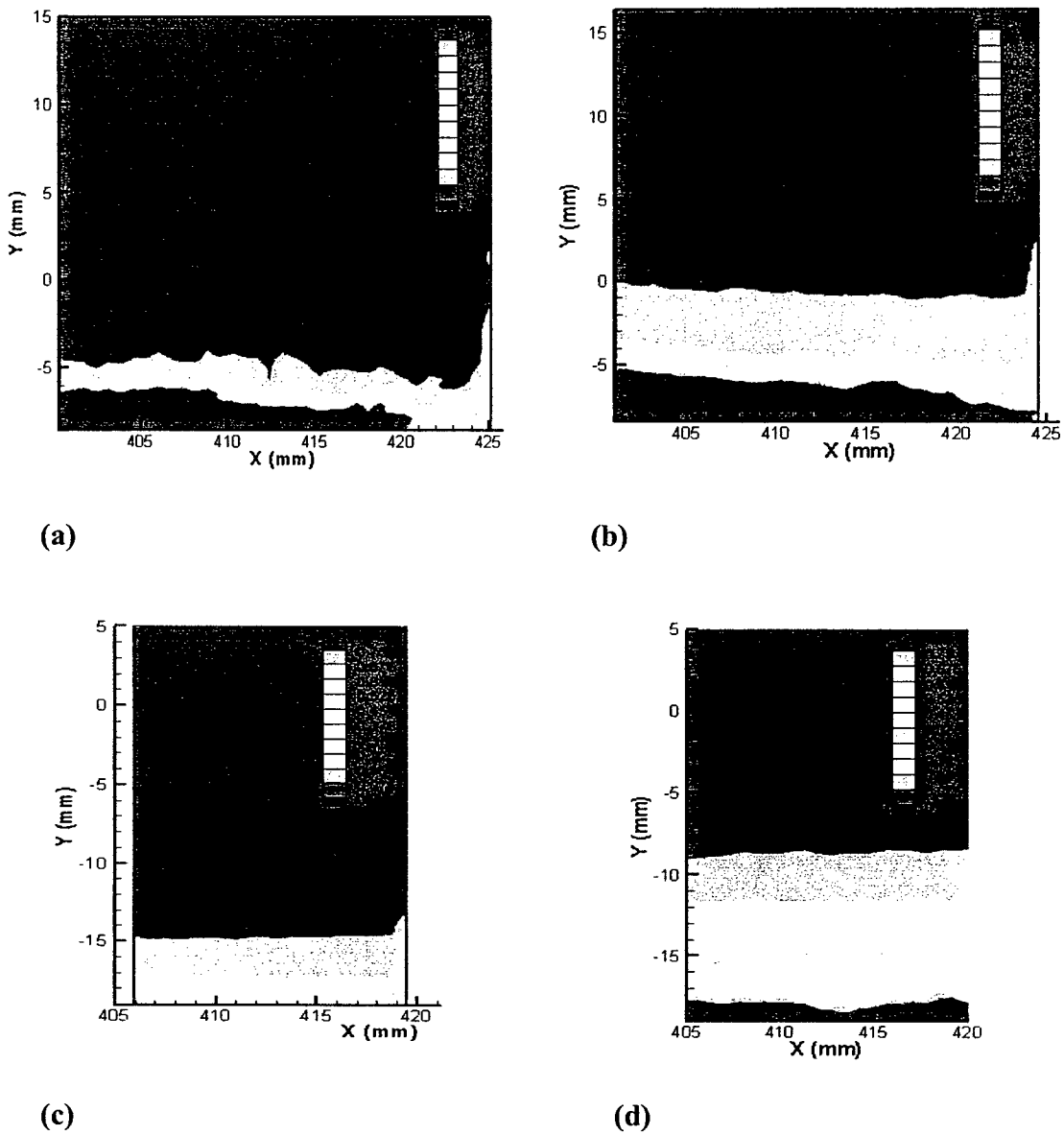

Figure 36: **Third measurement location axial turbulence intensity fields: (a) WPG smooth plate, (b) WPG rough plate, (c) MPG smooth, and (d) MPG rough.**

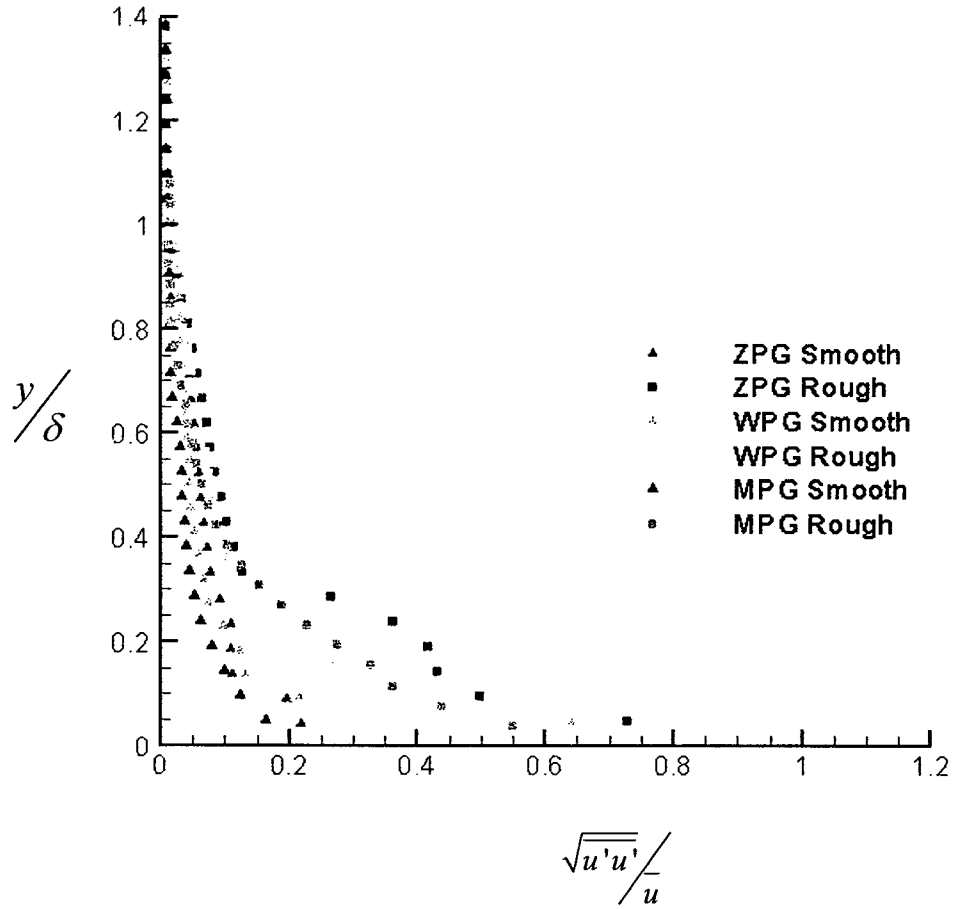

Figure 37: Third measurement location axial turbulence intensities.

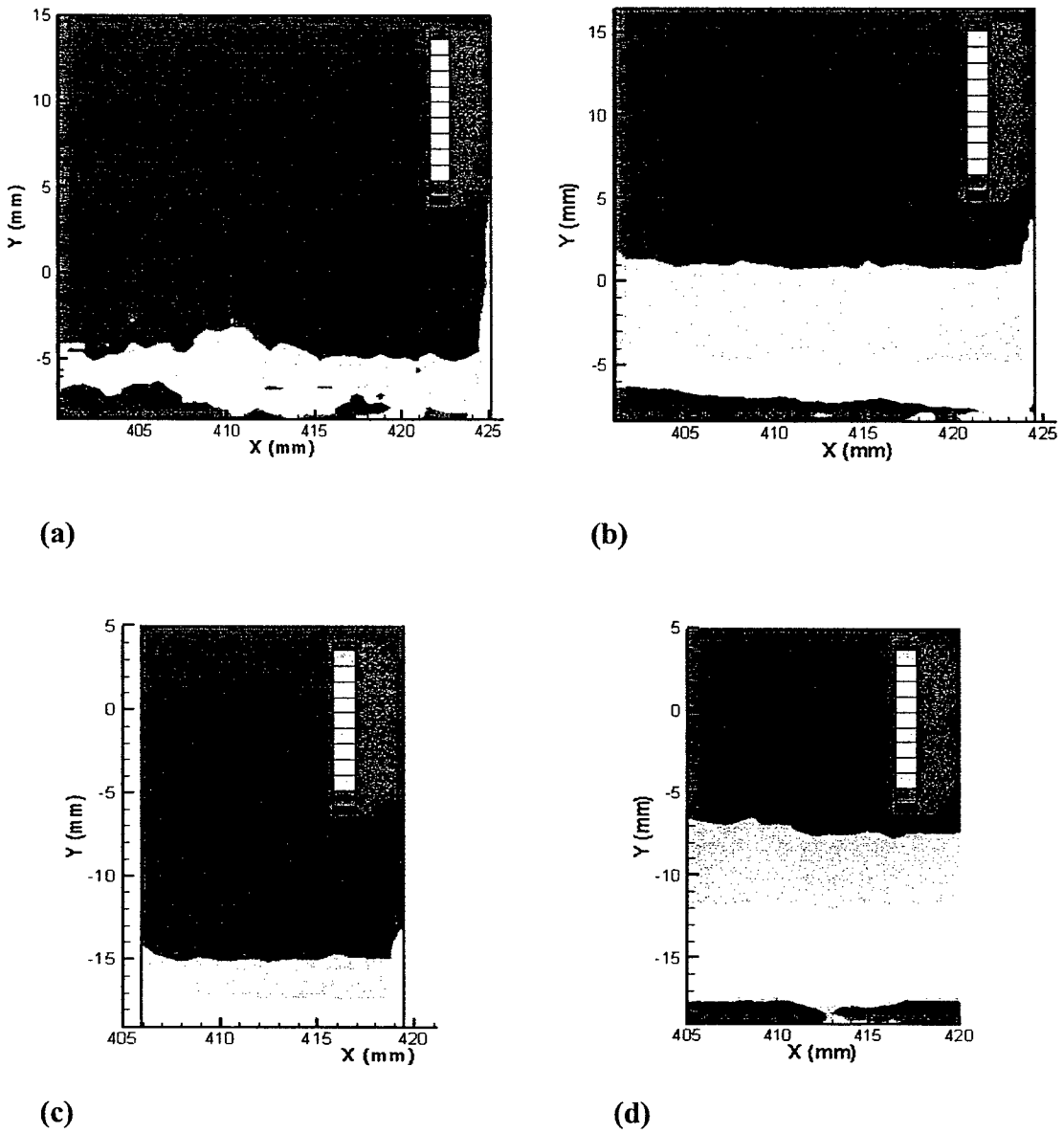

Figure 38: **Third measurement location transverse turbulence intensity fields: (a) WPG smooth plate, (b) WPG rough plate, (c) MPG smooth, and (d) MPG rough.**

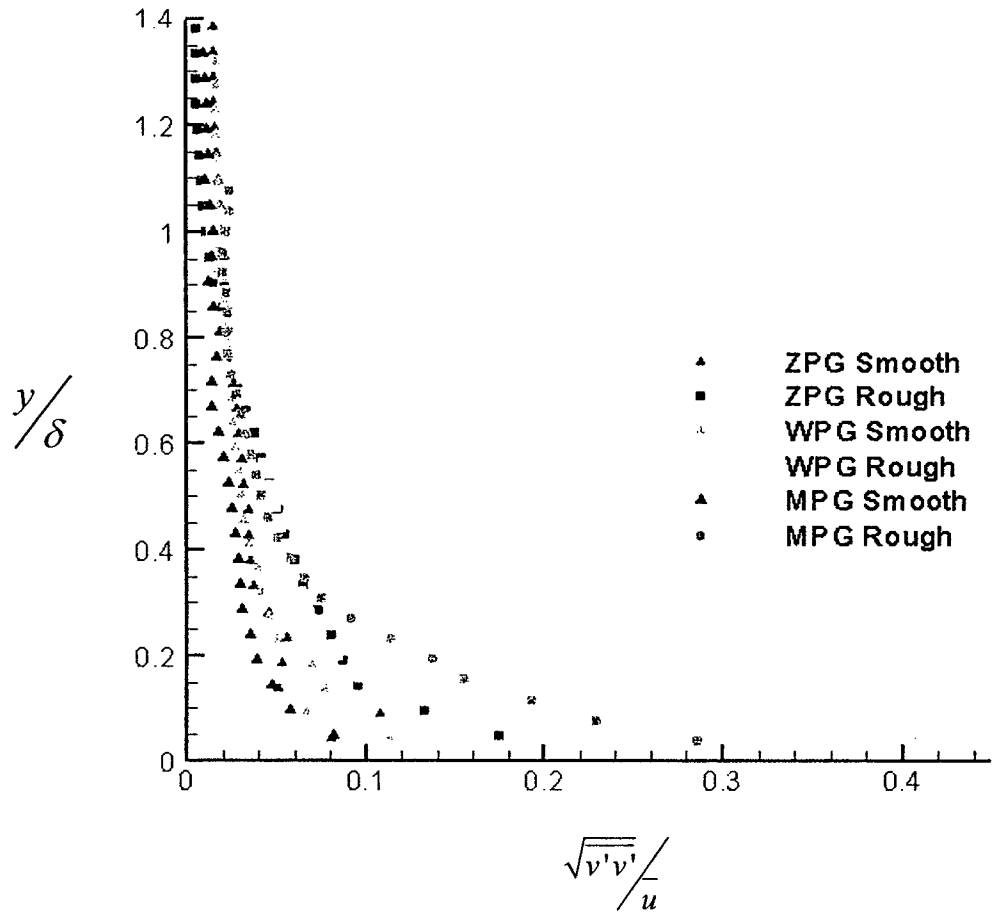

Figure 39: Third measurement location transverse turbulence intensities.

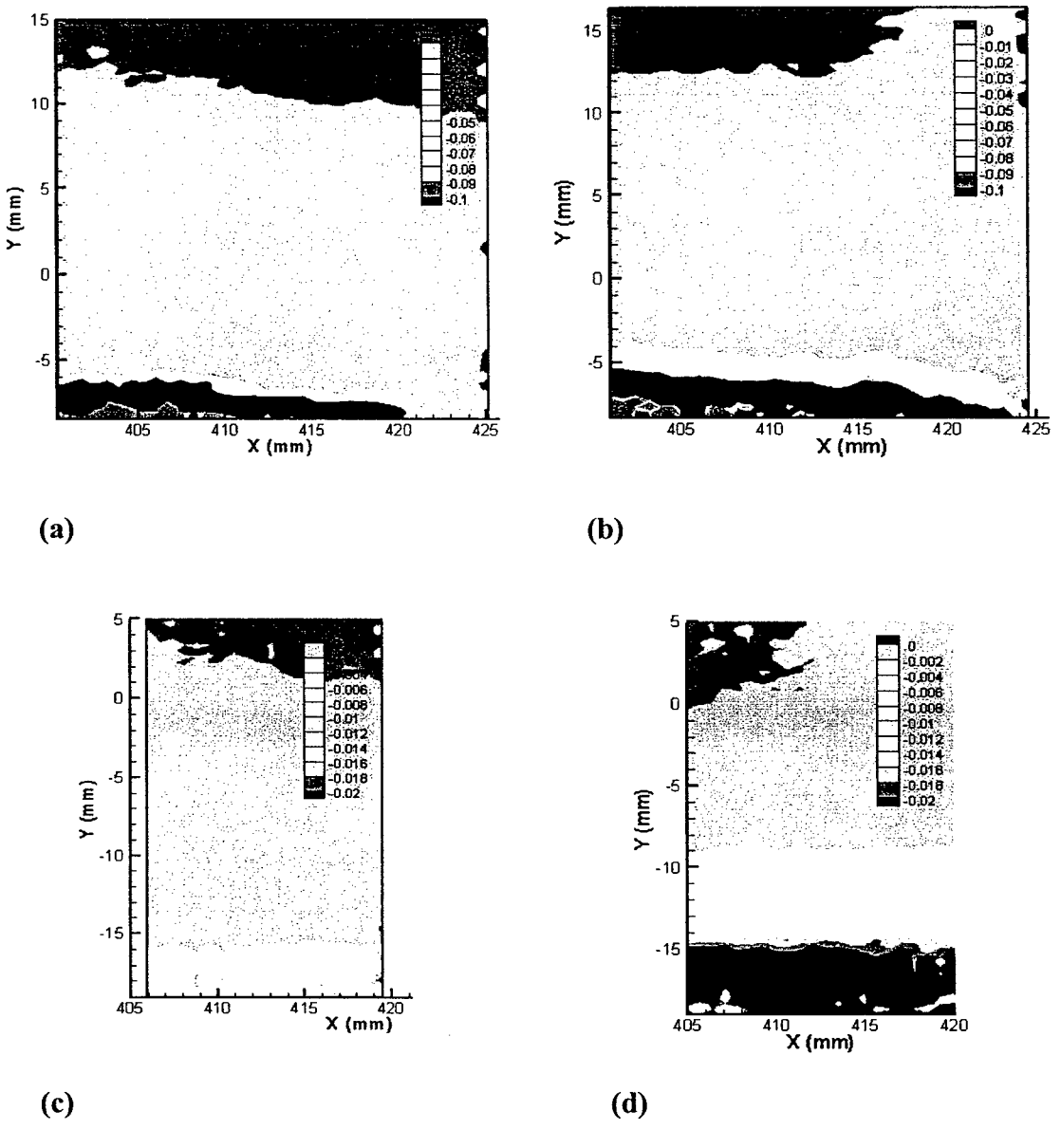

Figure 40: **Third measurement location normalized turbulent shear stress fields: (a) WPG smooth plate, (b) WPG rough plate, (c) MPG smooth, and (d) MPG rough.**

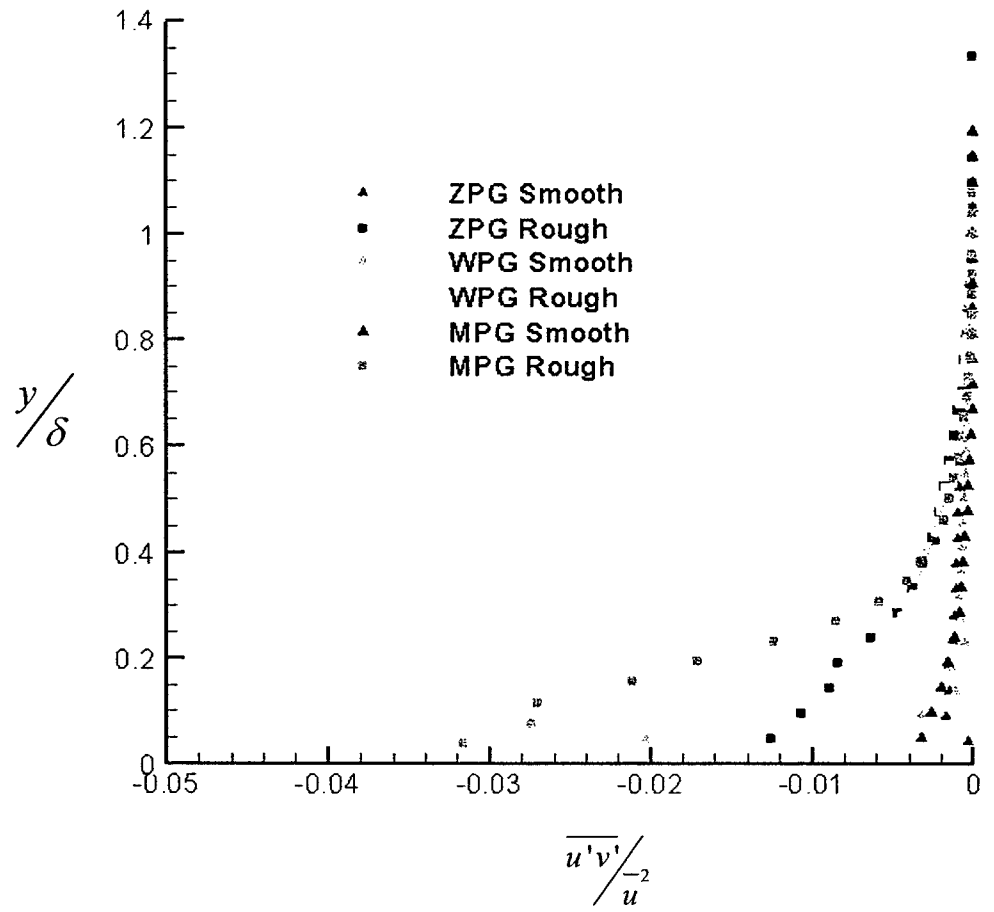

Figure 41: Third measurement location normalized turbulent shear stress profiles.

6. References

Adrian, R., "Laser Velocimetry," *Fluid Mechanics Measurements, 2nd Ed.,* Edited by R. Goldstein, Taylor & Francis, Washington DC, 1996, pp. 175-293.

Antonia, R. A., and Wood, D. H., "Calculation of Turbulent Boundary Layer Downstream of a small Step Change in Surface Roughness," Aeronautical Quarterly, Vol. 26, Aug. 1975, pp. 202-210.

Apsley, D., Chen, W.-L., Leschziner, M. and Lien, F.-S., "Non-Linear Eddy-Viscosity Modeling of Separated Flows," *J. Hydraulic Res.*, Vol. 35, 1997, p. 723.

Arnette, S. A., Samimy, M. and Elliott, G. S., "The Effects of Expansion Regions on the Turbulence Structure of Compressible Boundary Layers," AIAA Paper 96-0656, Jan. 1996.

Air Force, *New World Vistas, Aircraft and Propulsion Technologies*, 1995.

Air Force Office of Scientific Research, *Research Interests Of The Air Force Office Of Scientific Research And Broad Agency Announcement 2000-1*, AFOSR 64-1, Department Of The Air Force, Air Force Office of Scientific Research (AFRL), 801 North Randolph Street, Room 732, Arlington VA 22203-1977, June 1999.

Benedict, L. H., and Gould, R. D., "Towards Better Uncertainty Estimates for Turbulence Statistics," *Experiments in Fluids*, Vol. 22, 1996, pp. 129-136.

Berg, D., "Surface Roughness Effect on a Mach 6 Turbulent Boundary Layer," *AIAA Journal,* Vol. 17, No. 9, 1979, pp. 929, 930.

Bowersox, R., "Combine Laser Doppler Velocimetry and Cross-Wire Anemometry Analysis for Supersonic Turbulent Flow," *AIAA Journal,* Vol. 34, No. 11, 1996.

Bowersox, R., Schetz, J., Chadwick, K., and Deiwert, S., "A Technique for Direct Measurement of Skin Friction in High Enthalpy Impulsive SCRAMjet Flow fields," *AIAA Journal*, Vol. 33, No. 7, 1995, pp. 1286-1291.

Bowersox, R., and Buter, T., "Mass-Weighted Turbulence Measurements in a Mach 2.9 Boundary Layer with Mild Adverse and Favorable Pressure Gradient," *AIAA Journal*, Vol. 34, No. 12, 1996, pp. 2470-2483.

Bowersox, R., Wier, R., Glawe, D., and Gogineni, S., "Measurements of Turbulent Flow Structure in Supersonic Curved Wall Boundary Layers," *Journal of Propulsion and Power,* Vol. 16, No. 1, 2000, pp. 153-154.

Bradshaw, P., "The Analogy Between Streamline Curvature and Buoyancy in Turbulent Shear Flow." *Journal of Fluid Mechanics*, Vol. 36, 1969, pp. 177-191.

Bradshaw, P., *The Effect of Streamline Curvature on Turbulent Flow*, AGARDograph 169, 1973.

Bradshaw, P., "The Effect of Mean Compression or Dilatation on the Turbulence Structure of Supersonic Boundary Layers," *Journal of Fluid Mechanics*, Vol. 63, No. 3, 1974, pp. 449-464.

Bradshaw, P., "The Best Turbulence Model for Engineers," *Modeling Complex Flows,* Ed. by Salas, D., Hefner, J. and Sakell, L., ICASE/LaRC, Kluwer Academic Publishers, Boston, 1999.

Cebeci, Tuncer and Smith, A. M. O. *Analysis of Turbulent Boundary Layers.* Applied Mathematics and Mechanics, Academic Press, 1974.

Chenault, L., Beran, P., and Bowersox, R., "Second-Order Reynolds Stress Turbulence Modeling of Three-Dimensional Oblique Supersonic Injection," *AIAA Journal,* Vol. 37, No. 10, 1999, pp. 1257-1269.

Clauser, F. H., "The Turbulent Boundary Layer," *Advanced Applied Mechanics*, Vol. 4, pp. 1-51.

Coles, D., "The Law of the Wake in the Turbulent Boundary Layer," *Journal of Fluid Mechanics*, Vol. 1, 1956, pp. 191-226.

Corrsin, S., and Kistler, A., "Free-Stream Boundaries of Turbulent Flow," NACA Report 1244, 1955.

DALSA Corp. "One Megapixel CMOS Stop Action Camera Family User's Manual," 03-32-00525, Rev. 05, Waterloo, CN, Feb. 2004.

Depardon, S., Lasserre, J. J., Boueilh, J. C., Brizzi, L. E., and Boree, J., "Skin Friction Pattern Analysis Using Near-Wall PIV," *Experiments in Fluids*, Vol. 39, 2005, pp. 805-818.

Doligalski, T., "Army Turbulence Modeling Needs," *Modeling Complex Flows,* Ed. by Salas, D., Hefner, J. and Sakell, L., ICASE/LaRC, Kluwer Academic Publishers, Boston, 1999.

Donovan, J., Spina, E., and Smits, A., "The Structure of Supersonic Turbulent Boundary Layers Subjected to Concave Surface Curvature," *Journal of Fluid Mechanics*, Vol. 259, Jan. 1993, pp. 1-24.

dPIV, 32-Bit PIV Analysis Code, Software Package, Ver. 2.1, Innovative Scientific Solutions Inc., Dayton, OH, 2005.

Dussauge, J. P., and Gaviglio, J., "The Rapid Expansion of a Supersonic Turbulent Flow – Role of Bulk Dilatation," *Journal of Fluid Mechanics*, Vol. 174, Jan. 1987, pp. 81-112.

Dussauge, J. P., Smith, R., Smits, A., Fernholtz, H., Finley, P., and Spina, E., "Turbulent Boundary Layers in Subsonic and Supersonic Flow," AGARDograph 335, NATO, Canada Communication Group, Hull, QC, Canada, July 1996.

Fan, H. and Bowersox, "Numerical Analysis of High-Speed Flow over Rough Surfaces," AIAA-99-2381, 35th AIAA/ASME/SAE/ASEE Joint Propulsion Conference, Los Angeles CA, June 1999.

Fernholz, I., Finley, M., and Mikulla, V., "A Further Compilation of Compressible Turbulent Boundary Layer Data with a Survey of Turbulence Data," *AGARDograph 263* NATO, Technical Editing and Reproduction, London, Nov. 1981.

Gandy, W. T., *Scattering of Waves from Large Spheres*, Cambridge University Press, Cambridge, UK, 2000, ch. 2, 5.

Goddard, F., "Effects of Uniformly Distributed Roughness on Turbulent Skin-Friction Drag at Supersonic Speeds," *Journal of Aero/Space Sciences*, Vol. 26, No. 1, 1959, pp. 1-24.

Gogineni, S., Goss, L., Pestian, D., and Rivir, R., "Two-color Digital PIV Employing a Single CCD Camera," *Experiments in Fluids*, Vol. 25, 1998, pp. 320-328.

Hanjalic, K and Launder, B., "Contribution Towards a Reynolds-Stress Closure for Low-Reynolds-Number Turbulence, *Journal of Fluid Mech.,* Vol. 74, pt. 4, 1976, pp. 593-610.

Hayakawa, K., Smits, A., and Bogdonoff, S., "Hot-Wire Investigation of an Unseparated Shock-Wave/Boundary Layer Interaction," *AIAA Journal*, Vol. 22, 1984, pp. 579-585.

Hazelton, D., Bowersox, R., Neumann, D., and Hayes, J., "Skin Friction Measurements in a Mach 6 Inlet Test," AIAA-97-2884, 33rd AIAA/ASME/SAE/ASEE Joint Propulsion Conference, Seattle WA, July 6-9, 1997.

Hefner, J., "Current and Future Needs in Turbulence Modeling," *Modeling Complex Flows,* Ed. by Salas, D., Hefner, J. and Sakell, L., ICASE/LaRC, Kluwer Academic Publishers, Boston, 1999.

Hinze, O., *Turbulence,* MCGraw-Hill, New York, 1975.

Jayaram, M., Taylor, M., and Smits, A., "The Response of a Compressible Turbulent Boundary layer to Short Regions of Concave Surface Curvature," *Journal of Fluid Mechanics*, Vol. 175, Feb. 1987, pp. 343-362.

Johnson, D., Mentor, F., and Rumsey, C., "The Status of Turbulence Modeling for External Aerodynamics," AIAA 94-2226, June 1994.

Kassinos, S., and Reynolds, W., "Developments in Structure-based Turbulence Modeling," *Modeling Complex Flows,* Ed. by Salas, D., Hefner, J. and Sakell, L., ICASE/LaRC, Kluwer Academic Publishers, Boston, 1999.

Kikhanovsky, A., A., *Optics of Light Scattering Media: Problems and Solutions*, Wiley-Praxis, Chichester, 1999.

Kim, J., and Simon, T. W., 1988. "Measurements of the Turbulent Transport of Heat and Momentum in Convexly Curved Boundary Layers: Effects of Curvature, Recovery and Free-Stream Turbulence," *Journal of Turbomachinery*, Vol. 110, No. 1, pp. 80-87.

Klebanoff, P. S., "Characteristics of Turbulence in a Boundary Layer with Zero-Pressure-Gradient," NACA Report, 1247, May 1955.

Kompenhans, J. and Kahler, C., "Particle Image Velocimetry – An Advanced Experimental Tool for the Investigation of Turbulent Flow Fields," *Engineering Turbulence Modeling and Experiments – 5*, Ed. By Rodi, W. and Fueyo, N., Elsevier Science Ltd., Oxford, 2002.

Lakshminarayana, B, *Fluid Dynamics and Heat Transfer of Turbomachinery,* John Wiley & Sons, New York, 1996.

Latin, R. and Bowersox, R., "Temporal Turbulent Flow Structure for Supersonic Rough-Wall Boundary Layers," *AIAA Journal,* Vol. 40, No. 5, 2002, pp. 832-841.

Latin, R. and Bowersox, R., "Flow Properties of a Supersonic Boundary Layer with Wall Roughness," *AIAA Journal,* Vol. 38, No. 10, 2000, pp. 1804-1821.

Latin, R. and Bowersox, R., "Influence of Surface Roughness on Supersonic Boundary Layer Turbulent Flow Structure," Paper No. 99-7059, *14th International Symposium on Airbreathing Engines (XIV ISABE),* Florence, Italy, Sept. 5-10, 1999a.

Launder, B., Reece, G., and Rodi, W., "Progress in the Development of a Reynolds-Stress Turbulence Closure," *J. of Fluid Mech.*, Vol. 68, Pt. 3, 1975, pp. 537-566.

Liou, W. and Shih, T.-H., "On the Basic Equations for the Second-Order Modeling of Compressible Turbulence," NASA TM 105277, Oct. 1991.

Luker, J., Bowersox, R., and Buter, T., "Influence of A Curvature Driven Favorable pressure gradient on a supersonic turbulent boundary layer," *AIAA Journal*, Vol. 38, No. 38, Aug 2000, pp. 1351-1359.

Luker, J., Hale, C., and Bowersox, R., "Experimental Characterization of the Turbulent Shear Stresses for Distorted Supersonic Boundary Layers," *Journal of Propulsion and Power,* Vol. 14, No. 1, 1998, pp. 110-118.

Morrison, J, *A Compressible Navier Stokes Solver with Two-Equation and Reynolds Stress Turbulence Closure Models,* NASA CR 4440, 1992.

Morkovin, M. V., "Effects of Compressibility on Turbulent Flows," *The Mechanics of Turbulence*, AGARD, Gordon and Breach, New York, 1961, pp. 367-380.

Narasimha, R., and Sreenivasan, K., "Relaminarization in Highly Accelerated Turbulent Boundary Layers," *Journal of Fluid Mechanics*, Vol. 61, Oct.-Dec. 1973, pp. 417-447.

Nikuradse, J., "Stromungsgesetze in Rauhen Rohren," *Forschung Arb. Ingenieurwesen*, No. 361, 1933.

Perry, A. E., Schofield, W. H., and Joubert, P. N., "Rough Wall Turbulent Boundary Layers," *Journal of Fluid Mechanics*, Vol. 37, 1969, pp. 383-413.

Pope, S., *Turbulent Flows*, Cambridge University Press, Cambridge, 2000.

Pope, S. "A Perspective on Turbulence Modeling," *Modeling Complex Flows,* Ed. by Salas, D., Hefner, J. and Sakell, L., ICASE/LaRC, Kluwer Academic Publishers, Boston, 1999.

Pritchett, V. and Bowersox, "Flow Properties of Compressible and Incompressible Subsonic Turbulent Boundary Layers with Surface Roughness," 39th AIAA Aerospace Sciences Meeting, Reno NV, Jan 2001.

River, D., *Personal Communication,* 2000.

Salas, M., Hefner, J. and Sakell, L., *Modeling Complex Turbulent Flows,* ICASE/LaRC Interdisciplinary Series in Science and Engineering, Kluwer Academic Publishers, 1999.

Sarkar, S., Erlebacher, G., Hussaini, M. and Kreiss, H., "The Analyses and Modeling of Dilatational Terms in Compressible Turbulence," ICASE Report 89-79, Univ. Space Res. Assoc., Hampton, VA, 1989.

Schetz, J.A., *Boundary Layer Analysis*, Prentice Hall, Englewood Cliffs, N.J., 1993.

Schlichting, H., *Boundary-Layer Theory*, Springer, New York, 2003.

Sherman, F., *Viscous Flow,* McGraw-Hill, New York, 1991.

Shrivaprasad, B. G., and Ramaprian, B. R., "Turbulence Measurements in Boundary Layers Along Mildly Curved Surfaces," *Journal of Fluids Engineering*, Vol. 100, No. 1, 1978, pp. 37-46.

Simonich, J. and Bradshaw, P., "Effect of Freestream Turbulence on Heat Transfer Through a Turbulent Boundary Layer," *J. of Heat Trans.*, Vol. 100, 1978, pp. 671-676.

Simpson, R., "A Generalized Correlation of Roughness Density Effects on the Turbulent Boundary Layer," *AIAA Journal*, Vol. 11, No. 2, 1973, pp. 242-244.

Smith, D., and Smits, A., "The Rapid Expansion of a Turbulent Boundary Layer in a Supersonic Flow," *Theoretical Computational Fluid Dynamics*, Vol. 2, 1991, pp. 319-328.

Smith, D., and Smits, A., "The Effects of Streamline Curvature and Pressure Gradient on the Behavior of Turbulent Boundary Layers in Supersonic Flow," AIAA Paper 94-2227, June 1994.

Smits, A. and Dussuage, J-P., *Turbulent Shear Layers in Supersonic Flow*, American Institute of Physics, Woodbury New York, 1996.

Smits, A. and Lim, T., *Flow Visualization Techniques and Examples*, Imperial College Press, London, 2000.

Smits, A. J., Spina, E. F., Alving, A. E., Smith, R. W., Fernando, E. M., and Donovan, J. F. "A Comparison of the Turbulence Structure of Subsonic and Supersonic Boundary Layers," *Physics of Fluids*, A Vol. 1 No. 11, 1989, pp. 1865-1875.

Smits, A., Young, S., and Bradshaw, P., "The Effects of Short Regions of High Surface Curvature on Turbulent Boundary Layers," *Journal of Fluid Mechanics,* Vol. 94, Sept. 1979, pp. 209-242.

Spina, E. F., Donovan, J. F., and Smits, A. J., "Convection Velocity in Supersonic Turbulent Boundary Layers," *Physics of Fluids A*, Vol. 3, 1991, pp. 3124-3127.

Spina, E. F., Smits, A. J., and Robinson, S., "Supersonic Turbulent Boundary Layers," *Annual Review of Fluid Mechanics*, Vol. 26, 1994, pp. 287-319.

Speziale, G., "Modeling Non-Equilibrium Turbulent Flows," *Modeling Complex Turbulent Flows,* Ed. Sales, Hefner and Sakell, Kluwer Academic Publishers, Boston, MA, 1999.

Thomann, H., "The Effects of Axial Wall Curvature on Heat Transfer in Turbulent Boundary Layers to Short Regions of Concave Surface Curvature," *Journal of Fluid Mechanics*, Vol. 33, July 1968, pp. 283-292.

TSI Inc., "Model 9306A Six-Jet Atomizer Instruction Manual," 1930099, Rev. B, Shoreview, MN, Feb. 2003.

Turner, A., Tarada, F. and Bayley, F., "Effects of Surface Roughness on Heat Transfer of Gas Turbine Engines," AGARD CP 390, 1990.

Van Driest, E. R., "Turbulent Boundary Layer in Compressible Fluids", *Journal of Aeronautical Sciences*, Vol. 18, pp. 145-160.

White, F., *Viscous Fluid Flow*, McGraw-Hill Higher Education, New York, 2006.

Wilcox, D., *Turbulence Modeling for CFD, 2nd Ed.,* DCW Industries, Inc., La Canada, California, 2000.

Zhang, H., So, R., Gatski, T., and Speziale, C., "A Near-Wall Second Order Closure Compressible Turbulent Flows," *Near Wall Turbulent Flows,* Ed. By R. So, C. Speziale, and B. Launder, Elsevier, New York, 1993, pp. 209-218.

DATA FILES

Zero pressure gradient, Smooth surface, Measurement location 1						
x, mm	y, mm	U, m/s	V, m/s	u'u', m^2/s^2	v'v', m^2/s^2	u'v', m^2/s^2
158.0399	16.172461	630.58584	-1.169502	89.94269202	5.94170535	-0.005945877
158.0399	15.763008	630.54185	-1.130402	87.36280118	5.99220427	-0.529425710
158.0399	15.353555	630.49850	-1.060083	86.32962361	5.77864844	-1.064991823
158.0399	14.944103	630.42313	-0.950214	84.19702411	5.64709172	-0.980386934
158.0399	14.534650	630.49399	-0.851172	83.88474077	5.55776783	-0.944977200
158.0399	14.125197	630.57454	-0.752066	80.52720803	5.58745425	-1.102578471
158.0399	13.715745	630.76312	-0.699406	80.02525118	5.55486892	-1.193879227
158.0399	13.306292	630.72103	-0.604167	80.77989324	5.99408451	-1.651455178
158.0399	12.896840	630.70172	-0.584588	78.81505267	6.36970581	-2.476657481
158.0399	12.487387	630.44714	-0.557506	78.71727352	6.70229144	-2.631370443
158.0399	12.077934	629.93747	-0.458111	79.48026108	7.07466292	-2.592021523
158.0399	11.668482	629.30536	-0.348128	82.64519225	8.01462049	-4.122812846
158.0399	11.259029	628.29934	-0.248888	89.68546194	9.38744251	-5.724289905
158.0399	10.849576	626.91730	-0.187623	97.83585645	11.30133479	-7.445279254
158.0399	10.440124	624.95046	-0.086580	105.49795310	13.82316870	-9.586288709
158.0399	10.030671	622.43389	-0.196642	119.44368310	16.75305140	-12.068963320
158.0399	9.621219	619.33439	-0.256425	135.86096810	22.48658969	-15.627894630
158.0399	9.211766	616.01474	-0.383371	144.19258800	26.38927313	-16.986534780
158.0399	8.802313	612.34814	-0.619335	165.00790020	30.83482428	-20.585882140
158.0399	8.392861	607.52027	-0.757659	223.69066430	42.30200095	-32.951401540
158.0399	7.983408	602.40004	-0.959072	279.51110350	49.38492295	-45.527325840
158.0399	7.573955	596.55136	-1.121868	342.64910670	60.25444097	-57.607461980
158.0399	7.164503	590.11373	-1.149188	413.11107760	73.98322126	-73.891644630
158.0399	6.755050	582.73614	-1.314242	505.82929530	90.02477750	-96.210958490
158.0399	6.345598	575.89066	-1.700372	558.78896860	100.32840090	-108.464961400
158.0399	5.936145	568.66104	-1.844810	614.81490190	118.02896570	-127.516420200
158.0399	5.526692	560.92599	-2.156385	684.25661990	140.23516840	-149.429820300
158.0399	5.117240	552.29564	-2.172618	776.10642430	172.01559520	-180.682862500
158.0399	4.707787	543.51667	-2.224887	868.84927060	177.48818710	-190.290032400
158.0399	4.298334	534.38421	-2.133703	960.64131460	191.69333990	-213.032001100
158.0399	3.888882	524.80403	-2.121746	1076.18046400	210.91089420	-243.249421700
158.0399	3.479429	515.40621	-2.472299	1131.44875200	199.66825860	-232.895671700
158.0399	3.069977	504.79153	-2.666194	1268.90885500	220.97371630	-267.136046800
158.0399	2.660524	493.87494	-3.064962	1425.37258300	228.34049810	-279.547476200
158.0399	2.251071	483.15020	-3.139492	1552.43299700	233.88309640	-286.943426300
158.0399	1.841619	475.58446	-3.380261	1807.04368600	298.67976840	-306.667728000
158.0399	1.432166	468.36926	-2.995738	2630.62483800	430.73499610	-336.810533500
158.0399	1.022713	402.27668	-3.175596	22785.46604000	537.30499120	-453.107736400
158.0399	0.613261	305.64290	-3.039438	43082.99646000	522.70846800	-665.878428100
158.0399	0.203808	179.54965	-1.328121	41832.13989000	225.49104880	-419.712918700

Zero pressure gradient, Smooth surface, Measurement location 2						
x, mm	y, mm	U, m/s	V, m/s	u'u', m^2/s^2	v'v', m^2/s^2	u'v', m^2/s^2
294.6137	16.301497	632.85054	-1.609611	37.97488460	40.15183354	-0.118380319
294.6137	15.888468	632.61841	-1.843607	37.43353285	41.05210788	0.447914727
294.6137	15.475440	632.31497	-1.954631	36.43191649	40.01038090	1.782318913
294.6137	15.062411	632.11646	-1.828355	39.93062890	28.43231682	-0.202966842
294.6137	14.649382	631.69884	-2.462940	37.92737675	48.42639988	-1.120137564
294.6137	14.236353	631.39251	-2.611511	42.05281234	50.94281646	-1.271738896
294.6137	13.823324	630.93226	-2.445118	41.24629665	40.46477616	-3.220248123
294.6137	13.410295	630.38663	-2.732571	51.08333295	58.17094865	-4.075063301
294.6137	12.997266	629.78699	-2.573821	61.99929123	65.11099546	-5.562511131
294.6137	12.584237	628.87706	-2.552206	92.34064532	83.09352317	-8.809256446
294.6137	12.171209	627.49952	-2.235507	134.32395500	84.76774670	-16.809060780
294.6137	11.758180	625.65511	-2.113591	189.62367830	110.02089610	-26.389694160
294.6137	11.345151	623.24965	-1.775499	217.44690420	103.97151530	-34.759280460
294.6137	10.932122	620.52865	-1.576875	281.48022130	118.90151820	-44.840226910
294.6137	10.519093	616.55829	-1.138676	368.99255590	159.21887830	-72.733770240
294.6137	10.106064	612.66050	-1.198225	472.82374660	191.34603460	-78.569250620
294.6137	9.693035	607.79669	-0.860712	545.24293730	193.15936900	-92.891650240
294.6137	9.280006	602.71383	-1.083609	646.68584560	207.21106960	-101.646270800
294.6137	8.866977	596.87696	-1.106728	778.28936580	251.23593850	-122.726649300
294.6137	8.453949	590.71125	-1.220391	900.37350000	292.27401410	-166.082726200
294.6137	8.040920	584.42960	-0.995800	954.29268610	405.35012250	-154.245340400
294.6137	7.627891	577.69065	-1.315850	1112.11283800	352.76104360	-194.354418900
294.6137	7.214862	571.04185	-1.164993	1173.58082800	371.02555900	-178.797605200
294.6137	6.801833	564.22556	-1.310604	1235.22585400	411.66443820	-209.382706800
294.6137	6.388804	557.33920	-1.446243	1281.26646200	382.81105240	-230.111133100
294.6137	5.975775	549.45828	-1.342919	1432.52650100	433.67708070	-274.623096400
294.6137	5.562746	541.65651	-1.110771	1715.22463900	540.38234760	-272.474081100
294.6137	5.149717	534.30420	-1.625314	1957.04626100	570.47137720	-242.002826500
294.6137	4.736689	524.70913	-1.802291	3051.92715600	789.94507430	-195.186876600
294.6137	4.323660	517.12531	-1.371106	2614.35102500	679.04940270	-242.413884900
294.6137	3.910631	505.87288	-1.449332	3932.24833700	974.87960400	-225.370324700
294.6137	3.497602	494.25718	-0.744293	6320.65789300	1934.91971800	-235.723873800
294.6137	3.084573	483.22584	-1.102240	9180.07940400	2717.77688800	-181.207248200
294.6137	2.671544	469.72455	1.945513	11606.47970000	4466.14441300	-710.750071400
294.6137	2.258515	450.39926	2.793821	17898.47292000	7578.31449600	-1152.183248000
294.6137	1.845486	417.90305	5.514183	27133.40130000	8942.29744200	-915.700689100
294.6137	1.432458	352.89164	4.252576	41619.24731000	9251.44551600	-807.460250000
294.6137	1.019429	217.74427	-1.510925	47440.78902000	3254.80693400	-461.020553000
294.6137	0.606400	212.41653	-2.419466	49333.78434000	1350.07346000	-244.370241300
294.6137	0.193371	240.11644	-0.506593	56517.08810000	1407.89876300	273.470531600

Zero pressure gradient, Smooth surface, Measurement location 3						
x, mm	y, mm	U, m/s	V, m/s	u'u', m^2/s^2	v'v', m^2/s^2	u'v', m^2/s^2
410.62323	16.43954	632.10657	19.58772	8.76096	115.12292	0.80173
410.62323	16.10788	632.21025	19.63234	9.12141	118.44984	0.71594
410.62323	15.77622	632.32543	19.78456	10.05125	122.63466	-0.01754
410.62323	15.44456	632.20236	20.16511	19.26942	128.51976	-2.99586
410.62323	15.11290	632.15531	20.24234	24.64507	140.15865	-5.98064
410.62323	14.78124	632.18803	20.74079	24.78810	145.27780	-7.49169
410.62323	14.44958	632.04660	21.35165	28.95706	146.77148	-9.69875
410.62323	14.11792	631.57310	21.88736	48.94811	150.95133	-15.40525
410.62323	13.78626	631.12188	22.12389	62.89038	156.44480	-22.26274
410.62323	13.45460	630.52399	22.22304	77.52553	159.85512	-28.48950
410.62323	13.12294	629.51594	22.21312	108.48266	161.58945	-37.62097
410.62323	12.79128	628.13122	21.81225	152.70732	171.76282	-50.55341
410.62323	12.45961	626.41255	21.26378	200.41035	180.71248	-66.29596
410.62323	12.12795	624.43805	20.80922	253.92537	178.41977	-81.37444
410.62323	11.79629	622.31331	20.30430	309.17859	181.01319	-97.05964
410.62323	11.46463	619.88738	19.70216	356.24747	196.38677	-116.53100
410.62323	11.13297	616.97144	18.92729	415.11442	200.89216	-129.09061
410.62323	10.80131	613.77243	18.33270	476.47480	205.96207	-143.82348
410.62323	10.46965	610.20880	17.86205	538.05714	224.35834	-155.56245
410.62323	10.13799	606.70570	17.33793	590.23919	226.32392	-177.15331
410.62323	9.80633	602.81973	16.82456	633.91236	225.93101	-183.56977
410.62323	9.47467	598.74278	16.29257	657.43441	235.79410	-191.33235
410.62323	9.14301	594.80807	15.60247	718.88355	240.99509	-208.73831
410.62323	8.81135	590.68879	14.93633	773.31179	247.66686	-219.56652
410.62323	8.47968	586.47817	14.38187	818.56716	255.75915	-230.08193
410.62323	8.14802	582.00237	13.77971	879.63752	267.09108	-236.26704
410.62323	7.81636	577.19183	13.28325	941.14985	275.92379	-240.70463
410.62323	7.48470	572.43626	12.77689	993.48807	285.83574	-249.59414
410.62323	7.15304	567.78690	12.12212	1047.85777	295.06505	-264.01379
410.62323	6.82138	563.11654	11.51243	1112.23893	300.84589	-280.29512
410.62323	6.48972	558.45483	11.05869	1170.42411	312.41349	-291.35710
410.62323	6.15806	553.08698	10.63910	1189.10254	315.36838	-293.33789
410.62323	5.82640	548.02089	9.75601	1244.33398	324.60302	-299.96873
410.62323	5.49474	543.20162	9.51046	1318.69154	344.38740	-309.64804
410.62323	5.16308	537.77479	8.62385	1344.63068	344.80825	-304.28570
410.62323	4.83142	532.55547	7.97266	1357.12363	329.58829	-307.73590
410.62323	4.49975	526.78181	7.61963	1368.17486	331.97558	-296.88894
410.62323	4.16809	520.91409	6.91708	1440.43728	348.06226	-298.97938
410.62323	3.83643	515.11628	6.59683	1525.83881	371.30363	-307.85727
410.62323	3.50477	508.69263	5.72084	1577.26627	357.57334	-285.80498
410.62323	3.17311	501.67687	4.83028	1831.93793	397.44270	-283.84267
410.62323	2.84145	494.33864	4.15481	1992.09906	425.15514	-283.45710
410.62323	2.50979	486.31150	3.45420	1984.10943	389.79026	-287.66337
410.62323	2.17813	477.35271	2.57987	1988.44220	339.23639	-282.76288
410.62323	1.84647	471.04863	2.01096	2620.04042	505.73810	-251.51954
410.62323	1.51481	468.38257	2.07631	4209.37135	988.06756	-243.09506
410.62323	1.18315	457.49133	1.30825	4535.18551	1058.89267	-190.22544
410.62323	0.85149	443.76824	1.12999	3834.53262	786.28049	-257.90088
410.62323	0.51982	426.79446	-0.31369	3829.37015	497.79739	-276.11594
410.62323	0.18816	411.28172	-1.17805	5603.76230	160.38742	-56.09166

Zero pressure gradient, Rough surface, Measurement location 1						
x, mm	y, mm	U, m/s	V, m/s	u'u', m^2/s^2	v'v', m^2/s^2	u'v', m^2/s^2
161.58438	16.545560	628.38735	1.422985	10.74249132	8.50447625	-0.786954356
161.58438	16.126541	628.30687	1.463239	9.71874585	7.81376937	-0.843623247
161.58438	15.707521	628.14970	1.439839	8.95964921	7.10697723	-1.053688657
161.58438	15.288502	627.98740	1.384968	7.99714703	6.48987752	-0.788740558
161.58438	14.869483	627.83871	1.243423	7.41528574	5.89762989	-0.788366197
161.58438	14.450464	627.76855	1.124412	7.13339947	5.68136283	-0.788189315
161.58438	14.031444	627.69738	1.041378	6.70292077	5.13737278	-0.399575541
161.58438	13.612425	627.56575	0.970576	6.25363326	4.82495702	-0.478530091
161.58438	13.193406	627.52310	0.906020	6.12126497	4.53030893	-0.782003387
161.58438	12.774386	627.45962	0.904930	5.55897583	4.28267463	-0.559432648
161.58438	12.355367	627.38592	0.944245	5.65337481	4.31579776	-0.396396722
161.58438	11.936348	627.27950	1.028844	6.19106758	4.61843079	-0.396263859
161.58438	11.517329	627.17417	1.099262	7.13483806	5.04184127	-0.786697117
161.58438	11.098309	627.00108	1.183489	10.09838133	5.93926177	-0.898642121
161.58438	10.679290	626.64653	1.264636	12.66363625	7.23657283	-1.363112017
161.58438	10.260271	625.94722	1.328908	19.83936457	9.40855489	-2.585175940
161.58438	9.841251	624.76601	1.508460	38.03389499	12.48483274	-5.081173996
161.58438	9.422232	622.62877	1.662616	73.73867912	15.22249113	-8.228394664
161.58438	9.003213	618.63401	1.932131	163.50583330	22.49985943	-16.136229700
161.58438	8.584194	614.07038	2.316867	246.77458640	34.29225180	-26.867150640
161.58438	8.165174	608.47628	2.837429	345.60020180	52.58766596	-42.749407450
161.58438	7.746155	601.62141	3.622091	465.42421730	91.08067153	-76.672989780
161.58438	7.327136	594.73888	3.793411	546.65716070	123.46004050	-96.878519170
161.58438	6.908117	587.80718	3.738603	609.92230620	145.50713390	-111.776842600
161.58438	6.489097	579.13668	3.647670	785.80816560	184.87064220	-149.982187300
161.58438	6.070078	570.75074	3.276248	923.33325490	212.34401100	-177.841063600
161.58438	5.651059	561.08644	3.099150	1136.17592800	254.21053490	-224.389610600
161.58438	5.232039	550.49800	3.198921	1353.89910700	287.63990720	-273.938351800
161.58438	4.813020	537.91478	3.363443	1762.36717300	371.23122670	-359.402674100
161.58438	4.394001	524.49261	3.580242	2139.60002100	443.35748510	-455.464552200
161.58438	3.974982	510.25798	3.511406	2439.49468000	466.04640630	-486.018841200
161.58438	3.555962	495.61293	3.057472	2806.83998300	520.55727730	-552.325832900
161.58438	3.136943	479.70353	2.436464	3220.73826400	610.55880460	-648.991458900
161.58438	2.717924	464.00815	1.277211	3624.56281100	688.83461810	-735.673625700
161.58438	2.298905	448.75175	0.819306	3945.27732900	835.69880190	-799.349470100
161.58438	1.879885	435.27075	-0.063692	4673.81450600	974.64842540	-770.549054200
161.58438	1.460866	425.29150	-0.291082	5960.76510500	1312.18805800	-780.579613200
161.58438	1.041847	407.28936	-1.093936	7539.84934100	2004.15309500	-747.040464100
161.58438	0.622827	376.92680	-0.937470	12958.32016000	3002.45017000	-860.613684400
161.58438	0.203808	362.47888	-3.793203	13099.65328000	2310.99027600	-766.784020900

Zero pressure gradient, Rough surface, Measurement location 2						
x, mm	y, mm	U, m/s	V, m/s	u'u', m^2/s^2	v'v', m^2/s^2	u'v', m^2/s^2
302.71974	16.870004	627.49997	1.762070	7.03767604	8.79634347	-1.575037283
302.71974	16.442225	627.41001	1.595854	6.67425161	8.89818828	-1.574583190
302.71974	16.014446	627.30218	1.448018	6.83669308	8.91258012	-1.573192889
302.71974	15.586667	627.16330	1.236808	6.66498378	8.99333119	-1.312790749
302.71974	15.158888	626.97153	1.070322	7.23960781	8.89471399	-1.180130430
302.71974	14.731108	626.64962	0.984980	9.61329830	10.06502294	-1.596893136
302.71974	14.303329	626.20455	0.836392	17.88349004	11.43049240	-2.383242140
302.71974	13.875550	625.62869	0.775306	24.16160053	14.10778473	-3.889233249
302.71974	13.447771	624.90075	0.746324	33.05493724	17.20740135	-5.884023363
302.71974	13.019992	622.25108	0.941327	107.81752620	39.07488660	-17.481990140
302.71974	12.592212	619.77797	1.073756	163.85823250	50.52312418	-24.155266500
302.71974	12.164433	617.12365	0.737846	213.46255880	40.85120089	-25.160875940
302.71974	11.736654	612.85757	0.740242	316.89000470	61.98409502	-35.387026650
302.71974	11.308875	606.90525	1.271712	473.46007570	115.60270860	-69.383662260
302.71974	10.881096	600.62362	1.406221	605.98965110	140.76847390	-93.019348030
302.71974	10.453316	592.65365	1.701416	829.01144390	212.27468580	-149.074743100
302.71974	10.025537	585.64588	1.526611	934.84042680	258.88082610	-177.061503900
302.71974	9.597758	577.78150	1.501008	1062.55722700	307.86524270	-219.498770800
302.71974	9.169979	568.90110	1.288683	1293.32150000	364.11850890	-275.850656900
302.71974	8.742200	561.16165	0.807715	1421.12276900	386.19352670	-281.044708400
302.71974	8.314420	551.99402	1.102175	1643.83579400	485.05553790	-386.896878000
302.71974	7.886641	541.89064	1.150883	1933.48598800	549.52791150	-471.172879000
302.71974	7.458862	532.66964	0.628704	2102.78909900	583.04027220	-513.474088700
302.71974	7.031083	522.40700	0.582114	2269.25532800	647.58291470	-571.912009800
302.71974	6.603303	511.67206	0.216089	2573.73327000	727.74496550	-653.550014900
302.71974	6.175524	500.16662	-0.238932	2810.38714900	754.86451470	-680.934954300
302.71974	5.747745	490.01971	-0.155018	3055.76541300	836.26399300	-782.129204100
302.71974	5.319966	478.93679	-0.499144	3235.59696500	874.55980760	-813.312213700
302.71974	4.892187	466.68881	-0.818529	3525.99811300	938.55994790	-834.688630300
302.71974	4.464407	454.48851	-1.108644	3607.16532800	993.46726230	-862.785102500
302.71974	4.036628	443.00595	-2.373325	3755.93111500	929.78850630	-851.808638200
302.71974	3.608849	430.56046	-2.279591	4195.88954200	974.35890060	-815.980420700
302.71974	3.181070	417.00028	-2.749260	4735.31604100	1163.34172600	-833.042351900
302.71974	2.753291	401.77433	-2.855035	5103.12864700	1254.12153100	-933.899790700
302.71974	2.325511	388.88709	-3.767407	6064.94495000	1446.70343600	-942.422625800
302.71974	1.897732	376.29069	-4.416954	7935.50985400	1923.52606500	-917.309347800
302.71974	1.469953	365.82000	-1.783662	12320.55658000	3446.61238700	-810.140859300
302.71974	1.042174	347.22623	-4.984031	15578.34768000	4620.92227100	-893.242335000
302.71974	0.614395	323.63911	-9.061314	20759.99693000	4720.29363500	-903.727628500
302.71974	0.186615	307.66672	-4.140656	22844.28808000	1716.97480700	-259.676833500

Zero pressure gradient, Rough surface, Measurement location 3						
x, mm	y, mm	U, m/s	V, m/s	u'u', m^2/s^2	v'v', m^2/s^2	u'v', m^2/s^2
412.73784	16.11728	623.12264	1.36738	41.03259	30.18588	-3.68584
412.73784	15.79220	622.63606	1.29276	47.34880	34.32776	-4.74060
412.73784	15.46711	622.01374	1.14635	56.40987	38.35588	-5.46023
412.73784	15.14203	621.05780	0.96901	74.64763	44.71199	-8.59838
412.73784	14.81694	619.62622	0.94167	108.50431	54.75335	-16.46705
412.73784	14.49186	618.18644	0.80504	138.57528	63.05101	-23.63550
412.73784	14.16678	616.45021	0.57539	172.05935	70.27608	-29.96982
412.73784	13.84169	614.39381	0.37474	218.98805	80.82680	-38.15428
412.73784	13.51661	611.89056	0.19233	276.77567	94.08122	-49.37638
412.73784	13.19152	608.86587	-0.04033	345.63670	107.73311	-61.10047
412.73784	12.86644	605.04797	-0.17058	449.34662	125.89244	-77.14028
412.73784	12.54136	600.47004	-0.08834	585.89816	149.85809	-101.91143
412.73784	12.21627	596.48910	-0.21591	674.06757	167.55378	-120.92425
412.73784	11.89119	592.35204	-0.20375	763.71388	203.55430	-149.85498
412.73784	11.56610	587.65705	-0.46866	872.38794	234.44136	-177.80613
412.73784	11.24102	583.21297	-0.87026	941.19552	236.69728	-185.20628
412.73784	10.91594	578.81694	-1.46046	1018.76774	247.29220	-193.40420
412.73784	10.59085	574.00775	-1.64607	1097.36782	283.82564	-221.77261
412.73784	10.26577	568.67092	-1.70080	1191.21911	322.04067	-260.08569
412.73784	9.94068	562.74743	-1.99200	1321.10902	360.05675	-290.52996
412.73784	9.61560	556.66079	-2.08272	1447.61447	397.91329	-322.67015
412.73784	9.29052	550.75224	-2.04315	1545.52857	436.98138	-355.85516
412.73784	8.96543	545.19332	-2.32613	1629.26695	476.18893	-375.09497
412.73784	8.64035	539.97141	-2.55878	1710.70161	505.49396	-392.34884
412.73784	8.31526	533.97177	-2.81474	1825.19882	532.99756	-423.19277
412.73784	7.99018	527.46119	-2.59284	1922.33289	569.48684	-453.50647
412.73784	7.66510	520.94630	-2.99332	2076.02272	583.43976	-471.89594
412.73784	7.34001	514.11494	-3.16177	2266.19442	645.37885	-526.24312
412.73784	7.01493	507.86418	-3.03810	2393.64256	700.42528	-564.48471
412.73784	6.68984	501.36854	-3.59302	2490.54279	698.71960	-579.05009
412.73784	6.36476	494.00085	-3.77022	2615.01528	726.59720	-606.90860
412.73784	6.03968	487.11414	-3.86230	2798.22115	766.32657	-660.04670
412.73784	5.71459	480.17638	-4.09137	2962.67385	803.61912	-711.10851
412.73784	5.38951	472.28080	-4.03701	3097.66830	862.69419	-768.31609
412.73784	5.06442	464.23694	-3.67175	3280.44777	923.64283	-837.83408
412.73784	4.73934	456.38862	-3.71358	3456.41340	935.54191	-842.18839
412.73784	4.41426	448.47570	-4.34933	3607.77211	959.73586	-833.85089
412.73784	4.08917	439.37764	-3.66998	3660.13263	998.78114	-838.00640
412.73784	3.76409	431.67648	-4.56433	3881.91450	1014.60337	-850.96710
412.73784	3.43900	423.38844	-5.03628	4203.42229	989.36634	-871.10483
412.73784	3.11392	389.82446	-5.23518	12166.91217	1027.91117	-987.04786
412.73784	2.78884	375.71193	-5.07859	13603.52232	1028.74342	-961.98721
412.73784	2.46375	363.15279	-5.86497	14502.39319	990.59563	-947.49503
412.73784	2.13867	340.86330	-6.50130	18480.32945	1023.53536	-1015.85244
412.73784	1.81358	322.04228	-5.90947	22749.47207	1330.26251	-1101.17501
412.73784	1.48850	306.63278	-4.65418	25814.93375	1722.88968	-1128.66256
412.73784	1.16342	275.39399	-3.63337	28570.37416	1722.28145	-1019.80101
412.73784	0.83833	230.89828	-3.23951	29797.89443	1505.41662	-743.12565
412.73784	0.51325	175.82140	-3.69731	29208.63334	1079.71322	-644.10574
412.73784	0.18816	121.81044	-3.51373	23041.53027	509.63839	-544.20800

Weak pressure gradient, Smooth surface, Measurement location 1						
x, mm	y, mm	U, m/s	V, m/s	u'u', m^2/s^2	v'v', m^2/s^2	u'v', m^2/s^2
163.711	16.172461	632.62577	0.028218	48.70861706	22.66033801	-2.038282476
163.711	15.763008	632.27943	-0.298481	47.20691713	23.00900261	-3.003412343
163.711	15.353555	631.88433	-0.651168	43.42826178	22.44787252	-1.883473145
163.711	14.944103	631.71254	-0.930910	45.40779905	22.19963950	-1.422919198
163.711	14.534650	631.55722	-1.212534	45.13756934	22.69232991	-1.449073155
163.711	14.125197	631.29936	-1.467749	44.57405340	22.52295135	-0.679616611
163.711	13.715745	630.96902	-1.737209	44.86318927	23.53415461	-0.416832795
163.711	13.306292	630.51017	-2.179862	38.47461538	22.46796429	-1.178631006
163.711	12.896840	630.10006	-2.379799	37.24115845	23.62682093	-1.086800475
163.711	12.487387	629.60751	-2.598938	34.66550021	24.46857122	-0.778836592
163.711	12.077934	629.34617	-2.697263	40.13583869	25.61478332	-0.572606104
163.711	11.668482	629.00679	-2.796708	43.55130399	26.10811148	-0.665520634
163.711	11.259029	628.38914	-2.848415	49.37180066	29.16143484	-0.808342366
163.711	10.849576	627.42603	-2.845117	56.19477244	32.24065393	-1.949809422
163.711	10.440124	626.28022	-2.961497	58.84216052	32.91160030	-2.032518568
163.711	10.030671	624.29422	-2.941723	86.18235059	40.51496813	-6.271767449
163.711	9.621219	621.91611	-2.711189	113.62787580	46.33905641	-11.589208490
163.711	9.211766	619.01580	-2.305863	146.14344040	51.00594771	-18.068454910
163.711	8.802313	615.41457	-1.500395	199.37272710	55.49661500	-26.031637620
163.711	8.392861	610.79939	-0.321639	263.67969160	70.83734258	-39.265514290
163.711	7.983408	605.62828	0.803819	347.83949640	90.36247666	-60.084219070
163.711	7.573955	599.71667	2.151655	453.23360020	101.19596860	-83.203996020
163.711	7.164503	593.07686	3.078493	532.32830500	129.26396560	-112.952520200
163.711	6.755050	586.66719	3.524463	570.41150320	139.24780940	-127.500317600
163.711	6.345598	579.74515	3.756611	620.09300600	142.06291840	-140.661648200
163.711	5.936145	571.66276	4.003027	734.91366790	155.26897320	-164.88809000
163.711	5.526692	563.01868	4.193075	843.12868260	177.69829640	-191.134159000
163.711	5.117240	555.16362	3.698759	898.50530980	190.55766280	-203.557622600
163.711	4.707787	546.11148	3.617937	1021.58447000	216.42854200	-228.107788700
163.711	4.298334	536.67117	3.295507	1143.24115100	252.30728110	-261.621845600
163.711	3.888882	527.32995	2.884457	1254.11243200	269.26567240	-279.624927500
163.711	3.479429	517.39839	2.484542	1404.64340300	303.58519190	-285.074424700
163.711	3.069977	507.85365	1.960810	1660.58491800	323.64147510	-314.059617700
163.711	2.660524	497.53644	1.320463	1954.22320100	368.39571280	-312.029471600
163.711	2.251071	485.83987	0.447980	2462.28052700	491.73764390	-288.406223900
163.711	1.841619	474.78250	0.245629	4212.23102600	1191.11606700	-354.286059600
163.711	1.432166	465.54897	-0.106076	7723.47587000	2500.44876900	-228.612836600
163.711	1.022713	452.66707	-1.282202	9455.26618800	2660.10599000	-250.111908600
163.711	0.613261	438.71694	-1.035358	13093.16607000	2734.85867000	-560.748387400
163.711	0.203808	425.41618	1.256920	16543.30661000	2816.14648900	-1152.894323000

Weak pressure gradient, Smooth surface, Measurement location 2						
x, mm	y, mm	U, m/s	V, m/s	u'u', m^2/s^2	v'v', m^2/s^2	u'v', m^2/s^2
297.02376	19.035498	630.69675	-1.792190	25.71860385	8.30985670	0.823042642
296.99858	18.522181	630.72811	-1.971340	27.24234858	8.73499041	1.193465280
296.97340	18.008865	630.71983	-2.054932	28.53404577	9.32731019	1.353377915
296.94823	17.495548	630.80468	-2.065359	29.70574509	9.27653067	1.266323963
296.92305	16.982232	630.79208	-2.066225	29.80992682	9.52658287	0.967453260
296.89787	16.468915	630.79646	-2.073701	29.91661081	9.59767586	0.864949829
296.87270	15.955599	630.76538	-2.182889	31.38532171	10.26595183	0.504792052
296.84752	15.442282	630.40046	-2.403156	30.15136098	11.08821106	0.327873038
296.82235	14.928966	630.28214	-2.635401	29.57031819	11.07422286	0.203809023
296.79717	14.415649	630.18927	-2.822674	31.57714259	11.78688292	-0.094659231
296.77199	13.902332	629.99184	-3.013285	31.09081974	12.36945527	-0.279642397
296.74682	13.389016	629.80899	-3.192073	31.86556082	13.21364981	-1.181845956
296.72164	12.875699	629.47280	-3.431363	33.78868318	15.10805912	-1.768466073
296.69646	12.362383	629.15431	-3.635386	39.29426255	17.16356499	-2.662239913
296.67129	11.849066	628.41930	-3.932217	45.81424566	20.16393379	-3.381281455
296.64611	11.335750	627.34409	-4.206765	55.20761970	24.47785044	-4.805120139
296.62094	10.822433	625.49301	-4.581883	71.75912795	30.92111841	-8.220053851
296.59576	10.309117	622.58716	-5.202793	115.77132240	42.60945554	-14.395896170
296.57058	9.795800	619.58398	-5.892564	153.58543620	47.09770153	-18.194974820
296.54541	9.282483	615.25551	-6.801190	225.14732710	61.31686600	-32.412265370
296.52023	8.769167	610.35654	-8.110880	301.79403450	82.73268195	-48.274121360
296.49505	8.255850	605.13180	-9.304817	375.11704470	93.57618819	-65.774733580
296.46988	7.742534	599.33403	-10.316242	452.83328000	111.81569760	-87.145834300
296.44470	7.229217	592.81948	-10.960734	530.43896070	129.57225910	-110.799125900
296.41953	6.715901	586.21180	-11.533731	589.51385780	144.17047370	-128.587045000
296.39435	6.202584	579.15305	-11.955411	636.01074770	159.25236190	-145.636428100
296.36917	5.689268	571.42876	-12.106673	691.33543930	169.84015200	-157.649167400
296.34400	5.175951	563.22967	-12.236621	772.86628400	185.32391180	-177.741377500
296.31882	4.662634	555.03922	-12.438811	811.53715460	197.24029490	-186.917957500
296.29364	4.149318	546.51838	-12.548791	864.39897980	197.40857840	-191.904408000
296.26847	3.636001	537.40654	-12.524487	926.32189150	215.42988680	-207.311557300
296.24329	3.122685	528.25541	-12.491800	985.39375770	222.55761370	-215.791301700
296.21811	2.609368	518.20470	-12.410021	1079.87287500	229.76315380	-234.157716700
296.19294	2.096052	507.92150	-12.399604	1130.95069900	219.13449180	-232.425908400
296.16776	1.582735	496.08707	-12.648612	1249.49083800	227.03611690	-240.042585900
296.14259	1.069419	482.50128	-13.031112	1428.60917500	226.88516160	-243.495117300
296.11741	0.556102	466.89462	-13.873066	1941.32483200	278.47539710	-241.804500300
296.09223	0.042785	450.91854	-12.682481	4091.94407200	855.87232060	-225.639357300
296.06706	-0.470531	346.39393	-9.941967	24633.89412000	1559.30187500	-649.458661700
296.04188	-0.983848	225.89045	-3.463950	41766.34578000	342.32971470	-458.822643200

Weak pressure gradient, Smooth surface, Measurement location 3						
x, mm	y, mm	U, m/s	V, m/s	u'u', m^2/s^2	v'v', m^2/s^2	u'v', m^2/s^2
411.34226	12.782827	633.66925	-31.722579	21.21396214	102.63242900	3.098014400
411.30841	12.270438	633.70850	-32.105248	21.26283184	108.60053070	2.877788112
411.27456	11.758050	633.79183	-32.114998	19.82362856	109.89121570	1.787003651
411.24071	11.245661	633.74637	-32.017435	21.16208324	113.11244980	0.543027779
411.20686	10.733272	633.47154	-32.322047	27.41926813	117.79489730	-1.966476494
411.17301	10.220884	633.09180	-32.106073	35.09156653	108.43307560	-4.058728179
411.13915	9.708495	632.56783	-32.579970	45.31477011	114.22481410	-10.391594250
411.10530	9.196106	631.64135	-33.178335	64.64534279	116.28371680	-16.822923280
411.07145	8.683717	630.42482	-33.573241	87.90518630	135.55031300	-25.701255270
411.03760	8.171329	628.52964	-33.464493	128.49863540	139.80194410	-40.693868810
411.00375	7.658940	626.12910	-32.935399	167.71032120	119.30475800	-48.151419080
410.96990	7.146551	623.17052	-32.769399	207.31999560	124.24672630	-57.986397960
410.93605	6.634163	619.41238	-32.202486	250.10196120	137.43008490	-68.731801210
410.90219	6.121774	615.30782	-32.250544	282.34574850	152.77601380	-77.627592940
410.86834	5.609385	610.69897	-31.999715	315.56010910	151.78111370	-85.718705850
410.83449	5.096996	605.99496	-31.897557	341.23140270	166.27220770	-95.590413660
410.80064	4.584608	601.01855	-31.737342	356.39666050	187.01744490	-104.947691500
410.76679	4.072219	596.34746	-31.391377	370.48471870	183.48647680	-116.601763300
410.73294	3.559830	591.73392	-31.490521	398.74556710	197.74376920	-122.269548400
410.69909	3.047442	587.35831	-31.847497	433.36189040	211.12823170	-127.514872200
410.66523	2.535053	581.99261	-31.594075	484.49590400	230.80368140	-140.950975700
410.63138	2.022664	576.80116	-31.225263	526.67377940	243.35047980	-152.757913100
410.59753	1.510276	571.32394	-30.892740	555.77786620	249.49634290	-168.558120200
410.56368	0.997887	565.56872	-30.341923	593.67870250	269.49817080	-179.624700300
410.52983	0.485498	559.96910	-30.246965	667.47258270	283.84727230	-175.199304300
410.49598	-0.026891	553.25016	-30.052502	724.11657280	297.83473260	-179.373836600
410.46212	-0.539279	547.45131	-30.212318	793.48307720	338.67389740	-188.861271500
410.42827	-1.051668	541.72470	-30.264690	824.25092870	359.85642780	-170.241250600
410.39442	-1.564057	536.82649	-30.033563	721.47061810	317.97267490	-183.048652400
410.36057	-2.076445	530.75399	-30.015761	931.62480390	401.89680670	-191.363260700
410.32672	-2.588834	524.89108	-28.829416	1069.61002800	432.93997100	-221.590641000
410.29287	-3.101223	518.81935	-28.409397	1227.76996900	464.77294080	-257.445798400
410.25902	-3.613611	510.82337	-27.420609	1334.23925200	479.26626520	-231.781212800
410.22516	-4.126000	501.27112	-26.573712	1942.63328300	700.06407420	-256.646888100
410.19131	-4.638389	487.41787	-25.134364	2597.86611600	705.60333910	-299.428310500
410.15746	-5.150778	471.86249	-26.891734	3338.54616900	797.58023320	-281.803945000
410.12361	-5.663166	447.97679	-24.891634	6910.32026100	1020.97920600	-341.328840900
410.08976	-6.175555	255.05849	-17.763906	26087.46088000	369.93599850	-1642.238712000
410.05591	-6.687944	147.54386	-10.398464	21925.62293000	289.93335560	-1266.650588000
410.02206	-7.200332	3.99817	-0.178413	858.08140570	10.99800715	-42.618289370

Weak pressure gradient, Rough surface, Measurement location 1						
x, mm	y, mm	U, m/s	V, m/s	u'u', m^2/s^2	v'v', m^2/s^2	u'v', m^2/s^2
165.16614	16.545560	628.96412	-0.426566	6.10403444	5.90482642	-0.395596126
165.16614	16.126541	628.93085	-0.284985	6.13644176	5.39493927	-0.395553791
165.16614	15.707521	628.82469	-0.150110	6.03560449	4.90509287	-0.390926009
165.16614	15.288502	628.63497	-0.078947	5.38199996	4.38747827	-0.390687718
165.16614	14.869483	628.61365	-0.092642	6.26349454	4.05752018	-0.395155332
165.16614	14.450464	628.33060	-0.086122	4.82045401	3.97725508	-0.394799067
165.16614	14.031444	628.17687	-0.138921	4.12207034	3.74171241	-0.394606018
165.16614	13.612425	628.07484	-0.185666	4.40440103	4.10727669	-0.394478237
165.16614	13.193406	627.89281	-0.275199	4.20618664	4.53594684	-0.239113470
165.16614	12.774386	627.76718	-0.404614	4.60576915	5.18390838	-0.225389946
165.16614	12.355367	627.66447	-0.539365	5.81791460	5.81725298	-0.398435831
165.16614	11.936348	627.46558	-0.598838	18.93853955	7.32376422	-1.129686331
165.16614	11.517329	626.79126	-0.561894	29.20262903	9.73464268	-1.857610827
165.16614	11.098309	625.73330	-0.458438	50.71437675	13.34404796	-4.847437744
165.16614	10.679290	624.11378	-0.285390	84.08661357	14.79023789	-7.482352770
165.16614	10.260271	621.95360	-0.090820	133.84366800	18.91963816	-12.853678350
165.16614	9.841251	618.94178	0.137055	199.53449790	25.53468063	-20.578732150
165.16614	9.422232	615.17173	0.204009	267.26320120	35.66704676	-30.670227740
165.16614	9.003213	611.06771	0.518032	303.81400110	43.70612638	-35.988561800
165.16614	8.584194	604.95642	0.946345	407.75499800	66.17007704	-52.723060540
165.16614	8.165174	597.73539	1.639539	532.27670060	103.74363100	-86.180163810
165.16614	7.746155	590.46711	1.964374	609.99872290	124.19983610	-101.310724600
165.16614	7.327136	582.00722	2.251693	750.61178770	164.53888350	-131.094972900
165.16614	6.908117	573.78406	2.222426	880.29450590	198.65044710	-164.524064600
165.16614	6.489097	564.07317	1.993680	1093.50648300	224.84558970	-204.708174300
165.16614	6.070078	552.13977	2.025764	1437.49610600	279.29538870	-280.239781900
165.16614	5.651059	540.41775	1.779444	1690.98844600	321.16372280	-339.790018800
165.16614	5.232039	528.04669	1.294536	1923.00914300	342.80531830	-357.647448900
165.16614	4.813020	515.25262	1.016786	2251.06303200	396.07794190	-427.275723100
165.16614	4.394001	500.85208	0.357900	2646.91405400	461.74723240	-508.919713600
165.16614	3.974982	486.46751	-0.300675	3051.41940500	524.06655680	-590.898073300
165.16614	3.555962	470.53946	-0.426324	3565.14689500	607.12185710	-681.569201000
165.16614	3.136943	438.09327	-1.270495	10222.06172000	579.38533450	-661.700922500
165.16614	2.717924	404.01258	-2.069335	16129.71681000	627.24899950	-712.435464900
165.16614	2.298905	373.84693	-3.124872	19839.79574000	625.07779160	-777.711358400
165.16614	1.879885	343.13082	-3.548090	23135.43902000	679.98502590	-743.861767300
165.16614	1.460866	318.69355	-2.432857	25484.82106000	816.18221760	-751.535107300
165.16614	1.041847	282.88800	-2.633081	26796.08371000	874.29352820	-792.480779000
165.16614	0.622827	247.65183	-1.799607	29644.69559000	1019.06160600	-719.277114800
165.16614	0.203808	217.39079	-1.026291	31458.17705000	643.43047970	-668.788276400

Weak pressure gradient, Rough surface, Measurement location 2						
x, mm	y, mm	U, m/s	V, m/s	u'u', m^2/s^2	v'v', m^2/s^2	u'v', m^2/s^2
300.33032	18.943677	630.96949	-2.946713	16.84955266	11.76506115	-0.894197089
300.32216	18.429661	630.99563	-3.258926	16.75543187	11.64747397	-0.919151057
300.31400	17.915645	631.04657	-3.522246	18.45928466	11.84634442	-0.796464543
300.30584	17.401629	631.08584	-3.811331	18.02961175	12.33691643	-1.006852599
300.29768	16.887613	631.27203	-4.042799	18.92117296	13.23243511	-1.150678113
300.28953	16.373597	631.26458	-4.360385	19.48789848	14.55939219	-0.986055940
300.28137	15.859581	631.56253	-4.613905	27.76281963	16.13495501	-1.563648907
300.27321	15.345565	631.51967	-5.010946	30.37037669	18.17037912	-2.114532111
300.26505	14.831549	631.34561	-5.456787	29.38150751	20.91941156	-2.057947146
300.25689	14.317533	631.19745	-6.108878	34.51600410	25.40450703	-2.713994197
300.24873	13.803518	630.71963	-6.791312	41.78916629	31.27392376	-4.430668489
300.24057	13.289502	629.73052	-7.422897	54.59499698	35.84032769	-5.636244863
300.23241	12.775486	627.94899	-8.131218	81.53642729	45.36664663	-8.251931746
300.22425	12.261470	625.28837	-8.774205	127.47649070	57.15176397	-14.581885010
300.21610	11.747454	621.91928	-9.213335	190.15021930	68.19940243	-21.851496500
300.20794	11.233438	617.71730	-10.032360	263.92066050	83.20701613	-34.475706620
300.19978	10.719422	613.12671	-10.853444	332.67524340	103.81254770	-45.051830210
300.19162	10.205406	607.05093	-11.589517	460.26318110	126.63901190	-67.138739510
300.18346	9.691390	599.96074	-12.333176	604.21252610	181.78416810	-111.781365800
300.17530	9.177374	591.74544	-12.867351	791.95397580	228.23434620	-156.022398800
300.16714	8.663358	583.88018	-13.447064	921.55919330	249.76747960	-183.469926300
300.15898	8.149343	573.53240	-13.411590	1213.29068800	334.99242210	-266.701281700
300.15082	7.635327	562.91053	-13.255298	1451.07172000	435.49513210	-347.257524600
300.14266	7.121311	554.15760	-13.601477	1522.31167100	459.39171200	-360.148321500
300.13451	6.607295	542.36388	-13.683929	1744.96119600	549.21525450	-438.323734900
300.12635	6.093279	532.08657	-13.848583	1859.57972300	554.73882530	-457.630018000
300.11819	5.579263	520.79106	-13.845863	2066.33861200	626.86695910	-509.487534800
300.11003	5.065247	508.44508	-13.814631	2311.42837600	693.42406650	-586.079984800
300.10187	4.551231	496.61304	-13.904658	2480.62577800	752.54403110	-624.437882100
300.09371	4.037215	483.68365	-13.297783	2729.35913000	864.97117370	-688.321199400
300.08555	3.523199	469.87525	-13.432326	3034.75358500	921.68956750	-714.209396700
300.07739	3.009183	455.32935	-12.975515	3707.37011500	1034.72723600	-707.960815300
300.06923	2.495168	441.23871	-13.673555	3955.66938800	1027.32050000	-734.834933100
300.06107	1.981152	419.61418	-13.349823	7281.83266600	1065.00142800	-864.118980700
300.05292	1.467136	391.30224	-12.770642	11458.10129000	1075.68329900	-960.585108600
300.04476	0.953120	359.80673	-12.311418	16306.95247000	1223.23469800	-964.942172900
300.03660	0.439104	329.33044	-11.104307	21411.28144000	1632.65245000	-1175.381170000
300.02844	-0.074912	284.19189	-8.665943	27408.22189000	1890.30561400	-1209.681534000
300.02028	-0.588928	207.52176	-6.790140	31742.77127000	1695.66257000	-1482.706860000
300.01212	-1.102944	65.71021	-2.711952	11838.74007000	778.29859510	-534.680751200

Weak pressure gradient, Rough surface, Measurement location 3						
x, mm	y, mm	U, m/s	V, m/s	u'u', m^2/s^2	v'v', m^2/s^2	u'v', m^2/s^2
412.60246	12.722818	629.09270	-22.120952	31.10755212	49.77353134	-0.316057343
412.56246	12.210429	628.84415	-22.514222	32.88771943	52.51919513	-1.340382407
412.52245	11.698040	628.60093	-22.817763	37.30949592	57.47071448	-1.340833192
412.48244	11.185651	627.99026	-23.400552	42.29312259	62.92559523	-3.096865623
412.44244	10.673263	627.12068	-23.935440	48.67962228	70.91727810	-4.601213526
412.40243	10.160874	625.93083	-24.581362	59.77730283	78.96851596	-6.524941444
412.36243	9.648485	624.18853	-25.171388	80.32602297	92.06201054	-12.325797490
412.32242	9.136097	621.61818	-25.235023	125.62829630	119.00626800	-27.248347110
412.28241	8.623708	618.62535	-25.721649	168.70376300	132.44358380	-38.033436660
412.24241	8.111319	615.42154	-26.033458	216.75722470	151.80592960	-50.989682120
412.20240	7.598931	611.22491	-26.202572	273.31098100	171.98874200	-70.065091060
412.16239	7.086542	606.85454	-26.291022	338.68726590	197.03763750	-87.183231150
412.12239	6.574153	600.72099	-26.128025	483.30314070	226.60100430	-133.170316600
412.08238	6.061764	594.55987	-25.910013	590.53682670	254.80054320	-164.378126700
412.04237	5.549376	588.66250	-25.907173	654.94191920	272.44066000	-182.725069500
412.00237	5.036987	581.78720	-26.001572	765.58284180	300.69810560	-208.580030900
411.96236	4.524598	573.91933	-25.415436	899.13003640	361.72448520	-256.818199100
411.92236	4.012210	566.56683	-25.610164	949.17220220	371.67516970	-255.443146600
411.88235	3.499821	558.56782	-25.471094	1050.39015600	396.55546020	-277.842801800
411.84234	2.987432	549.49104	-24.599778	1245.48791400	483.98943870	-357.514451400
411.80234	2.475043	540.58897	-24.211342	1384.23012200	533.50637770	-402.485568700
411.76233	1.962655	532.08888	-24.212177	1445.39893000	556.02987550	-418.272561200
411.72232	1.450266	523.71666	-24.277025	1527.74700200	595.00077140	-453.272459900
411.68232	0.937877	513.68993	-24.356343	1741.54851300	634.49281340	-514.879634400
411.64231	0.425489	503.87743	-23.887627	1894.04266100	651.28058260	-546.740762800
411.60230	-0.086900	494.71446	-24.182596	1953.59442400	657.19443840	-536.334970300
411.56230	-0.599289	482.71641	-24.172974	2196.16088500	700.49367280	-605.232319800
411.52229	-1.111677	470.76880	-24.018702	2429.81706700	757.98259620	-646.506247000
411.48229	-1.624066	458.53411	-23.906018	2718.98798300	798.25126430	-729.564108000
411.44228	-2.136455	446.30728	-23.844652	2823.30622400	828.47861000	-786.800427700
411.40227	-2.648844	432.23883	-23.862294	3131.20411300	868.61596650	-848.586692700
411.36227	-3.161232	418.16662	-23.462056	3331.58879800	914.06240980	-877.792734100
411.32226	-3.673621	403.47959	-23.895818	3527.25261300	966.26372610	-892.617170300
411.28225	-4.186010	386.52668	-24.029270	4102.80877300	1041.67719200	-952.261516300
411.24225	-4.698398	336.50746	-22.010403	13725.34354000	1150.14835100	-1436.346508000
411.20224	-5.210787	273.72672	-19.130059	21736.42136000	1289.18842900	-1907.108236000
411.16224	-5.723176	183.72969	-13.192826	26742.26309000	1072.70730300	-2146.295016000
411.12223	-6.235564	104.57004	-7.664747	21973.48439000	795.56380320	-1575.335731000
411.08222	-6.747953	54.22818	-3.602924	13962.55737000	714.41885060	-907.315905600
411.04222	-7.260342	24.22547	-0.591790	8280.37079100	485.85239340	-298.466170500

Strong pressure gradient, Smooth surface, Measurement location 1						
x, mm	y, mm	U, m/s	V, m/s	u'u', m^2/s^2	v'v', m^2/s^2	u'v', m^2/s^2
151.6226	15.836671	627.71378	-2.447592	19.66892728	11.37701609	1.974654653
151.6226	15.435828	627.60650	-2.368941	20.13843878	11.71828173	1.978483089
151.6226	15.034986	627.48495	-2.347863	20.43699029	11.71616411	1.982223524
151.6226	14.634143	627.53987	-2.211028	22.14879600	11.70890574	1.982565058
151.6226	14.233301	627.48272	-2.207040	22.61957318	11.64107434	1.806637921
151.6226	13.832458	627.38423	-2.222532	22.81520539	11.91130088	1.836130281
151.6226	13.431615	627.65089	-2.130338	29.24068326	13.57999095	2.843228293
151.6226	13.030773	627.64831	-2.046834	31.64986450	14.11217427	2.825365132
151.6226	12.629930	627.32134	-2.039868	27.57264437	12.56582082	1.998487350
151.6226	12.229087	627.43624	-2.001536	33.35434590	14.44640992	2.320498758
151.6226	11.828245	627.09849	-1.856525	34.70642287	15.12323433	1.879262576
151.6226	11.427402	626.46830	-1.935103	31.60912412	14.75826657	1.437478902
151.6226	11.026559	625.93109	-1.864533	35.51193303	15.85454612	0.425143526
151.6226	10.625717	625.05285	-1.867034	41.20746623	17.37907028	-1.097540151
151.6226	10.224874	623.84147	-1.960046	52.25853188	19.60001181	-2.995804116
151.6226	9.824032	622.23789	-1.999812	64.75721242	21.74382413	-5.167695164
151.6226	9.423189	619.86405	-1.968182	83.56696289	27.80559443	-9.619057130
151.6226	9.022346	617.11724	-2.087561	108.57616090	29.89407753	-13.753383070
151.6226	8.621504	613.29756	-2.110234	154.75336270	36.25114401	-21.697993680
151.6226	8.220661	608.58609	-2.164150	218.33326460	44.18211340	-33.795200790
151.6226	7.819818	603.36984	-2.189384	293.19454640	52.14216070	-47.447406270
151.6226	7.418976	598.14528	-2.310443	346.09603020	62.45978198	-57.482622600
151.6226	7.018133	592.11705	-2.298386	406.09877020	75.94739964	-67.803043670
151.6226	6.617290	585.39001	-2.215243	491.91868280	87.80929567	-87.238766050
151.6226	6.216448	578.70240	-2.076589	544.93102260	95.42748417	-96.409730070
151.6226	5.815605	571.33234	-2.103092	616.35617870	107.10561350	-114.585492400
151.6226	5.414762	563.96264	-2.126355	685.58109690	125.30523730	-133.765785600
151.6226	5.013920	556.05511	-2.031443	760.32220200	141.58083700	-151.398843300
151.6226	4.613077	547.63014	-1.967446	853.83180070	168.32594650	-177.780551000
151.6226	4.212235	538.74788	-1.881550	988.25931230	187.79596270	-208.426248100
151.6226	3.811392	529.83807	-1.922071	1078.72439200	209.02253960	-230.631159800
151.6226	3.410549	520.06323	-2.006656	1209.09152200	228.51064670	-254.047443000
151.6226	3.009707	509.93207	-1.971740	1312.71787100	256.79901600	-274.394998000
151.6226	2.608864	499.31435	-1.647794	1420.15846100	275.50132600	-288.623467400
151.6226	2.208021	489.36389	-1.749029	1522.94490800	280.44785060	-281.068046400
151.6226	1.807179	482.82005	-1.774073	1814.90935300	368.56807560	-313.838887600
151.6226	1.406336	476.52977	-2.246215	2321.04242800	570.73087000	-390.077144000
151.6226	1.005493	461.70455	-2.385530	3127.35884000	801.28742600	-402.359074600
151.6226	0.604651	445.40967	-2.188034	4536.18526000	955.07172840	-407.651363400
151.6226	0.203808	433.50150	-3.783714	5304.51653900	1087.45863000	-362.094731100

Strong pressure gradient, Smooth surface, Measurement location 2						
x, mm	y, mm	U, m/s	V, m/s	u'u', m^2/s^2	v'v', m^2/s^2	u'v', m^2/s^2
300.48706	14.868245	637.63493	-34.719859	39.68652338	52.77847569	0.640664387
300.39809	14.359633	638.34747	-35.757569	40.31650901	53.64835287	0.164089094
300.30913	13.851021	638.94472	-37.121558	33.45800519	47.26402806	1.781018817
300.22016	13.342409	639.60415	-38.522670	34.69780378	49.13445744	0.093222687
300.13120	12.833797	640.19438	-39.989774	42.03191621	56.93401883	1.536095223
300.04223	12.325185	640.36714	-42.049754	46.03168741	57.09251506	1.929552672
299.95327	11.816573	640.42188	-44.009217	46.38948818	53.12969068	2.630385824
299.86430	11.307962	640.01861	-45.956770	64.83201014	52.99489500	4.258881153
299.77534	10.799350	639.43025	-47.768922	75.41995166	52.15350256	3.042508574
299.68637	10.290738	638.31492	-49.690482	96.91619669	52.27574916	1.859092105
299.59741	9.782126	636.89065	-51.460192	120.42826810	54.68194785	1.239769463
299.50844	9.273514	634.94197	-53.297485	143.98989780	63.93028075	0.334132056
299.41948	8.764902	632.37769	-55.391150	175.77539920	87.46841483	-2.496628983
299.33051	8.256290	629.39881	-57.432092	208.67994560	96.59776716	-6.042731910
299.24155	7.747678	626.38317	-59.501985	235.63958080	108.61912920	-10.661150720
299.15258	7.239067	623.16193	-61.761461	250.60265040	138.49100590	-18.326506520
299.06362	6.730455	619.21178	-63.935369	296.77423760	168.51307110	-29.931853660
298.97465	6.221843	615.25786	-66.081924	340.52389470	184.74619150	-36.152210640
298.88569	5.713231	611.25660	-68.262314	361.37264480	186.78539600	-40.763086270
298.79672	5.204619	607.17589	-70.374518	413.89492380	212.36568120	-55.918939680
298.70776	4.696007	602.75950	-72.265982	467.64814570	227.78195960	-67.996676240
298.61879	4.187395	598.39294	-74.099822	494.85817160	218.62914460	-77.585576980
298.52983	3.678783	593.68375	-75.759751	537.94043760	239.33882280	-86.781423590
298.44086	3.170171	588.73346	-77.277662	591.71730790	223.79680180	-96.420576990
298.35190	2.661560	583.86045	-78.296762	602.59757880	231.78130160	-104.102233800
298.26293	2.152948	579.03365	-79.375032	617.78303080	227.06796940	-106.981676300
298.17396	1.644336	573.93749	-80.274665	633.72026170	236.51147940	-110.440926100
298.08500	1.135724	568.84599	-81.118649	624.74040230	235.40415220	-112.365529300
297.99603	0.627112	563.23492	-81.861456	624.69725520	241.92364300	-115.381248000
297.90707	0.118500	557.88660	-82.470262	620.66949610	231.89130580	-118.816403800
297.81810	-0.390112	551.53660	-82.924086	644.73689540	222.48809520	-117.512650300
297.72914	-0.898724	545.13819	-83.535604	664.87905960	234.61077320	-128.594048800
297.64017	-1.407335	538.47808	-83.892791	695.11542460	227.55860750	-132.276598500
297.55121	-1.915947	532.81990	-84.142351	741.47918490	252.04921190	-125.450778300
297.46224	-2.424559	527.02625	-84.424760	1158.83951200	391.98688520	-134.091427300
297.37328	-2.933171	515.56153	-77.775100	7946.61102900	3594.04885400	-420.281069900
297.28431	-3.441783	475.20209	-55.901763	27790.19927000	13226.43290000	-1657.074211000
297.19535	-3.950395	444.92331	-49.692651	43269.57128000	13479.00949000	-2253.496841000
297.10638	-4.459007	428.72539	-29.822832	49848.61316000	8771.33300700	-2517.861904000
297.01742	-4.967619	40.06321	-2.677589	4563.61092500	843.00133400	-272.059583300

Strong pressure gradient, Smooth surface, Measurement location 3						
x, mm	y, mm	U, m/s	V, m/s	u'u', m^2/s^2	v'v', m^2/s^2	u'v', m^2/s^2
411.71062	-0.982248	632.80227	-62.022574	61.86802951	94.01735532	-14.506050610
411.71062	-1.437564	631.17358	-56.168740	66.76504602	78.09336514	-16.419344640
411.71062	-1.892881	629.07407	-50.882875	72.23225659	67.46029910	-16.150409400
411.71062	-2.348198	626.97671	-45.939082	77.19390818	60.77963724	-14.326623480
411.71062	-2.803515	624.84803	-41.732310	86.02525626	52.63419535	-13.596491060
411.71062	-3.258831	622.74497	-37.628917	102.13900910	61.70107861	-15.737000980
411.71062	-3.714148	620.03040	-33.320861	117.18949530	95.85160891	-22.408925800
411.71062	-4.169465	616.78758	-27.417720	124.24386480	119.86998400	-29.849069650
411.71062	-4.624782	613.17547	-21.215723	122.51669660	138.96525640	-31.762012480
411.71062	-5.080098	609.43671	-15.114216	97.67320667	122.02147800	-24.601697780
411.71062	-5.535415	606.07269	-10.561706	68.76618281	95.90077684	-16.554194860
411.71062	-5.990732	603.53123	-7.374195	71.83475841	84.45025354	-15.377830700
411.71062	-6.446049	600.48031	-5.245406	90.59056931	78.67893080	-21.849240570
411.71062	-6.901366	596.60649	-3.752902	138.65619050	84.33876039	-32.628339000
411.71062	-7.356682	592.45939	-2.655789	184.20739980	87.27246791	-44.302262510
411.71062	-7.811999	587.62715	-1.727717	234.07635130	99.87896633	-59.420678400
411.71062	-8.267316	581.82772	-1.033146	272.83295080	105.38151880	-65.476963580
411.71062	-8.722633	575.59264	-0.328761	298.99742550	129.64807960	-80.224458790
411.71062	-9.177949	569.14813	0.397411	320.71734020	160.93914500	-97.647390480
411.71062	-9.633266	562.80142	0.540933	335.14373210	184.00160280	-109.829713200
411.71062	-10.088583	556.64022	1.140910	355.59087570	201.51698780	-124.790915400
411.71062	-10.543900	550.50467	1.639683	378.76893230	207.85779400	-138.631237400
411.71062	-10.999216	544.24746	1.921817	410.80855690	216.55617350	-151.800822500
411.71062	-11.454533	537.57458	1.848116	432.79127410	228.98855650	-160.887045000
411.71062	-11.909850	530.74872	2.244419	487.07710830	220.62331360	-172.445212200
411.71062	-12.365167	523.76072	2.181822	518.41356020	228.23598540	-181.778785200
411.71062	-12.820484	516.14669	1.706842	606.70967380	230.61680450	-198.272845700
411.71062	-13.275800	508.81680	1.200902	662.03249950	236.74040560	-202.438796400
411.71062	-13.731117	500.31144	0.740512	758.15620620	244.41649730	-216.813586900
411.71062	-14.186434	490.91686	0.053125	880.47012510	261.88541850	-241.503675800
411.71062	-14.641751	480.23007	-0.408956	1091.39438900	282.71502660	-286.437215500
411.71062	-15.097067	468.12163	-1.046394	1418.46253600	344.12613370	-350.856801400
411.71062	-15.552384	454.69841	-1.366691	1797.09259300	425.24945940	-388.421494400
411.71062	-16.007701	439.43501	-1.226148	2313.34298500	523.31361580	-456.554981900
411.71062	-16.463018	423.47855	-1.797998	2669.64254300	621.63787720	-495.003410000
411.71062	-16.918334	406.82640	-2.614859	2970.22855300	621.22080340	-484.302425100
411.71062	-17.373651	395.71413	-2.506231	5951.63136100	1467.21739000	-430.674529600
411.71062	-17.828968	378.54563	-3.166973	7899.76590000	1727.62221800	-340.402815100
411.71062	-18.284285	360.35629	-1.948903	9237.41384700	1870.36198600	-537.188746000
411.71062	-18.739602	346.03024	-0.871352	6966.17138400	697.74228960	-342.232902700

Strong pressure gradient, Rough surface, Measurement location 1						
x, mm	y, mm	U, m/s	V, m/s	u'u', m^2/s^2	v'v', m^2/s^2	u'v', m^2/s^2
160.53970	16.545560	629.72422	-1.092861	19.31379371	9.86392141	0.783116101
160.53970	16.126541	629.42162	-1.114442	19.50756946	8.97211631	0.789019408
160.53970	15.707521	629.18968	-1.083648	19.55401081	8.46052286	0.788442246
160.53970	15.288502	628.88604	-0.976120	20.37849621	7.69575951	0.787677719
160.53970	14.869483	628.64031	-0.799565	21.04743814	7.24579946	0.793694572
160.53970	14.450464	628.36411	-0.481014	21.83317803	6.89478807	0.792999464
160.53970	14.031444	628.47530	-0.073908	24.47664969	6.63335627	0.804400220
160.53970	13.612425	628.30109	0.238733	24.99280028	6.34053854	1.099426100
160.53970	13.193406	628.15444	0.544247	25.19177994	5.90807487	0.789156251
160.53970	12.774386	628.09251	0.672035	27.24050923	5.67632671	0.563355635
160.53970	12.355367	627.93606	0.710024	30.01726057	5.51190590	0.390993579
160.53970	11.936348	627.69316	0.700714	31.89665460	5.42882106	0.024675554
160.53970	11.517329	627.36010	0.701861	32.42148168	5.47699862	-0.432540071
160.53970	11.098309	626.86919	0.710152	38.27742316	6.08382376	-0.891684620
160.53970	10.679290	626.42439	0.741615	52.79996187	7.74592459	-1.534762857
160.53970	10.260271	625.10997	0.716615	50.27107806	8.43575348	-2.448933917
160.53970	9.841251	623.67351	0.668136	49.87475231	10.50575094	-3.680752574
160.53970	9.422232	622.19136	0.620566	59.77272482	13.68089346	-4.651941979
160.53970	9.003213	619.96737	0.664169	87.66767734	21.07741212	-8.355347183
160.53970	8.584194	616.19028	0.868372	161.72176230	39.42692167	-19.517116510
160.53970	8.165174	611.08972	1.196549	257.89027080	66.83730388	-38.131289880
160.53970	7.746155	605.66598	1.120079	355.71953810	77.14936567	-50.701234520
160.53970	7.327136	598.54438	1.264412	525.46287550	129.78372180	-93.524573150
160.53970	6.908117	591.40870	1.146525	662.82179100	151.93418770	-115.600994200
160.53970	6.489097	583.64888	0.672598	813.67516230	177.12060110	-150.667658100
160.53970	6.070078	574.90609	0.366450	1026.01861100	227.86330010	-189.448771500
160.53970	5.651059	565.78001	0.045673	1197.33163700	271.43103510	-227.527056600
160.53970	5.232039	555.89977	-0.678234	1361.47441100	312.05544170	-258.284190900
160.53970	4.813020	544.64124	-0.681934	1791.32294300	444.73616250	-337.595062500
160.53970	4.394001	532.62907	-0.921144	2475.87461400	539.44116550	-464.104655800
160.53970	3.974982	509.23389	-1.707565	7051.46268200	643.59384690	-460.151844800
160.53970	3.555962	450.28400	-1.640937	24199.37672000	694.98081020	-471.613910100
160.53970	3.136943	394.95263	-2.032003	38676.38621000	743.86437450	-673.075975400
160.53970	2.717924	369.74398	-2.057625	40280.52050000	817.75748930	-707.518974700
160.53970	2.298905	352.01731	-2.907629	40080.13961000	929.36319840	-757.349451200
160.53970	1.879885	349.76557	-4.307799	36315.16723000	1604.52235500	-1075.936560000
160.53970	1.460866	344.58467	-2.688194	36469.91768000	2717.41258100	-994.868468800
160.53970	1.041847	334.91818	-2.759878	35081.05265000	3377.75307700	-1025.315607000
160.53970	0.622827	313.67027	-3.422372	35887.22080000	4364.99491000	-1148.108477000
160.53970	0.203808	261.59804	-3.465948	33798.46303000	2229.72757600	-990.712022700

Strong pressure gradient, Rough surface, Measurement location 2						
x, mm	y, mm	U, m/s	V, m/s	u'u', m^2/s^2	v'v', m^2/s^2	u'v', m^2/s^2
301.59996	14.671850	635.57234	-29.950650	32.11224111	49.81845918	-1.363850649
301.50764	14.168274	636.20505	-31.818489	33.14216064	48.64181797	-0.835808318
301.41532	13.664698	636.63663	-33.426902	33.91797422	45.55560266	-1.143778173
301.32299	13.161122	637.23657	-34.781847	32.01477454	43.22395497	-1.327979579
301.23067	12.657546	637.77005	-36.175503	34.86151941	43.55042144	-1.088372127
301.13835	12.153969	638.22000	-37.440029	42.86013159	49.02103960	-0.640980090
301.04603	11.650393	638.66834	-38.820121	41.29177551	49.93886738	-1.156562675
300.95371	11.146817	638.61850	-40.198452	55.94106886	64.51137365	-2.043153220
300.86138	10.643241	638.32161	-41.665034	63.71921669	65.52471307	-0.818436194
300.76906	10.139665	637.50257	-43.336938	89.18384933	73.72771551	-0.872313482
300.67674	9.636089	635.90919	-45.121091	119.95652160	88.57466055	0.583862048
300.58442	9.132513	633.84464	-46.900937	160.10903570	104.82427680	-2.105044254
300.49209	8.628937	631.65641	-48.601626	190.05021010	107.84749840	-2.313838312
300.39977	8.125360	628.23997	-50.317542	254.00204480	121.57505010	-7.605719539
300.30745	7.621784	624.40062	-51.900664	322.89917520	148.02578130	-24.739999270
300.21513	7.118208	620.56707	-53.380125	365.44832830	167.39330280	-32.505058380
300.12280	6.614632	615.63360	-54.338345	474.35922080	186.41507440	-49.794494750
300.03048	6.111056	610.44078	-55.377436	563.12091770	207.30333430	-69.093130970
299.93816	5.607480	605.33795	-56.812773	631.80263250	225.43614650	-82.799082580
299.84584	5.103904	598.83799	-57.653616	775.81362860	269.74585870	-117.355105300
299.75352	4.600328	592.71838	-58.792722	865.02274590	305.17766140	-147.652596100
299.66119	4.096752	585.82972	-59.764079	986.80132100	352.43346380	-191.186523100
299.56887	3.593175	578.75920	-60.886935	1098.93378200	390.79354040	-216.212665000
299.47655	3.089599	571.87180	-61.953633	1184.74084700	429.33657320	-236.811692900
299.38423	2.586023	564.44466	-62.512486	1283.10067600	497.30577090	-271.213362500
299.29190	2.082447	556.94631	-63.222811	1334.63289000	546.98589430	-304.733183100
299.19958	1.578871	549.66837	-63.460207	1377.92764900	575.50563000	-329.926339600
299.10726	1.075295	541.47465	-64.075917	1495.45998100	650.07161120	-352.739775800
299.01494	0.571719	533.11110	-64.307073	1791.33891700	736.02965160	-339.386446900
298.92261	0.068143	524.22253	-63.916110	2042.08604500	874.13628630	-435.398470400
298.83029	-0.435434	514.79453	-64.943395	2158.40089600	828.09129090	-435.715084500
298.73797	-0.939010	505.52856	-64.704281	3067.14057000	1045.45743000	-459.988955200
298.64565	-1.442586	496.44680	-64.224384	3537.24439700	1331.95406800	-422.142312300
298.55333	-1.946162	487.09528	-64.602513	3277.39242300	1223.46763100	-478.983159300
298.46100	-2.449738	477.46332	-63.475523	3604.27841000	1620.11553100	-475.310178100
298.36868	-2.953314	466.51000	-62.915719	4839.93162900	2042.88827700	-685.686124600
298.27636	-3.456890	451.61697	-61.784580	8139.80871500	3121.51749300	-611.189603800
298.18404	-3.960466	435.62599	-63.032368	12615.90857000	2574.47557400	-1342.029791000
298.09171	-4.464043	391.64822	-57.670748	25838.22741000	3981.16599100	-2805.106428000
297.99939	-4.967619	96.43826	-12.394055	10283.47852000	1656.04077000	-936.435974700

Strong pressure gradient, Rough surface, Measurement location 3						
x, mm	y, mm	U, m/s	V, m/s	u'u', m^2/s^2	v'v', m^2/s^2	u'v', m^2/s^2
409.88349	1.707376	630.56972	-52.369610	112.88821520	236.89162620	3.454120682
409.88349	1.289154	629.42964	-49.340174	113.51492850	242.24302900	0.169445751
409.88349	0.870933	628.10651	-45.849846	107.67839920	226.37071220	0.271631495
409.88349	0.452712	626.99966	-42.334993	114.06078830	228.22777960	-4.665927273
409.88349	0.034491	626.12882	-39.479693	137.00795950	253.29539420	-6.528623081
409.88349	-0.383730	624.61322	-35.957816	164.50235710	282.44543490	-19.944912220
409.88349	-0.801952	622.77715	-32.491678	182.00046770	316.16003650	-31.170660980
409.88349	-1.220173	620.30915	-30.480761	180.96085750	310.43125850	-34.547858290
409.88349	-1.638394	617.50019	-28.240529	192.58514390	303.57157710	-43.254294040
409.88349	-2.056615	613.90113	-25.548112	208.34952930	288.33567890	-58.597784500
409.88349	-2.474837	609.95784	-23.091134	242.74780680	288.29098510	-71.632048900
409.88349	-2.893058	605.67999	-20.741550	285.55376330	307.82913760	-92.718454300
409.88349	-3.311279	600.41021	-19.029110	334.64271630	312.30613790	-109.802187000
409.88349	-3.729500	594.90330	-17.619231	406.82929360	335.92229560	-139.802661500
409.88349	-4.147721	588.83837	-16.124477	463.88380060	361.34767270	-174.361773300
409.88349	-4.565943	582.34507	-14.982039	530.33278330	368.27347120	-192.630208100
409.88349	-4.984164	575.70693	-13.942997	613.61690860	383.86525320	-221.812121000
409.88349	-5.402385	568.51669	-12.999077	696.60371140	408.60032040	-232.964286800
409.88349	-5.820606	561.56079	-12.400472	728.03004200	427.33163800	-265.087225500
409.88349	-6.238828	553.97253	-12.119465	815.69120190	452.23751960	-298.470584400
409.88349	-6.657049	545.95537	-11.671956	919.62529630	477.61289670	-334.376490000
409.88349	-7.075270	537.68348	-11.247838	1034.39185300	498.87561430	-375.120143500
409.88349	-7.493491	529.76936	-10.361967	1118.68299900	531.46616530	-407.466170200
409.88349	-7.911712	521.43716	-9.473450	1245.10636200	553.83422000	-452.873096200
409.88349	-8.329934	512.33328	-9.303783	1414.89110800	585.93710720	-480.065489200
409.88349	-8.748155	503.36150	-9.328067	1624.86253900	632.96596280	-525.256607900
409.88349	-9.166376	493.59121	-9.258513	1885.44576800	711.39098740	-590.696922100
409.88349	-9.584597	483.02285	-9.512525	2134.85473200	721.16775950	-647.761639700
409.88349	-10.002819	473.36988	-10.179294	2442.78456500	759.94288420	-696.469483400
409.88349	-10.421040	461.88263	-10.545924	2957.12047200	837.45131370	-759.099954000
409.88349	-10.839261	449.56444	-10.836142	3490.08601600	954.93606150	-820.844674300
409.88349	-11.257482	436.98991	-10.715122	4028.19250400	1090.86307200	-946.646192100
409.88349	-11.675704	423.41616	-10.989053	4808.87340900	1174.20490100	-1031.433137000
409.88349	-12.093925	409.36796	-11.841346	5387.43838800	1297.92684100	-1132.425786000
409.88349	-12.512146	393.78110	-11.630220	6328.28619800	1495.54777400	-1324.486293000
409.88349	-12.930367	376.58224	-11.348003	7347.02685500	1758.76321600	-1510.152735000
409.88349	-13.348588	359.68464	-12.351008	7749.91548600	1884.41867900	-1586.535906000
409.88349	-13.766810	342.79037	-12.014668	8470.99705100	2106.95666100	-1678.725790000
409.88349	-14.185031	325.55119	-11.872035	8490.99402700	2267.28721500	-1786.840349000
409.88349	-14.603252	305.53433	-11.244284	9418.33038400	2212.00078900	-1713.381683000

Boundary layer edge conditions										
	Pressure Gradient	Zero			Weak			Strong		
	Location	1	2	3	1	2	3	1	2	3
Smooth	Uedge (m/s)	625	627.5	628.7	626.2	625.5	629.4	623.8	637.2	631.1
	delta (m)	0.0104	0.0122	0.0127	0.0104	0.0118	0.0154	0.0102	0.0144	0.172
Rough	Uedge (m/s)	625.9	624.9	619	624.1	625.3	624.7	625.1	635.6	628.4
	delta (m)	0.0103	0.0134	0.0147	0.0107	0.0139	0.0169	0.0103	0.0143	0.0195

Uedge is the resultant velocity at the edge of the boundary layer
delta is the boundary layer thickness in the wall normal direction

PART II

(Numerical Computation)

Introduction

The study of supersonic boundary layer structure has been very important for design and operation of high-speed aircraft, missiles, and reentry vehicles. The effects of the interactions between the air and the object surface, such as drag, lift and heat transfer, are initiated in the boundary layer. All these systems experience surface roughness during manufacturing, through wear and tear because of prolonged operation, and for various other reasons. Thus, accurate quantification of the effects of roughness on the boundary layer above the system surface is important in practical applications.

Analysis of both low and high-speed turbulent flows over smooth surfaces has been performed extensively in the past. The experimental data has been well correlated for smooth equilibrium boundary layer flow over flat plates, and the numerical analysis for low and high-Reynolds-number flow over smooth walls is well documented and developed. The algebraic (mixing length for example), one-equation (Spalart-Almaras model for example) and two-equation $k-\varepsilon$ and $k-\omega$ family of turbulence models have been quite successful in predicting the turbulent boundary layer over smooth flat surfaces. However, for non-equilibrium boundary layers with adverse pressure gradients, the performance of these models is not as satisfactory especially in the separated region. The Reynolds stress transport models with either a transport equation for ε representing the length scale or a transport equation for ω representing the length scale (in which case the model is referred to as the stress$-\omega$ model) have been used with some success for separated flows. Another major weakness of the turbulence models is the surface roughness issue and incorporating the surface roughness effects in the model. Typically, the wall function along with a shift of the near wall velocity profile by an amount denoted

as ΔB is used for incorporating the roughness effects. However, "the uncertainty in the dependence of ΔB on the size and type of roughness and also in the effective location of the fictitious wall from which the distance is measured," [1] makes this approach less reliable.

For low-speed flow over rough wall, the mean and turbulent flow properties have been studied thoroughly by experiment and the turbulence models have been demonstrated to perform well for both modified two-layer $k-\varepsilon$ model and $k-\omega$ model. The widely used standard $k-\varepsilon$ model is unable to describe the near-wall zone. The two-layer approach [2] seems to have the ability to fix that flaw. It consists of patching together the $k-\varepsilon$ and $k-l$ models, with modified l and k boundary conditions for roughness concern. The rough wall version of the $k-\omega$ model [3] has the similar feature of incorporating roughness into the ω boundary condition, and it has been shown to perform well even in flow with separations [4].

However, for high-speed flow over rough wall with compressible boundary layer, there are no accordant turbulence models. Even the experimental data are not widely available as the smooth surface cases. It is also important to point out that all current high-speed turbulence models, with the exceptions of LES or DNS, were developed by "extending" existing low-speed formulations. Based on Morkovin's [5] observation, "the essential dynamics of supersonic boundary layer follows the incompressible pattern," along with similarity of the compressible Favre-averaged Navier-Stokes equation to the incompressible Reynolds averaged equations, has led researchers to use incompressible turbulence models for flows up to Mach 5. Recent research by Bowersox and Buter [6], Smits et al. [7], and Spina [8] has indicated that the realm of applicability of Morkovin's

hypothesis is more restrictive than originally believed, and has suggested the need for further research in high-speed compressible boundary layer flows. Fan and Bowersox [9] studied three low-speed rough-wall mixing-length models, namely van Driest [10], Cebeci-Chang [11], and Kragstad [12], by applying them to high-speed flows. The simulation results agree reasonably well with the experimental data of Latin and Bowersox [13]. Their work demonstrated that the three simple turbulence models have the essential physics necessary to predict the supersonic turbulent flow over a rough flat plate when there is no separation or adverse pressure gradient. The mixing length models, however, are not appropriate for flows with adverse pressure gradient and separation.

By using the perturbation methods, Wilcox [14] has shown that the $k-\omega$ model can efficiently capture the compressible law of the wall. Sharing the same boundary conditions as $k-\omega$ model for smooth surface, the stress-ω model [14] also performs very well in the compressible boundary layer. The main advantage of the ω-based models over the ε-based model is the way in which ε and ω are specified on the boundary surface. For ε-based models, ε is defined as $\partial\varepsilon/\partial y|_{y=0}=0$ on the boundary. Even though this Neumann boundary condition has been shown to be very robust, it is completely *ad hoc* without theoretical or experimental justification. For the ω-based models, such as in the $k-\omega$ model, ω at the wall is prescribed in terms of the equivalent sand grain roughness height. The stress$-\omega$ model uses the similar boundary condition for ω and solves for the individual Reynolds stress components instead of solving the transport equation for turbulent kinetic energy, k. As mentioned above, the surface roughness effects have been intrinsically incorporated into these models through the ω boundary condition. This formulation for ω on the rough boundary, however, is

derived and validated based on the incompressible sublayer flow over rough surfaces. Its validity for compressible flow is yet to be examined.

Turbulence data and detailed surface roughness statistics allow for the development and validation of turbulence models that include the underlying physics involved with high-speed turbulent boundary layer flow over rough surface. Motivated by the lack of data for high-speed turbulent boundary layers with surface roughness, Latin and Bowersox [13] obtained experimental data for several surface roughness configurations. Their data provides an effective basis for the development and evaluation/validation of turbulence model for supersonic boundary layer flow over rough wall. The objective of this work is to evaluate the performance of the $k-\omega$ model, against the experimental data reported in Part I of this report, for the calculation of supersonic compressible turbulent boundary layer over plane and curved walls with wall roughness.

Governing equations

The mean conservation equations of mass, momentum, and energy for the compressible turbulent flow of an ideal gas are given by the Favre-averaged Navier-Stokes (FANS) equations [14] as:

$$\bar{\rho}_{,t}+(\bar{\rho}\tilde{u}_i)_{,i}=0 \tag{1}$$

$$(\bar{\rho}\tilde{u}_i)_{,t}+(\bar{\rho}\tilde{u}_j\tilde{u}_i)_{,j}=-P_{,i}+(\bar{t}_{ji}+\bar{\rho}\tau_{ji})_{,j} \tag{2}$$

$$(\bar{\rho}\tilde{E})_{,t}+(\bar{\rho}\tilde{u}_j\tilde{H})_{,j}=(-q_{Lj}-q_{Tj}+\overline{t_{ji}u_i^{"}}-\frac{1}{2}\overline{\rho u_j^{"}u_i^{"}u_i^{"}})_{,j}+(\tilde{u}_i\bar{t}_{ij}+\bar{\rho}\widetilde{u_i}\tau_{ij})_{,j} \tag{3}$$

where $(\cdot)_{,s}$ indicates a derivative with respect to the variable s. Furthermore, $\tilde{E}=\tilde{e}+\frac{1}{2}\tilde{u}_i\tilde{u}_i+K$ is the specific total energy, $\tilde{H}=h+\frac{1}{2}\tilde{u}_i\tilde{u}_i+K$ is the specific total

enthalpy, $\tilde{t}_{ji} = 2\bar{\mu}\tilde{S}_{ik} + \bar{\lambda}\tilde{S}_{jj}\delta_{ik}$ are the components of the shear-stress tensor where by Stokes hypothesis $\lambda = -\frac{2}{3}\mu$, $S_{ik} = \frac{1}{2}(\tilde{u}_{i,k} + \tilde{u}_{k,i})$ are the components of the strain-rate tensor, $q_{Lj} = -\kappa T_{,j}$ is the convective heat flux, $q_{Tj} = \overline{\rho u_j'' h''}$ is the turbulent heat flux, $\overline{t_{ji} u_i''}$ is the molecular diffusion, $\frac{1}{2}\overline{\rho u_j'' u_i'' u_i''}$ is the turbulent transport, $K = \tau_{ii}/2$ is the turbulent kinetic energy, and $\tau_{ij} = -\overline{u_i'' u_j''}$ is the Favre-averaged Reynolds-stress tensor. In addition, an equation of state must be specified for system closure which is taken as the perfect gas equation of state $P = \bar{\rho} R \tilde{T}$. Depending on the turbulence model used, the above equations are augmented by the transport equations for the turbulence quantities.

The $k-\omega$ model

Two-equation turbulence models have been a favorite for the computational fluid dynamics analysis. However, all two-equation models are limited to an eddy viscosity assumption of the Reynolds shear stresses. The Reynolds stresses, τ_{ij}, are related to the mean rates of strain via:

$$\tau_{ij} = 2\nu_T(S_{ij} - \frac{1}{3}\tilde{u}_{k,k}\delta_{ij}) - \frac{2}{3}\bar{\rho}k\delta_{ij} \tag{3}$$

and the eddy viscosity ν_t is related to the turbulent kinetic energy k and specific dissipation rate ω by $\nu_t = k/\omega$. The quantities k and ω are determined from the transport equations:

$$k_{,t} + U_j k_{,j} = \tau_{ij} U_{i,j} - \beta^* k\omega + ((\nu + \sigma^* \nu_t)k_{,j})_{,j} \tag{4}$$

$$\rho\omega_{,t}+\rho U_j\omega_{,j}=\alpha\frac{\rho w}{k}\tau_{ij}U_{i,j}-\beta\rho\omega^2+((\mu+\sigma\mu_t)\omega_{,k}),_k \tag{5}$$

The closure coefficients and auxiliary relations are given as:

$$\alpha=13/25\ \ \sigma=1/2 \qquad \sigma^*=1/2 \qquad \beta_0=9/125 \qquad \beta_0^*=9/100$$

$$\beta=\beta_0 f_\beta \quad \beta^*=\beta_0^* f_{\beta^*} \qquad f_\beta=\frac{1+70\chi_\omega}{1+80\chi_\omega}$$

$$\chi_\omega=\left|\frac{\Omega_{ij}\Omega_{jk}S_{ki}}{(\beta_0^*\omega)^3}\right| \qquad \chi_k=\frac{1}{\omega^3}k_{,j}\,\omega_{,j}$$

$$f_{\beta^*}=\begin{cases}1, & \chi_k\le 0\\ \dfrac{1+680\chi_k^2}{1+400\chi_k^2} & \chi_k>0\end{cases}$$

The wall boundary condition for ω is given as $\omega|_{y=0}=\left(u_\tau^2/\nu\right)S_R$ where $S_R=(50/k_s^+)^2$ if $k_s^+<25$ and $S_R=100/k_s^+$ if $k_s^+\ge 25$ for the $k-\omega$ model. The dimensionless roughness height is defined as $k_s^+=u_\tau k_s/\nu$ where k_s is the equivalent sand-grain roughness height. For "hydraulically-smooth surface" a value of $k_s^+ \le 5$ is set.

The stress – ω model

The two-equation $k-\omega$ model previously mentioned uses Boussinesq eddy-viscosity approximation. This assumes that the principal axes of both Reynolds stress tensor and the mean strain-rate tensor are coincident everywhere in the flow. The Boussinesq approximation weakens in flows with sudden changes in the mean strain rate, flows with strong curved surfaces, flows with separation and flows with three-dimensional features. Second-order turbulence models are assumed to capture more of the true physical nature of a flow field because they allow direct computation of the Reynolds stress tensor

components, and in theory, they circumvent the deficiencies of the Boussinesq approximation.

The high Reynolds number compressible version of the stress$-\omega$ model is expressed as:

$$\rho\tau_{ij,t} + \rho U_k \tau_{ij,k} = -\rho P_{ij} + \frac{2}{3}\beta^* \rho\omega k\delta_{ij} - \rho\prod_{ij} + ((\mu + \sigma^*\mu_t)\tau_{ij,k})_{,k} \tag{6}$$

$$\rho\omega_{,t} + \rho U_j \omega_{,j} = \alpha\frac{\rho\omega}{k}\tau_{ij}U_{i,j} - \beta\rho\omega^2 + ((\mu + \sigma\mu_t)\omega_{,k})_{,k} \tag{8}$$

The pressure-strain correlation is based on the LRR model [20] and requires no wall reflection term which can be due to a wall-reflection effect. It is given as:

$$\prod_{ij} = \beta^* C_1 \omega(\tau_{ij} + \frac{2}{3}k\delta_{ij}) - \hat{\alpha}(P_{ij} - \frac{2}{3}P\delta_{ij}) - \hat{\beta}(D_{ij} - \frac{2}{3}P\delta_{ij}) - \hat{\gamma}k(S_{ij} - \frac{1}{3}S_{kk}\delta_{ij})$$

The auxiliary relations are used as follows:

$$P_{ij} = \tau_{im}U_{j,m} + \tau_{jm}U_{i,m} \qquad P = \frac{1}{2}P_{kk} \qquad D_{ij} = \tau_{im}U_{m,j} + \tau_{jm}U_{m,i}$$

And all the closure coefficients are defined as:

$$C_1 = 9/5 \quad C_2 = 13/25 \quad \alpha = 13/25 \quad \sigma = 1/2 \quad \sigma^* = 1/2 \quad \beta_0 = 9/125$$

$$\beta_0^* = 9/100 \quad \beta = \beta_0 f_\beta \quad \beta^* = \beta_0^* f_{\beta^*} \quad \hat{\alpha} = (8 + C_2)/11 \quad \hat{\beta} = (8C_2 - 2)/11$$

$$\hat{\gamma} = (60C_2 - 4)/55 \quad f_\beta = \frac{1 + 70\chi_\omega}{1 + 80\chi_\omega} \qquad \chi_\omega = \left|\frac{\Omega_{ij}\Omega_{jk}S_{ki}}{(\beta_0^*\omega)^3}\right| \qquad \chi_k = \frac{1}{\omega^3}k_{,j}\,\omega_{,j}$$

$$f_{\beta^*} = \begin{cases} 1, & \chi_k \le 0 \\ \dfrac{1 + 640\chi_k^2}{1 + 400\chi_k^2} & \chi_k > 0 \end{cases}$$

Wilcox [14] designed the stress$-\omega$ model similar to the $k-\omega$ model. The transport equation for ω is very similar, along with the wall boundary condition for ω. In general,

Reynolds stress model is not as practical as one and two-equation models due to the extra computational cost. While in theory a Reynolds stress model should perform better than a first order turbulence model, there is no guarantee of that happening.

The wall boundary condition for ω is given as $\omega|_{y=0} = (u_\tau^2 / \nu) S_R$ where $S_R = (50/k_s^+)^2$ if $k_s^+ < 25$ and $S_R = 500/(k_s^+)^{3/2}$ if $k_s^+ \geq 25$.

Problem Geometry

The test section geometry, described in details in Part I, consisted of a channel whose top surface is a plane surface while the bottom surface is plane or curved depending on the pressure gradient. A schematic of the problem geometry is shown in Fig. 1. The derivation of the bottom surface equation is described in detail in Part I of this report. The coefficients *a*, *b*, *c*, and *d* for various pressure gradients are given in Table 1. The nozzle exit plane is taken as the origin for distances in the *x* direction. The distances x_1 and x_2 in Table 1 are the start and end of the curved bottom surface.

PIV measurements were taken at 3 longitudinal locations 1, 2, and 3 and boundary layer data was extracted in the wall normal directions as shown in Fig. 1.

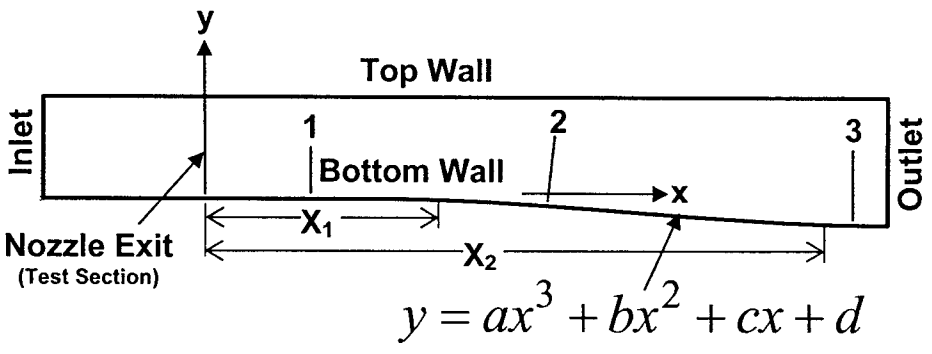

Fig.1 Problem geometry.

Table 1. Coefficients for the bottom surface profile equation*.

Pressure gradient	*a*	*b*	*c*	*d*	x_1, inch	x_2, inch
zero (zpg)	0	0	0	0	_	_
weak (wpg)	4.18906e-04	2.17531e-02	3.02998e-01	-1.27467e+00	9.66	24.95883
strong (spg)	6.89047e-03	-2.61862e-01	3.13020e+00	-1.20132e+01	9.66	15.675625

*x in the equation is in inches from the nozzle exit.

Computational Model

In the computational model the inlet boundary was extended beyond the nozzle exit. The length of this extension was determined by some numerical experimentation such that the boundary layer thickness closely matches that at the experimental value at the measurement location 1. This was necessary because the constant pressure inlet boundary condition with uniform velocity at the inlet was prescribed and the boundary layer thickness in the inlet in that case would be zero. The incoming boundary layer affects the solution at subsequent downstream solutions. If the nozzle exit were taken as the inlet boundary, then this boundary condition could not be applied. In that case, experimental velocity profile at the inlet had to be applied but measurement of the velocity profile at the nozzle exit was not taken. The total (stagnation) pressure, p_o, and temperature, T_o, at the inlet was specified as 689 kPa and 320 K, respectively, producing a Mach number of 2.86 at the inlet. The static pressure at the inlet was specified to be equal to the measured value at the nozzle exit. The turbulence intensity at the inlet was specified as 10% while the length scale was taken equal to the channel width at the inlet. Constant pressure outlet condition at the outlet was specified with the static pressure

there equal to the measured value. No-slip adiabatic conditions were specified at the top and bottom walls.

The mesh was clustered towards the channel walls such that the y^+ values to the first nodes next to the walls were of the order of 1 and a few nodes were inside the viscous sublayer. This was achieved through numerical experiment and grid refinement studies and 150 nodes in the wall normal direction was deemed satisfactory. A sample mesh is shown in Fig. 2.

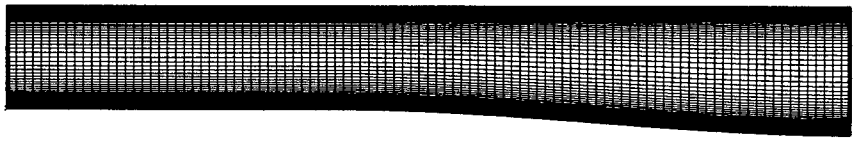

Figure 2. Sample mesh

All computations in this study were performed using the FLUENT commercial code version 6.1. The code uses an unstructured collocated mesh finite volume based algorithm to solve the governing equations. The compressible flow computations were done using the coupled implicit iterative solution procedure using the second-order upwind scheme for the convective terms. Convergence and steady-state is not only examined by noting the diminishing normalized residual levels ($< 10^{-5}$), but also by monitoring relevant integrated quantities such as mass flux through the. The mesh is generated by the GAMBIT preprocessor of the FLUENT code.

The $k-\omega$ turbulence model was used in the computation because of its advantage in specifying the surface roughness directly through the wall boundary condition for ω as mentioned earlier. The computations using the Reynolds stress model is underway and is not complete.

Experiments were conducted for three geometrical configurations (pressure gradients – zero, weak, and strong) and each case having smooth and rough surfaces. Thus a total of 6 cases were measured. Computations are done to date for the strong pressure gradient case with smooth and rough surfaces. Computations for other cases are ongoing. In the computations for the rough surface cases the equivalent sand-grain roughness height has to be specified. This was estimated by the Texas A&M group after analyzing the experimental velocity profile for the strong pressure gradient case and was reported to be 0.25 mm. This value was used in the computation.

Results

The contours of the Mach number distribution in the channel is shown in Figs. 3 and 4 for the strong pressure gradient case with smooth and rough bottom surfaces, respectively. The effect of surface roughness is clearly discernible from these figures (closeup wiews). The boundary layer thickens and maximum Mach number reduces (flow slows down) due to the surface roughness compared to the smooth surface case.

The predicted profiles of the x velocity component in the wall normal direction at measurement locations 1, 2, and 3 are compared with the experimental data in Figs. 5, 6, and 7, respectively. The Reynolds stresses ($\overline{u_i'u_j'}$) are computed from the mean flow field ($\bar{u}$) and eddy viscosity (μ_t) from the stress tensor equation

$$-\bar{\rho}\overline{u_i'u_j'} = \mu_t\left(\frac{\partial u_i}{\partial x_j}+\frac{\partial u_j}{\partial x_i}\right)-\frac{2}{3}\bar{\rho}k\delta_{ij} \tag{9}$$

where k is the turbulent kinetic energy ($\overline{u_i'u_j'}/2$) and δ_{ij} is the Kronecker delta. The computed Reynolds stress profiles in the wall normal directions at measurement locations

1, 2, and 3 are also compared with the experimental data for the smooth and rough surface cases in Figs. 8-16. It may be noticed from these figures that, in general, the agreement between prediction and experiment is not quite satisfactory. While the agreement is somewhat better for the smooth surface cases, it is much worse for the rough surface cases. Also the Reynolds stresses are severely under or over-predicted especially for the rough surface cases and at measurement locations 2 and 3. The reasons for these disagreements can be associated with several factors. First, the inlet boundary conditions greatly affect the downstream solutions especially for supersonic flow simulation. The incoming boundary layer profiles should be accurately provided at the inlet the lack of which may generate unsatisfactory solutions. In the present simulations the inlet profiles were not available from the experiment so the channel was extended in the upstream direction and uniform flow was specified at the inlet on an ad-hoc basis so that the boundary develops and closely matches to that at the measurement location 1 in the experiment. For turbulence model validation, accurate inlet profiles within the boundary layer and very close to the wall should be available. Second the $k-\omega$ turbulence model itself may have some inadequacy for the supersonic flow calculation. The model constants and boundary conditions for ω at the surface were derived from incompressible flow data which may be inappropriate for supersonic compressible flow. Further research for re-deriving the model constants and ω boundary conditions at the surface for supersonic turbulent flow is warranted. Third, the value of the equivalent sand-grain roughness height for the rough surface cases is very crucial for the numerical computation of the surface roughness effects. The equivalent sand-grain roughness height is obtained from the analysis of the experimental data (velocity profile in the boundary

layer) by adjusting the skin friction coefficient, c_f, so that the slope in the log region is equal to von-Karman's constant, κ. Any inaccuracy in the derivation of this value would greatly affect the computation. Fourth, the experimental uncertainty is another factor to be considered. Some of the data points show abnormal trend close to the surface. Also, experimental data very close to the surface is needed for turbulence model development/validation especially if roughness effects are to be investigated. This could not be obtained in the present experiments probably due to the limitations of the PIV technique.

Even though the experiment was performed for three pressure gradients associated with three different configurations of the bottom surface of the test section, the calculations are done for only one pressure gradient, namely the strong pressure gradient case. The design and fabrication of the experiment, calibration and testing of the associated equipments and instrumentation, and conducting the actual measurements consumed most of the project duration. The data were available very late in the project timeline and for this reason computation of all three cases and testing other turbulence models such as the stress-ω model could not be included in the present report. The numerical investigation on these aspects is ongoing and will be published later.

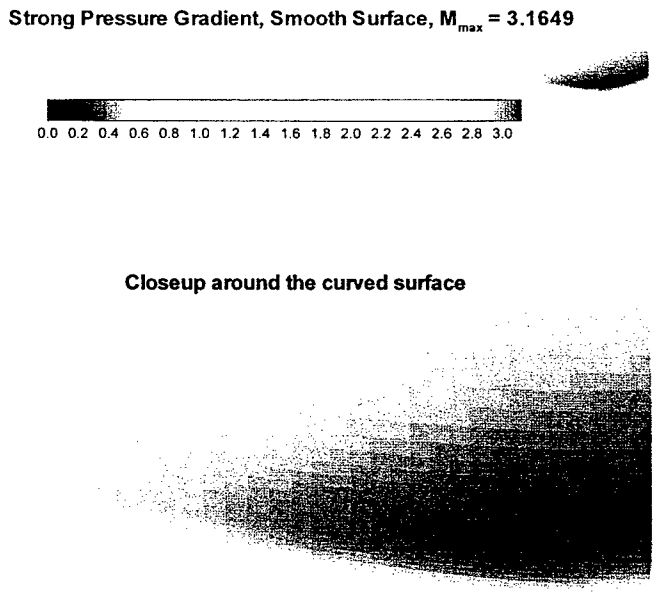

Figure 3. Contours of Mach number distribution for the strong pressure gradient case with smooth bottom surface.

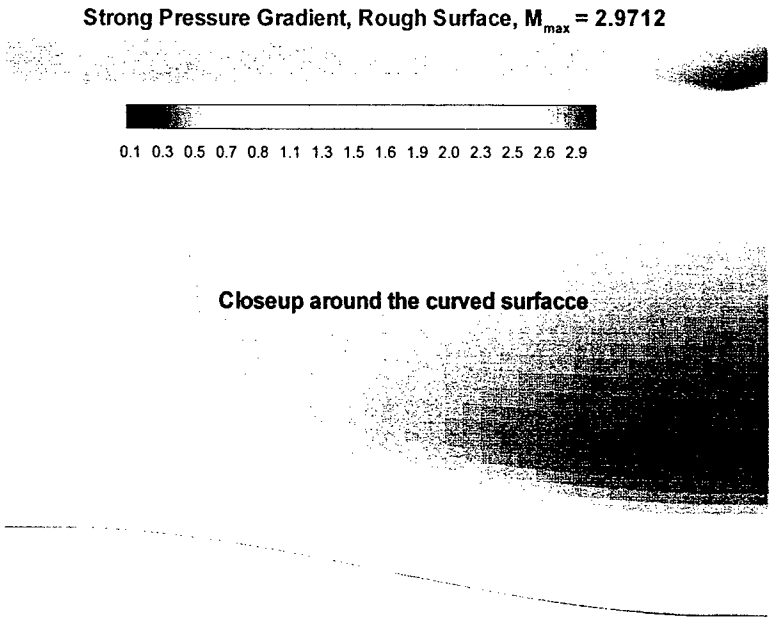

Figure 4. Contours of Mach number distribution for the strong pressure gradient case with rough bottom surface.

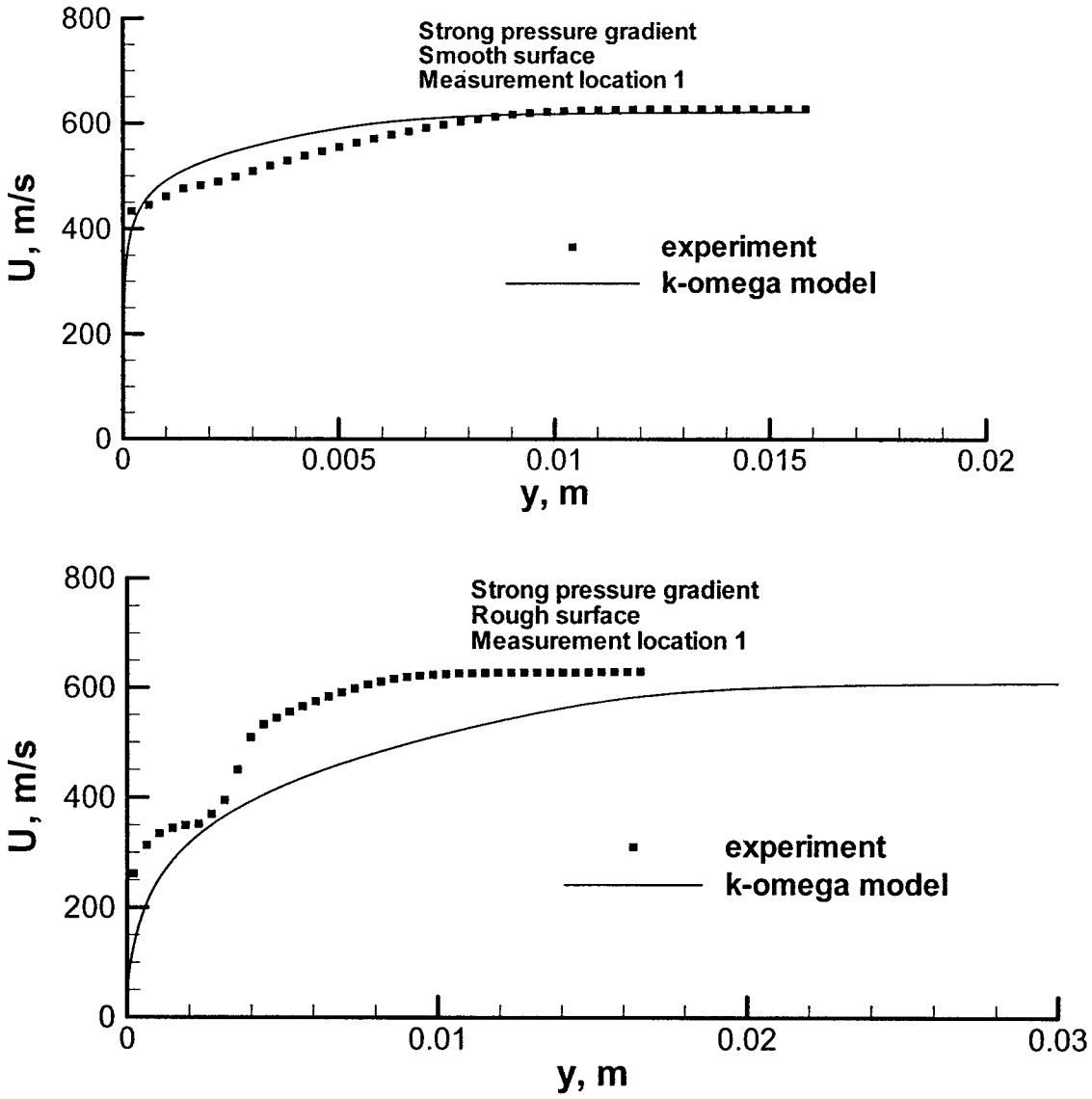

Figure 5. Comparison of the predicted and experimental x velocity profiles in the wall normal direction within the boundary layer for smooth and rough surface cases at measurement location 1.

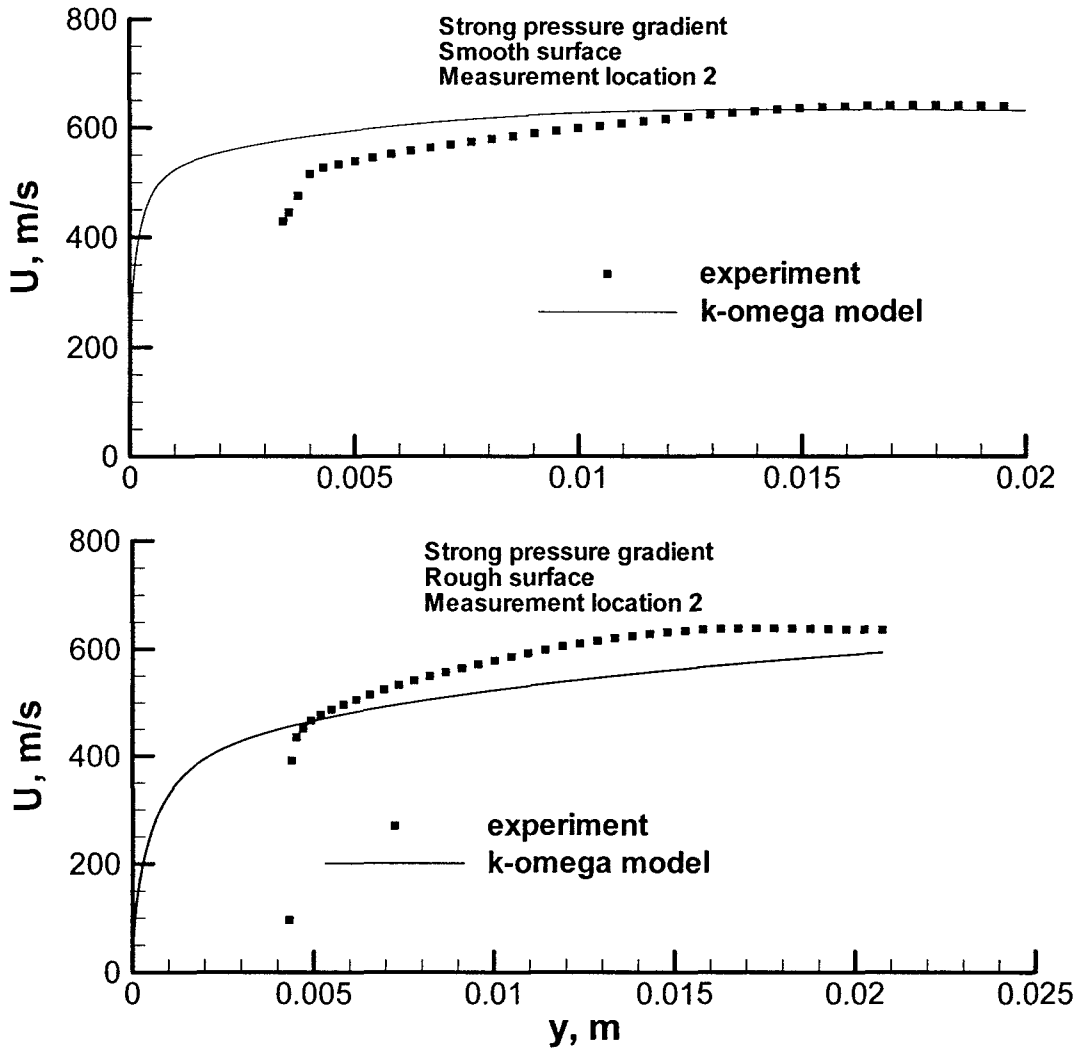

Figure 6. Comparison of the predicted and experimental x velocity profiles in the wall normal direction within the boundary layer for smooth and rough surface cases at measurement location 2.

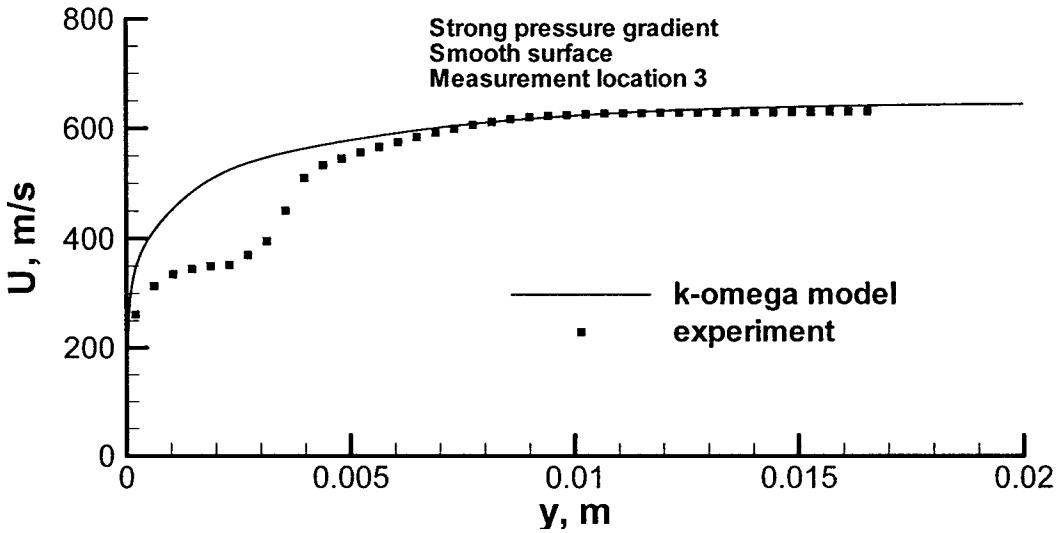
Strong pressure gradient
Smooth surface
Measurement location 3
k-omega model
experiment
U, m/s
y, m
0
200
400
600
800
0
0.005
0.01
0.015
0.02

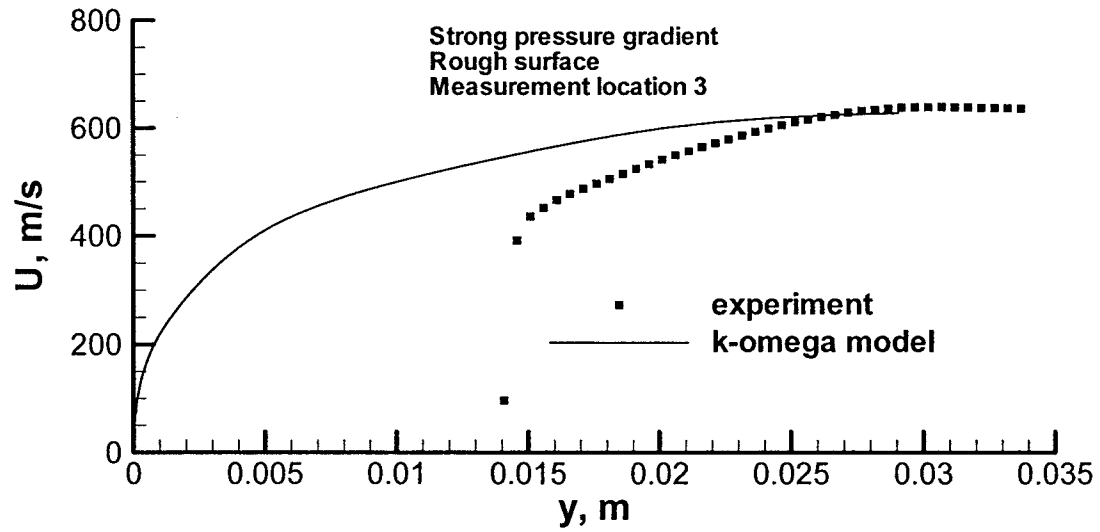
Strong pressure gradient
Rough surface
Measurement location 3
experiment
k-omega model
U, m/s
y, m
0
200
400
600
800
0
0.005
0.01
0.015
0.02
0.025
0.03
0.035

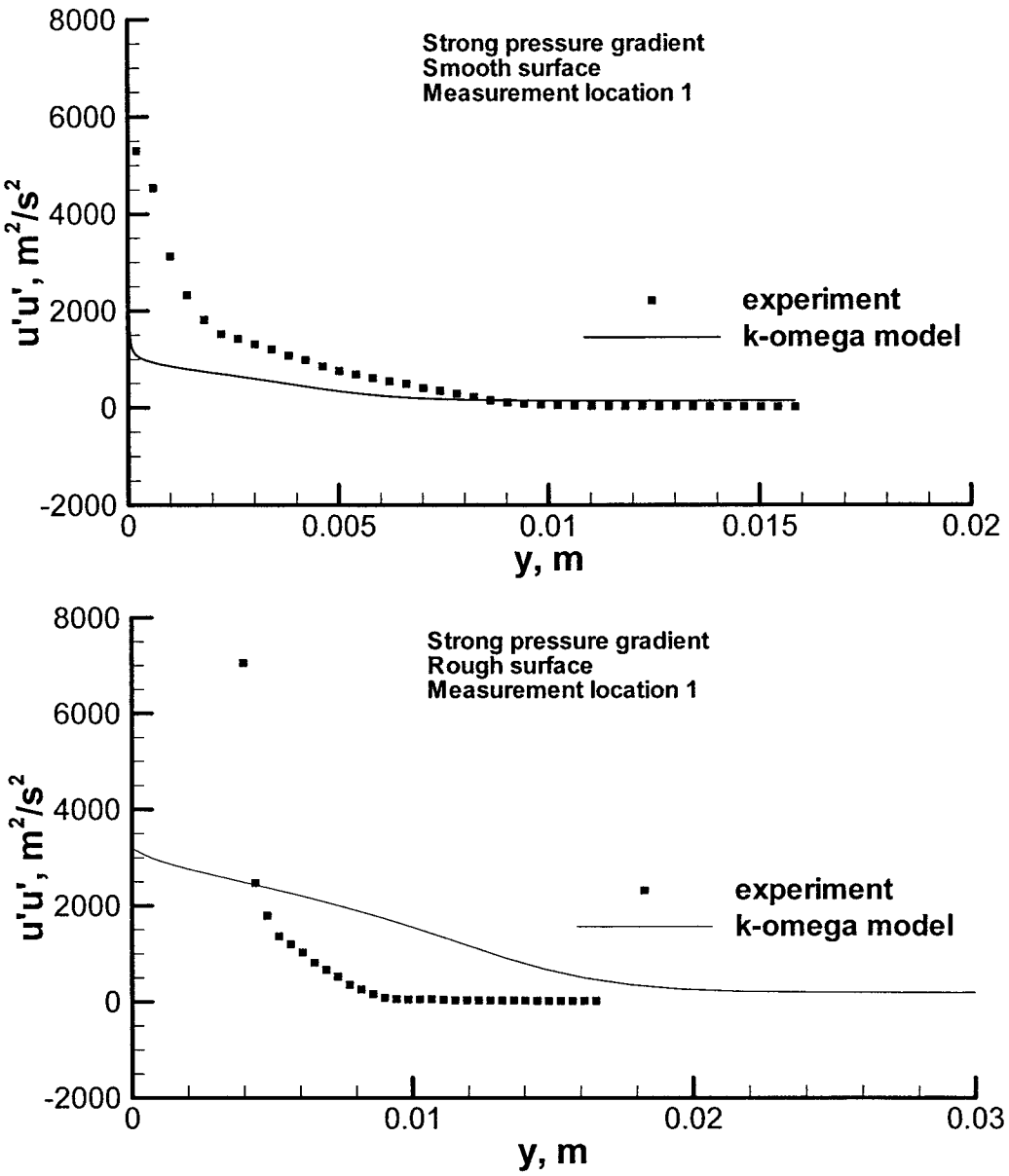

Figure 8. Comparison of the predicted and experimental $\overline{u'u'}$ profiles in the wall normal direction within the boundary layer for smooth and rough surface cases at measurement location 1.

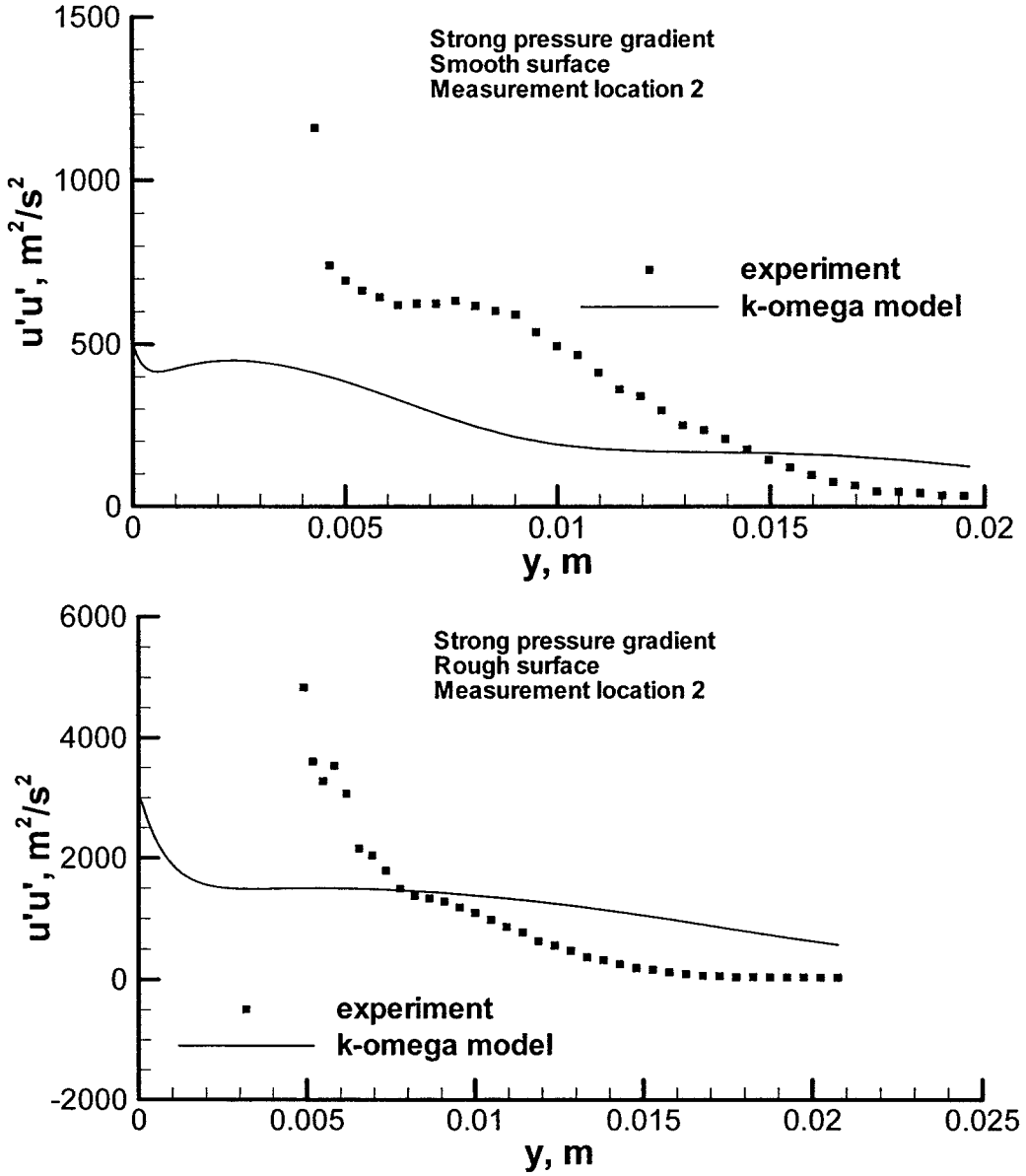

Figure 9. Comparison of the predicted and experimental $\overline{u'u'}$ profiles in the wall normal direction within the boundary layer for smooth and rough surface cases at measurement location 2.

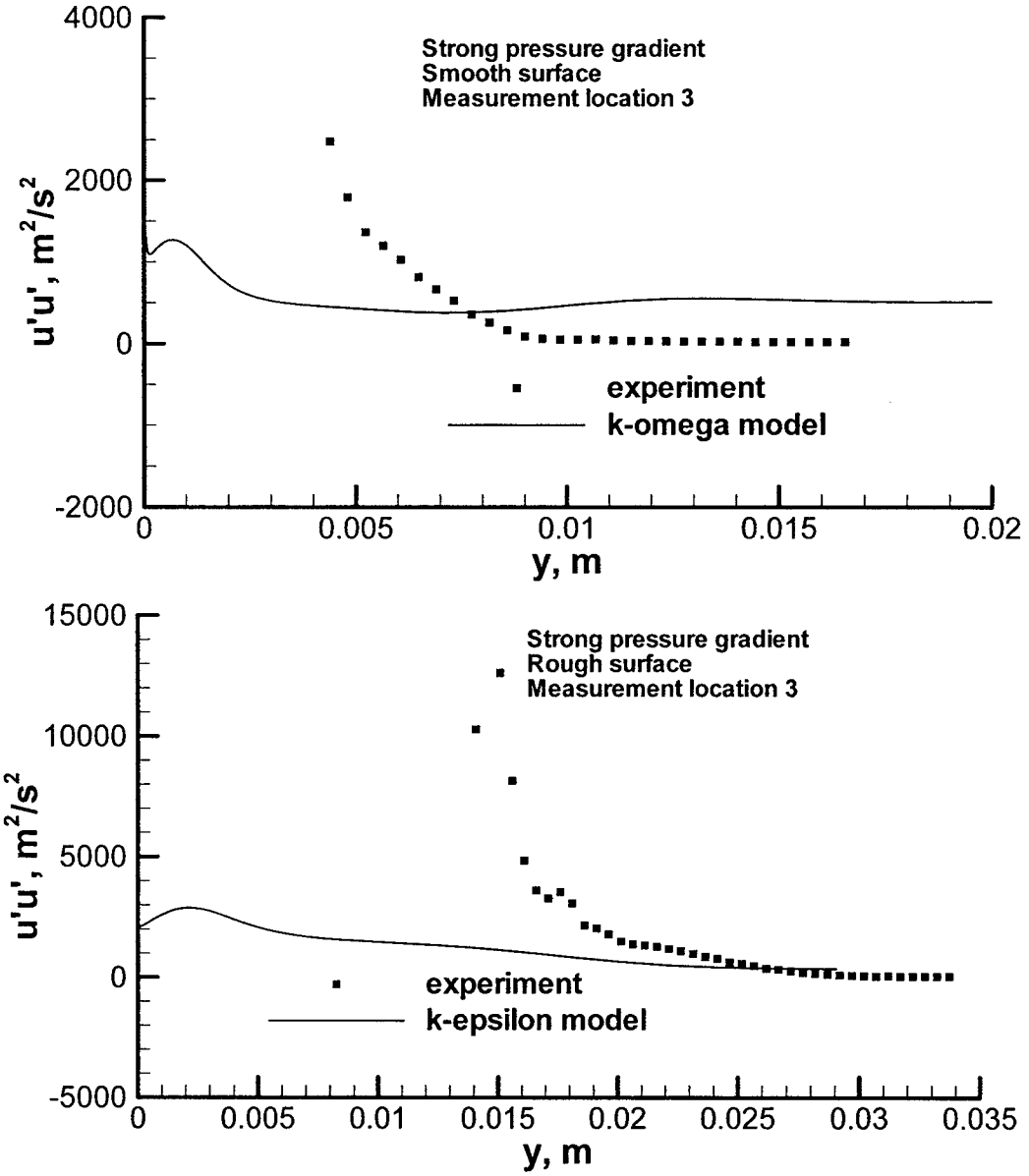

Figure 10. Comparison of the predicted and experimental $\overline{u'u'}$ profiles in the wall normal direction within the boundary layer for smooth and rough surface cases at measurement location 3.

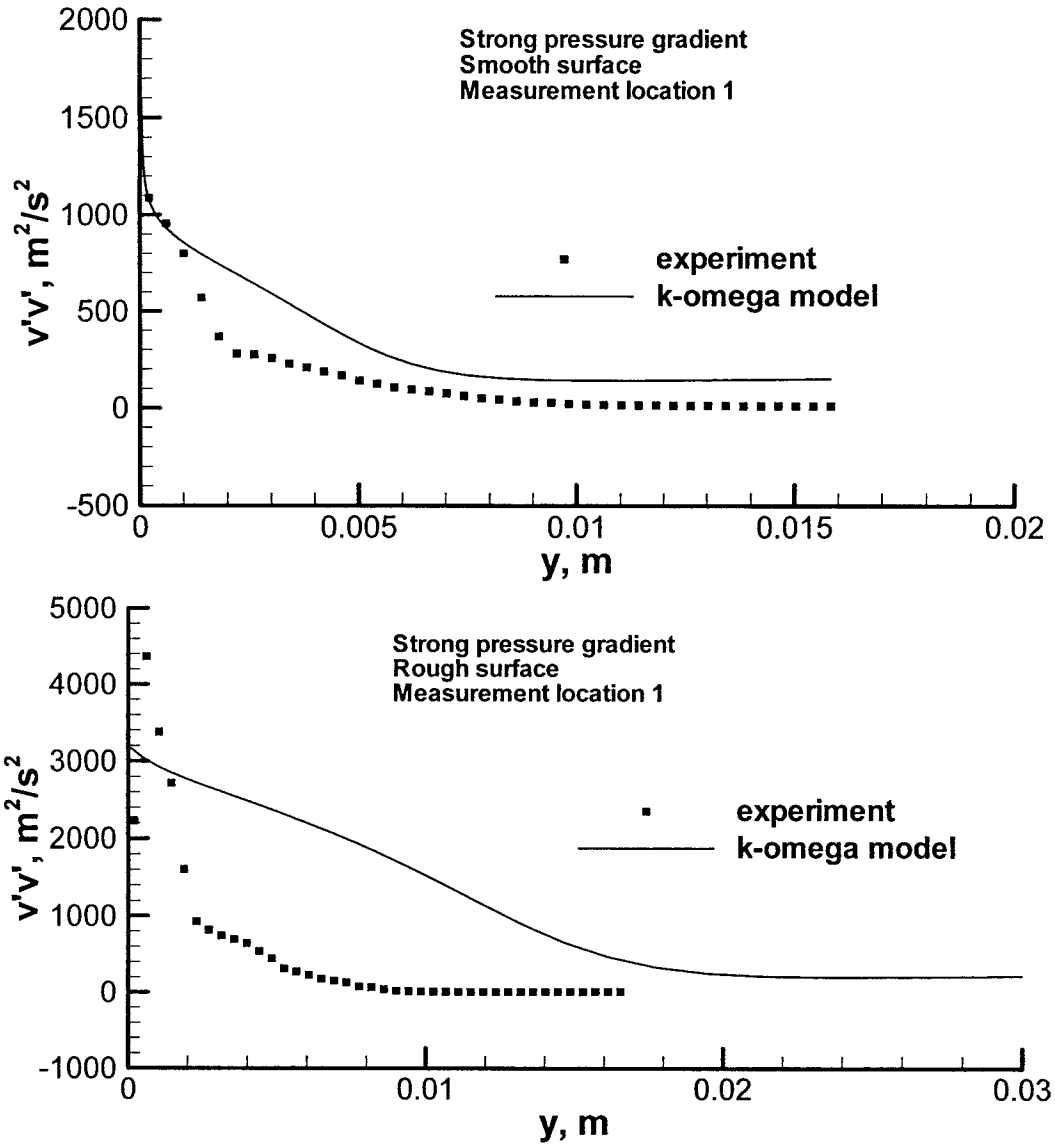

Figure 11. Comparison of the predicted and experimental $\overline{v'v'}$ profiles in the wall normal direction within the boundary layer for smooth and rough surface cases at measurement location 1.

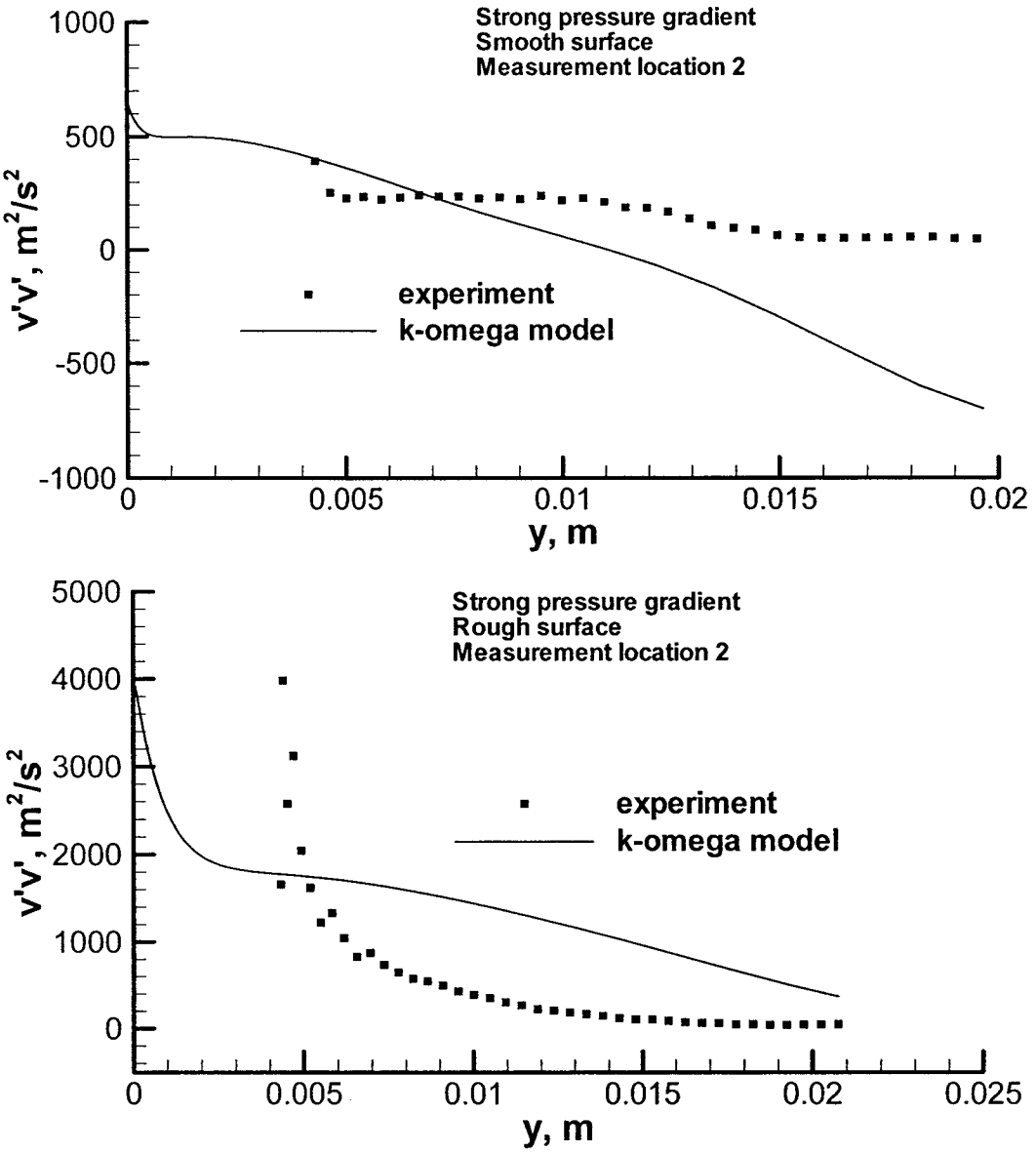

Figure 12. Comparison of the predicted and experimental $\overline{v'v'}$ profiles in the wall normal direction within the boundary layer for smooth and rough surface cases at measurement location 2.

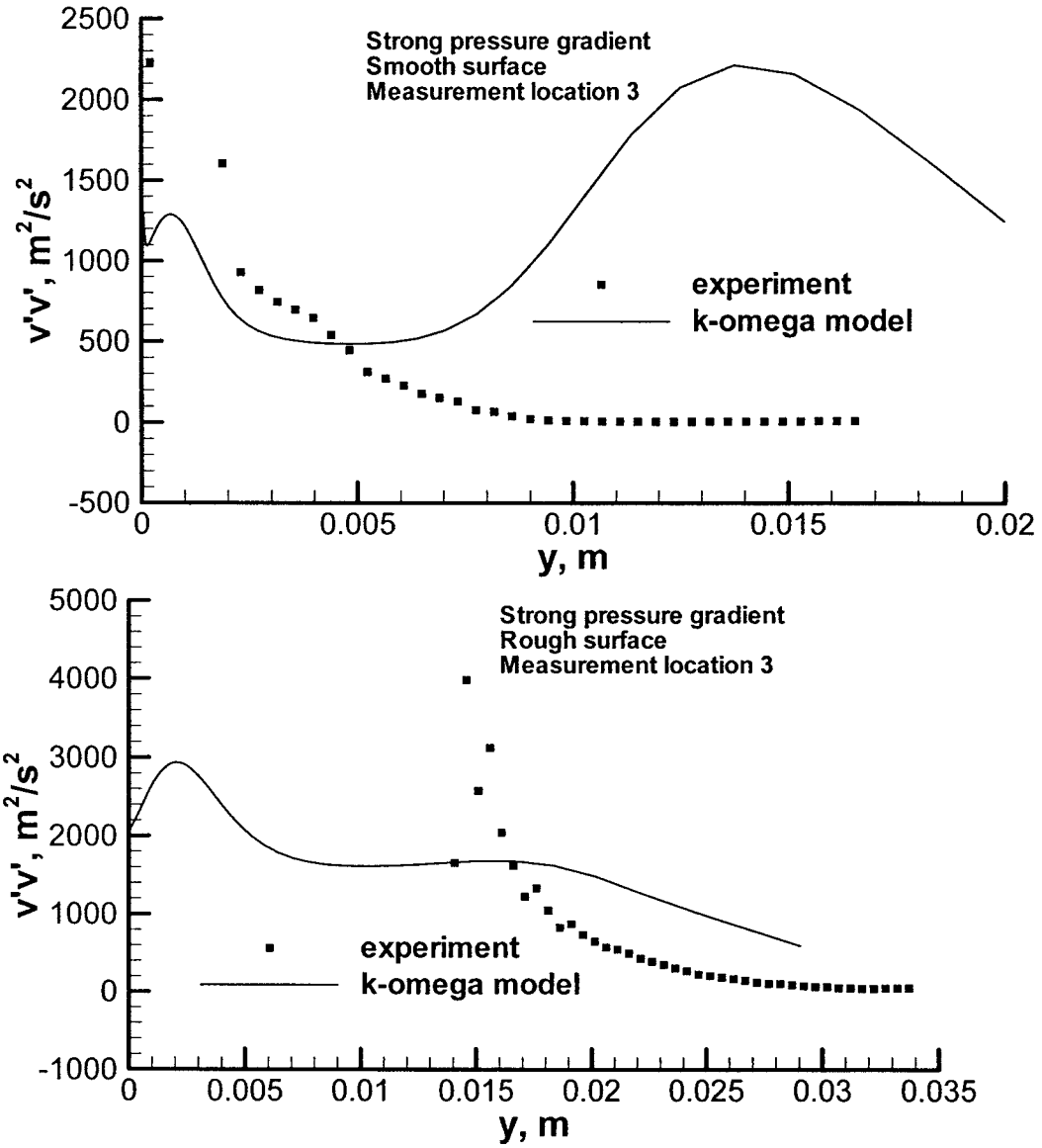

Figure 13. Comparison of the predicted and experimental $\overline{v'v'}$ profiles in the wall normal direction within the boundary layer for smooth and rough surface cases at measurement location 3.

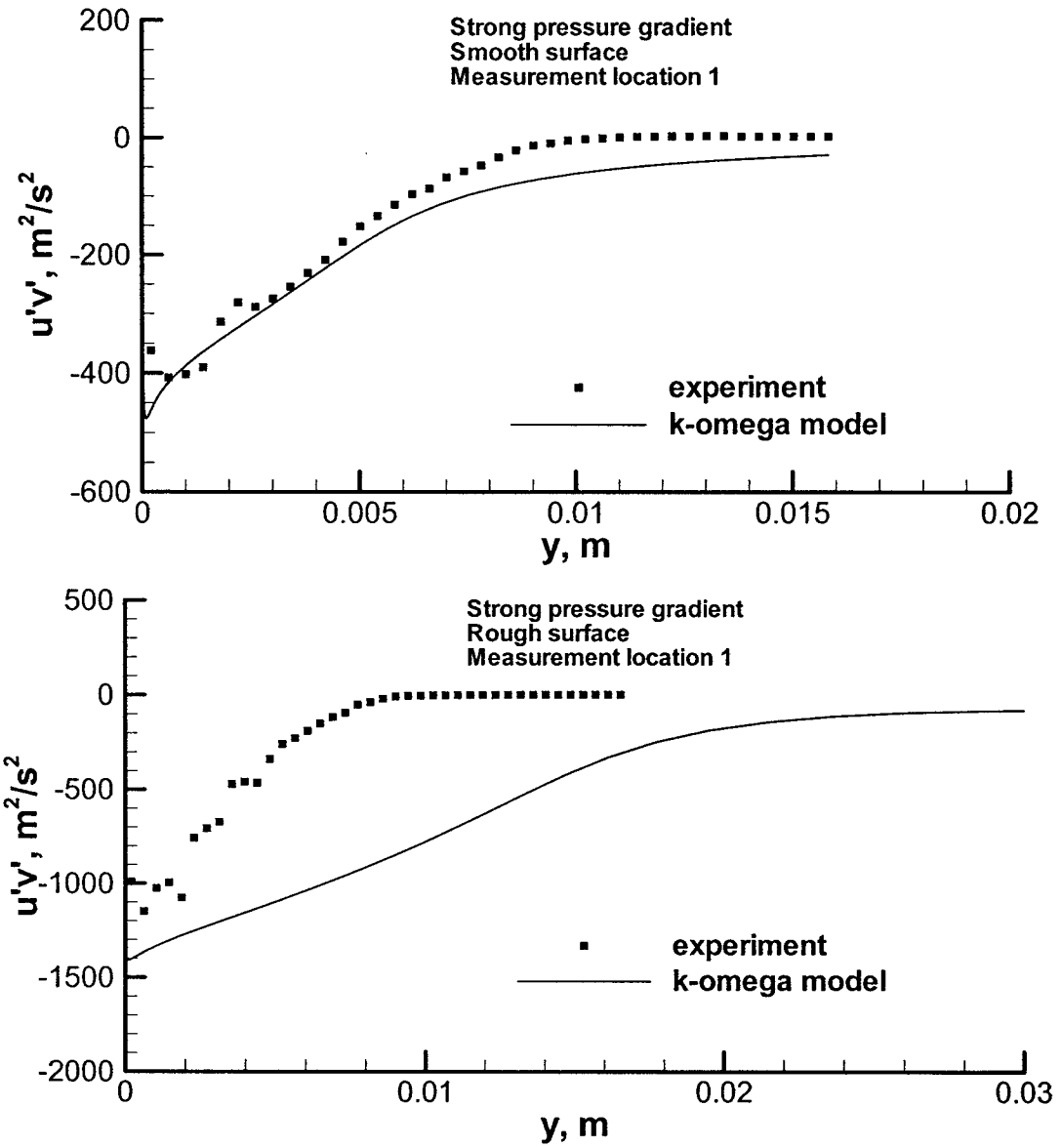

Figure 14. Comparison of the predicted and experimental $\overline{u'v'}$ profiles in the wall normal direction within the boundary layer for smooth and rough surface cases at measurement location 1.

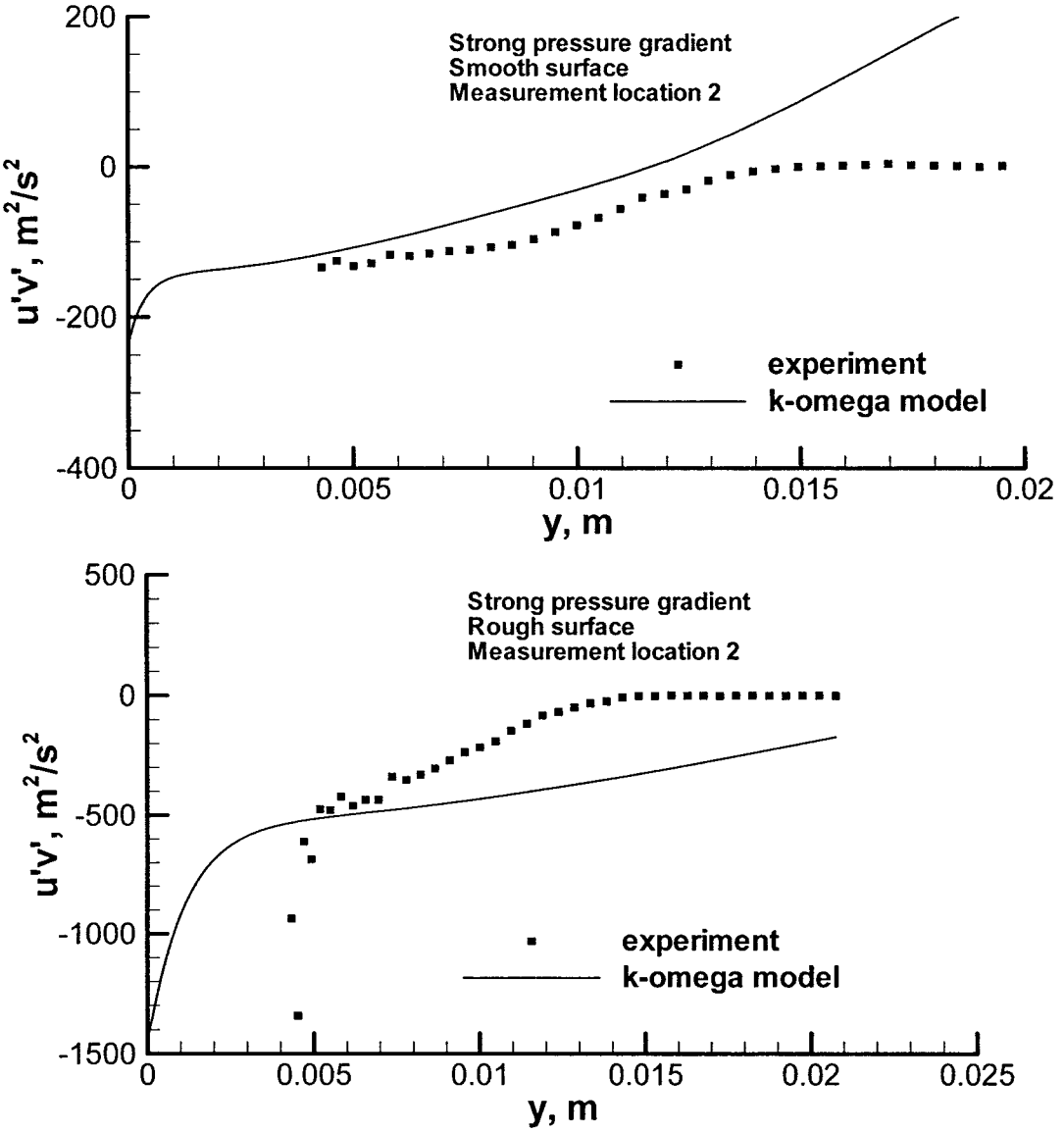

Figure 15. Comparison of the predicted and experimental $\overline{u'v'}$ profiles in the wall normal direction within the boundary layer for smooth and rough surface cases at measurement location 2.

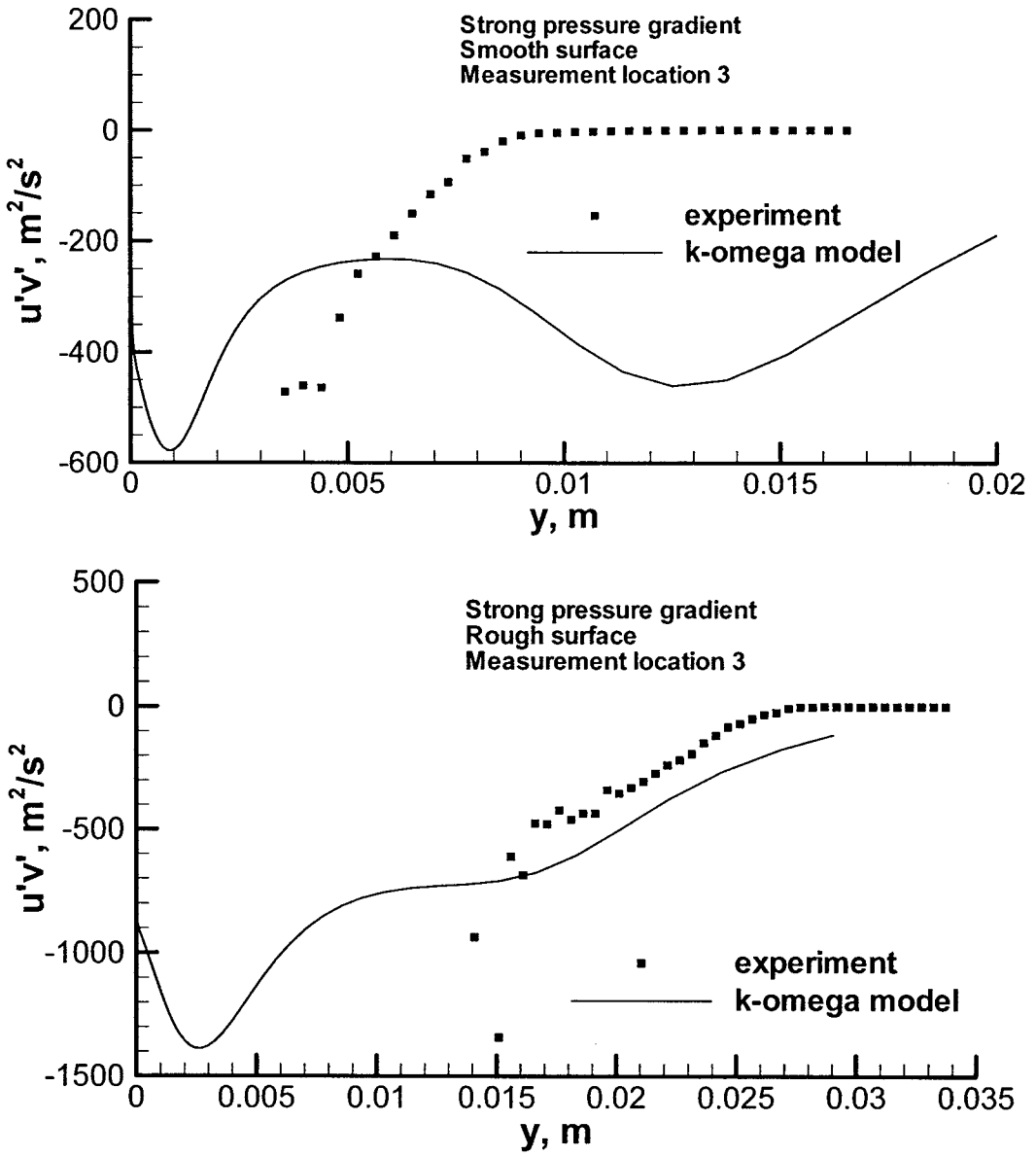

Figure 16. Comparison of the predicted and experimental $\overline{u'v'}$ profiles in the wall normal direction within the boundary layer for smooth and rough surface cases at measurement location 3.

References

[1] J.A. Shetz, Boundary Layer Analysis, Prentice Hall, New Jersey, 1993.

[2] P.A. Durbin, G. Medic, J.M. Seo, Rough wall modification of two-layer $k-\omega$, Journal of Fluids Engineering. 123 (2001) 16-21.

[3] Kays, W.M. and Crawford, M.E., Convective Heat and Mass Transfer, 3rd ed., McGraw-Hill, New York, 1993.

[4] V.C. Patel, J.Y. Yoon, Application of turbulence models to separated flow over rough surfaces, Journal of Fluids Engineering. 117 (1995) 234-241.

[5] M. Morkovin, Fluctuations and Hot-Wire Anemometry in Compressible Flow, AGARDOGRAPH, 24, 1956.

[6] R.D.W. Bowersox, T.A. Buter., Turbulence measurements in a mach 2.9 boundary layer including mild pressure gradients, AIAA Journal. 34 (1996) 2479-2483

[7] A.J. Smits, E.F. Spina, A.E. Alving, R.W. Smith, E.M. Fernando, J.F. Donovan, A comparison of the turbulence structure of subsonic and supersonic boundary layers, Physics of Fluids, A1. 11 (1989) 1865-1875.

[8] E.F. Spina, Organized Structures in a Supersonic Turbulent Boundary Layer. PhD dissertation, Princeton University, 1988.

[9] H. Fan, R.D.W. Bowersox, Numerical Analysis of High-Speed Flow over Rough Surfaces, Proceedings of the 35th AIAA/ASME/SAE/ASEE Joint Propulsion Conference and Exhibit, Los Angeles, California, 20-24 June, 1999, 1-8.

[10] E.R. van Driest, On turbulent flow near a wall, Journal of Aerospace Science. 23, (1956) 1007-1011.

[11] T. Cebeci, K.C. Chang, Calculation of incompressible rough-wall boundary-layer flows, AIAA Journal. 16 (1978) 730-735.

[12] P. Kragstad, Modification of the van Driest damping function to include the effects of surface roughness, AIAA Journal. 29 (1990) 888-894.

[13] R.M. Latin, R.D.W. Bowersox, Flow properties of a supersonic turbulent boundary layer with wall roughness, AIAA Journal. 38 (2000) 1804-1821.

[14] D.C. Wilcox, Turbulence Modeling for CFD, 2nd ed., DCW Industries, La Canada, California, 2000.

[15] R.E. Neel, A.G. Godfrey, D.C. Slack, 2003, Turbulence Model Validation in GASP Version 4, AIAA 2003-3740, 2003.

[16] T. Cebeci and A. Smith, Analysis of Turbulent Boundary Layer, Academic Press, New York, 1974.

[17] H. Schlichting, Boundary Layer Theory, McGraw-Hill, New York, 1979.

[18] R. M. Latin, R.D.W. Bowersox, Influence of Surface Roughness on Supersonic High Reynolds Number Turbulent Boundary Layer Flow, AFRL-PR-TR-1999-2004, Wright-Patterson AFB, 1998.

[19] R.D.W. Bowersox, Combined laser doppler velocimetry and cross-wire anemometry analysis, AIAA Journal. 34 (1996) 2269-2275.

[20] A.E. Perry, W.H. Schofield, P.N. Joubert, Rough wall turbulent boundary layers, Journal of Fluid Mechanics. 37 (1969) 383-413.

[21] J. Jimenez, Turbulent flows over rough walls, Annual Review of Fluid Mechanics. 36 (2004) 173-196.

APPENDIX

35th AIAA Fluid Dynamics Conference and Exhibit
6-9 June 2005, Toronto, Ontario, Canada

AIAA 2005-4637

Performance of Turbulence Models in the Computation of Transonic Flow over a Circular Arc Bump

Johnson Mendonca[1] and M.A.R Sharif.[2]
Aerospace Engineering and Mechanics Department, The University Of Alabama, Tuscaloosa, AL 35487-0280

Transonic turbulent boundary layer flow over a circular arc bump is computed with the commercial CFD code FLUENT to determine the effect of surface roughness on turbulent shock/boundary layer interaction. The Inger and Gendt[23] experiment at a supercritical M_∞ of 0.73M and Re/m = 1.7×10^{-6} is computed using the one-equation Spalart-Allmaras model, the standard $k-\varepsilon$ and $k-\omega$ models, and the Reynolds Stress Transport model for the circular arc bump with smooth surface. These predictions are critically compared with the available experimental data in order to identify the most appropriate model. The $k-\omega$ model with enhanced wall treatment, as implemented in the FLUENT code, on the whole showed a reasonably better performance when compared with the other turbulence models. Hence the $k-\omega$ model is subsequently employed for the surface roughness study whereby four different configurations of uniform sand grain roughness are modeled. Results are presented for these flow configurations. The influence of the increase in surface roughness height transcends over onto the shock boundary layer zone and the observations are discussed.

Nomenclature

a	=	speed of sound
C_f	=	skin friction coefficient, $2\tau_w / \rho_\infty U_\infty^{\,2}$
C_p	=	pressure coefficient, $2(p-p_\infty)/\rho_\infty U_\infty^{\,2}$
e	=	internal energy per unit mass
E	=	total internal energy per unit mass
$\vec{F}$	=	flux vector
H	=	enthalpy
k	=	turbulent kinetic energy
k_s	=	roughness height
l	=	mixing length for turbulent viscosity
K_T	=	total thermal conductivity coefficient
M	=	flow Mach number
n	=	local normal distance from the wall
$\vec{n}$	=	normal unit vector
Re	=	Reynolds Number
p	=	hydrostatic pressure
q	=	heat flux
t	=	time
T	=	static temperature
u, v, w	=	mean velocity components in the x-, y- and z- directions.
U	=	velocity in x direction

---

[1] Graduate Student, Aerospace Engineering and Mechanics Department, The University of Alabama, Tuscaloosa, Alabama Box 870280, USA, Member AIAA.

[2] Associate Professor, Aerospace Engineering and Mechanics Department, The University of Alabama, Tuscaloosa, Alabama Box 870280, USA, Associate Fellow AIAA.

$\vec{U}$ = mean velocity vector (u,v,w)
U_∞ = free-stream velocity
x = streamwise coordinate
y = vertical coordinate
y^+ = Law of the Wall coordinate

Greek Symbols
γ = specific heat ratio
Ω = flow domain
μ = coefficient of viscosity
μ_t = turbulent viscosity
δ = boundary layer thickness
ρ = density
τ = shear stress
$\bar{\bar{\tau}}$ = stress tensor

Subscripts
0 = upstream condition
l = laminar quantity
∞ = free stream condition
w = wall condition
n = time step counter

Introduction

Transonic flow occurs when there is mixed subsonic and supersonic local flows in the same flow field. This usually happens when the subsonic free-stream flow Mach number is above a critical value. The subsonic flow accelerates to supersonic speeds while flowing over a bump like structure and subsequently a shock discontinuity terminates the supersonic region. Shock wave/boundary layer interactions that occur in transonic flows are crucial in many practical applications such as turbo machine component flows in compressors and turbines, aircraft propulsion systems, flow over tip regions of helicopter rotors and high speed propellers, and transonic airfoils and wings. As the shock strength increases so does the effect of separation and reattachment influencing the whole gamut of the overall flow-field physics. Since this phenomenon is so multifaceted, several investigations were carried out by pioneering researchers initialized by Liepmann[1] and summarized by Green[2]. In many practical high-speed flow problems, shock/boundary layer interaction usually occurs at a transonic speed on curved surfaces leading to detrimental flow features such as adverse losses in pressure, increased drag, and flow alteration/distortion. When these flows are subjected to perturbation in external conditions such as curvature, roughness, blowing, rotation, pressure gradients etc., the responses are much more complex depending on the perturbation strength. For example, near wall shear production of turbulent stresses are enhanced due to perturbation in surface curvature or pressure gradient, hence being responsible for the internal layer formation. In a number of studies, boundary layer response to singular perturbations in pressure gradient or curvature has been examined. The effect of step applications of curvature on a turbulent boundary layer is now reasonably well known due to the works of So and Mellor[3], Gillis and Johnston[4], and Hoffmann et al.[5] among others. A step variation in stream-wise pressure gradient has also been the subject of a number of investigations of which the works of Bradshaw and Galea[6] and Samuel and Joubert[7] can be mentioned. Perturbations in both pressure gradient and curvature show that the combined influence of external perturbations is not a simple summation of their separate effects as reported by Smits et al.[8] and Smits and Wood[9].

The analysis of transonic viscous flow is difficult because it is innately nonlinear and the steady solution changes from being elliptic in the subsonic flow path to hyperbolic in the supersonic part of the flow. Thus analytical solution was very difficult to obtain and researchers had to rely on experimental investigation. Experimental investigations have been conducted by independent researchers such as Delery[10], Johnson et al.[11], Bachalo and Johnson[12,13], and Liu and Squire[14,15], among others, on dissimilar bump geometry configurations. With the advent of numerical methods, transonic flow analysis was possible since late 1960s. The experimental investigations showed enhanced flow complexity in the transonic regime due to the flow separation and adverse pressure gradients. These features form an enormous challenge to numerical methods and turbulence models. Furthermore, the unavailability

of reliable turbulence models hinders successful numerical analysis of these types of flows. Typically, RANS (Reynolds Averaged Navier-Stokes) solutions are obtained utilizing one or two-equation eddy-viscosity models and Reynolds stress transport models. RANS numerical analysis of transonic flows were conducted by Johnson et al.[11], Johnson[16], Sahu and Danberg[17] and Barakos and Drikakis[18,19], among others. More recently, Sandham et al.[20] obtained LES (Large Eddy Simulation) solutions for transonic flow over bumps.

Investigations using the Reynolds stress model have shown the best feature in predicting the inception of the separation process, mean velocity profiles and turbulent normal and shear stresses in the separation region. It does not envisage the mean flow-field well but needs further expansion/progress in predicting the main characteristic in the shock wave/boundary layer interactions such as turbulent quantities in the regions near shock or expansion wave.

An added complexity in the flow physics of transonic flow is incorporated when the surface roughness is considered as a flow parameter. Fluid flow over rough surfaces occurs in varied situations. Some of its effects are resistance to the flow (drag) and heat transfer, with the primary effect of roughness being change in the velocity and turbulence distributions near the surface. Lately, it has been observed that the effect of surface roughness is extended across the entire boundary and into the main flow instead of being confined to the inner layer only. Though advances have been made in complex flow computation, very little progress has been achieved in modeling flow over rough surfaces. Generally, most of the turbulence models employ the wall-function in treating roughness near the wall whereby no numerical solution is computed but the local velocity distribution near the wall is given by the classical semi-logarithmic law of the wall for rough surfaces. However, recent investigations on smooth walls differ with this approach and tend to favor near-wall turbulence models because the 'law of the wall' does not apply in flows with strong pressure gradients and separation as reported in the study of smooth sinusoidal wavy wall by Patel et al.[21]. Experiments on the effect of surface roughness on the boundary layer flow have been conducted for rectangular wavy wall channels by Nakagawa and Hanratty[22]. Recent experiments and theoretical study include the study of roughness over a transonic bump with flow Mach number being 0.73 as reported in Inger and Gendt [23], and roughness study for flat plate at Mach 2.5 in Babinsky and Inger[24]., and Babinsky et al. [25]. Computational study of surface roughness effects on transonic flow over circular arc bumps has not been performed till date.

In the present study the numerical solution of transonic flow over a smooth circular bump surface is obtained using several turbulence models and compared/validated against experimental data in order to identify the most suitable model for these types of flows and predictions are made. It is observed that the $k-\omega$ and the Reynolds stress models perform better than other models. Furthermore the performance of the $k-\omega$ model is very comparable despite the fact that much larger processing time is required by the Reynolds stress model. Hence the $k-\omega$ model is chosen to further investigate the effects of surface roughness on the transonic flow over a bump. Various surface roughness configurations are computed and analyzed and the results are presented in the form of contour plots, surface pressure and skin friction coefficients, and variation of drag coefficient with changing roughness.

Governing Equations

The differential equations used to describe the mean flow for this study are the time dependent, mass averaged Navier Stokes equations for plane or axially symmetric flow of a compressible fluid. Depending on the turbulence model used, these equations are augmented by additional equations. All models use the eddy viscosity hypothesis; that is, the Reynolds stress, heat flux, and kinetic energy flux terms are implicitly related to the mean flow velocity, temperature and kinetic energy gradients through an eddy transport coefficient. Additional restrictions on the equations include the perfect gas assumption, constant specific heats, and zero bulk viscosity.

The Reynolds-Averaged Navier Stokes in Cartesian co-ordinate system can be written as,

$$\frac{\partial W}{\partial t}+\frac{\partial F_c}{\partial x}+\frac{\partial G_c}{\partial y}+\frac{\partial H_c}{\partial z}=\frac{\partial F_v}{\partial x}+\frac{\partial G_v}{\partial y}+\frac{\partial H_v}{\partial z} \tag{1}$$

where W is the vector of dependent variables, F_c, G_c and H_c are the convective flux vectors, and F_v, G_v and H_v are the viscous flux vectors. They are given by

$$W = \begin{bmatrix} \rho \\ \rho u \\ \rho v \\ \rho w \\ \rho E \end{bmatrix}, \quad \vec{F_c} = \begin{bmatrix} \rho\vec{U} \\ \rho u\vec{U} + p\vec{i} \\ \rho v\vec{U} + p\vec{j} \\ \rho w\vec{U} + p\vec{k} \\ \rho H\vec{U} \end{bmatrix}, \vec{F_v} = \begin{bmatrix} 0 \\ \vec{\tau}_x \\ \vec{\tau}_y \\ \vec{\tau}_z \\ \overline{\overline{\tau}}.\vec{U} - \vec{q} \end{bmatrix} \tag{2}$$

where,

$$\overline{\overline{\tau}} = \vec{\tau}_x\vec{i} + \vec{\tau}_y\vec{j} + \vec{\tau}_z\vec{k}$$

$$\overline{\overline{\tau}}_i = \vec{\tau}_{ix}\vec{i} + \vec{\tau}_{iy}\vec{j} + \vec{\tau}_{iz}\vec{k}$$

$$\vec{q} = -c_p\left(\frac{\mu_l}{\mathrm{Pr}_l} + \frac{\mu_t}{\mathrm{Pr}_t}\right)\vec{\nabla}T$$

$$\vec{F}_c = F_c\vec{i} + G_c\vec{j} + H_c\vec{k}$$

$$\vec{F}_v = F_v\vec{i} + G_v\vec{j} + H_v\vec{k}$$

$$\rho E = \rho e + \frac{1}{2}\rho(u^2 + v^2 + w^2) \tag{3}$$

In Integral form, equation (1) is redrafted as,

$$\frac{\partial}{\partial t}\int_\Omega W dV + \int_{\delta\Omega}\vec{F}_c.\vec{n}_s dS = \int_{\delta\Omega}\vec{F}_v.\vec{n}_s dS \tag{4}$$

The above governing equations are written in non-dimensional form using free stream flow conditions and a reference length.

Numerical Considerations

The bump geometry is one of the most broadly used configurations for validating turbulence models in shock/boundary layer interaction in transonic flows. The present study incorporates the experimental configuration of Inger and Gendt[23] consisting of a channel with a flat floor wall, while the upper surface has a circular arc bump. For the validation exercise conducted in this study the custom design of Inger and Gendt[23] was used, which employed a circular arc of 580 mm radius of curvature and 20 mm height. The flow approaching the bump is subsonic and there are no incoming standing waves. The schematic of the flow geometry and a representative mesh are shown in Fig. 1. The grid resolution close to the surface is very crucial for accuracy and systematic grid independency on the predictions is conducted. For the initial computation a 152x60 grid with clustering towards the walls is employed which resulted in y^+ values for the next to wall cell centers of the order of 175 with the $k-\omega$ model. In order to resolve the boundary layer more accurately the y^+ values for the next to wall cell centers should be of the order of 1. Hence the grid is refined to 182x160 with clustering near the wall which produced y^+ values of about 0.5. Fig. 2 shows the comparison of the predicted Mach number variation along the channel obtained with

the coarse and the fine mesh along with the experimental data of Inger and Gendt[23] which demonstrates substantial improvement due to higher mesh resolution. Further mesh refinement did not produce any significant improvement and the 182x160 mesh is used for subsequent computations.

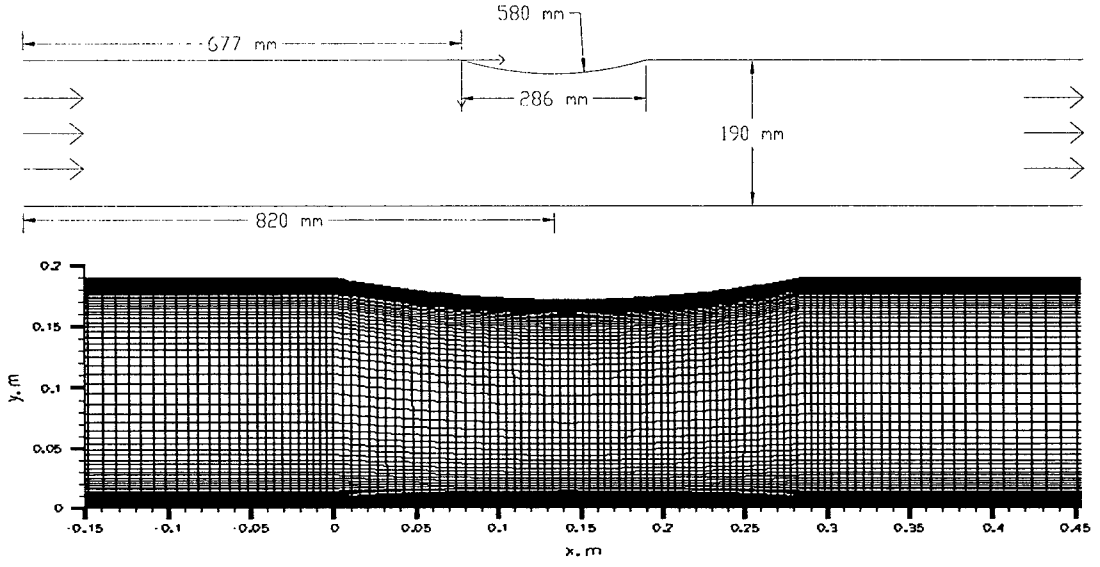

Figure 1. Schematic of the flow geometry and a magnified view of the representative meshing around the transonic bump.

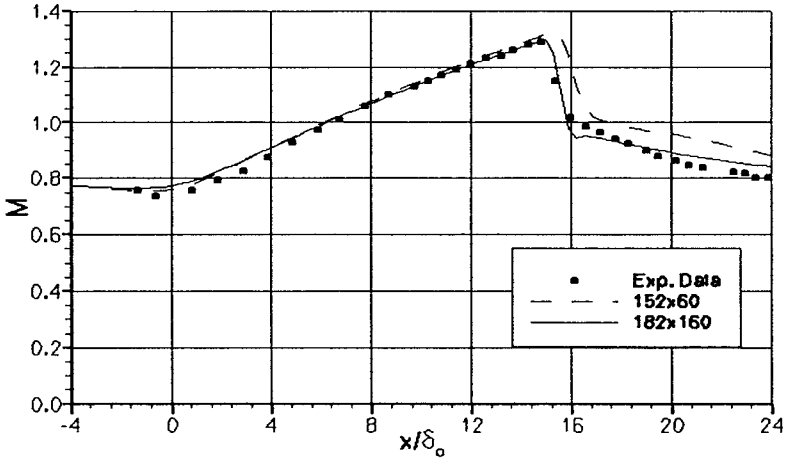

Figure 2. Improvement of the Mach number variation with grid

The computations are done using the FLUENT commercial flow solver. Following the experimental conditions[23], the stagnation pressure is taken as 140 kPa and the stagnation temperature is set at 310° K with a test flow Mach number of M_∞ = 0.73, having a Reynolds number based on model chord of $1.7x10^6$. The downstream/exit pressure is adjusted to approximate numerically the experimental shock location on the upper wall. This is essentially a trial and error exercise. Based on this exercise a back exit pressure of p/p_∞= 0.68 is specified in the computation. The floor and the bump on the upper surface are solid walls having no-slip condition imposed with

a constant temperature of 310° K. The experimental pressure measurements in the span-wise directions showed uniform C_p and hence the flow could be categorically termed a 2-D stream-wise flow.

To evaluate the performance of various turbulence models for the prediction of transonic flow ov

er the bump geometry mentioned above, calculations are done using 4 different turbulence models as implemented in the FLUENT code. These models are (*i*) the one-equation Spalart-Allmaras model (SAM), (*ii*) the two-equation $k-\varepsilon$ model (KEM), (*iii*) the two-equation $k-\omega$ model (KOM), and (*iv*) the Reynolds Stress Transport Model (RSM). Results and comparison with the experimental data are presented here.

The predicted Mach number variation along the channel at vertical locations outside of the boundary layer is plotted in Fig. 3 for the above mentioned models. The streamwise distance in this figure is normalized with δ_o, which is the boundary layer thickness at the beginning of the bump. The variation of the surface pressure coefficient along the bump surface, as predicted by the different turbulence models, is plotted in Fig. 4. The experimental data of Inger and Gendt[23] are also plotted in these figures for comparison and to assess the performance of the turbulence models.

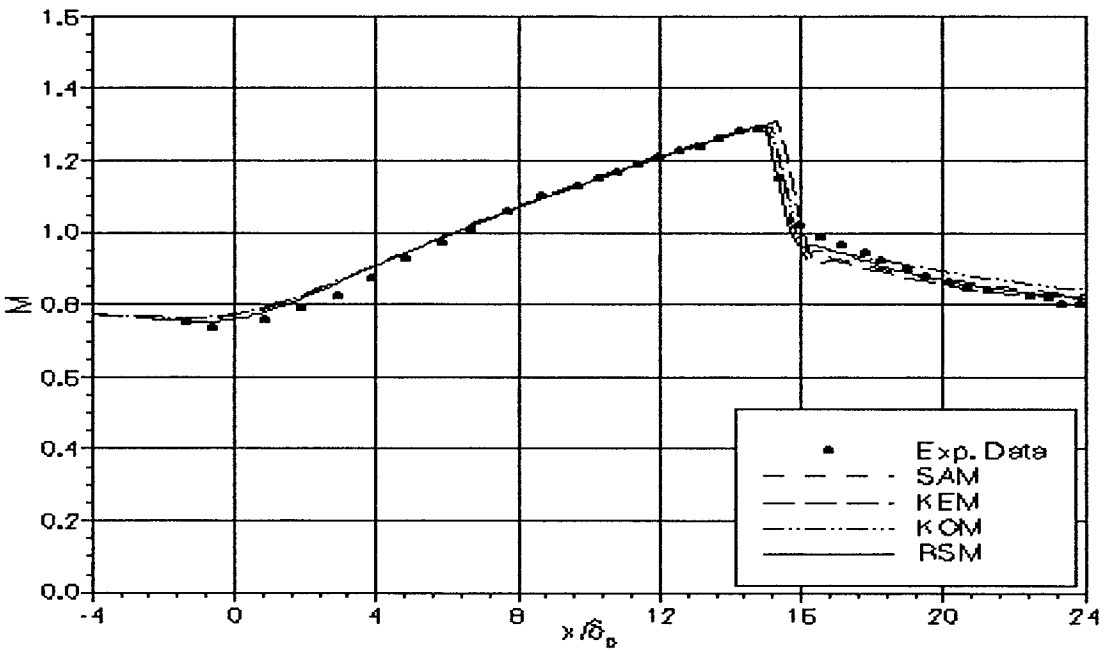

Figure 3. Local Mach Number Distribution (Smooth surface)

The bump extends from $x = 0$ to 0.286 m. As there is a surface discontinuity at $x = 0$, between the upstream flat surface and the leading edge of the circular arc bump (no smoothing), an overshoot in the pressure distribution is observed at the leading edge of the bump. This is followed by a rapid decrease in pressure on the bump surface which is terminated by a downstream shock after the mid chord of the bump. After the normal shock the total pressure decreases and the flow turns subsonic again.

All predictions before the shock are in good agreement with the experimental data for all models. The shock wave is located at about 70% chord length, with the local Mach number before the shock being 1.30. The largest streamwise gradient of the mean Mach number is seen near the crest of the bump. No shock induced separation is noted from the surface pressure measurements. All four turbulence models seem to show an overall good agreement with the experiment. The results from Figs. 3 and 4 indicate that the all of the turbulence models evaluated have captured the shock location and after-shock behavior reasonably well (slight delay in the shock position). However, on further introspection of the flow separation feature at the trailing edge of the bump and boundary layer analysis it is noticed that the RSM and KOM perform better than the other two models compared to the experimental data for the smooth surface. The ultimate objective of this study is to investigate the effect of surface roughness on the flow

development. Since the RSM consumes significantly more cpu time than the KOM while producing comparable accuracy, it is decided to use the KOM for further investigation of the surface roughness effects.

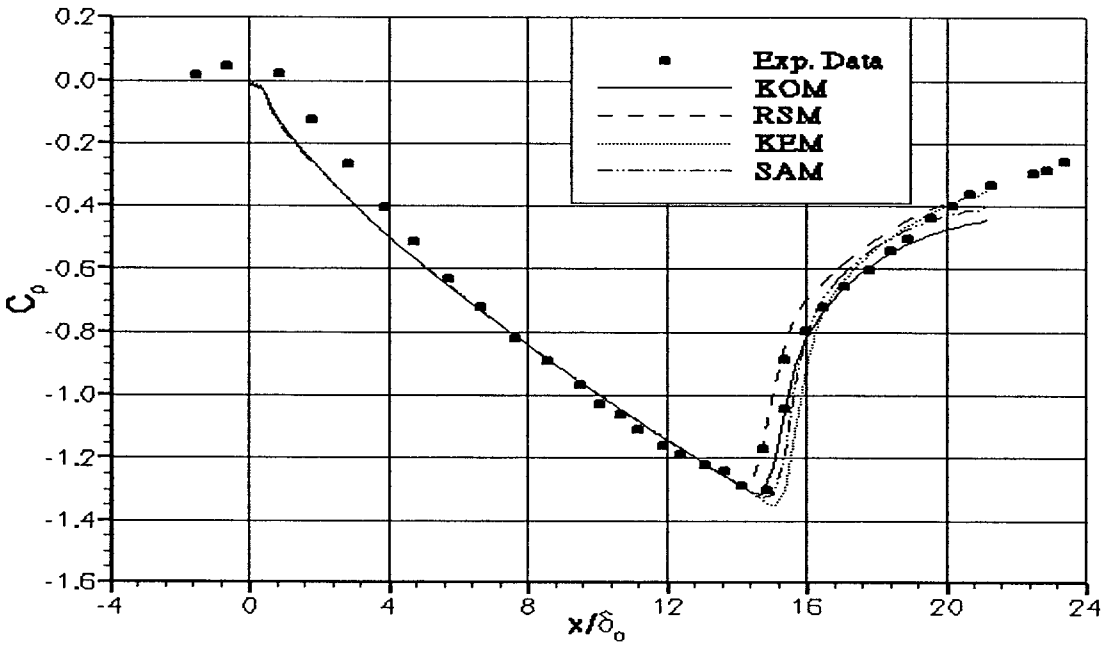

Figure 4. Wall Pressure Distribution (Smooth

Results and Discussion

Four different roughness heights covering the hydraulically smooth to fully rough regimes are investigated in the present study. Roughness heights of 50 μm, 250 μm, 580 μm (silicon carbide grit), and 1470 μm (cold iron grit) are used in the study. The last two roughness heights produce fully rough regimes. The roughness is assumed to be uniformly distributed sand grain roughness and is added over the whole bump domain.

Roughness increases the local boundary layer thickness and the interaction length. From the streamwise pressure distribution we observe that separation occurs with a reduction of pre-shock Mach number and spreading out of the shock interaction zone with increasing roughness height. The pressure gradient also decreases as the roughness becomes more severe indicating a less severe adverse pressure gradient due to the larger interaction length. Roughness drag effect enhances the momentum loss at the bottom of the boundary layer as well as the overall thickness of the layer which makes it more susceptible to separation.

Figs. 5 and 6 illustrate the predicted wall pressure distribution along with the experimental data for roughness heights of 580 μm and 1470 μm, respectively for validation of the turbulence model performance with roughness incorporated. It is noted that the wall pressure distribution is reasonably well predicted by the KOM except that the wall pressure is somewhat over-predicted after the shock. This over prediction/disparity could be due to the presence of the residual roughness effect which is predicted by theory and confirmed by experiments which are subjected to non-equilibrium effects in the boundary layer[24] or as a result of turbulence model limitations for the overall flowfield at transonic configurations. Furthermore, intrinsic variations to the CFD code such as optimizing the FAS multigrid parameters to obtain optimal sweep parameters such as relaxation factors, fixed and flexible cycle parametric investigation and other modifications to the turbulent compressible correlation corrections would enable significant improvement on simulation results. For instance, replacing Wilcox correlation for dilatation dissipation with either Sarkar or Zeman correlations[26]. Lack of full recovery is thought to be associated with the noninteractive downstream nonequilibrium relaxation of turbulent wall boundary layers and is under further study.

The contours of the Mach number, pressure, temperature, and turbulent kinetic energy in the flow domain are shown in Figs. 7-10 for the various surface roughness conditions used in this study. In these figures the formation and locations of the shock are clearly portrayed even though the effect of roughness variation is not easily discernible. As the surface roughness height increases the diminutive shift of the core shock upstream from $x = 0.22$ m to 0.2 m can be discerned with the curvature reduction. The stagnation pressure and density are constant outside

the boundary layer and upstream of the shock It is seen that upstream of the shock the contour lines are spaced much closer near the bump than near the top. This shows that the flow accelerates faster on the bump than on the top. Very close to the wall, viscous damping relegates the tangential velocity fluctuations, while kinematic blocking diminishes the typical fluctuations. Turbulence is briskly augmented by the production of turbulence kinetic energy due to the significant gradients in the mean velocity at the outer part of the near-wall region.

The exploded view of the streamline patterns near the trailing edge of the bump is shown in Fig. 11 where the formation of the recirculation bubble is clearly visible. The bubble size increases slightly with increasing roughness. The 50 μm roughness streamline plot shows no separation since this roughness height is smaller than the laminar sublayer thickness whereby no effects are seen due to this hydraulically smooth surface. If separation changes from trailing edge separation, to shock induced separation, the Mach number is termed critical peak Mach

The variation of the skin friction coefficient along the bump surface characterizing the near wall flow behavior is plotted in Fig. 12 for various roughness conditions. Also the surface pressure distribution is shown in Fig. 13 for various roughness conditions. The effect of roughness is visible in these figures where it is observed that the shock location moves upstream as the roughness increases. The smooth wall case has the least upstream influence and the wall with the largest roughness height has the most upstream influence. The surface pressure distributions show that an increasing roughness height results in a larger amount of upstream influence. The skin friction distribution along the surface direction reveals many flow features. The influence of the bump is felt at $x = 0$ where it grows rapidly and the friction increases. The skin friction increases rapidly as the boundary layer thins and when it reaches the shock location the pressure minimum is reached and then a strong adverse pressure gradient serves to separate the boundary layer for the given roughness heights. The skin friction coefficient decreases across the interaction as a result of the lower velocity gradient at the wall. A full boundary layer profile has a large velocity gradient near the wall and hence more skin friction compared to a less full profile. Since roughness decreases the fullness of the velocity profile, it should lead to lower skin friction values. However, rough surfaces are observed to have more skin friction values than a smooth surface, due to the effect of increased surface area due to the individual roughness elements and also a smooth surface has no profile drag while roughness elements cause small amounts of profile drag. The relative importance of these two opposing effects resolves the final skin friction level on a given surface. For the smooth bump the c_f never becomes negative indicating no separation, but it is nevertheless critical. Reattachment transpires downstream (not shown in figure). It is also noticed that the value of c_f at a particular streamwise location increases significantly with roughness before the shock while the skin friction at a fixed location dwindles with roughness after the shock. On the other hand, the wall pressure increases with roughness at a fixed streamwise location.

The Mach number variation along the channel outside of the boundary layer is shown in Fig. 14 for increasing roughness. The upstream shifting of the shock is also evident from this figure. This increased upstream influence is due to the increased subsonic portion of the boundary layer, which lets pressure information to be transmitted further upstream.

The surface roughness also affects the pressure drag and viscous drag. At transonic speeds there are pockets of supersonic flow terminated by shock waves. Shock waves and shock-induced boundary layer separation are a consistent source of drag at these speeds. Higher pressure generates more pressure drag. Pressure drag comes from the eddying motions that are set up in the fluid by the passage of the body. This drag is linked with the formation of a wake turbulent transport of momentum and is very effective at replenishing the near-wall momentum. So when a turbulent boundary layer enters a region of adverse pressure gradient, it can endure for a longer distance without separating because the momentum near the wall is higher to begin with, and it is frequently being replenished by turbulent mixing. The coefficients of pressure, viscous and total drag as a function of the roughness is plotted in Fig. 15. In general the pressure drag coefficient decreases slightly while the viscous drag coefficient increases slightly with increasing roughness thus counterbalancing each other resulting in very slight change total drag coefficient. Pressure drag increases with flow separation however streamlining reduces pressure drag.

Roughness seems to prolong the interaction region and diminishes the fullness of the boundary layer profile. These two effects have differing affinities, since an extended interaction region spreads out the pressure rise, reducing the severity of the adverse pressure gradient and reducing the likelihood of separation, whereas a less full boundary layer is more vulnerable to separation.

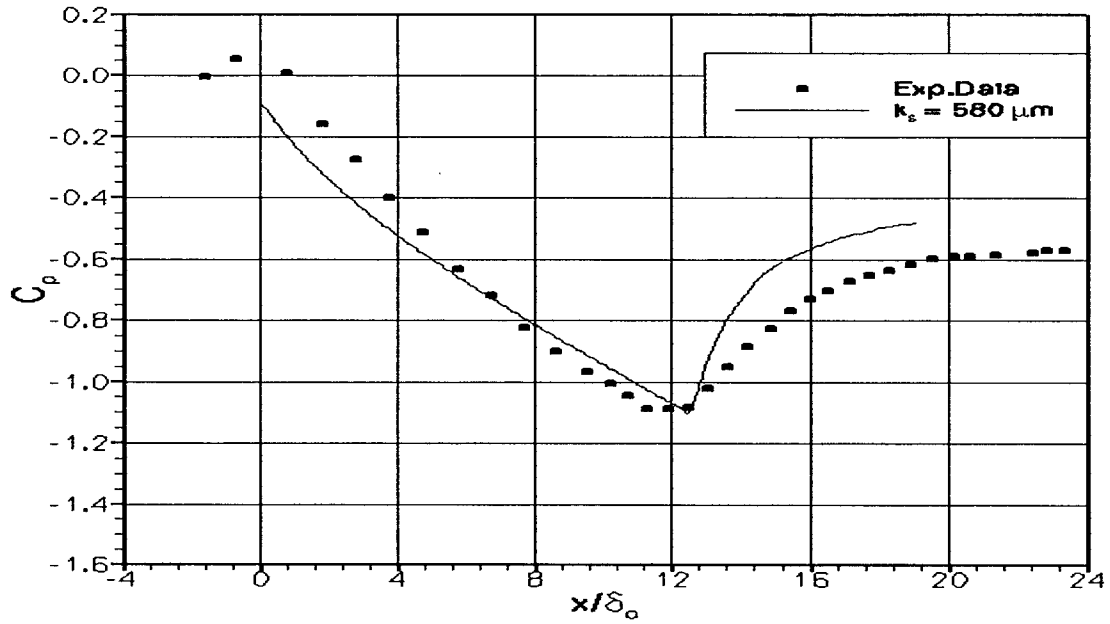

Figure 5. Wall Pressure Distribution.

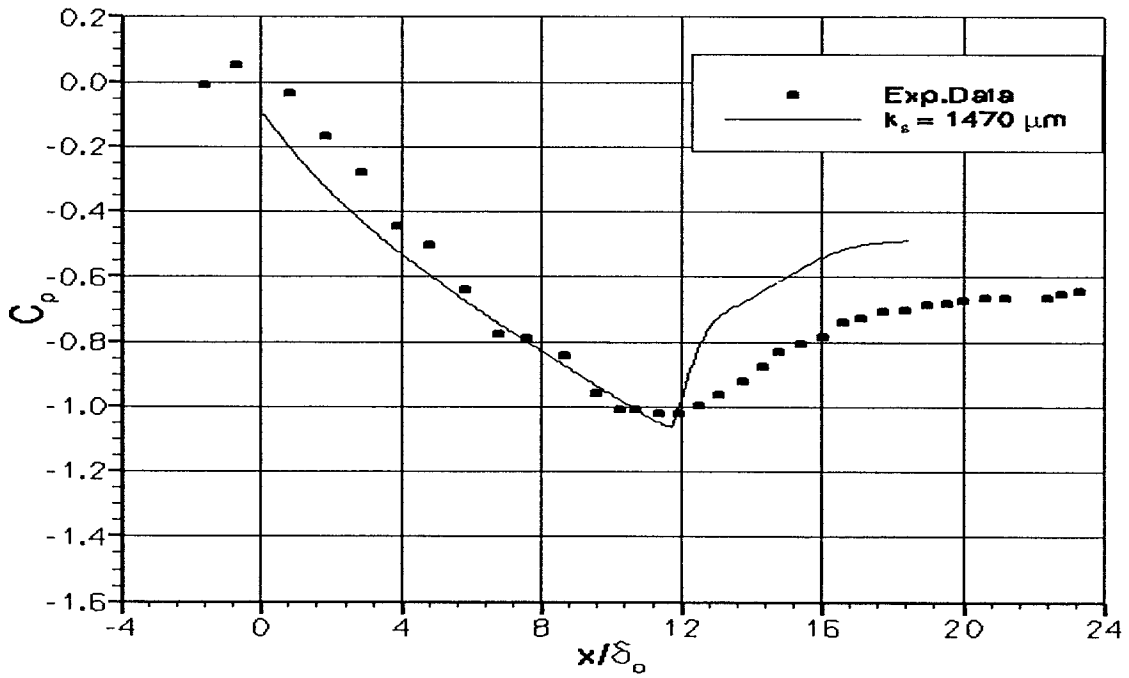

Figure 6. Wall Pressure

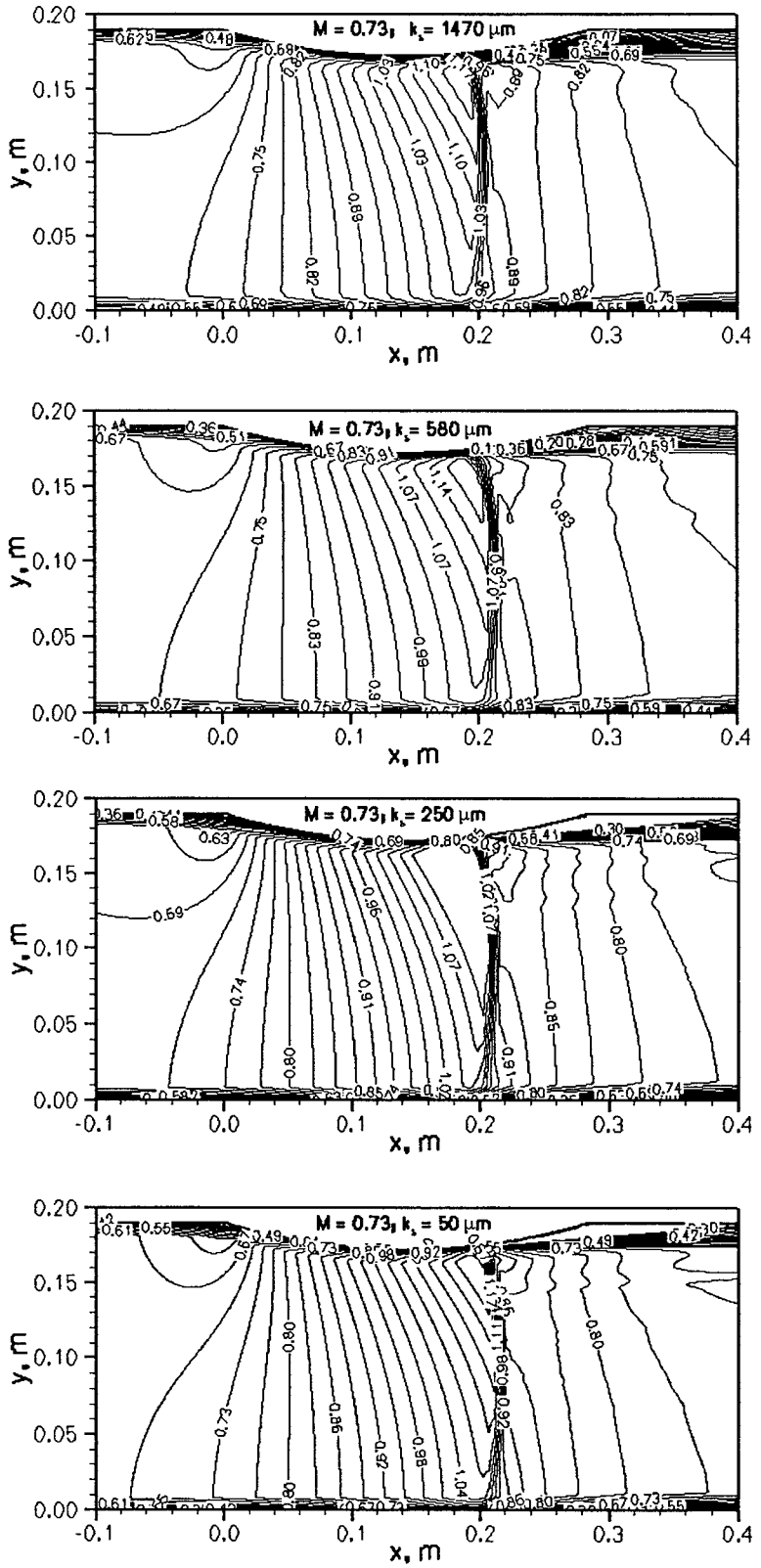

Figure 7. Mach Contours for surface roughness height of (1470, 580, 250, 50 μm).

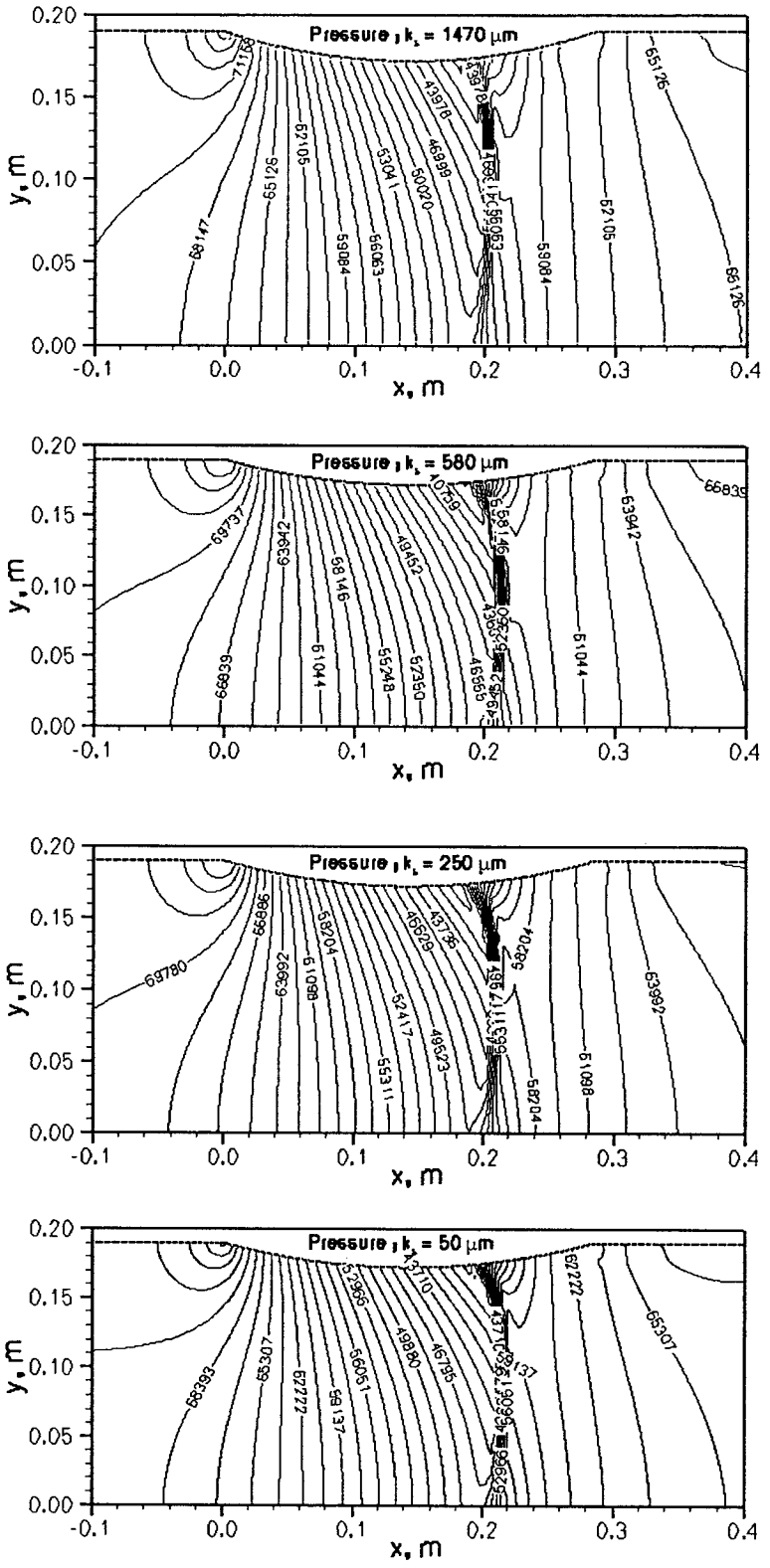

Figure 8: Pressure Contours for surface roughness height of (1470, 580, 250, 50 μm)

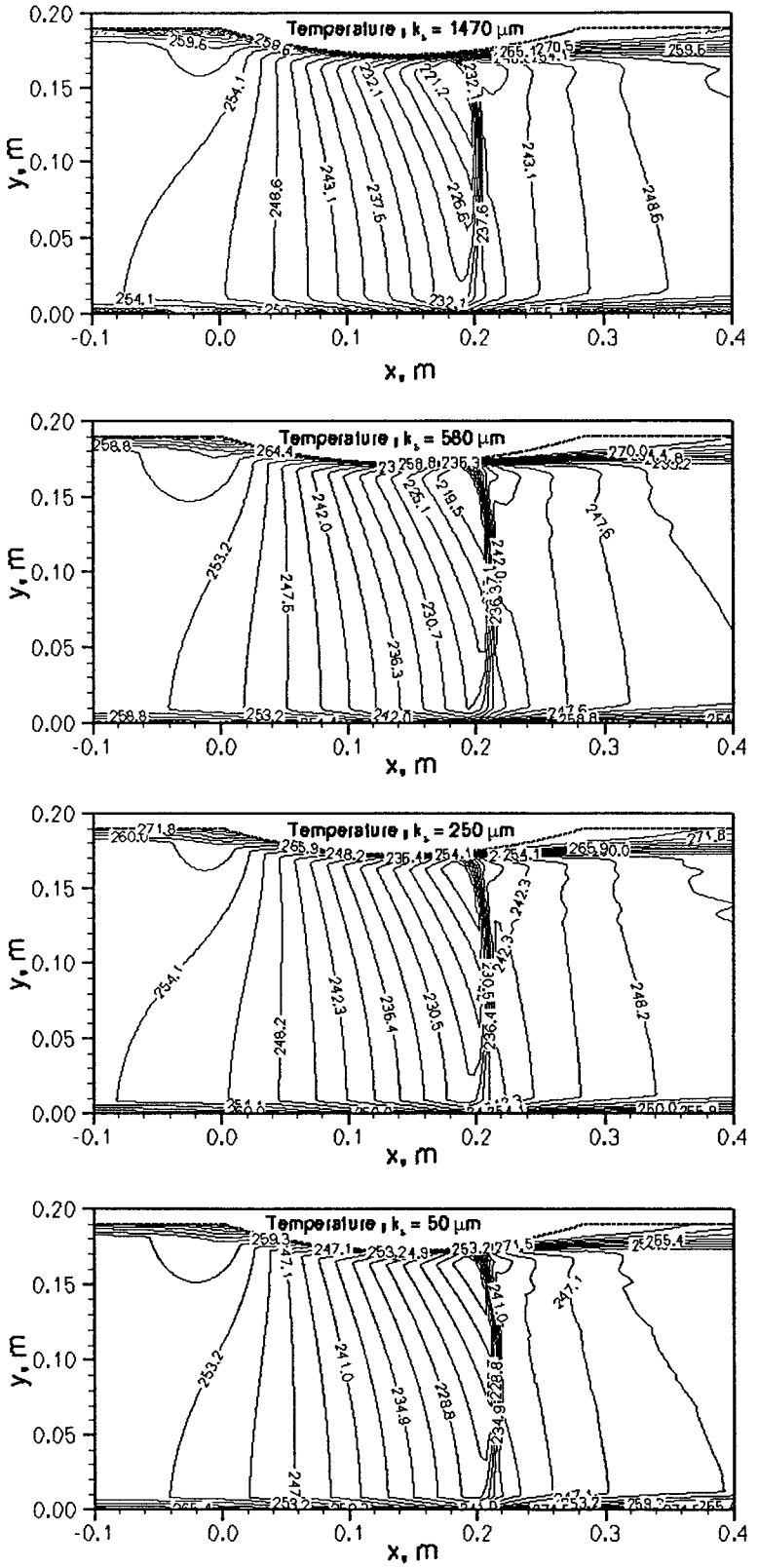

Figure 9. Temperature Contours for surface roughness height of (1470, 580, 250, 50 μm)

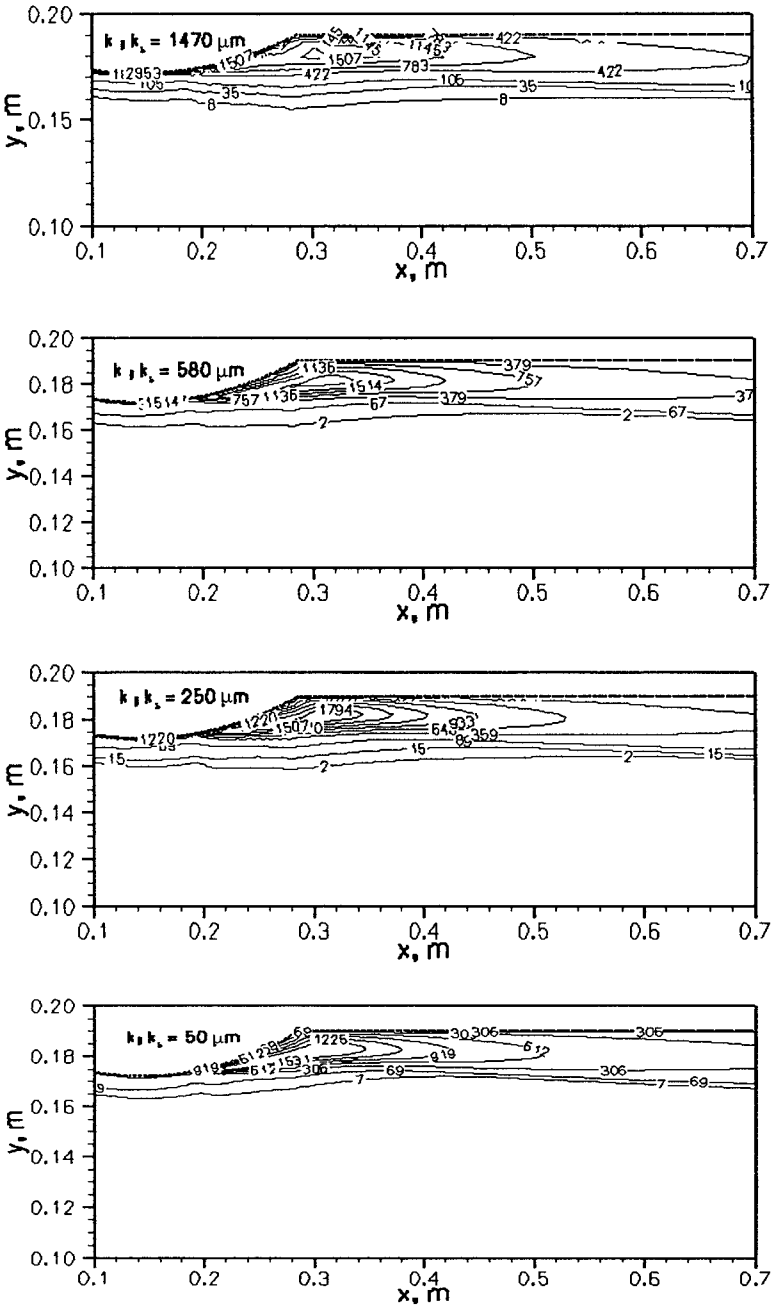

Figure 10. Contours of turbulent kinetic energy for surface roughness height of (1470, 580, 250, 50 μm)

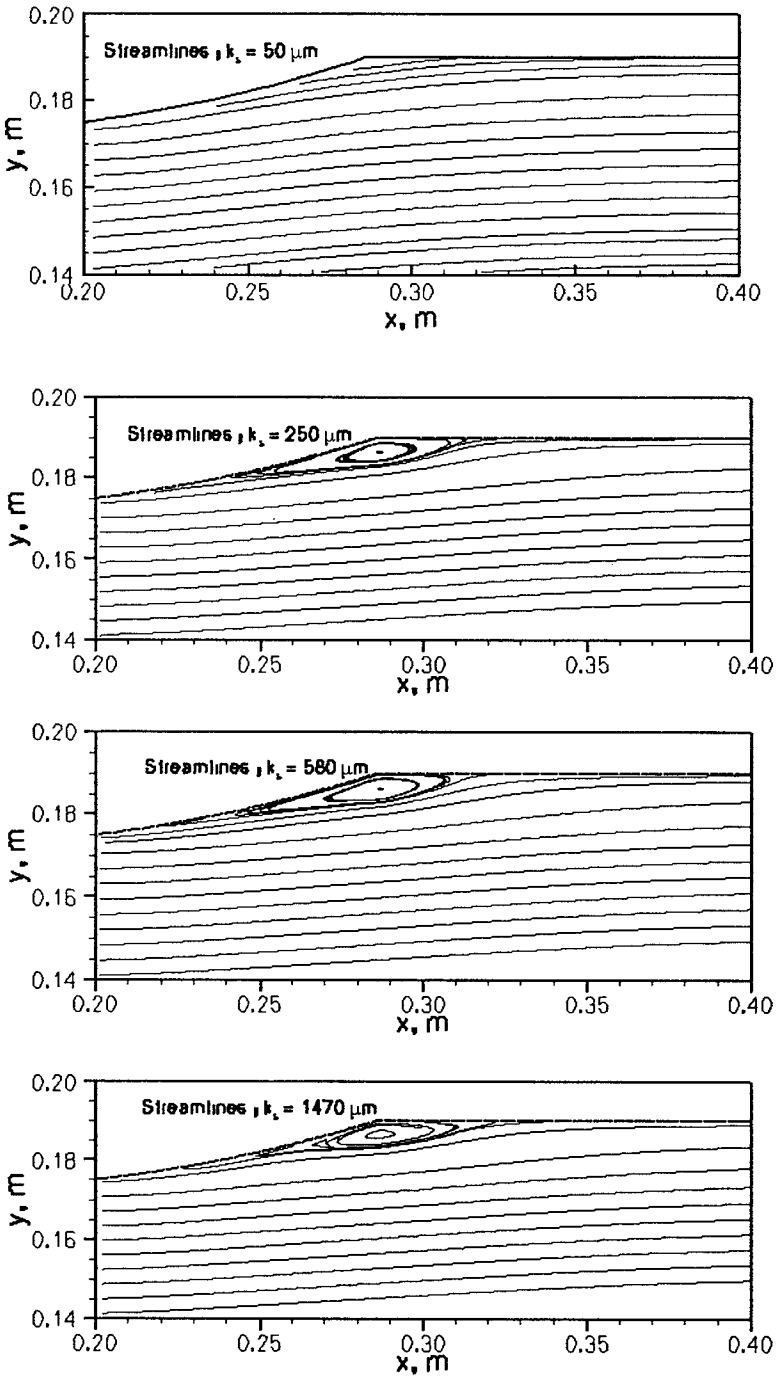

Figure 11. Stream-Lines for surface roughness height of (1470, 580, 250, 50 μm)

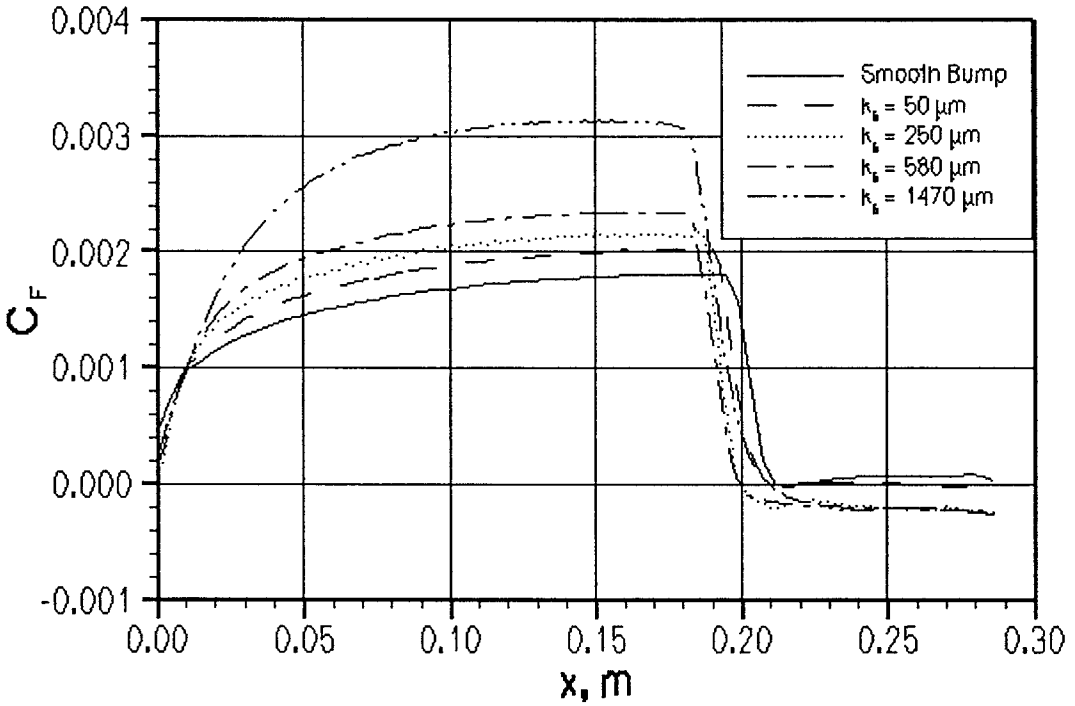

Figure 12. Skin Friction Co-efficient Distribution

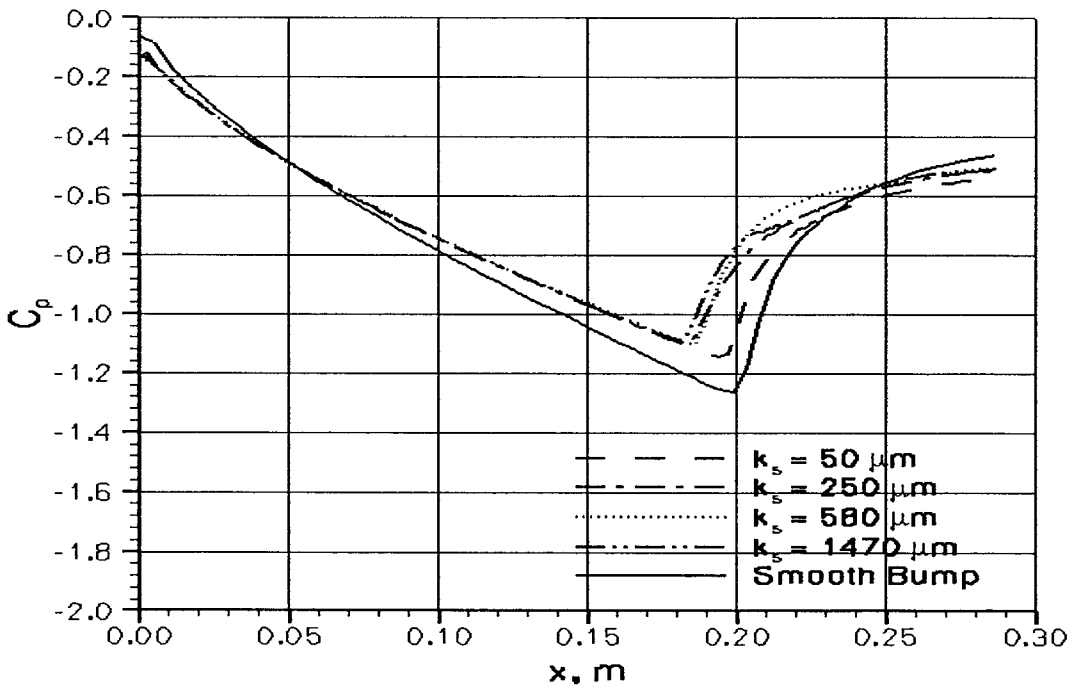

Figure 13. Wall Pressure Distribution

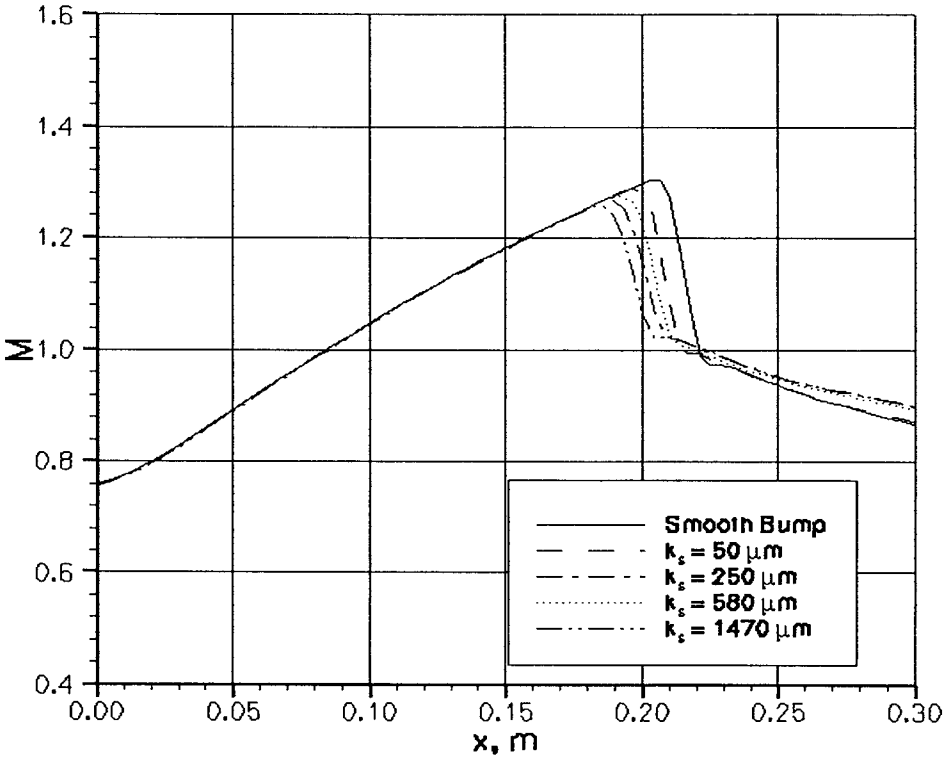

Figure 14. Mach Number Distribution

Conclusion

Numerical simulations of the Inger and Gendt[23] roughness study on transonic flow over a circular arc bump are presented. The computations are done using the FLUENT commercial CFD code. The performance of several turbulence models, as implemented in the FLUENT code, is evaluated for smooth bump surface against experimental data[23]. The $k-\omega$ turbulence model predicts the shock location and surface pressure variation reasonably well when handled with the same constraints as the other turbulence models and is chosen to further investigate the flow physics for rough surfaces. Four different sand grain roughness heights ranging from the hydraulically smooth to fully rough configuration are investigated. The contour plots of the field variables give an overview into the flow physics and also depict the effect of shock boundary layer interaction. This study corroborates the fact that sand grain roughness considerably modifies the flow-field of a transonic shock- boundary layer interaction region as noted in the Mach number, wall pressure and skin friction coefficient distributions, with the upstream movement of shock as the roughness increases clearly seen proliferating. Hence, with the variation of roughness height, the incoming boundary layers grow thicker than the smooth wall profile and enhance the upstream influence and augments separation with increasing roughness. It is concluded that turbulence model performance is limited here by the prerequisite to capture the rapid rise and fall of turbulence levels in the separated shear layer when roughness is employed. To define more realistic turbulence models, precise quantitative measurements of the turbulence properties are needed. The accuracy of turbulence models relies on the ability of the model to reproduce the fundamental mechanisms of turbulence production and dissipation through the interaction. This requires the model to be calibrated and tested against experimental data.

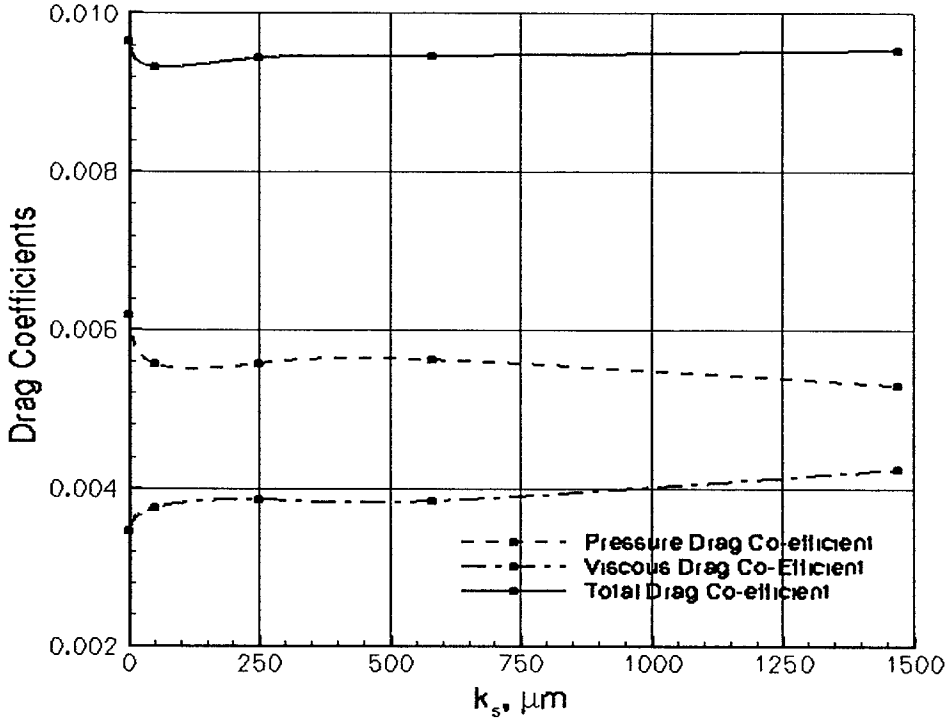

Figure 15. Variation of Drag Coefficients with surface

Acknowledgement

Financial support for this work was provided by a grant from the Air Force Office of Scientific Research F49620-02-1-0365.

References

[1]Liepmann, H. W., "The Interaction between Boundary Layer and Shock Waves in Transonic Flows," *Journal of Aerospace Sciences,* Vol. 13 (12), 1946, pp. 623-638.

[2]Green, J. E., "Interactions between Shock Waves and Turbulent Boundary Layers," *Progress in Aerospace Sciences* 11, 1970, pp. 235-340.

[3]So, R. M. C. and Mellor, G. L., "Experiment on Convex Curvature Effects in Turbulent Boundary Layers," *Journal of Fluid Mechanics*, Vol. 60, 1973, pp. 43-62.

[4]Gillis, J. C. and Johnston, J. P., "Turbulent Boundary Layer Flow and Structure on a Convex Wall and its Redevelopment on a Flat Wall," *Journal of Fluid Mechanics*, Vol. 135, 1983, pp. 123-153.

[5]Hoffmann, P. H., Muck, K. C., and Bradshaw, P., "The Effect of Concave Surface Curvature on Turbulent Boundary Layers," *Journal of Fluid Mechanics*, Vol. 161, 1985, pp. 371-403.

[6]Bradshaw, P. and Galea, P. V., "Step Induced Separation of a Turbulent Boundary Layer in Incompressible Flow," *Journal of Fluid Mechanics*, Vol. 27, 1967, pp. 111-130.

[7]Samuel, A. E. and Joubert, P. N., "A Boundary Layer Developing in an Increasingly Adverse Pressure Gradient," *Journal of Fluid Mechanics*, Vol. 66, 1974, pp. 481-505.

[8]Smits, A. J., Eaton, J., and Bradshaw, P., "The Response of a Turbulent Boundary Layer to Lateral Divergence," *Journal of Fluid Mechanics*, Vol. 94, 1979, pp. 243-268.

[9]Smits, A. J. and Wood, D. H., "The Response of Turbulent Boundary Layer to Sudden Perturbations," *Annual Review of Fluid Mechanics*, Vol. 17, 1985, pp. 321-358.

[10]Delery, J. M., "Experimental Investigation of Turbulence Properties in Transonic Shock / Boundary Layer Interactions," *AIAA Journal*, Vol. 21, 1982, pp. 180-185.

[11]Johnson, D. A., Horstman, C. C., and Bachalo, W. D., "Comparison between Experiment and Prediction for a Transonic Turbulent Separated Flow," *AIAA Journal*, Vol. 20, 1982, pp. 737-744.

[12]Bachalo, W. D. and Johnson, D. A., "An Investigation of Transonic Turbulent Boundary Layer Separation Generated on an Axisymmetric Flow Model," *AIAA 12th Fluid and Plasma Dynamics Conference*, July 23-25, 1979.

[13]Bachalo, W. D. and Johnson, D. A., "Transonic, Turbulent Boundary Layer Separation Generated on an Axi-symmetric Flow Model," *AIAA journal*, Vol. 24, 1986, pp. 437-443.

[14]Liu, X. and Squire, L. C., "Interaction on Curved Surface at Transonic Speed," *Turbulent Shear Layer-Shock Wave Interactions*, Springer, Berlin, 1986, pp. 93-104.

[15]Liu, X. and Squire, L. C., "An Investigation of Shock / Boundary Layer Interactions on Curved Surfaces at Transonic Speeds," *Journal of Fluid Mechanics*, Vol. 187, 1988, pp. 467-486.

[16]Johnson, D. A., "Transonic Separated Flow Predictions with an Eddy Viscosity/ Reynolds Stress Closure Model," *AIAA Journal*, Vol. 25, 1985, pp. 252–259.

[17]Sahu, J. and Danberg, J. E., "Navier Stokes Computations of Transonic Flows with a Two-Equation Turbulence Model," *AIAA journal,* Vol. 24, 1985, pp. 1744-1751.

[18]Wilcox, D. C., "Turbulence Modeling for CFD," DCW Industries Inc., Ed 2, 2002.

[19]Barakos, G. and Drikakis, D., "Assessment of Various Low-Reynolds Number Turbulence Models in Shock Boundary Layer Interaction," *Computer Methods in Applied Mechanics and Engineering,* 160, 1998, pp. 155-174.

[20]Sandham, N. D., Yao, Y. F., and Lawal, A. A., "Large Eddy Simulation of Transonic Turbulent Flow over a Bump," *International Journal of Heat and Fluid Flow*, 24, 2003, pp. 584-595.

[21]Patel, V. C., Chon, J. T., and Yoon, J. Y., "Turbulent Flow in a Channel with a Wavy Wall," *ASME Journal of Fluids Engineering*, Vol. 113, pp. 579-586.

[22]Nakagawa, S. and Hanratty, T. J., "Influence of a Wavy Boundary on Turbulence. II. Intermediate Roughened and Hydraulically Smooth Surfaces," *Experiments in Fluids,* Vol. 35, 2003, pp. 437-447.

[23]Inger, G. R. and Gendt, C., "An Experimental Study of Transonic Shock/Boundary Layer Interaction on a Roughened Surface," *AIAA Aerospace Sciences Meeting and Exhibit*, 35th, Reno, NV, Jan 6-9, 1997.

[24]Babinsky, H. and Inger, G. R., "The Effect of Surface Roughness on Shock Wave/Turbulent Boundary Layer Interactions," *AIAA Paper* 2000-3918, 2000.

[25]Babinsky, H., Inger, G. R., and McConnell, A., D., "A Basic Experimental/Theoretical study of Rough Wall Turbulent Shock/Boundary Layer Interactions," *Proceedings of the 22nd International Symposium on Shock Waves :* Imperial College, London, UK, July 18th to 23rd 1999.

[26]Goodheart, K. A., Dykas, S., and Schnerr, G. H., "Numerical Insights into the Solution of Transonic Flow Test Cases using the Wilcox $k-\omega$, EASM, and SST Models," *41st Aerospace Sciences Meeting and Exhibit,* Reno, Nevada, Jan. 6-9, 2003.

Proceedings of FEDSM2005
ASME Fluids Engineering Summer Conference
June 19-23, 2005 Houston, TX, USA

FEDSM2005-77443

Analysis of supersonic turbulent boundary layers over rough surfaces using the k-omega and stress-omega models

Guanghong Guo and M.A.R. Sharif
Aerospace Engineering and Mechanics Department
The University of Alabama, Tuscaloosa, Alabama 870280, USA

ABSTRACT

In this study, the influence of surface roughness in the prediction of the mean flow and turbulent properties of a high-speed supersonic (M=2.9, Re/m=2.0e7) turbulent boundary layer flow over a flat plate is performed using the $k-\omega$ and the stress-ω models. Six wall topologies, including a smooth and five rough surfaces consisting of three random sand-grain plates and two uniformly machined plates were tested. Experimental data are available for these configurations. It is observed that, for smooth surface, both $k-\omega$ and stress-ω models perform remarkably well in predicting the mean flow and turbulent quantities in supersonic flow. For rough surfaces, both models matched the experimental data profiles fairly well for lower values of the roughness height. Overall, the $k-\omega$ model performed better than the stress$-\omega$ model. The stress$-\omega$ model did not show any strong advantages to make up for the extra computational cost associated with a Reynolds stress model. The simulation results indicated that the prescription for the surface boundary conditions for ω in both models, especially for the stress$-\omega$ model, need to be refined encountering high roughness numbers and reconsidered to include the geometric factor.

INTRODUCTION

The study of supersonic boundary layer structure has been very important for design and operation of high-speed aircraft, missiles, and reentry vehicles. The interactions between the air and the object surface, such as drag, lift and heat transfer, happen in the boundary layer. All these systems experience surface roughness through wear and tear because of operation. Thus, accurate quantification of the effects of roughness on the boundary layer above the system surface is important for practical applications.

Analysis of both low and high-speed turbulent flows over smooth surfaces has been performed extensively in the past. The experimental data has been well correlated for smooth equilibrium boundary layer flow over flat plates, and the numerical analysis for low and high-Reynolds-number flow over smooth walls is well documented and developed. The zero-equation (mixing length for example), one-equation (Spalart-Almaras model for example) and two-equation $k-\varepsilon$ and $k-\omega$ family of turbulence models have been quite successful in predicting the turbulent boundary layer over smooth flat surfaces. However, for nonequilibrium boundary layers with adverse pressure gradients, the performance of these models is not as satisfactory especially in the separated region. The Reynolds stress transport models with either a transport equation for ε representing the length scale or a transport equation for ω representing the length scale (in which case the model is referred to as the stress$-\omega$ model) have been used with some success for separated flows. Another major weakness of the turbulence models is the surface roughness issue and incorporating the surface roughness effects in the model. Typically, the wall function along with a shift of the near wall velocity profile by an amount denoted as ΔB is used for incorporating the roughness effects. However, "the uncertainty in the dependence of ΔB on the size and type of roughness and also in the effective location of the fictitious wall from which the distance is measured," [1] makes this approach less reliable.

For low-speed flow over rough wall, the mean and turbulent flow properties have been studied thoroughly by experiment and the turbulent models have been demonstrated to perform well for both modified two-layer $k-\varepsilon$ model and $k-\omega$ model. The widely used $k-\varepsilon$ model is unable to describe the near-wall zone. The two-layer approach [2] seems

to have the ability to fix that flaw. It consists of patching together the $k-\varepsilon$ and $k-l$ models, with modified l and k boundary conditions for roughness concern. The rough wall version of the $k-\omega$ model [3] has the similar feature of incorporating roughness into the ω boundary condition, and it has been shown to perform well even in flow with separations [4].

However, for high-speed flow over rough wall with compressible boundary layer, there are no accordant turbulent models. Even the experimental data are not widely available as the smooth surface cases. Fan and Bowersox [5] studied three low-speed rough-wall mixing-length models, namely van Driest [6], Cebeci-Chang [7] and Kragstad [8], by extending them to high-speed flows. The simulation results agree well with the experimental data of Latin and Bowersox [9]. Their work demonstrated that the three simple turbulence models have the essential physics necessary to accurately predict supersonic turbulent flow over a rough flat plate.

By using perturbation methods, Wilcox [10] has shown that the $k-\omega$ model can efficiently capture the compressible law of the wall. Sharing the same boundary conditions as $k-\omega$ model for smooth surface, the stress-ω model also performs very well in the compressible boundary layer [10]. The main advantage of ω-based models over ε-based model is the way in which ε and ω are specified on the boundary surface. For ε-based models, ε is defined as $\partial\varepsilon/\partial y|_{y=0}=0$ on the boundary. Even though this Neumann boundary condition has been shown to be robust, it is completely *ad hoc* without theoretical or experimental justification. For ω-based models, empirical equations are prescribed [10] with the value of roughness height incorporated. This formulation for ω on the rough boundary, however, is derived and validated based on the incompressible sublayer flow over rough surfaces. Its validity for compressible flow is yet to be examined.

So the objective of this paper is to evaluate the performance of the $k-\omega$ and the stress$-\omega$ models for the calculation of supersonic compressible turbulent boundary layer with wall roughness and identify the specific weaknesses to guide the development of improved models.

NOMENCLATURE

C	Constant in the logarithmic law of wall region
C_f	Skin friction coefficient
k	Roughness height, thermal conductivity
k_s	Equivalent roughness height
k^+	Roughness Reynolds number
M	Mach number
p	Pressure
P_r	Prandtl number
Re	Reynolds number
T	Temperature
u,v	x and y velocity components, respectively
u^*	Friction velocity
u^+	u/u^*

GREEK SYMBOLS

δ	Boundary layer thickness
μ	Dynamic viscosity
ν	Kinematic viscosity
θ	Momentum thickness
ρ	Fluid density
τ	Shear stress
Δu	Velocity shift

SUBSCRIPT

i,j	Grid node in x and y direction, Einstein index
w	Wall
t	Turbulent
e	Boundary layer edge

SUPSCRIPT

`	Reynolds averaging fluctuating components
``	Favre averaging fluctuating components
–	Reynolds averaged components
~	Favre averaged components

GOVERING EQUATIONS

The mean conservation equations of mass, momentum, and energy for the compressible turbulent flow of an ideal gas are assumed to be the unsteady, compressible, Favre-averaged Navier-Stokes (FANS) equations [8]:

$$\bar{\rho}_{,t}+(\bar{\rho}\tilde{u}_i)_{,i}=0$$

$$(\bar{\rho}\tilde{u}_i)_{,t}+(\bar{\rho}\tilde{u}_j\tilde{u}_i)_{,j}=-P_{,i}+(\bar{t}_{ji}+\bar{\rho}\tau_{ji})_{,j}$$

$$(\bar{\rho}\tilde{E})_{,t}+(\bar{\rho}\tilde{u}_j\tilde{H})_{,j}=(-q_{Lj}-q_{Tj}+\overline{t_{ji}u_i^{"}}-\frac{1}{2}\overline{\rho u_j^{"}u_i^{"}u_i^{"}})_{,j}+(\tilde{u}_i\bar{t}_{ij}+\bar{\rho}\tilde{u}_i\tau_{ij})_{,j}$$

where $(\cdot)_{,*}$ indicates a derivative with respect to time or the spatial coordinate x_i. Furthermore, $\tilde{E}=\tilde{e}+\frac{1}{2}\tilde{u}_i\tilde{u}_i+K$ is the specific total energy, $\tilde{H}=h+\frac{1}{2}\tilde{u}_i\tilde{u}_i+K$ is the specific total enthalpy, $\bar{t}_{ji}=2\bar{\mu}\tilde{S}_{ik}+\bar{\lambda}\tilde{S}_{jj}\delta_{ik}$ are the components of the shear-stress tensor where by Stokes hypothesis $\lambda=-\frac{2}{3}\mu$, $S_{ik}=\frac{1}{2}(\tilde{u}_{i,k}+\tilde{u}_{k,i})$ are the components of the strain-rate tensor, $q_{Lj}=-\kappa T_{,j}$ is the convective heat flux, $q_{Tj}=\overline{\rho u_j^{"}h^{"}}$ is the turbulent heat flux, $\overline{t_{ji}u_i^{"}}$ is the molecular diffusion and

$\frac{1}{2}\overline{\rho u_j'' u_i'' u_i''}$ is the turbulent transport, $K = \tau_{ii}/2$ is the turbulent kinetic energy, and $\tau_{ij} = -\overline{\rho u_i'' u_j''}$ is the Favre-averaged Reynolds-stress tensor.

In addition to the turbulence models, an equation of state must be specified for system closure. The perfect gas equation of state used is $P = \overline{\rho}\widetilde{RT}$.

The documentation for the $k-\omega$ and the stress$-\omega$ models are available in [8] and is, therefore, not repeated here.

BOUNDARY CONDITIONS

The inflow, freestream and wall boundary conditions were needed to obtain a unique solution for the compressible Navier-Stokes equations. The freestream flow conditions were based on the Pitot pressure measurements [9] for the six flow models (described in the next section). The uniform inflow boundary condition is starting at the wind tunnel nozzle throat. Along with the usual no-slip boundary condition, the Dirichlet type condtion for temperature was used, where the temperature was fixed at the experimental values.

In the $k-\omega$ model, the boundary condition for ω is:

$$\omega|_{y=0} = (u_\tau^2/\nu)S_R; \qquad k_s^+ = u_\tau k_s/\nu$$

$$S_R = \begin{cases} (50/k_s^+)^2, & k_s^+ < 25 \\ 100/k_s^+ & k_s^+ \geq 25 \end{cases}$$

In stress-omega model, the resulting correlations are a little different from those appropriate for the $k-w$ model:

$$S_R = \begin{cases} (50/k_s^+)^2, & k_s^+ < 25 \\ 500/(k_s^+)^{3/2} & k_s^+ \geq 25 \end{cases}$$

NUMERICAL SOLVER

The numerical solver used for this study is GASP which is a commercial CFD flow solver developed by AeroSoft, Inc. It solves the integral form of the time-dependent Reynolds-Averaged Navier-Stokes (RANS) equations in three dimensions. GASP has been demonstrated to be a mature solver with documented validations for all the turbulence models incorporated in its solution algorithm including the $k-\omega$ model and stress-ω model [11].

TEST CONDITIONS

The experimental configuration of Latin and Bowersox [9] was used as the test bed for the present simulations, where six different roughness floor sections were studied. The experimental conditions, along with the Mach number and temperature, listed in Table 1, were used to generate the freestream, inflow and wall boundary conditions for the present predictions.

Table 1. Summary of Experimental Roughness Data

Model	k_s^+	T_w	M_∞	δ	θ	C_f
		(K)		(mm)	(mm)	
Smooth	0	276	2.75	12.4	0.80	0.0016
2D	289	274	2.73	16.8	1.32	0.0038
3D	241	273	2.73	15.8	1.29	0.0037
80 Grit	104	273	2.73	14.7	1.11	0.0030
36 Grit	395	273	2.72	18.0	1.43	0.0040
20 Grit	571	273	2.70	17.7	1.45	0.0041

One of the six models was a smooth plate. Three models were sand-grain roughened plates, where Varathane brand 80, 36, and 20 grit flooring sandpaper was adhered to three aluminum flat plates. The last two models were uniformly machined plates consisting of two-dimensional rectangular lateral grooves and three-dimensional model cubic pillars, where the wavelength of the roughness elements was 2.18 mm and roughness height was 0.559 mm for both.

RESULTS AND DISCUSSION

A two-dimensional grid was used for the computation. The simulation started at the x-location where the roughness began. The inflow velocity and temperature profiles were constructed by calculating over a flat plate until the boundary layer thickness matched that of experimental data ($\delta = 5$). The grid dimension was 101 x 81 and was decided upon after a grid-convergence study. The rough plate was 1.0 meter in length, the mesh extended to a height of 0.06 meters. Grid points were clustered to the wall in order to resolve the laminar sublayer. The first point off the wall yields a value y^+ less than 1 for all the models, as required by GASP for near wall boundary layer calculations.

The predicted boundary layer height, momentum thickness and skin friction coefficient at a distance of 54 cm from the beginning of the rough plate for all six plates predicted by the two turbulence models are listed in Table 2. From an examination of the numerical results, it can be seen that for the $k-\omega$ model with increasing roughness height, the boundary layer thickness increased according to additional turbulence mixing and entrainment of freestream fluid, as did the experimental data listed in Table 1. For the stress$-\omega$ model, it gave smaller boundary layer thickness for 36 grit plate and 20 grit plate even though their roughness is higher. This means that the ω boundary condition in stress$-\omega$ model may not capture the underlying physics for the compressible boundary layer flow with roughness. The predicted results of stress$-\omega$ model are less than the ones of $k-\omega$ model, and compared with the experimental data, the simulation of $k-\omega$ model matches better than stress$-\omega$ model.

Representative numerical velocity profiles for all six plates are plotted in Fig. 1. As the results indicate, the two models produced similar profiles, and under-predicted the value of u/u_e. Considering the measurement uncertainty, they were still in good agreement with the experimental data. The smaller roughness heights gave better prediction results than the larger ones. Shown in Fig. 2 are the velocity profiles for all six plates plotted with defect law [1, 12, 13] scaling. The collapsing of the defect law profiles was the expected result based on the low-speed database [1, 12, 13] and the high speed data of Latin and Bowersox [14]. The $k-\omega$ model and the stress$-\omega$

model predicted similar velocity defect profiles. They both under-predicted the velocity defect.

Fig. 3 shows the numerically predicted Van Driest velocity profiles for the six plate models using both $k-\omega$ model and stress$-\omega$ models. The match between the smooth plate Pitot and LDV, the logarithmic "law of the wall", and the model predictions is considered excellent. For the rough surface plates, the turbulence models under-predict the downward velocity shift, $\frac{\Delta u}{u^*}$ attributed to the numerically predicted friction velocity values. The numerically predicted friction velocity values were under predicted by as much as 15%, indicating the method used to numerically determine the skin friction and friction velocity for the turbulence models may require refinement. As roughness height increases, the stress$-\omega$ model gave very different velocity profile through the boundary layer, especially in the sublayer, showing that the ω boundary condition in stress$-\omega$ model is not performing satisfactorily with high values of k_s.

Table 2. Summary of Numerical Roughness Data

	δ	θ	C_f
Model	(mm)	(mm)	
Smooth, $k-w$	10.77	0.75	0.00155
Smooth, stress$-\omega$	10.41	0.71	0.00145
2D, $k-w$	15.47	1.18	0.00372
2D, stress$-\omega$	14.69	1.05	0.00346
3D, $k-w$	15.17	1.09	0.00354
3D, stress$-\omega$	14.42	1.02	0.00338
80 Grit, $k-w$	13.61	0.98	0.00293
80 Grit, stress$-\omega$	13.47	0.96	0.00255
36 Grit, $k-w$	16.01	1.31	0.00399
36 Grit, stress$-\omega$	13.3	0.95	0.00352
20 Grit, $k-w$	16.63	1.34	0.00441
20 Grit, stress$-\omega$	13.08	0.93	0.00355

Since the turbulence models are based on Favre-averaging, $\tau_{xy}^T = -\bar{\rho}\widetilde{u''v''}$. Bowersox [15] has shown that $\bar{\rho}\widetilde{u''v''} = \bar{\rho}\overline{u'v'}$ (to third order). Hence the turbulence model shear stress predictions can be compared to the LDV data. The kinematic Reynolds shear stress numerical predictions for each turbulence model are shown with LDV experimental data in Fig. 4. For the smooth plate, and low roughness height plates (3D plate and 80 Grit plate), the turbulence models predicted the incompressible Reynolds shear stress very well. The simulation results show more discrepancy when the roughness height increases. The values of k_s^+ for 20 grit plate and 36 grit plate are 571 and 395, respectively, which are more than or close to the critical k_s^+ value of 400. Though the 2D plate has a small k_s^+ equal to 280, its roughness is a "d-type" roughness [16], in this case the geometric factor should be included for considering roughness effect [17]. This indicates that the ω boundary conditions in both models, especially stress$-\omega$ model, need to be refined encountering high roughness numbers and reconsidered to include the geometric factor.

CONCLUSION

The principle objective of the present study was to investigate the applicability of current ω based turbulence models for high speed flow with roughness. The models were evaluated against mean flow and turbulent shear stress data at Mach 2.7. In summary, both models performed equally well for the smooth plate case. When roughness is incorporated, both models matched the experimental data profiles fairly well for lower roughness heights. Overall the $k-\omega$ model gave better performance than stress$-\omega$ model. The stress$-\omega$ model did not show any strong advantages to make up for the extra computational cost associated with a Reynolds stress model. The simulation results indicated that the ω boundary conditions in both models, especially stress$-\omega$ model, need to be refined encountering high roughness numbers and reconsidered to include the geometric factor.

ACKNOWLEDGMENTS

The authors would like to thank Reece E. Neel of AeroSoft, Inc. for the help on GASP. We would also like to thank Robert M. Latin and Rodney D. W. Bowersox for their provision of the experimental data.

REFERENCES

[1] Shetz, J.A., 1993, Boundary Layer Analysis, Prentice Hall, New Jersey

[2] P. A. Durbin, G. Medic and J.-M Seo etc., 2001, "Rough Wall Modification of Two-layer $k-\omega$," Journal of Fluids Engineering, **123**, pp. 16-21.

[3] Kays, W. M., and Crawford, M. E., 1993, Convective Heat and Mass Transfer, 3rd ed., McGraw-Hill, NY.

[4] V. C. Patel and J. Y. Yoon, 1995, "Application of Turbulence Models to Separated Flow over Rough Surfaces," Journal of Fluids Engineering, **117**, pp. 234-241.

[5] H. Fan and R. Bowersox, 1999, "Numerical Analysis of High-Speed Flow over Rough Surfaces," 35th AIAA/ASME/SAE/ASEE Joint Propulsion Conference & Exhibit, pp. 1-8.

[6] van Driest, E.R., 1956, "On Turbulent Flow Near a Wall," Journal of Aerospace Science, Vol. 23, pp. 1007-1011.

[7] Cebeci, T. and Chang, K.C., 1978, "Calculation of Incompressible Rough-Wall Boundary-Layer Flows," AIAA Journal, Vol. 16, No.7, pp. 730-735.

[8] Kragstad, P., 1990, "Modification of the van Driest Damping Function to Include the Effects of Surface Roughness," AIAA Journal, Vol. 29, No. 6, pp. 888-894.

[9] Robert M. Latin and Rodney D. W. Bowersox, 2000, "Flow Properties of a Supersonic Turbulent Boundary Layer with Wall Roughness," AIAA Journal, Vol. 38, No. 10, pp. 1804-1821.

[10] David C. Wilcox, 2000, Turbulence Modeling for CFD, 2nd ed., DCW Industries, CA

[11] Reece E. Neel, Andrew G. Godfrey and David C. Slack, 2003, "Turbulence Model Validation in GASP Version

4," 33rd AIAA Fluid Dynamics Conference and Exhibit, Orlando, FL

[12] Cebeci, T. and Smith, A., 1974, Analysis of Turbulent Boundary Layer, Academic Press, New York

[13] Schlichting, H., 1979, Boundary Layer Theory, McGraw-Hill, New York

[14] Latin, R. and Bowersox, R., 1998, "Influence of Surface Roughness on Supersonic High Reynolds Number Turbulent Boundary Layer Flow," AFRL-PR-TR-1999-2004, Wright-Patterson AFB

[15] Bowersox, Rodney D. W. 1996, "Combined Laser Doppler Velocimetry and Cross-Wire Anemometry Analysis," AIAA Journal, Vol. 34, pp. 2269-2275.

[16] Perry, A. E., Schofield, W. H., and Joubert, P.N., 1969, "Rough Wall Turbulent Boundary Layers," Journal of Fluid Mechanics, Vol. 37, pp. 383-413.

[17] Javier Jiménez, 2004, "Turbulent Flows over Rough Walls", Annual Review Fluid Mechanics, pp. 173-196.

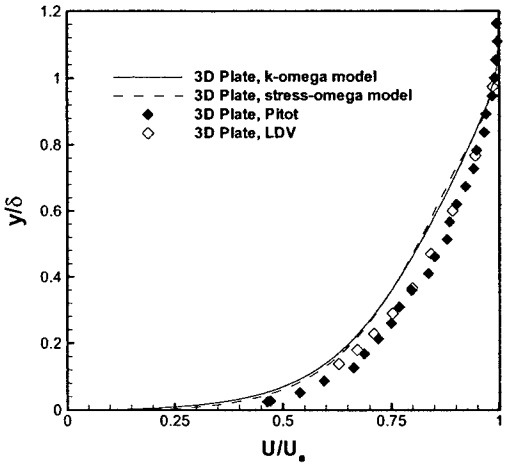

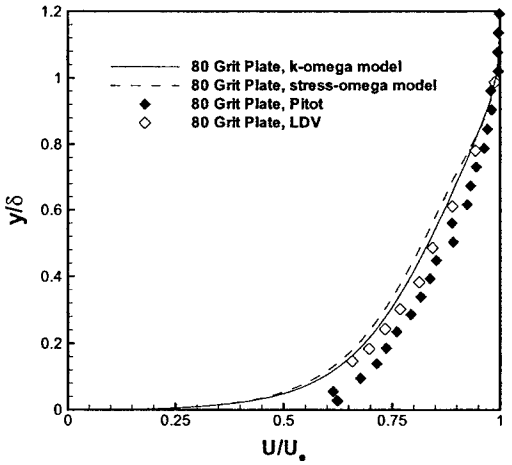

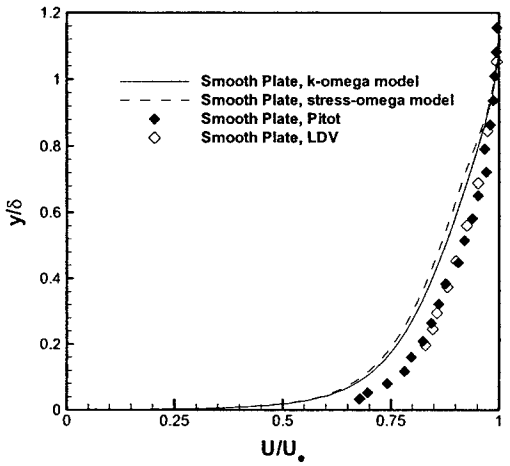

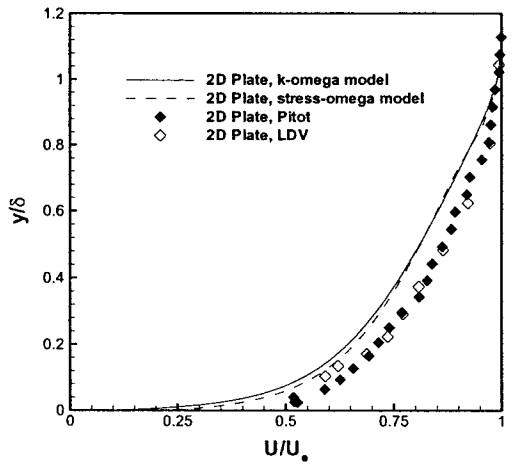

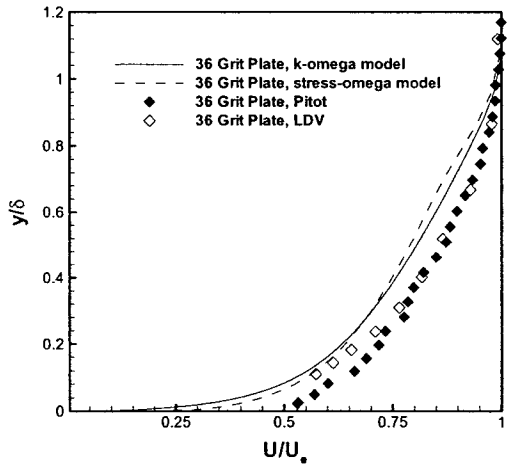

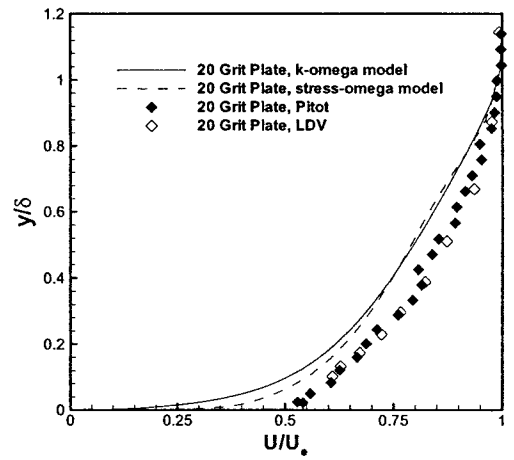

Fig. 1 Representative velocity profiles, with comparison to Pitot and LDV data of Latin and Bowersox [9]

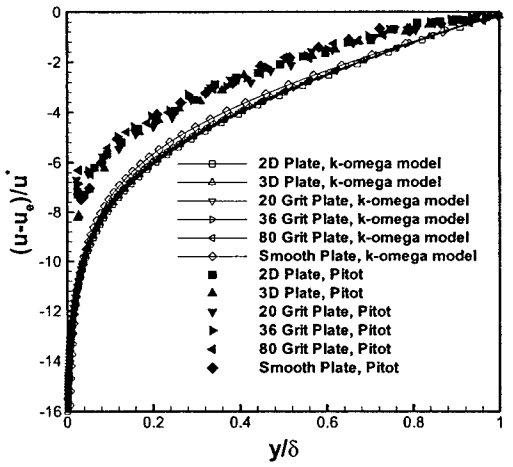

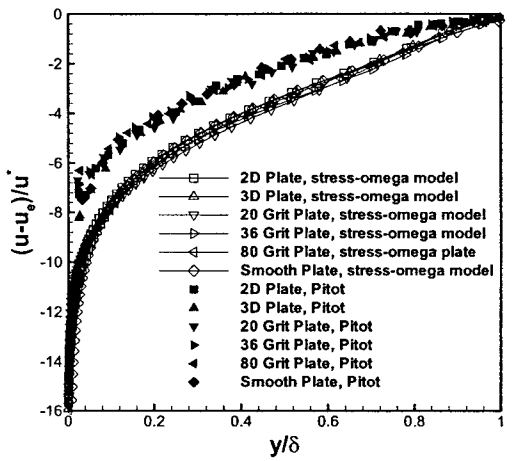

Fig. 2 Defect Law Plot, with comparison to Pitot and LDV data of Latin and Bowersox [9]

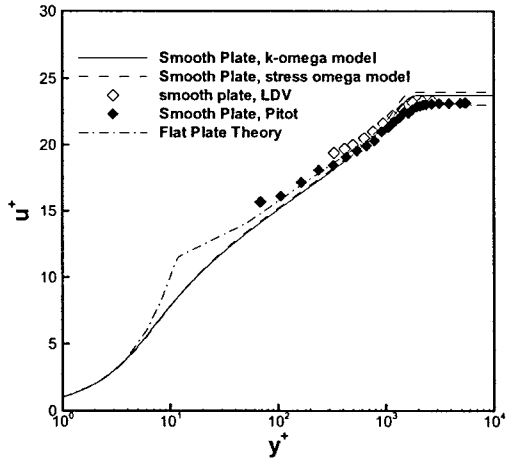

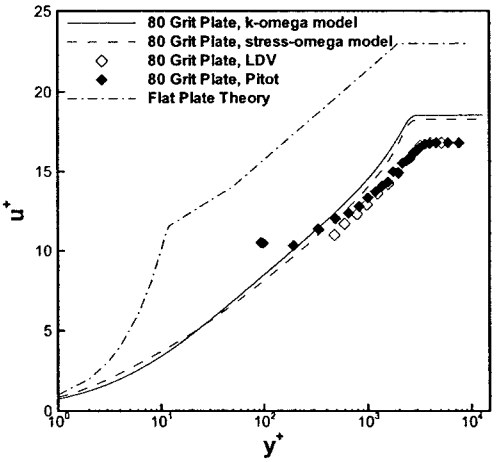

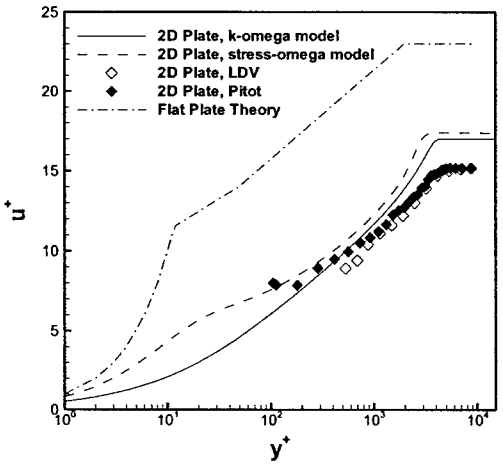

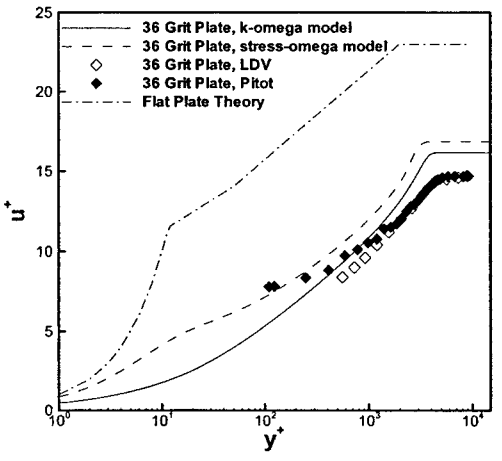

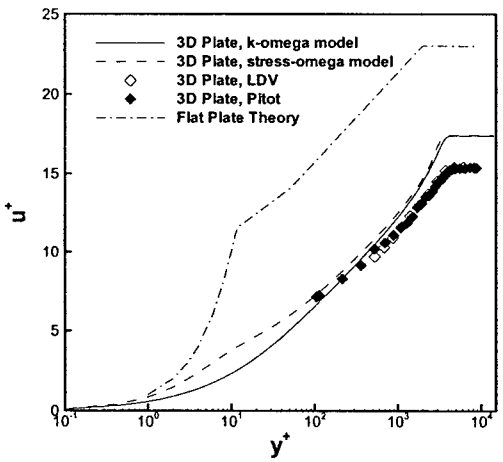

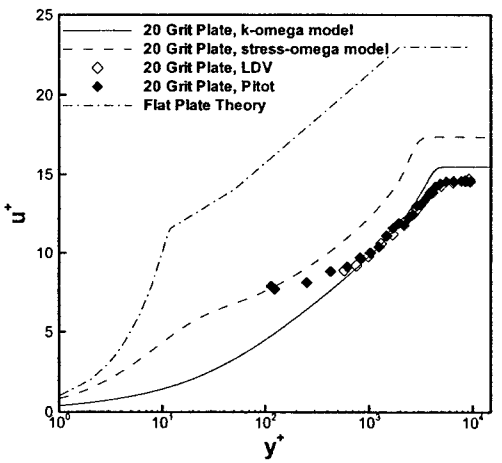

Fig. 3 Representative Law of the Wall plots, with comparison to Pitot and LDV data of Latin and Bowersox [9]

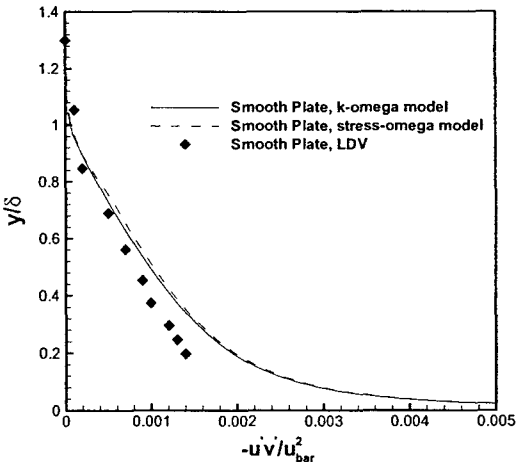

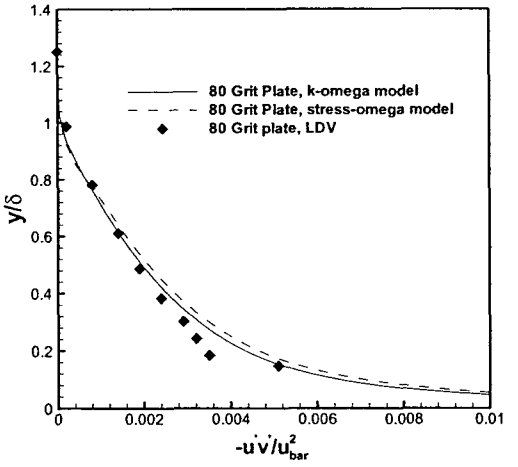

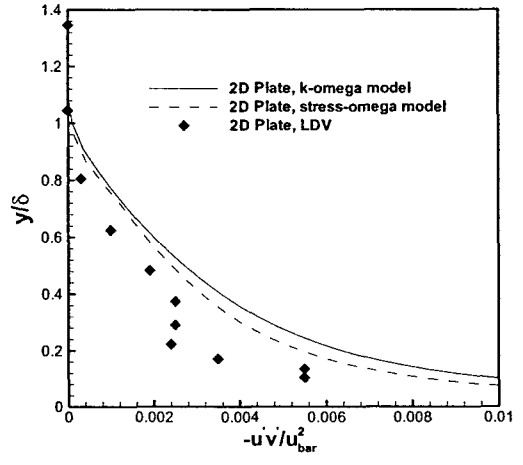

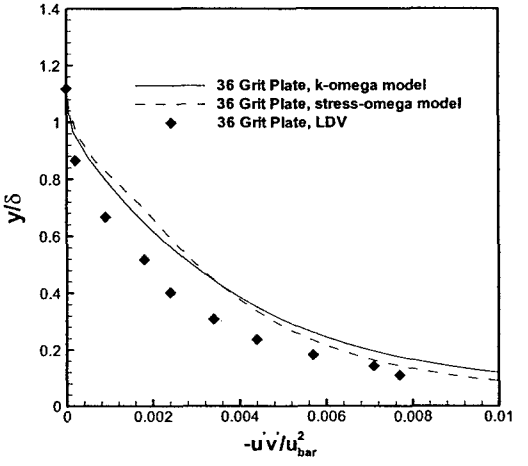

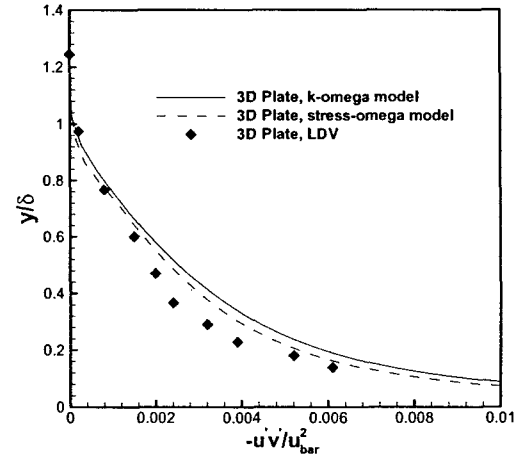

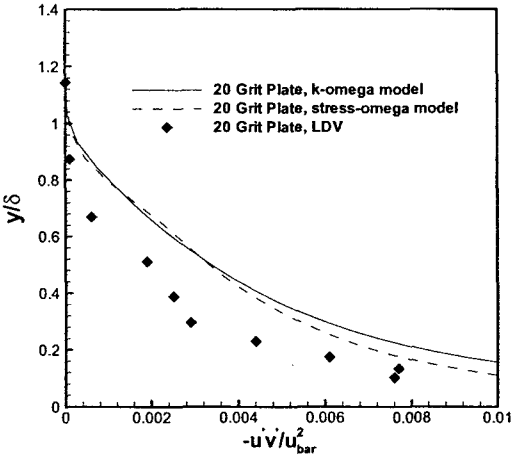

Fig. 4 Representative turbulent shear stress plots, with comparison to the LDV and Pitot data of Latin and Bowersox [9]

44th AIAA Aerospace Sciences Meeting and Exhibit
9-12 January 2006, Reno, Nevada

AIAA 2006-0718

Assessment of the Omega Based Models in the Prediction of Incompressible Turbulent Flows over Flat Rough Surfaces

Kiran Kumar Mothe[3] and Muhammad A.R. Sharif.[4]
University of Alabama, Tuscaloosa, AL, 35401

Prediction of the effect of surface-roughness on turbulent flows is important in many engineering applications. The present numerical study is aimed at assessing the adequacy of omega based turbulence models currently available, namely, the $k-\omega$ and the Stress-ω models in predicting the turbulent boundary layer flow over flat rough surfaces. The focus is mainly on the ability of these models to predict the mean velocity and Reynolds stresses. Incompressible turbulent flow over a flat plate with different types of roughness is simulated and the results obtained are compared with experimental results available in the literature. Both the models were able to predict the mean stream-wise velocity profile in the logarithmic region very well. The Stress-ω model was found to predict all Reynolds stress components reasonably well when compared with the experimental results. The $k-\omega$ model was found to predict the Reynolds shear stresses reasonably well but fails to predict the normal Reynolds stress components accurately.

Nomenclature

B	=	Constant in the log-law equation
ΔB	=	Roughness function
κ	=	von Karman constant
k_s	=	Equivalent sand grain roughness height
x,y	=	Tangential and wall-normal Cartesian co-ordinates
U,V	=	Mean velocity in the tangential and wall-normal directions
u,v	=	Fluctuating component of the velocity in tangential and wall-normal direction
τ	=	Shear Stress
ρ	=	Density
δ	=	Boundary layer thickness.
μ_t	=	Eddy Viscosity
K	=	Turbulence viscosity
τ_w	=	Shear stress at wall
τ_{xx}	=	Normal Reynolds stress in the stream-wise direction
τ_{yy}	=	Normal Reynolds stress in the wall-normal direction
τ_{xy}	=	Reynolds shear stress
u_τ	=	Friction velocity, $\sqrt{\tau_w/\rho}$
U^+	=	Nondimensional mean velocity, U/u_τ

[3] Graduate Student, Department of Aerospace Engineering and Mechanics, The University of Alabama, Tuscaloosa, Student Member, AIAA.
[4] Associate Professor, Department of Aerospace Engineering and Mechanics, The University of Alabama, Tuscaloosa, Associate Fellow, AIAA.

$\overline{u^{+2}}$ = normalized Reynolds stress in the tangential direction

Introduction

THE effect of surface roughness on turbulent boundary layer flows has long been a topic of research. All bodies exhibit some sort of effective roughness associated either with fabrication, nature, wear or a combination of these factors. Surface roughness can affect flight vehicles in many different ways. Roughness can have an impact on airfoil and wing performance, lift and drag, boundary layer separation, etc. As a result, it is important to be able to predict the effect of roughness on engineering quantities in turbulent boundary layer flows.

Various turbulence models, ranging from simple mixing length models to two-equation eddy viscosity models, with some modification, were used in the past, to predict the effect of roughness. These models were able to predict the shift in the mean flow velocity observed in flows over rough surfaces. But the ability of these models to predict the Reynolds stresses is unknown. To the authors' knowledge, no known computation of Reynolds stresses arising in turbulent flows over flat plates with roughness, using $k-\omega$ and $\tau-\omega$ models exist. Hence, in the present work, the experiments conducted by Krogstad and Antonia[1] and Flack and Schultz[2] were simulated in GASP, a commercial CFD solver, and the Reynolds stresses obtained from simulations as well as experimental results are compared with each other. The flow considered is incompressible and the roughness height is in the fully rough regime. The complete experimental conditions are given in the references mentioned above and hence, are not repeated here.

Literature Review

The best known early experiments on turbulent flows over rough surfaces are the ones by Nikuradse[3], who studied pipes roughened with carefully graded closely packed sand. The principal result obtained from these experiments is that the velocity distribution near a rough wall when plotted in the semi-logarithmic form of the law of the wall, has the same slope (giving the same von Karman constant, κ) as on a smooth wall, but different intercepts (additive constant, B) :

$$U^+ = \frac{1}{\kappa}\ln y^+ + B \quad \Delta B \tag{1}$$

Where, $\kappa \approx 0.41$ and $B \approx 5.0$ for both smooth and rough surfaces. The dependence of the shift ΔB, also called the roughness function, on the type and size of roughness is a subject of considerable research and much uncertainty, as is the definition of the effective location of the wall, from which the distance y is measured and where the average velocity is zero. From the experiments conducted by Nikuradse, it was found that, for sandgrain roughness,

$$\Delta B = \frac{1}{\kappa}\ln k_s^+ \quad 3.5 \tag{2}$$

Where, $k_s^+ = k_s u_\tau / \nu$. This makes the log-law for surfaces with sandgrain roughness,

$$U^+ = \frac{1}{\kappa}\ln \frac{y}{k_s} + 8.5 \tag{3}$$

The experimental measurements by Nikuradse were devoted exclusively to sand grain roughness. Therefore the applicability of his experimental results to other types of wall roughness is uncertain. Schlichting[4] introduced the idea of *equivalent sandgrain roughness* such that the data on rough-wall skin friction obtained by Nikuradse can still be used.

There are several different levels at which models of roughness are made, apart from the classical analysis in which Eq. (1) is integrated to derive friction formulas for pipes in the Moody diagram, and similar results for channels and flat plates.

Rotta[5] proposed a simple modification to the well know van Driest formula for mixing length to account for roughness by adding a shift to the distance from the wall and making it a function of the equivalent sand grain roughness height as,

$$l^+ = k(y^+ + \Delta y^+)\left[1 - \exp\left(-\frac{y^+ + \Delta y^+}{A^+}\right)\right] \tag{4}$$

Where,

$$\Delta y^+ = 0.9\left(\sqrt{K_s^+} - K_s^+ \exp\left[-\frac{K_s^+}{6}\right]\right) \tag{5}$$

Cebeci and Chang[6] used this model to perform some of the earliest calculations of boundary layer flows over rough walls. The model of Rotta along with several others were reviewed by Granville[7] to relate the van Driest damping function and the distribution of mixing length and eddy viscosity, to the roughness function ΔB of Eq. (1).

Krogstad[8] has suggested yet another version of mixing length model for sandgrain roughness. His method differs from previous methods since it stimulates the turbulent shear stresses near the wall by manipulating the amount of viscous damping rather than introducing a shift in the wall location.

The various mixing length models differ in the manner in which the effect of roughness is introduced, ranging from a shift in the wall distance (effectively specifying a non-zero mixing length at the wall) to introduction of roughness dependent damping functions in formulas of the van Driest type. Unfortunately these flows cannot be readily generalized to apply to flows with separation and to three-dimensional flows.

Another level of modeling involves the modification of smooth-wall turbulence-model equations to treat rough walls. The models used in the present study i.e. $k-\omega$ and $\tau-\omega$ fall into this category, in which the same equations are employed for smooth as well as rough surfaces but the effect of roughness is accounted for through the boundary condition at the wall. Unlike most Reynolds stress models which use the dissipation of turbulence kinetic energy to compute the dissipation, $\tau-\omega$ model uses the turbulence frequency, ω. In the present work the above two models are chosen as these models provide a natural way to incorporate effects of surface roughness in terms of ω.[9]

In the $k-\omega$ model, the boundary condition for ω is:

$$\omega|_{y=0} = \left(u_\tau^2/\nu\right)S_R; \qquad k_s^+ = u_\tau k_s/\nu \tag{6}$$

where,

$$S_R = \begin{cases} (50/k_s^+)^2, & k_s^+ < 25 \\ 100/k_s^+ & k_s^+ \geq 25 \end{cases}$$

In $\tau-\omega$ model, the resulting correlations are a little different from those of the $k-\omega$ model:

$$S_R = \begin{cases} (50/k_s^+)^2, & k_s^+ < 25 \\ 500/(k_s^+)^{3/2} & k_s^+ \geq 25 \end{cases}$$

All the eddy viscosity models use the Boussinesq assumption in order to calculate the turbulent stresses i.e. the turbulent stresses behave analogous to the laminar viscous diffusion terms as

$$-\rho\overline{u_i' u_j'} = \mu_t\left(\frac{\partial u_i}{\partial x_j}+\frac{\partial u_j}{\partial x_i}-\frac{2}{3}\delta_{ij}\frac{\partial u_k}{\partial x_k}\right)-\frac{2}{3}\delta_{ij}\rho K \tag{7}$$

Whereas, the $\tau-\omega$ model, which is a Reynolds stress model (RSM), solves six equations for the six Reynolds stresses which, in theory, will circumvent the deficiencies associated with the Boussinesq assumption.

Numerical Considerations

Flow solver

GASP version 4 is a commercial CFD flow solver developed by Aerosoft, Inc. It solves the integral form of the time-dependent "Reynolds Averaged Navier-Stokes" (RANS) equation in three dimensions. The turbulence models implemented in GASP include Wilcox's $k-\omega$ model (1998) and Wilcox's $\tau-\omega$ model and are validated by Reece et al.[10]. The $k-\omega$ model implemented in GASP calculates the Reynolds stresses using Boussinesq approximation, whereas the $\tau-\omega$ model solves the transport equations for the Reynolds stresses. Artificial compressibility method has been used in this study for resolving inviscid fluxes.

Grid Convergence

A flat plate grid with size 129x129 was used in this study. This grid size was decided upon, after getting comparable results with a higher grid size. The grid points are clustered towards the wall to resolve the turbulence parameters close to the wall. The y^+ corresponding to the first grid point off the wall is less than unity for all the simulations

Solution Convergence

The solution convergence was monitored by plotting the integrated force values in the tangential and wall-normal directions as a function of the iterative cycle. Convergence was assured in all the simulations by noting that the solution ceased to change after a certain number of iterations.

Boundary Conditions

At the inflow, total pressure and total temperature are set. For the wall surface, no slip adiabatic condition is used. At the top wall, boundary values are extrapolated from the interior cells. At the outflow boundary, back pressure is specified (equal to the free stream pressure in this case) and all other values are extrapolated from the first interior cell.

Results and discussion

In this section, the experimental results of flow over flat plates with different types of roughness, obtained experimentally by Flack et al.[2] and Krogstad et al.[1] are compared with the computational results. The Reynolds stresses are normalized by the square of friction velocity, u_τ, and plotted for comparison with experimental results. The experimental flow conditions are given in table 1.

		U_e (m/s)	Re_θ	K (mm)	K_s (mm)	K_s^+	ΔU^+ (mm)
Flack et al.[2]	Mesh	3.81	14120	0.32	0.68	138	8.5
	Sand paper	3.77	14340	0.69	0.51	100	7.7
Krogstad et al.[1]	Mesh	20	12800	0.69	4.96	382	11
	Circular rods	7	4806	1.6	9.7	311	10.5

Table 4: Experimental flow conditions

Flat plate with woven mesh roughness, experimental results by Flack et al.[2]

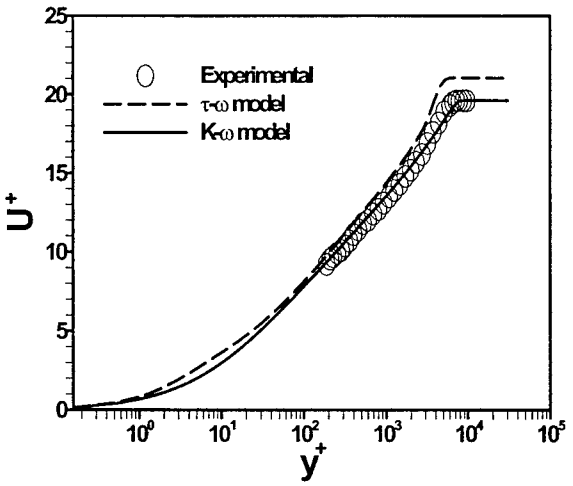

Figure 1: Mean velocity profile in wall

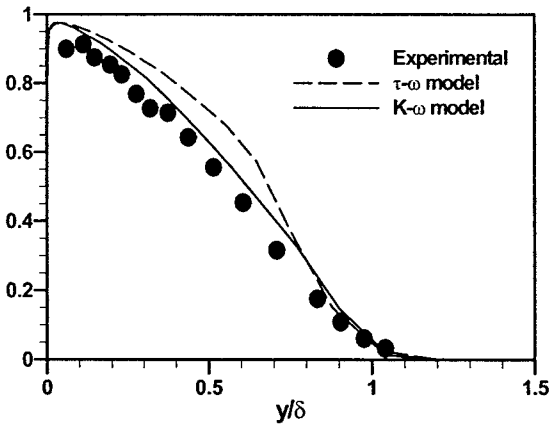

Figure 2: $\overline{u^+v^+}$ profile

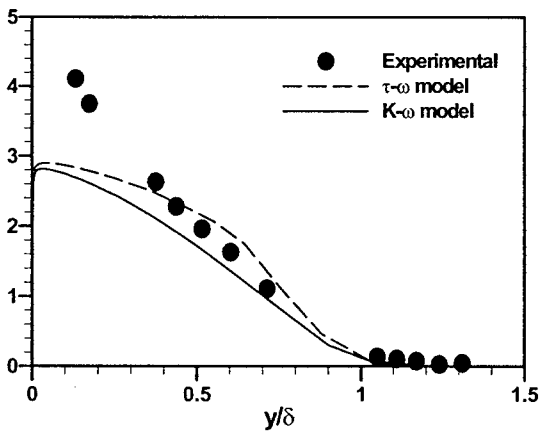

Figure 3: $\overline{u^{+2}}$ profile

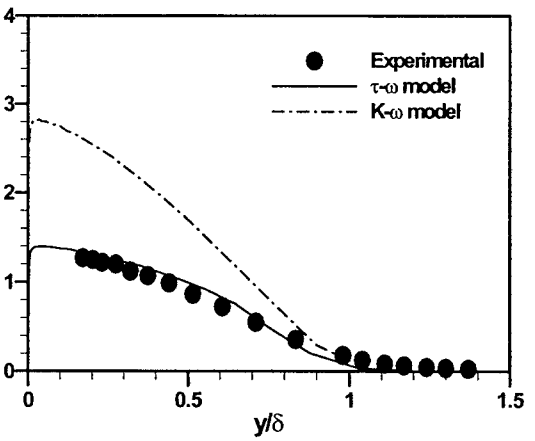

Figure 4: $\overline{v^{+2}}$ profile

In figure (1), the mean velocity profile is plotted in wall units. It can be seen from figure 1 that both $k-\omega$ and $\tau-\omega$ models predict the velocity profile very well. In figure (2), the Reynolds shear stress, τ_{xy} normalized by the friction velocity, u_τ is plotted. Similarly, the normal components of Reynolds stress tensor, τ_{xx} and τ_{yy}, normalized by the friction velocity, are plotted in figures (3) and (4) respectively. From figure (2) it can be seen that both the turbulence models used in this study are able to predict the Reynolds shear stress very well, although $k-\omega$ model is slightly over-predicting. From figure (3), It can be noticed that both of the models have under-predicted the peak in τ_{xx} profile. Figure (4) shows that the $\tau-\omega$ model is in excellent agreement with the experimental results, whereas, $k-\omega$ model is unable to predict the Reynolds stress in the wall-normal direction.

Flat plate with sandpaper roughness, experimental results by Flack et al.[2]

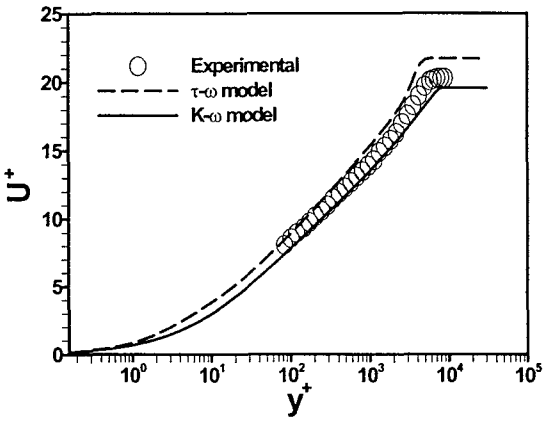

Figure 5: Mean velocity profile in wall units

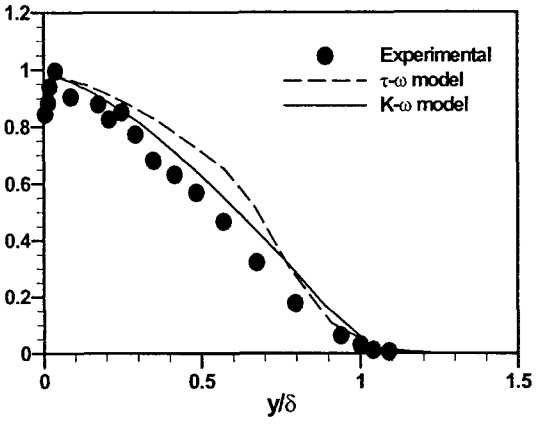

Figure 6: $\overline{u^+v^+}$ profile

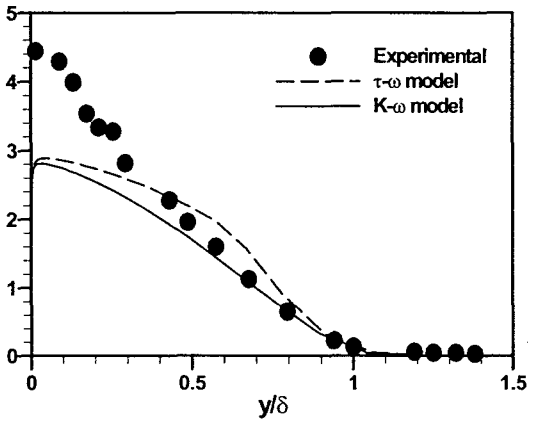

Figure 7: $\overline{u^{+2}}$ profile

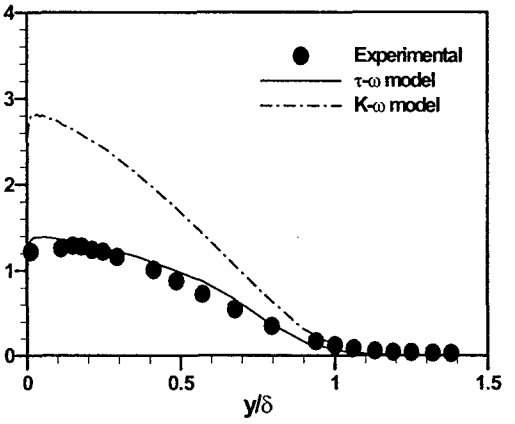

Figure 8: $\overline{v^{+2}}$ profile

Figure (5) shows the mean velocity profile plotted in wall units. Both $k-\omega$ and $\tau-\omega$ models are found to be in excellent agreement with the experimental results. Figure (6) shows the normalized Reynolds shear stress profile. Both of these models are able to predict the Reynolds shear stress reasonably well. The normal components of Reynolds stress tensor, τ_{xx} and τ_{yy}, normalized by the friction velocity, are plotted in figures (7) and (8) respectively. Figure (8) shows that $\tau-\omega$ model is in excellent agreement with the experimental results.

The results obtained for the flat plate with sandpaper roughness are quite similar to the ones obtained with mesh roughness, since the roughness chosen in the above two cases has more or less the same effect on mean velocity profile. Also, it has been shown by Flack et al.[2] that the normalized Reynolds stresses collapse for both mesh roughness and sandpaper roughness cases studied by them.

Flat plate with mesh roughness, experimental results by Krogstad et al.[1]

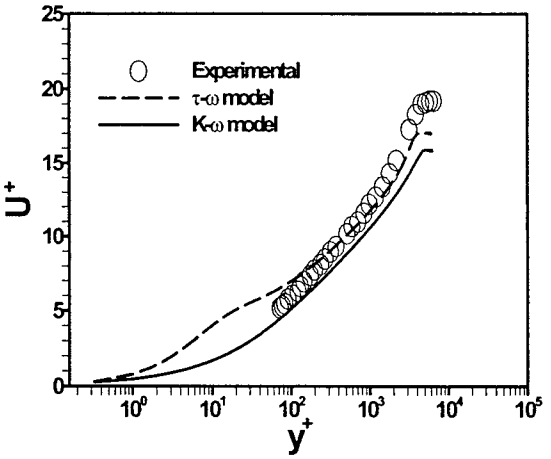

Figure 9: Mean velocity profile in wall units

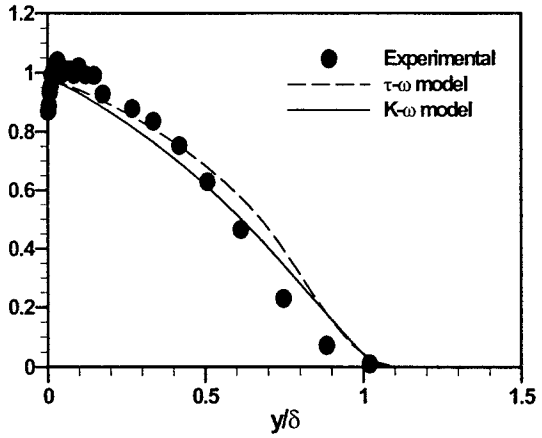

Figure 10: $\overline{u^+v^+}$ profile

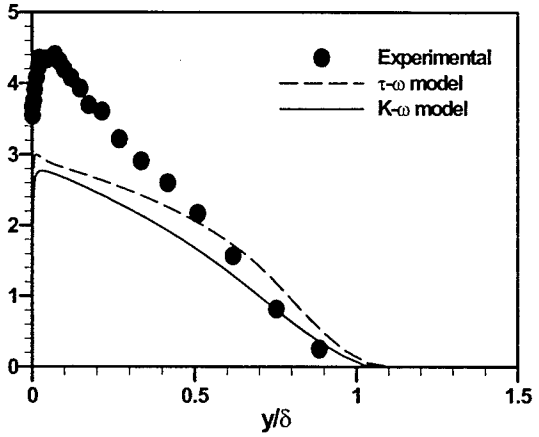

Figure 11: $\overline{u^{+2}}$ profile

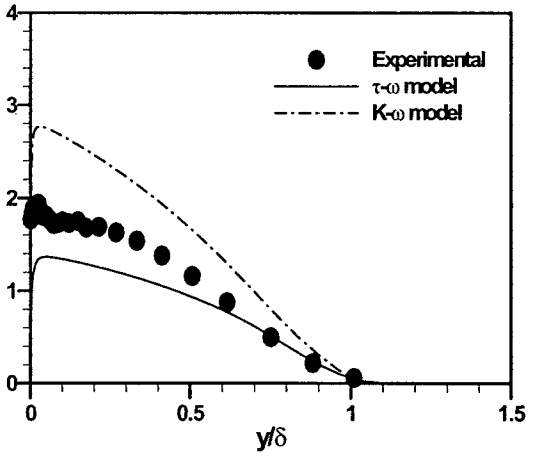

Figure 12: $\overline{v^{+2}}$ profile

The mean velocity profile in wall units is plotted in Figure (9). Figures (10) to (12) show the normalized Reynolds stress tensor components. Mean velocity profile and the Reynolds shear stress are well predicted by both the models. The turbulence models are unable to predict the normal components of the Reynolds stress tensor, τ_{xx} and τ_{yy}.

Flat plate with circular rods, experimental results by Krogstad et al.[1]

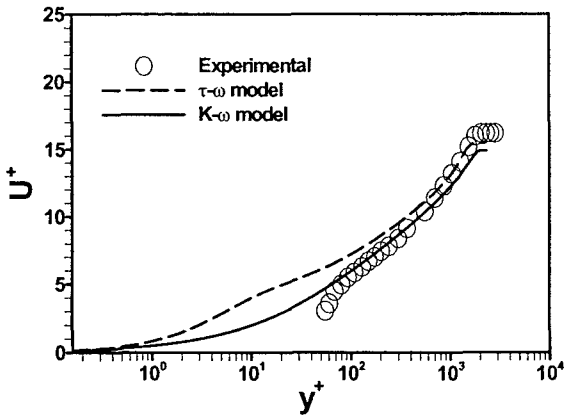

Figure 13: Mean velocity profile in wall

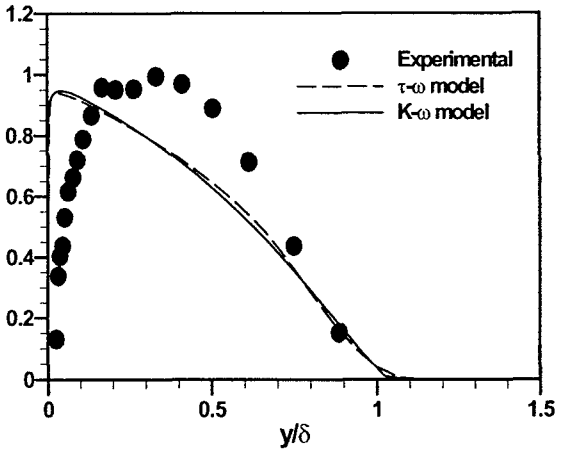

Figure 14: $\overline{u^+v^+}$ profile

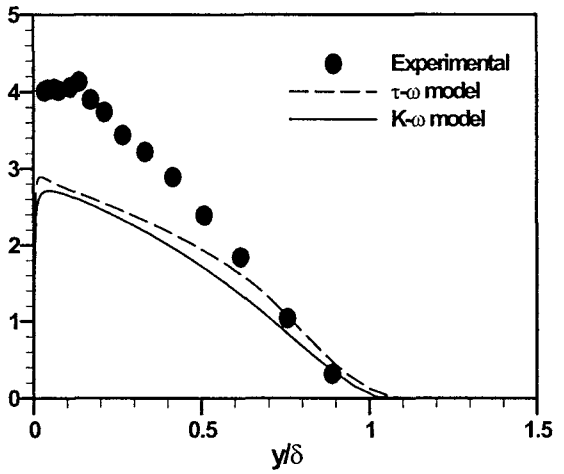

Figure 15: $\overline{u^{+2}}$ profile

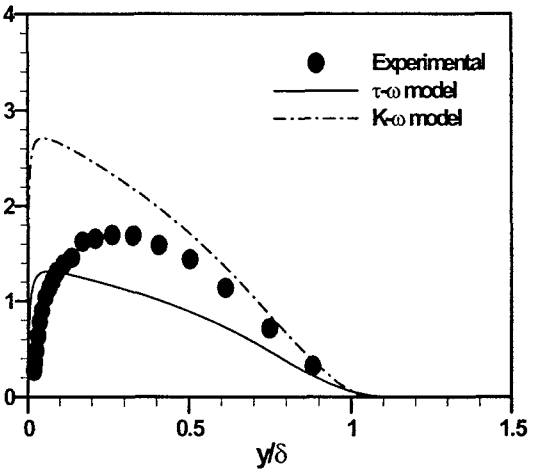

Figure 16: $\overline{v^{+2}}$ profile

The mean velocity profile in wall normal units is plotted in figure (13). Normalized Reynolds stress components are plotted in figures (14) to (16). From figure (14) it can be seen that there is a shift in peak in the experimental result, which the turbulence models are unable to predict. Also, the turbulence models used are unable to predict the normal components of the Reynolds stress tensor, τ_{xx} and τ_{yy}.

In all of the above plots, it can be seen that the $k-\omega$ model is completely unable to predict the Reynolds stress in the wall-normal direction. This is due to the use of Boussinesq assumption, eq. (7) which is valid only for isotropic turbulence. Hence the calculated Reynolds stresses are more or less equal in the wall-normal and stream-wise direction. But the Reynolds stress models do not have this assumption and hence the $\tau-\omega$ model is able to calculate the Reynolds stresses more accurately for all types of surface roughness considered in this study. The difference can also be attributed to the determination of u_τ in the corresponding experiments. In most cases u_τ has

been determined by a profile matching technique, which has been proven to be very accurate for smooth surfaces. However in the rough wall case the uncertainty is much higher since both the exact location of the wall and ΔU^+ are unknown.

Conclusion

A numerical assessment of k-omega and stress-omega models in the prediction of turbulent stresses arising from incompressible flow over a flat plate with different types of roughness is conducted. Both the models predicted the mean flow velocity profile fairly well. These models predicted the shape of the turbulent stress profiles reasonably well, but there is room for improvement in the accuracy of the prediction. The difference can also be attributed to the determination of u_τ in the corresponding experiments. In most cases u_τ has been determined by a profile matching technique, which has been proven to be very accurate for smooth surfaces. However in the rough wall case the uncertainty is much higher since both the exact location of the wall and ΔU^+ are unknown. Also, apparently, the equivalent sandgrain roughness, K_s is not a good indicator for different types of roughness as far as calculating the Reynolds stresses is concerned. Additional parameters like roughness density and blockage effect may be needed to accurately calculate the Reynolds stresses for various types of roughness. K-Omega model is particularly unable to predict the turbulent stresses in the wall-normal direction due to the inherent isotropic eddy viscosity assumption in the model.

Acknowledgments

Financial support for this work was provided by a grant from the Air Force Office of Scientific Research F49620-02-1-0365.

References

[1]Krogstad, P.A., Antonia R.A., "Surface roughness effects in turbulent boundary layers," *Experiments in Fluids*, Vol. 27, 1999, pp. 450-460

[2]Karen A. Flack, Michael P.Schultz, and Thomas A. Shapiro, "Experimental support for Townsend's Reynolds number similarity hypothesis on rough walls," *Physics of Fluids*, Vol. 17, 2005.

[3]Nikuradse, J., "Laws of flow in rough pipes," *NACA TM 1292*, National Advisory committee on Aeronautics.

[4]Schlichting, H., 1936, "Experimental investigation of the problem of surface roughness," *NACA TM 832*, National Advisory committee on Aeronautics.

[5]Rotta, J. C., "Turbulent boundary layers in incompressible flow," *Progress in Aeronautical sciences*, Pergamon, Oxford, England, UK, Vol. 2, 1962, pp. 1-219.

[6]Cebeci, T., and Chang, K. C., "Calculation of incompressible rough wall boundary-layer flows," *AIAA journal*, Vol. 16, No. 7, 1978, pp. 730-735.

[7]Granville, P. S., "Mixing-length formulations for turbulent boundary layers over arbitrary rough surfaces," *Journal of ship research*, Vol. 29, No. 4, 1985, pp. 367-381.

[8]Krogstad, P. A., "Modification of the van Driest damping function to include the effects of surface roughness," *AIAA Journal*, Vol. 29, pp. 888-894.

[9]Wilcox, D. C., *Turbulence Modeling for CFD*, DCW Industries, 2nd ed., 1998

[10]Reece E. Neel, Andrew G. Godfrey, David C. Slack, "Turbulence model validation in GASP version 4," *AIAA fluid dynamics conference and exhibit*, Orlando, FL, 2003

[11]Raupach, M. R., Antonia R.A., and Rajagopalan, S., "Rough wall turbulent boundary layers," *Applied Mechanics Review* Vol.44, 1 (1991).

[12]Patel, V. C., "Perspective: flow at high Reynolds number and over rough surfaces-Achilles heel of CFD," *Journal of Fluids Engineering*, Vol. 120, 434 (1998).

[13]Krogstad, P.A., Antonia R.A., Browne, L. W. B., "Comparison between rough- and smooth-wall turbulent boundary layers," *J. Fluid Mech.*, vol. 245, 1992, pp. 599-617.

[14]Krogstad, P.A., Antonia R.A., "Structure of turbulent boundary layers on smooth and rough walls," *J. Fluid Mech.*, vol. 277, 1994, pp. 1-21